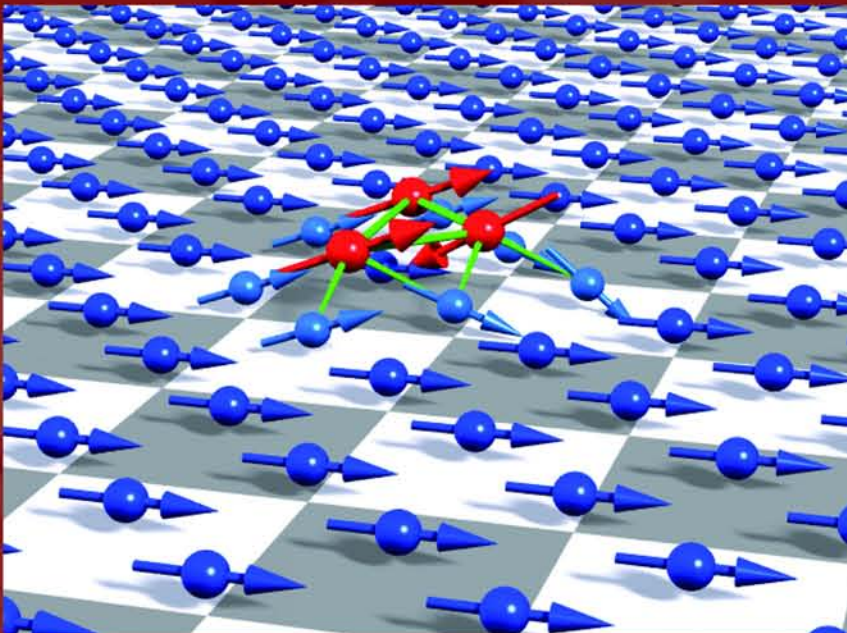




# Theory of Magnetic Transition Metal Nanoclusters on Surfaces

Samir Lounis



Schriften des Forschungszentrums Jülich  
Reihe Materie und Material/Matter and Materials Band/Volume 41

---



Forschungszentrum Jülich GmbH  
Institut für Festkörperforschung (IFF)  
Quanten-Theorie der Materialien (IFF-1)

# **Theory of Magnetic Transition Metal Nanoclusters on Surfaces**

Samir Lounis

Schriften des Forschungszentrums Jülich  
Reihe Materie und Material/Matter and Materials Band/Volume 41

---

ISSN 1433-5506

ISBN 978-3-89336-501-2

Bibliographic information published by the Deutsche Nationalbibliothek.  
The Deutsche Nationalbibliothek lists this publication in the Deutsche  
Nationalbibliografie; detailed bibliographic data are available in the  
Internet at <http://dnb.d-nb.de>.

Publisher  
and Distributor: Forschungszentrum Jülich GmbH  
Zentralbibliothek, Verlag  
D-52425 Jülich  
phone:+49 2461 61-5368 · fax:+49 2461 61-6103  
e-mail: [zb-publikation@fz-juelich.de](mailto:zb-publikation@fz-juelich.de)  
Internet: <http://www.fz-juelich.de/zb>

Cover Design: Grafische Medien, Forschungszentrum Jülich GmbH

Printer: Grafische Medien, Forschungszentrum Jülich GmbH

Copyright: Forschungszentrum Jülich 2007

Schriften des Forschungszentrums Jülich  
Reihe Materie und Material/Matter and Materials Band/Volume 41

D 82 (Diss., RWTH Aachen, 2007)

ISSN 1433-5506  
ISBN 978-3-89336-501-2

The complete volume is freely available on the Internet on the Jülicher Open Access Server (JUWEL)  
at <http://www.fz-juelich.de/zb/juwel>

Neither this book nor any part may be reproduced or transmitted in any form or by any means,  
electronic or mechanical, including photocopying, microfilming, and recording, or by any  
information storage and retrieval system, without permission in writing from the publisher.

*"The task is not so much to see what nobody has seen yet, but to think what nobody has thought yet about that everybody sees"*

*A. Schopenhauer*



# Abstract

The question how magnetism behaves when the dimension of materials is reduced to increasingly smaller sizes has attracted much research and led to the development of the field of magnetic nanostructures. This research has been fueled by the technological potential of these systems for the field of high-density magnetic storage media and has been accelerated by the many novel experimental methods and techniques developed exhibiting atomic resolution. This thesis is motivated by the quest for the understanding and the exploration of complex magnetism provided by atomic scale magnetic clusters deposited on surfaces or embedded in the bulk. The nature of magnetism in these systems can be very rich, in that the properties depend on the atomic species, the cluster size, shape and symmetry or choice of the substrate. Small variations of the cluster parameter may change the properties dramatically. Particularly rich and particularly challenging for experiment and theory is the behavior of clusters with competing magnetic interactions either between the cluster atoms or between the cluster and the substrate. In both cases magnetic frustration can lead to non-collinear magnetic structures for which the magnetic quantization axis changes from atom to atom.

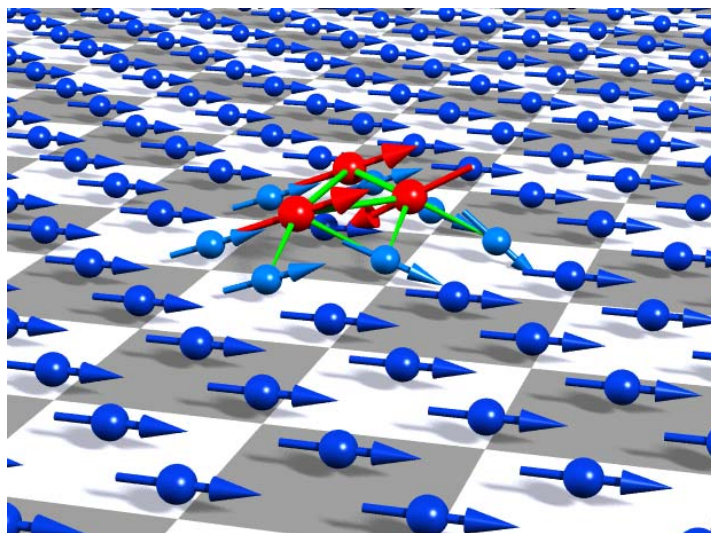
This thesis sheds light onto these systems from a theoretical perspective. Use is made of the density functional theory (DFT), the most successful material specific theory for describing electronic and derived properties from first-principles. Acting within this framework, we have developed and implemented the treatment of non-collinear magnetism into the Jülich version of the full-potential Korringa-Kohn-Rostoker Green Function (KKR-GF) method. The KKR-GF method provides several advantages compared to other first-principles methods. Based on solving the Dyson equation it allows an elegant treatment of non-periodic systems such as impurities and clusters in bulk or on surfaces. Electronic, magnetic properties and the observables provided by experimental techniques such as x-ray, scanning tunneling microscopy and spectroscopy can be accessed with the KKR-GF method.

Firstly, the method was applied to  $3d$  transition-metal clusters on different ferromagnetic surfaces. Different types of magnetic clusters were selected. Clusters of Fe, Co, Ni atoms are ferromagnetic and thus magnetically collinear. In order to investigate magnetic frustration due to competing interactions within the ad-cluster we considered a (001) oriented surface of *fcc* metals, a topology which usually does not lead to non-collinear magnetism. We tuned the strength of the magnetic coupling between the ad-clusters and the ferromagnetic surface by varying the substrate from the case of Ni(001) with a rather weak hybridization of the Ni *d*-states with the adatom *d*-states to the case of Fe<sub>3ML</sub>/Cu(001) with a much stronger hybridization due to the larger extend of the Fe wavefunctions. On Ni(001), the interaction between the Cr- as well as the Mn-dimer adatoms is of antiferromagnetic nature, which is in competition with the interaction with the substrate atoms. If we allow the magnetism to be non-collinear, the moments rotate such the Cr-(Mn) adatom moments are aligned antiparallel to each other and are basically perpendicular to the substrate moments. However, the weak AF(FM) interaction with the substrate causes a slight tilting towards the substrate, leading to an angle of  $94.2^\circ$  ( $72.6^\circ$ ) instead of  $90^\circ$ . After performing total energy calculations we find that for Cr-dimer the ground state is collinear whereas the Mn-dimer prefers the non-collinear configuration as ground state. The Heisenberg model is shown

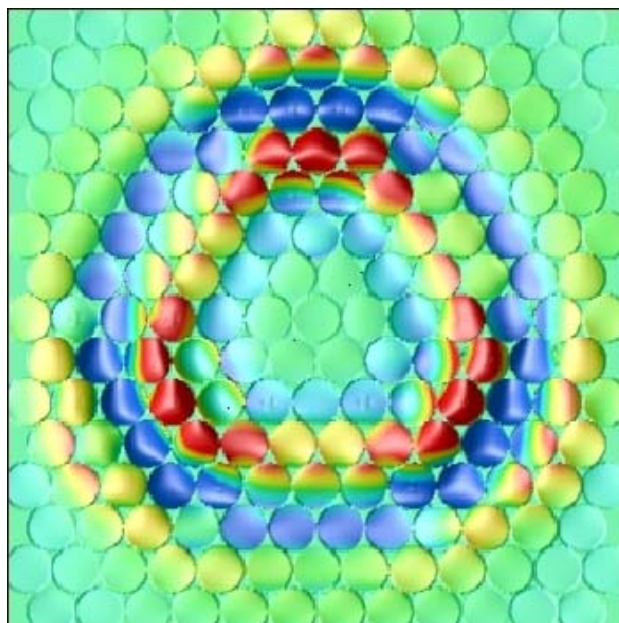
to be good for the prediction of local energy minima but not for describing the magnetic ground state. Bigger clusters are found to be magnetically collinear. These calculations were extended to  $3d$  multimers on  $\text{Fe}_{3\text{ML}}/\text{Cu}(001)$ . Here the strong hybridization with the substrate leads to a collinear AF coupling of both Cr adatoms to the substrate Fe atoms while the Mn-dimer is non-collinear. The ground states for both trimers are non-collinear. All neighboring Cr (Mn) moments in the compact tetramer are antiferromagnetically aligned in-plane, with the directions slightly tilted towards (outwards from) the substrate to gain some exchange interaction energy. Note that among different shapes of tetramers the non-collinear compact Cr-tetramer appeared to be the most stable one. The second type of frustration was investigated employing a Ni(111) surface, a surface with a triangular lattice of atoms, where both kind of competing magnetic interactions occur: intra-cluster magnetic frustration and cluster-substrate magnetic interaction. The magnetic configurations for compact Cr or Mn ad-trimers are very similar to the expected topological non-collinear configuration of a free frustrated trimer (angle of  $120^\circ$  between successive adatoms). Additional trimer shapes considered have collinear ground states with very small energy differences, in particular for Mn, with respect to the non-collinear local minimum. Among the investigated tetramers only the compact ones are Ferrimagnetic. Parity of number of adatoms in finite antiferromagnetic nanowires is shown to be crucial in predicting whether the magnetic ground state is non-collinear or collinear. We show that nanochains with an even number of adatoms are always magnetically non-collinear while an odd number of adatoms leads under given conditions to a collinear ferrimagnetic ground state.

In the second part of the thesis we applied the KKR-GF method to reveal experimental issues related to scanning tunneling microscopy (STM). Hence, we investigated the scattering of a two-dimensional surface state at adatoms. Here it is shown theoretically for some special cases as well as experimentally (STM) that any attractive potential should lead to a localized state. With a systematic study, including  $sp$  as well as  $d$  adatoms on or in the surface, we demonstrate that the cited statement, that any attractive potential should lead to a localized state, is not correct. Indeed, we derive a better criteria based on the scattering length of the adatom.

At last, we show that Fermi surfaces can be imaged through STM. The Fermi surface is one of the most important properties in metals as they determine many transport properties as well as long-ranged interactions. The new effect is explained by means of scattering of electrons at subsurface impurities. Since the electrons propagate away from the impurities with velocity vectors perpendicular to the Fermi surface, flat regions on this surface focus the electrons in special space-angle directions, leading in real space to highly symmetric STM spots around the impurity.



Non-collinear magnetic structure of a Mn-trimer deposited on the surface of Ni(001).



Real space imaging of the Fermi surface of Cu(111) by STM, simulated with the KKR-GF method, considering a buried Co impurity as local probe.



---

# Contents

<b>1</b>	<b>Introduction</b>	<b>1</b>
<b>2</b>	<b>Density Functional Theory</b>	<b>7</b>
2.1	Born-Oppenheimer Approximation . . . . .	8
2.2	Hohenberg-Kohn Theorems . . . . .	8
2.3	The Kohn-Sham Ansatz . . . . .	9
2.4	The Local Spin Density Approximation . . . . .	11
2.5	Non-collinear Spin Density . . . . .	12
<b>3</b>	<b>The KKR Green Function Method</b>	<b>15</b>
3.1	Introduction . . . . .	15
3.2	Green Function Method . . . . .	16
3.3	Single-Site Scattering . . . . .	18
3.4	Multiple-Scattering Theory . . . . .	21
3.5	Multiple-Scattering: The Green Function Approach . . . . .	23
3.6	Description of the Full Potential . . . . .	25
3.7	Self-Consistency Algorithm . . . . .	27
<b>4</b>	<b>KKR for Non-collinear Magnetism</b>	<b>31</b>
4.1	Introduction . . . . .	31
4.2	Non-collinear KKR Formalism . . . . .	33
4.3	Rotation Matrices . . . . .	34
4.4	Host Green Functions and $t$ -matrices . . . . .	37
4.4.1	Screened (tight-binding) KKR Method . . . . .	39
4.4.2	Two-Dimensional Systems: Finite-Thickness Slabs and Half-Infinite Crystals . . . . .	40

---

4.5	t-matrix for Perturbed Atoms . . . . .	41
4.6	Structural Green Function . . . . .	43
4.7	Green Function for Perturbed Atoms . . . . .	44
4.8	Total Energy . . . . .	46
4.9	Lloyd's Formula . . . . .	48
4.10	Frozen Potential Approximation for Magnetic Interactions . . . . .	50
4.11	Formula for Exchange Interactions $J_{ij}$ . . . . .	52
4.12	Test of the Implementation . . . . .	55
<b>5</b>	<b>Complex Magnetism of 3d Clusters on Ni(001)</b>	<b>59</b>
5.1	Introduction . . . . .	59
5.2	Calculational Details . . . . .	59
5.3	Magnetic Properties of Ni(001) Surface . . . . .	60
5.4	3d Single Adatoms . . . . .	61
5.5	3d Single Inatoms . . . . .	63
5.6	Adatom Dimers . . . . .	64
5.7	Inatom Dimers . . . . .	71
5.8	Trimers . . . . .	72
5.9	Tetramers and Pentamers . . . . .	74
5.10	Summary . . . . .	76
<b>6</b>	<b>Complex Magnetism of Small Clusters on Fe<sub>3ML</sub>/Cu(001)</b>	<b>81</b>
6.1	Introduction . . . . .	81
6.2	Magnetic Properties of Fe/Cu(001) Surface . . . . .	81
6.3	Calculations Setup for Clusters . . . . .	82
6.4	Single Adatoms . . . . .	83
6.5	Adatom Dimers . . . . .	84
6.6	Trimers . . . . .	86
6.7	Tetramers . . . . .	89
6.8	Cr-pentamer . . . . .	92
6.9	Comparison with Experiment: Case of Cr . . . . .	93
	6.9.1 Experimental Setup . . . . .	93
	6.9.2 Comparison . . . . .	94
6.10	Comparison with Experiment: Case of Mn . . . . .	97

---

6.11	Summary	98
<b>7</b>	<b>Cr and Mn Clusters on Ni(111)</b>	<b>101</b>
7.1	Introduction	101
7.2	Computational Details	102
7.3	Surface of Ni(111)	103
7.4	Single Adatoms	103
7.5	Adatom dimers	104
7.6	Trimers	106
7.7	Tetramers	111
7.8	Discussion of Technical Assumptions within our Simulations	113
7.9	Summary	115
<b>8</b>	<b>Strong Even-Odd Effects in Magnetism of Nanochains</b>	<b>117</b>
8.1	Introduction	117
8.2	Ab-initio Results	117
8.3	Heisenberg Model Results	119
	8.3.1 Case of Constant Rotation Angles	120
	8.3.2 General Case	123
8.4	Summary	127
<b>9</b>	<b>Surface State Scattering by Small Clusters</b>	<b>129</b>
9.1	Introduction	129
9.2	Computational Aspects	131
9.3	Tersoff-Hamann Model	132
9.4	Origin of the Localization	134
9.5	Surface State of Cu(111)	135
9.6	3d-impurities as Adatoms	135
9.7	sp-impurities as Adatoms	141
9.8	Impurities in the Surface Layer	143
9.9	Limitations of the LSDA	144
9.10	Summary	144

---

<b>10 Focusing Effect due to Subsurface Impurities</b>	<b>145</b>
10.1 Introduction . . . . .	145
10.2 Origin of the Effect . . . . .	148
10.3 Computational details . . . . .	155
10.4 Co impurity below Cu(111) . . . . .	155
10.5 Magnetic effect: Interface Cu/Co(111) . . . . .	158
10.6 Co impurity below Cu(001) . . . . .	161
10.7 Summary . . . . .	162
<b>11 Conclusion</b>	<b>165</b>
<b>A Force Calculations</b>	<b>169</b>
<b>B Lattice Relaxations</b>	<b>171</b>
<b>Bibliography</b>	<b>173</b>
<b>Acknowledgments</b>	<b>181</b>
<b>Curriculum Vitae</b>	<b>183</b>

# Chapter 1

## Introduction

“Plenty of room at the bottom” was the title of the by now classic talk of Richard P. Feynman [1], given on December 29th 1959 at the annual meeting of the American Physical Society at the California Institute of Technology (Caltech), in which he envisaged exciting new phenomena that may revolutionize science and technology and affect our everyday lives – if only we were able to manipulate and control things on a small scale, on the atomic scale. Some of these visions became reality. With the invention of new experimental techniques, such as the scanning tunneling microscope (STM), invented by Binnig and Rohrer in 1982 [2] who were awarded the Nobel prize in 1986, or the atomic force microscope (AFM), a powerful tool which measures the force acting on conducting and non-conducting probes in the vicinity of their surfaces, manipulating and positioning of individual atoms and probing their physical properties has developed into a big scientific activity. Another example is the development of the x-ray magnetic circular dichroism (XMCD) which measures the dependence of x-ray absorption on the helicity of the light by a magnetic material, with a sensitivity down to extremely low coverages of magnetic materials deposited on substrates including chains [3] and adatoms [3, 4, 5]. So-called sum rules [6] have been derived allowing to determine from those data the atom- and orbital-specific spin and orbital magnetic moments.

These unprecedented capabilities inspire the exploration of new physics and sparked this thesis. The focus of the thesis is on the properties and behavior of atomic scale magnetism, the magnetism of ad-atoms and atomic scale clusters on surfaces, in particular ferromagnetic surfaces, as well as the simulation of STM images for adatoms or clusters buried below the surface. The results in this thesis are of theoretical and simulational nature in that we used the density functional theory (DFT) [7, 8], at present the most powerful and most widely applied theory, to describe the physical properties on the level of quantum theory of interacting electrons without adjustable parameters.

Small atomic clusters deposited on surfaces constitute extremely interesting systems, as their electronic structure lies between the structure of the bulk and that of free molecules or atoms. In particular, the electronic structure is characteristic of the cluster, in the sense that it depends on the chemical nature of the adatoms, the shape, and size of the cluster and orientation of the moments as well as on the substrate material and the surface orientation on which the cluster is deposited. Each cluster constitutes a new system as the electronic structure changes discretely from cluster to cluster. Thus, it is a *terra incognita* for the electronic properties. Small clusters of magnetic atoms on surfaces are expected to experience an enhancement of the magnetic properties. As the cluster size decreases and the average coordination of the atoms becomes smaller, the decreased hybridization of the atomic wavefunctions should lead to more pronounced magnetic effects. The motivation to study magnetic clusters has also a profound practical background as they have the potential of increasing the bit-density in magnetic information storage. One may envision that future magnetic hard discs with information carried by magnetic clusters will have a storage density two orders of magnitude larger than those used today.

Recent remarkable experiments on small magnetic clusters on metal surfaces have opened up unprecedented opportunities for atomic engineering of new magnetic materials [3, 9, 10, 11, 12, 13]. By increasing the cluster size in atom-by-atom fashion, Gambardella *et al.* [3] have studied how the magnetization and the magnetic anisotropy energy (MAE) develop in cobalt nanoparticles on Pt(111). They have reported the MAE of 9 meV for single cobalt adatoms, which is about 200 times larger than that of Co atoms in a bulk crystal while Rusponi *et al.* [9] have revealed that the MAE in supported clusters is nearly exclusively caused by the edge atoms alone. These results suggested that only a few hundred atoms would be needed to make a stable magnetic bit. Experiments of the group of Crommie [10, 11] have raised the possibility to study the Kondo effect in small clusters and interactions between magnetic adatoms. Theoretically, Stepanyuk *et al.* [14] confirmed the experimental measurements obtained by Silly *et al.* [12] concerning the stabilization of nanostructures at very low temperatures being weakly bounded by the long-range adsorbated exchange interactions mediated by surface-state electrons. Following the procedure used by Edmonds *et al.* [15] to study by XMCD graphite-supported Fe nanoclusters with an average size of a few hundred atoms, Lau *et al.* [4, 5] have used the same technique to study size dependence of the magnetic properties of  $\text{Fe}_n$  clusters ( $n=2-9$ ) that were deposited on ultrathin Ni films grown on a Cu(001) surface. The *Achilles heel* of such an XMCD experiment is the absence of any information on the geometric structures of these clusters which complicates the understanding of the measurements.

So far there are no combined XMCD and STM experiments where information on the geometry and magnetism can be extracted which explains the focus of the-

---

ory and experiment on rather *simple cases* like deposited ferromagnetic clusters. Less work is done towards antiferromagnetic clusters because of the complications induced by the competition of magnetic interactions which would generate magnetic structures of unprecedented complexity, *e.g.* non-collinear magnetic structures, with magnetic moments much more difficult to measure. For monolayers, spin-polarized STM experiments on such system exist [16] and are able to unravel complex magnetic superstructures with atomic resolution. However, the resolution needed to apply it on small clusters has not been realized yet. Very recently, a breakthrough in STM has been achieved [17] in investigating the magnetism of small chains of 1 to 10 Mn atoms on a thin insulating layer. The spin excitation spectra of these structures has even been measured using the inelastic electron tunneling spectroscopy [18]. From the theory side, as we will explain later on, the availability of methods which would allow a theoretical description of clusters and in particular of non-collinear magnetic clusters is very limited.

In this thesis we address magnetic clusters with antiferromagnetic coupling between the constituting cluster atoms. The treatment of clusters on surfaces is a highly non-trivial problem as the clean surface provides an environment with broken translational and inversion symmetry while the deposited clusters break the two-dimensional translation symmetry in the plane. Different parameters such as strength of the magnetic interactions, symmetry and shape influence dramatically the magnetic ground state and makes the investigation of small nanostructures a challenging task for theory and experiment.

Understanding the electronic structure and the magnetic properties of clusters on surfaces is an unsurmountable quantum-mechanical many-body problem. Hohenberg and Kohn [7] and Kohn and Sham [8] stated that the ground state properties of a many electron system are completely determined by the electronic charge density and that the quantum mechanical many particle problem, which cannot be solved for large systems, can be replaced by a much simpler effective single particle problem. This is the birth of the density functional theory. With its realization in terms of the Kohn-Sham model, DFT developed over the past 15 years to the most important materials specific theory to describe materials properties on the basis of quantum theory of electronic properties. A wide spectrum of DFT methods have been developed to solve the Kohn-Sham equations for different structural and chemical circumstances. The majority of the methods take advantage of the reciprocal space to simulate periodic systems. Hence, the treatment of clusters on surfaces requires huge supercells and limits therefore the cluster shapes and sizes to be investigated. Moreover, a full-potential treatment is necessary as the coordination number of atoms is lowered. In this thesis, the Korringa-Kohn-Rostoker Green Function (KKR-GF) method is used, which is one of the most accurate and flexible all-electron ab-initio methods. Besides the natural treatment of periodic systems taking advantage of the Bloch theorem

as any other method does, a real space treatment can be considered for localized perturbations. The KKR method is based on multiple scattering theory and was originally proposed independently by Korringa [19] and by Kohn and Rostoker [20]. Within a Green function approach, Dupree, Beeby and Morgan [21] developed a first version of the KKR method being able to treat localized perturbations, and successively Zeller and Dederichs [22] integrated it in the frame of the DFT for realistic self-consistent calculations of point defects in metals. Since then, the Jülich group is leader in many of the developments and improvements of the KKR-GF method inventing as an example its tight-binding treatment, developing its full-potential formulation needed for lattice relaxation and participating actively in the coherent potential approximation (CPA) as well as the relativistic version of the method [23].

In order to investigate general cases of non-collinear magnetic coupling, we undertook the task of developing and implementing the treatment of complex magnetic structures in the Jülich version of the full potential Korringa-Kohn-Rostoker Green function method. The phase space of the magnetic solutions of such nanosystems is such complicated that it bares numerous local minima increasing in number dramatically with the degrees of freedom. Using a mapping of the DFT calculations to a Heisenberg model allows the access to a detailed magnetic map of the ground as well as the excited states. Hence, investigating these low dimensional systems with state of the art all-electron ab-initio methods have the advantage of providing the electronic, magnetic properties of the individual atoms and can therefore resolve and allow the interpretation of the measured observables by experimental techniques such as XMCD, STM, scanning tunneling spectroscopy (STS) etc.

The thesis is organized as following. After an introduction to the basics of density functional theory in Chapter 2 and a description of the Korringa-Kohn-Rostoker method in Chapter 3, we will detail in Chapter 4 the theory of non-collinear magnetism as we implemented it in our KKR-GF code. We also give a derivation of the frozen potential approximation and of the so-called Lichtenstein formula [24], which is used to determine magnetic exchange interactions.

The Chapters 5 to 8 contain four different applications of our new code. Complex magnetism of ad-cluster on surfaces including non-collinear structures is presented in Chapter 5 for the case of Ni(001) substrate, in Chapter 6 for the case of Fe<sub>3ML</sub>/Cu(001), in Chapter 7 for the case of Ni(111) surface and in Chapter 8 concerning the strong even-odd effect of number of adatoms in nanochains on the stabilisation of non-collinear magnetism. Thus we will oversee the interplay of two different kinds of magnetic frustration: (i) frustration in the ad-cluster and (ii) frustration between the ad-clusters and the substrate.

---

STM is a powerful experimental tool to investigate local electronic properties of adatoms. Formation of surface states can be monitored from the initial adatom localized state which can merge into the well known two-dimensional Shockley surface state by bringing together several adatoms [25]. Very recently, Limot *et al.* [26] investigated in detail a state which is split off the bottom of Cu(111) surface band due to a Co or Cu adatom. Their results were confirmed by Olsson *et al.* [27]. These results obtained by STM confirmed, in fact, an old theoretical prediction by Simon [28], stating that any attractive potential should lead to a bound state. It is, however, less known if this condition holds for any adatom deposited on Cu(111). Thus, we discuss in Chapter 9 the recently published results on noble metal surface state localization due to the presence of adatoms. We will give a simple explanation of its origin. Moreover we will present a systematic study including *sp* and *3d* impurities sitting in the Cu(111) surface or as adatoms. Contrary to the general statement that such a localization appears always for an attractive impurity, we will see that is not always true and give a more consistent criteria for its realization.

Crampin [29] showed already in 1994 that buried impurities below surfaces scatter the surface state electrons and give rise to characteristic standing wave patterns in the local density of states at the surface, similar to those detected with STM due to scattering by adatoms. In 1999, it was shown for the first time through STM experiments and by first-principles calculations [30] that defect structures below a metal surface, in particular for Ir buried below Cu(001) surface, can be detected by STM. A further investigation [31] shows that when Ar bubbles are buried below Cu(111) and Cu(100), interference patterns are also detectable by STM, proposing the focusing of electrons in certain crystallographic directions as explanation without convincing proof. Fascinating measurements were performed recently by Weismann *et al.* [32] who had shared their results with us prior to publication. They found anisotropic charge oscillations due to the presence of Co impurities buried below the Cu(111) surface.

Hence, Chapter 10 deals with another exciting subject of anisotropic charge oscillations on noble metal surfaces due to the presence of buried impurities at several monolayers under the surface. These anisotropies are very often observed experimentally but left without any explanation. Weismann *et al.* [32] proposed a relation to the anisotropy of the bulk Fermi surfaces and verified it by a simple model. From our side, heavy calculations were done (up to 3000 atomic cells were included in our simulations) considering different orientations of a Cu surface. We will present a concise formulation on the relation between the Fermi surface and the charge at long distances which bares similarity to the well-known theory of interlayer exchange coupling (IEC) (see *e.g.* the paper of Bruno [33]). After analyzing our results we will propose a new experimental technique allowing to determine the position as well as the magnetism of any two dimensional imperfec-

tion, such as an interface, in the range of a local probe atom which is nothing else than the buried impurity. Finally we give the perspective of imaging the Fermi surface in real space with the STM.

# Chapter 2

## Density Functional Theory

The fundamental statement of density functional theory is that any property of a system of interacting electrons can be viewed as a *functional* of the ground state density  $n_0(\vec{r})$ ; that is, a single scalar function  $n_0(\vec{r})$  of the position vector  $\vec{r}$  determines all the information inherent in the many-electron wavefunction for the ground state. The existence proofs for such functionals, given in the original works of Hohenberg and Kohn and of Mermin [7, 34], are disarmingly simple. However, they provide no guidance whatsoever for constructing the functionals, and no exact functionals are known for any system with more than one electron. Density functional theory (DFT) would remain a minor curiosity today if it were not for the *ansatz* made by Kohn and Sham [8] which has provided a way to find useful, approximate ground state functionals for real systems with many electrons.

Density functional theory has become the primary tool for calculating the electronic structure in condensed matter, and is increasingly important for quantitative studies of molecules and other finite systems. The remarkable successes of the approximate local density (LDA) and generalized-gradient approximation (GGA) functionals within the Kohn-Sham approach have led to widespread interest in density functional theory as the most promising approach for accurate, practical methods in the theory of materials.

The modern formulation of density functional theory originated in a famous paper written by P. Hohenberg and W. Kohn in 1964 [7]. These authors showed that a special role can be assigned to the particle density in the ground state of a quantum many-body system: the density can be considered as a “basic variable”, *i.e.* all properties of the system can be considered to be unique *functionals* of the ground state density. Shortly following in 1965, Mermin [34] extended the Hohenberg-Kohn arguments to finite temperature canonical and grand canonical ensembles. Although the finite temperature extension has not been widely used, it illuminates both the generality of density functional theory and the difficulty of realizing the promise of exact density functional theory. Also in 1965 appeared the other classic work of this field by W. Kohn and L. J. Sham [8], whose formulation of density functional theory has become the basis of most of present-day methods

for treating electrons in atoms, molecules, and condensed matter.

## 2.1 Born-Oppenheimer Approximation

One of the most important approximations used in solid state physics is the *Born-Oppenheimer Approximation* which deals with motion of nuclei of atoms with respect to electrons. Since the many-body problem of electrons is already not easy, adding the nuclei of atoms into the equation is too complicated to be solved numerically or analytically. A way to avoid these additional complications is to use the fact that the mass of the electrons is much smaller than the mass of the nuclei, meaning that the electrons move much faster than the nuclei and adjust adiabatically to the position of the nuclei, which change on a much longer time scale. Therefore one may consider for the electronic problems the positions of ions as fixed and determine the ground state energy  $E_0(\vec{R}_0, \dots, \vec{R}_n)$  for these given positions  $\vec{R}_0, \dots, \vec{R}_n$  of the nuclei. The motion of the nuclei then requires the solution of the Hamiltonian  $\sum_{n'} -\frac{1}{2M_{n'}} \nabla_{n'}^2 + E_0(\vec{R}_0, \dots, \vec{R}_n)$  where the ground state energy of the electronic problem acts as an interaction potential for the nuclei.

Here and in the following atomic units are used ( $\hbar = 1$ ;  $m_e = \frac{1}{2}$ ;  $e^2 = 2$ ; energies in Rydberg, 1 Ry = 13.6058 eV; lengths in units of Bohr radius).

## 2.2 Hohenberg-Kohn Theorems

The approach of Hohenberg and Kohn is to formulate a density functional theory as an *exact theory of many-body systems*. The formulation applies to any system of interacting particles in an external potential  $V_{ext}(\vec{r})$ , including the problem of electrons in the field of the fixed nuclei, for which the Hamiltonian can be written as

$$\mathcal{H} = \sum_{i=1}^N -\nabla_i^2 + \sum_{i,j} \frac{1}{|\vec{r}_i - \vec{r}_j|} - \sum_i V_{ext}(\vec{r}_i). \quad (2.1)$$

Density functional theory is based upon the two following theorems first proved by Hohenberg and Kohn [7]:

### Theorem I

For any system of interacting particles in an external potential  $V_{ext}(\vec{r})$ , the potential  $V_{ext}(\vec{r})$  is determined uniquely, up to a constant, by the ground state particle  $n_0(\vec{r})$ , provided the ground state is not degenerate.

## Corollary I

Since the Hamiltonian is thus fully determined, except for a constant shift of the energy, it follows that the many-body wavefunctions for all states (ground state and excited) are determined if the ground state is not degenerate. Therefore all properties of the system are completely determined by the ground state density  $n_0(\vec{r})$ .

## Theorem II

A universal functional for the energy  $E[n]$  in terms of the density  $n(\vec{r})$  can be defined, valid for any external potential  $V_{ext}(\vec{r})$ . For any particular  $V_{ext}(\vec{r})$ , the exact ground state energy of the system is the global minimum value of this functional, and the density  $n(\vec{r})$  that minimizes the functional is the exact ground state density  $n_0(\vec{r})$ .

## Corollary II

The functional  $E[n]$  alone is sufficient to determine the exact ground state energy and density. In general, excited states of the electrons must be determined by other means. Nevertheless, the work of Mermin shows that thermal equilibrium properties such as specific heat are determined directly by the free-energy functional of the density.

## 2.3 The Kohn-Sham Ansatz

Although the basic facts of density-functional theory have now been stated, we still need a key to its application. This was given by Kohn and Sham [8], who used the variational principle implied by the minimal properties of the energy functional to derive single-particle Schrödinger equations. For this the energy functional is first splitted into four parts:

$$E[n] = T[n] + \int \int \frac{n(\vec{r})n(\vec{r}')}{|\vec{r} - \vec{r}'|} d\vec{r}d\vec{r}' + E_{xc}[n] + \int n(\vec{r})V_{ext}(\vec{r})d\vec{r} \quad (2.2)$$

which describes the kinetic, the Hartree, the exchange-correlation and the external energy. In contrast to the Hartree integral, an explicit form of the other functionals,  $T$  and  $E_{xc}$ , is not known in general. Ignoring this problem for the moment, the variational principle is used and we obtain

$$\frac{\delta E[n]}{\delta n(\vec{r})} = -\mu \frac{\delta(N - \int n(\vec{r})d\vec{r})}{\delta n(\vec{r})} = \mu, \quad (2.3)$$

where  $\mu$  is a Lagrange multiplier taking care of particle conservation following Kohn and Sham. The kinetic energy is now splitted up into a term  $T_0$  implying the kinetic energy functional  $T_0[n(\vec{r})]$  of noninteracting particles and  $T_{xc}$  which stands for the rest, *i.e.* we write

$$T = T_0 + T_{xc}. \quad (2.4)$$

This is an important step because it is known how to calculate the kinetic energy  $T_0$  for noninteracting particles and hence one can determine the functional derivative  $\delta T_0[n]/\delta n(\vec{r})$  by using

$$n(\vec{r}) = \sum_{i=1}^N |\Phi_i(\vec{r})|^2 \quad (2.5)$$

where the summation is over  $N$  states with lowest eigenvalues and

$$T_0[n] = \sum_{i=1}^N \int \nabla \Phi_i^*(\vec{r}) \nabla \Phi_i(\vec{r}), \quad (2.6)$$

$\Phi$  being a single particle wave function.

By varying the latter equation and after adding a potential-energy term the Euler-Lagrange equation is obtained which is also, in fact, a single-particle Schrödinger equation:

$$(-\nabla^2 + v'(\vec{r}))\Phi_i(\vec{r}) = \epsilon_i \Phi_i(\vec{r}) \quad (2.7)$$

We try to determine the potential energy  $v'(\vec{r})$  such that the density  $n(\vec{r})$  obtained from eq. (2.5) minimizes the total energy. Thus, multiplying eq. (2.7) with  $\Phi_i^*(\vec{r})$ , requiring the functions  $\Phi_i(\vec{r})$  to be normalized, integrating and summing up, we obtain

$$T_0[n] = \sum_{i=1}^N \epsilon_i - \int v'(\vec{r}) n(\vec{r}) d\vec{r}. \quad (2.8)$$

The variation (eq. (2.3)) is now easily carried out. We note that terms containing  $\delta \epsilon_i$  cancel  $\delta v'$  (because of eq. (2.7)) and obtain  $v'(\vec{r})$  which is called the effective single particle potential  $v_{eff}(\vec{r})$ :

$$v_{eff}(\vec{r}) = v_{ext}(\vec{r}) + 2 \int \frac{n(\vec{r}')}{|\vec{r} - \vec{r}'|} d\vec{r}' + v_{xc}(\vec{r}) \quad (2.9)$$

with

$$v_{xc}(\vec{r}) = \frac{\delta(E_{xc} + T_{xc})}{\delta n(\vec{r})} \quad (2.10)$$

By varying  $E[n(\vec{r})]$  with respect to  $\Phi_i(\vec{r})$  instead of  $n(\vec{r})$  and adding the Lagrange constraint  $\sum_i \epsilon_i (\int d\vec{r} \Phi^*(\vec{r}) \Phi(\vec{r}) - 1)$  for the normalisation of the

$\Phi$ , the following so-called Kohn-Sham equation is obtained for the single partial wave function  $\Phi_i$

$$[-\nabla^2 + v_{eff}(\vec{r}) - \epsilon_i]\Phi_i(\vec{r}) = 0. \quad (2.11)$$

It is a Schrödinger equation with the external potential replaced by the effective potential which depends on the density. The density itself depends on the single-particle states  $\Phi_i$  via eq. (2.5). The Kohn-Sham equation thus constitutes a self-consistent field problem.

The Kohn-Sham equation furthermore allows us to derive an alternative expression for the total energy. As we do not know the ground state density  $n_0(\vec{r})$ , let us generate  $n(\vec{r})$  by a trial potential  $v_{eff}^{trial}(\vec{r})$  which might be calculated in fact by a trial density  $n^{trial}(\vec{r})$  using eq. (2.9) *i.e.*

$$v_{eff}^{trial}(\vec{r}) = V_{ext}(\vec{r}) + 2 \int \frac{n^{trial}(\vec{r}')}{|\vec{r} - \vec{r}'|} d\vec{r}' + v_{xc}[n^{trial}(\vec{r})] \quad (2.12)$$

but we note that also more general  $v_{eff}^{trial}$  potentials are allowed. Then this can be plugged in eq. (2.8) to give

$$T_0[n] = \sum_{i=1}^N \epsilon_i - \int v_{eff}^{trial}(\vec{r}) n(\vec{r}) d\vec{r}. \quad (2.13)$$

and

$$E[n] = \sum_{i=1}^N \epsilon_i - \int v_{eff}^{trial}(\vec{r}) n(\vec{r}) d\vec{r} + \int v_{ext}(\vec{r}) n(\vec{r}) + \int \int \frac{n(\vec{r}) n(\vec{r}')}{|r - r'|} d\vec{r} d\vec{r}' + E_{xc}[n]. \quad (2.14)$$

The total energy thus consists of the sum over the eigenvalue,  $\epsilon_i$ , minus the so-called double counting terms. Note that eq. (2.14) gives the exact ground state energy only if  $n^{trial}(\vec{r}) = n(\vec{r})$ , *i.e.* input and output density must be the same requiring full self-consistency.

Although density-functional theory as outlined above provides a scheme to reduce the entire many-body problem to a Schrödinger-like effective single-particle equation, the eigenvalues  $\epsilon_i$  have no direct physical meaning since they have been introduced only as Lagrange parameters. Nevertheless, they are often and quite successfully taken as approximate excitation energies.

## 2.4 The Local Spin Density Approximation

Already in their paper, Kohn and Sham pointed out that solids can often be considered as close to the limit of the homogeneous electron gas. In that limit, it is known that the effects of exchange and correlation are local in character, and they proposed making the local density approximation (LDA) or more generally

the local spin density approximation (LSDA), in which the exchange-correlation energy is simply an integral over all space with the exchange-correlation energy density at each point assumed to be the same as in a homogeneous electron gas with the corresponding local density,

$$E_{xc}^{LSDA} = \int d\vec{r} n(\vec{r}) \epsilon_{xc}^{hom}(n^\uparrow(\vec{r}), n^\downarrow(\vec{r})) \quad (2.15)$$

$$= \int d\vec{r} n(\vec{r}) [\epsilon_x^{hom}(n^\uparrow(\vec{r}), n^\downarrow(\vec{r})) + \epsilon_c^{hom}(n^\uparrow(\vec{r}), n^\downarrow(\vec{r}))]. \quad (2.16)$$

The part of the Kohn-Sham potential due to exchange and correlation  $v_{xc}^s(\vec{r})$  is defined by the functional derivative of the exchange and correlation energies  $E_{xc}(\vec{r})$  for each spin channel. In the LDA the form is very simple,

$$\delta E_{xc}[n] = \sum_s \int d\vec{r} \left[ \epsilon_{xc}^{hom} + n \frac{\partial \epsilon_{xc}^{hom}}{\partial n^s} \right]_{\vec{r},s} \delta n(\vec{r}, s), \quad (2.17)$$

so that the potential,

$$v_{xc}^s(\vec{r}) = \left[ \epsilon_{xc}^{hom} + n \frac{\partial \epsilon_{xc}^{hom}}{\partial n^s} \right]_{\vec{r},s}, \quad (2.18)$$

involves only ordinary derivatives of  $\epsilon_{xc}^{hom}(n^\uparrow, n^\downarrow)$ . Here the subscripts  $\vec{r}, s$  mean that quantities in square brackets are evaluated for  $n^s = n(\vec{r}, s)$ . It is common to split  $\epsilon_{xc}(n)$  into exchange and correlation parts  $\epsilon_{xc}(\rho) = \epsilon_x(n) + \epsilon_c(n)$ . The LDA exchange terms are particularly simple: since  $\epsilon_x^{hom}(n^s)$  scales  $(n^s)^{\frac{1}{3}}$  it follows that

$$v_x^s(\vec{r}) = -2 \left( \frac{3n(\vec{r}, s)}{\pi} \right)^{\frac{1}{3}} \quad (2.19)$$

On the other hand, accurate values for  $\epsilon_c(n)$  have been determined from Quantum Monte Carlo (QMC) calculations. These have then been interpolated to provide an analytic form for  $\epsilon_c(n)$ . In this thesis we use the functional proposed by Vosko *et al.* [35].

## 2.5 Non-collinear Spin Density

In the usual collinear case of a spin polarized system, there are two different densities  $[n^\uparrow(\vec{r}), n^\downarrow(\vec{r})]$  and potentials  $[v_{xc}^\uparrow(\vec{r}), v_{xc}^\downarrow(\vec{r})]$  for spin up and spin down. This is not, however, the most general form since the spin axis can vary in space. In this “non-collinear spin” case [36], the density at every point is represented by a vector giving the spin direction, or equivalently, by a local spin density matrix:

$$\mathbf{n}(\vec{r}) = \frac{n(\vec{r})}{2} \mathbf{1} + \frac{\vec{m}(\vec{r})}{2} \cdot \vec{\sigma} \quad (2.20)$$

Here  $\mathbf{1}$  is the  $2 \times 2$  unit matrix,  $n(\vec{r})$  the charge density,  $\vec{m}(\vec{r})$  the magnetization density and  $\vec{\sigma} = (\sigma_x, \sigma_y, \sigma_z)$  are the Pauli spin matrices.

In this general magnetic case, each one-electron state is represented by a spinor function:

$$\psi_i(\vec{r}) = \begin{pmatrix} \alpha_i(\vec{r}) \\ \beta_i(\vec{r}) \end{pmatrix}, \quad (2.21)$$

where  $\alpha_i$  and  $\beta_i$  are the two spin projections. Moreover, all operators need to be represented as  $2 \times 2$  matrices. The explicit form of the charge and magnetization density is then

$$n(\vec{r}) = \sum_{i=1}^N |\psi_i(\vec{r})|^2, \quad (2.22)$$

and

$$\vec{m}(\vec{r}) = \sum_{i=1}^N \psi_i^\dagger(\vec{r}) \vec{\sigma} \psi_i(\vec{r}), \quad (2.23)$$

and the density matrix has the form

$$\rho(\vec{r}) = \sum_{i=1}^N \begin{pmatrix} |\alpha_i(\vec{r})|^2 & \alpha_i(\vec{r})\beta_i^*(\vec{r}) \\ \alpha_i^*(\vec{r})\beta_i(\vec{r}) & |\beta_i(\vec{r})|^2 \end{pmatrix}. \quad (2.24)$$

The sum of the diagonal elements give the charge density while the off-diagonal elements can give rise to non-collinear magnetism since the two spin projections are allowed to hybridize. The Kohn-Sham Hamiltonian becomes a  $2 \times 2$  matrix

$$H_{KS}^{ss'}(\vec{r}) = -\nabla^2 \delta_{ss'} + V_{KS}^{ss'}(\vec{r}) \quad s, s' = 1, 2, \quad (2.25)$$

where the only part of  $V_{KS}^{ss'}$  that is non-diagonal in spin space is the exchange correlation potential  $V_{xc}^{ss'}$  which has to be rotated to a local frame of reference in which the density matrix becomes diagonal. Although this looks like a major complication, the only real difficulty is in the nature of the functional  $\epsilon_{xc}^{ss'}$ . In the local approximation it is calculated simply by finding the local axis of spin quantization and using the same functional form  $\epsilon_{xc}^{hom}(n^\uparrow(\vec{r}), n^\downarrow(\vec{r}))$  as given previously, but  $n^\uparrow(\vec{r})$  and  $n^\downarrow(\vec{r})$  are corresponding to diagonal components for the local axis.

In the case of collinear magnetism, a unique global magnetization axis can be defined in, for instance, the  $z$ -direction. Then the density matrix and operators all reduce to a diagonal form. The two spin projections have different potentials and can be solved independently of each other so that the density matrix is completely described by the scalar quantities  $n = n_\uparrow + n_\downarrow$  and  $m_z = n_\uparrow - n_\downarrow$ .



# Chapter 3

## The KKR Green Function Method

### 3.1 Introduction

The multiple-scattering method of Korringa, Kohn and Rostoker (KKR) for the calculation of the electronic structure of materials was introduced in 1947 by Korringa [19] and in 1954 by Kohn and Rostoker [20]. In order to solve the Schrödinger equation, the scattering properties of each scattering center (atom) are determined in a first step and described by a scattering matrix, while the multiple-scattering by all atoms in the lattice is determined in a second step by demanding that the incident wave at each center is the sum of the outgoing waves from all other centers. In this way, a separation between the potential and geometric properties is achieved.

A further significant development of the KKR scheme came when it was reformulated as a Green function method [21, 37]. By separating the single-site scattering problem from the multiple-scattering effects, the method is able to produce the crystal Green function efficiently by relating it to the Green function of free space via the Dyson equation. In a second step the crystal Green function can be used as a reference in order to calculate the Green function of an impurity in the crystal [22], again via a Dyson equation. This way of solving the impurity problem is extremely efficient, avoiding the construction of huge supercells of finite clusters which are usually used in wavefunction methods.

The development of *screened*, or *tight-binding*, KKR was a further breakthrough for the numerical efficiency of the method [38]. Via a transformation of the reference system remote lattice sites are decoupled, and the principal layer technique allows the calculation time to scale linearly with the number of atoms. This is especially useful for layered systems (surfaces, interfaces, multilayers) and allows the study of, e.g., interlayer exchange coupling or ballistic transport through junctions.

A short list of successful applications of the KKR method for electronic structure of solids, combined with density-functional theory, includes bulk materi-

als [39], surfaces [40], interfaces and tunnel junctions [41], and impurities in bulk and on surfaces [42]. Spectroscopic properties [43] and transport properties [44, 45, 46] have also been studied within this method. The KKR scheme can incorporate the Dirac equation, whenever relativistic effects become important [47].

## 3.2 Green Function Method

In density functional calculations the solution of the Kohn-Sham equations for the single particle wave functions  $\varphi_\alpha(\vec{r})$  and the corresponding eigenvalues  $\varepsilon_\alpha$ , the single particle energies, represents the central problem. Thus most of electronic structure calculations follow this route, i.e. calculating eigenfunctions  $\varphi_\alpha$  and eigenvalues  $\varepsilon_\alpha$ . However, the calculation of  $\varphi_\alpha$  and  $\varepsilon_\alpha$  can be avoided, if instead the single particle Green function  $G(\vec{r}, \vec{r}'; E)$  of the Kohn-Sham equation is determined, since this quantity contains all the information about the ground state. In particular the charge density and the local density of states can be directly calculated from the Green function, which is the solution of the Schrödinger equation for an energy  $E$  with a source at position  $\vec{r}'$ :

$$(-\partial_r^2 + V(\vec{r}) - E) G(\vec{r}, \vec{r}'; E) = -\delta(\vec{r} - \vec{r}') \quad , \quad (3.1)$$

with atomic units  $\hbar^2/2m = 1$  used. Using the spectral representation for the (retarded) Green function

$$G(\vec{r}, \vec{r}'; E + i\epsilon) = \sum_\alpha \frac{\psi_\alpha(\vec{r})\psi_\alpha^*(\vec{r}')}{E + i\epsilon - E_\alpha} \quad (3.2)$$

it is easy to show that the charge density  $n(\vec{r})$  can be directly expressed by an energy integral over the imaginary part of the Green function:

$$n(\vec{r}) = 2 \sum_{\substack{\alpha \\ E_\alpha < E_F}} |\psi_\alpha(\vec{r})|^2 = -\frac{2}{\pi} \int^{E_F} dE \operatorname{Im} G(\vec{r}, \vec{r}; E) \quad (3.3)$$

This relation directly allows to calculate the charge density from the imaginary part of the diagonal components of the Green function, which can be interpreted as the local density of states at the position  $\vec{r}$ . The local density of states of a particular atom in a volume  $V$  is obtained by integrating over this volume

$$n_V(E) = -\frac{2}{\pi} \int_V d\vec{r} \operatorname{Im} G(\vec{r}, \vec{r}; E) \quad (3.4)$$

In this way the evaluation of the wave-functions  $\psi_\alpha(\mathbf{r})$  can be avoided. Due to the strong energy-dependent structure of the density of states, the evaluation of

the energy integral is usually very cumbersome and typically about  $10^3$  energy points are needed in an accurate evaluation of this integral.

The numerical effort can be strongly decreased, if the analytical properties of the Green function  $G(z)$  for complex energies  $z = E + i\Gamma$  are used. Since  $G(z)$  is analytical in the whole complex energy plane, the energy integral can be transformed into a contour integral in the complex energy plane

$$n(\mathbf{r}) = -\frac{2}{\pi} \operatorname{Im} \int_{E_B}^{E_F} dz G(\mathbf{r}, \mathbf{r}; z) \quad (3.5)$$

where the contour starts at an energy  $E_B$  below the bottom of the valence bands, goes into the complex plane and comes back to the real axis at the Fermi level. Since for complex energies all structures of the Green function are broadened by the imaginary part  $\Gamma$ , the contour integral can be accurately evaluated using rather few energy points, typically 20-30, leading to a large saving of computer time. In this way Green function methods are competitive to diagonalization methods. Additional advantages occur for systems with two- or three-dimensional symmetry, since as a result of the energy broadening the  $\mathbf{k}$ -integration over the Brillouin zone requires for complex energies much less  $\mathbf{k}$ -points. In the evaluation of the contour integral, special care is necessary for the piece of the path close to  $E_F$ , since here the full structure of  $G(E)$  on the real axis reappears. Therefore the energy mesh should become increasingly denser when approaching  $E_F$ .

The integration over a complex energy contour can also be extended to finite temperatures by using the analytical properties of the Fermi-Dirac distribution. Here the essential point is that the contour close to  $E_F$  is replaced by a sum over Matsubara energies  $z_j = E_F + i\pi(2j-1)kT$ ,  $j = 1, 2, \dots$ . Then only complex energies are needed, since the energy point closest to  $E_F$  has still an imaginary part of  $\pi kT$ . This is of particular advantage, when a discrete  $k$ -mesh is used, like e.g. in the special points method.

The real problem is the evaluation of the Green function for the system of interest. Since we want to avoid evaluation of all eigenvalues  $\varepsilon_\alpha$  and wave functions  $\varphi_\alpha$  we try to calculate the Green function  $G$

$$G(E) = \frac{1}{E + i\varepsilon - H} = \frac{1}{E + i\varepsilon - H_o - V} \quad (3.6)$$

of a system with Hamiltonian  $H = H_o + V$  to the Green function  $G_o = \{E + i\varepsilon - H_o\}^{-1}$  of a reference system, which is analytically known or easy to calculate. Then  $G(E)$  can be obtained from the Dyson equation

$$G(E) = G_o(E) + G_o(E) V G(E) = G_o \frac{1}{1 - V G_o} \quad (3.7)$$

For instance, for a bulk crystal one starts with the free space Green function  $G_o(H_o = -\partial_r^2)$ , such that  $V$  is the sum of the potentials of all atoms. For the

surface Green function,  $G_o$  is identified with the bulk Green function, such that  $V$  is the difference between the potentials at the surface and in the bulk. Analogously for an impurity in a crystal one starts again with the bulk Green function  $G_o$ , such that  $V$  represents the change of the impurity potential with respect to the bulk potential as well as the perturbation of the potentials of the neighboring host atoms. Most important is, that the perturbed potential  $V$  is well localized near the impurity, while the perturbed wavefunctions are not localized and accurately described by the Dyson equation.

Such impurity problems are often described by an 'Ersatzgeometry', e.g. an impurity in a relatively small cluster of bulk atoms or by a supercell geometry with a periodic array of impurities. In these cases the boundary conditions for the wave functions are changed violently, since e.g. for a cluster all wave functions are restricted to the size of the cluster. Therefore the introduction of the host Green function  $G_o$  solves the so-called "embedding problem", since it correctly describes the embedding of the impurity in the infinite bulk system. Needless to say, that the Green function method cannot only be applied to a single impurity, but also to a small cluster of impurity atoms in the bulk, provided that the perturbation of the potential is localized in a restricted area. Moreover, once the Green function of the surface is known, one can calculate with an analogous Dyson equation the electronic structure of an impurity or of small clusters at surfaces.

### 3.3 Single-Site Scattering

We turn now to the scattering problem of a spherical atomic potential embedded in free space (actually in an environment of constant potential). The reference system is thus a free-electron system (where the Hamiltonian contains only the kinetic energy term, and the eigenfunctions are plane waves). The Green function of a free-electron system has the form [48, 49]

$$g(\vec{r}, \vec{r}'; E) = -\frac{1}{4\pi} \frac{e^{ik|\vec{r}-\vec{r}'|}}{|\vec{r}-\vec{r}'|}. \quad (3.8)$$

with  $k = \sqrt{E}$ . In the case of scattering by a central potential, it is useful to work in angular-momentum representation. We therefore represent an incoming plane wave as

$$\psi_{\vec{k}}^{\text{inc}}(\vec{r}) = e^{i\vec{k}\vec{r}} = \sum_L 4\pi i^l j_l(\sqrt{E}r) Y_L(\vec{r}) Y_L(\vec{k}) \quad (3.9)$$

where  $j_l$  is the spherical Bessel function, while  $Y_L$  are the real spherical harmonics. We use the combined index  $L := (l, m)$ , where  $l$  and  $m$  are angular momentum indexes. On the other hand, the free space Green function (3.8) can be expanded

as:

$$g(\vec{r}, \vec{r}'; E) = \sum_L Y_L(\vec{r}) g_l(r, r'; E) Y_L(\vec{r}') \quad (3.10)$$

with  $g_l$  given by

$$g_l(r, r'; E) = -i\sqrt{E} j_l(\sqrt{E}r_<) h_l(\sqrt{E}r_>), \quad (3.11)$$

where  $h_l = j_l + in_l$  are spherical Hankel functions,  $n_l$  are spherical Neumann functions [50], while  $r_<$  ( $r_>$ ) is the smaller (bigger) of the radii  $r$  and  $r'$ . The Bessel functions  $j_l(x)$  are finite as  $x \rightarrow 0$ , while  $h_l(x)$  and  $n_l(x)$  are diverging as  $x \rightarrow 0$ .

Suppose now that there is a scattering potential of finite range, of the form

$$V(\vec{r}) = \begin{cases} V(r) & r \leq S \\ 0 & r > S. \end{cases} \quad (3.12)$$

Then the radial wavefunctions  $R_l(r; E)$  satisfy the radial Schrödinger equation

$$\left[ -\frac{1}{r} \frac{\partial^2}{\partial r^2} r + \frac{l(l+1)}{r^2} + V(r) - E \right] R_l(r; E) = 0. \quad (3.13)$$

The asymptotic form of  $R_l(r; E)$  for  $r \rightarrow \infty$  is

$$R_l(r; E) \rightarrow \frac{A_l}{\sqrt{Er}} \sin \left( \sqrt{Er} - \frac{l\pi}{2} + \delta_l(E) \right) \quad (3.14)$$

where  $A_l$  is a constant and  $\delta_l(E)$  is the phase shift with respect to the wavefunction for vanishing potential.

Since for  $r > S$  the potential  $V(r)$  vanishes and the general solution of the radial equation is in this region a sum of two linearly independent special solutions:

$$R_l(r; E) = B_l j_l(\sqrt{Er}) + C_l n_l(\sqrt{Er}) \quad (3.15)$$

where  $B_l$  and  $C_l$  are constants. Using the asymptotic form of Bessel functions,

$$\lim_{x \rightarrow \infty} j_l(x) = \frac{1}{x} \sin(x - l\pi/2) \quad (3.16)$$

$$\lim_{x \rightarrow \infty} n_l(x) = -\frac{1}{x} \cos(x - l\pi/2) \quad (3.17)$$

together with eqs. (3.14) and (3.15), we obtain

$$R_l(r; E) = A_l \left( j_l(\sqrt{Er}) \cos \delta_l - n_l(\sqrt{Er}) \sin \delta_l \right) \quad \text{for } r > S. \quad (3.18)$$

On the other hand, the Lippmann-Schwinger equation gives

$$R_l(r; E) = j_l(\sqrt{E}r) + \int_0^S g_l(r, r'; E) V(r') R_l(r'; E) r'^2 dr' \quad (3.19)$$

which, using (3.11), yields for  $r > S$ :

$$R_l(r; E) = j_l(\sqrt{E}r) - ih_l(\sqrt{E}r)\sqrt{E} \int_0^S j_l(\sqrt{E}r') V(r') R_l(r'; E) r'^2 dr'. \quad (3.20)$$

The integral is just the  $t$ -matrix element in angular-momentum representation,

$$t_l(E) = \int_0^S j_l(\sqrt{E}r) V(r) R_l(r; E) r^2 dr, \quad (3.21)$$

so that we obtain

$$R_l(r; E) = j_l(\sqrt{E}r) - i\sqrt{E} t_l(E) h_l(\sqrt{E}r) \quad (r > S) \quad (3.22)$$

with the  $t$ -matrix related to the phase shift by (cf. (3.18))

$$t_l(E) = -\frac{1}{\sqrt{E}} \sin \delta_l(E) e^{i\delta_l(E)}. \quad (3.23)$$

Finally, we give without proof the Green function for the scattering problem by a central potential. It can be written as the product of two linearly independent solutions,  $R_l$  (regular, i.e., converging as  $r \rightarrow r^l$  at the origin) and  $H_l$  (irregular, i.e., diverging as  $r \rightarrow \frac{1}{r^{l+1}}$ ), of the radial equation:

$$\begin{aligned} G(\vec{r}, \vec{r}'; E) &= -i\sqrt{E} \sum_L R_l(r_{<}; E) H_l(r_{>}; E) Y_L(\vec{r}) Y_L(\vec{r}') \quad (3.24) \\ &\equiv \sum_L G_l(r, r'; E) Y_L(\vec{r}) Y_L(\vec{r}'). \end{aligned}$$

The boundary conditions of  $R_l$  are given by (3.22). In order to find the boundary conditions of  $H_l$  we use the identity  $G_l = g_l + g_l t_l g_l$  with  $g_l$  given by (3.11) and obtain

$$H_l(r; E) = h_l(\sqrt{E}r) \quad (r > S). \quad (3.25)$$

In practice, we integrate (3.13) numerically outwards from the origin to  $r = S$  in order to obtain  $R_l$ . At  $r = S$  the requirement for continuity of the logarithmic derivative yields the  $t$ -matrix elements. Analogously, a numerical integration inwards yields the diverging radial wavefunction  $H_l$ , uniquely determined by the boundary condition (3.25) at  $r = S$ .

### 3.4 Multiple-Scattering Theory

In the previous section we discussed the solution of the scattering problem for an isolated scattering potential. In this section we will extend the study to a set of scatterers. Let us consider in this section the multiple scattering of an incoming wave  $\overset{\circ}{\psi}_E(\vec{r})$  of energy  $E$  at  $N$  spherical potentials  $v_n(\vec{r})$  located at the positions  $\vec{R}^n$  with  $n = 1, \dots, N$ . In each cell  $n$  around the different potentials  $v_n(\vec{r} - \vec{R}^n)$ , the wave function  $\overset{\circ}{\psi}_E(\vec{r})$  can be expanded in spherical harmonics  $Y_L(\hat{r})$ . The general expansion can be written as a sum of  $j_l(r; E)Y_L(\hat{r})$ , since the incoming wave  $\overset{\circ}{\psi}_E(\vec{r})$  has an energy  $E$  and is regular, such that in the expansion the Hankel function do not enter. Thus

$$\overset{\circ}{\psi}_E(\vec{r}) = \sum_n C_L^n j_l(r; E) Y_L(\hat{r}) \quad \text{for } \vec{r} \text{ in cell } n \quad (3.26)$$

As derived in the last section, the single scattering process at potential  $v_n(\vec{r})$  means, that the incoming wave  $j_l(r; E)Y_L(\hat{r})$  goes over into the radial function  $R_L^n(\vec{r}; E) = R_l^n(r; E)Y_L(\hat{r})$ , where  $R_l^n$  varies as

$$R_l^n(r; E) = j_l(r; E) - i\sqrt{E}t_l^n(E)h_l(r; E) \quad \text{for } r > S. \quad (3.27)$$

The multiple scattering at all potentials can be described, if we consider in each cell  $n$  an effective incident wave with the amplitude  $\Phi_L^n$ , as the superposition of the unperturbed incident wave with the amplitude  $C_L^n$  and the scattered waves originating from all other cells  $n' \neq n$ .

The scattered wave with angular momentum  $L'$  from such a cell  $n'$ , given by  $-i\sqrt{E}t_{l'}^{n'}(E)h_{L'}(\vec{r}; E)$  has then also to be multiplied by the effective, but unknown, wave coefficients  $\Phi_{L'}^{n'}$  on this site.

We know from the addition theorem [51] that the expansion the Hankel function in the cell  $n$  is given by

$$h_L(\vec{r} + \vec{R}^n - \vec{R}^{n'}; E) = \frac{i}{\sqrt{E}} \sum_{L'} g_{LL'}^{nn'}(E) j_{L'}(\vec{r}; E). \quad (3.28)$$

However we are interested in the expansion of the Hankel function in the cell  $n'$  with the orbital momentum  $L'$ :

$$h_{L'}(\vec{r} + \vec{R}^{n'} - \vec{R}^n; E) = \frac{i}{\sqrt{E}} \sum_L g_{L'L}^{n'n}(E) j_L(\vec{r}; E), \quad (3.29)$$

or

$$h_{L'}(\vec{r} + \vec{R}^{n'} - \vec{R}^n; E) = \frac{i}{\sqrt{E}} \sum_L j_L(\vec{r}; E) g_{LL'}^{nn'}(E), \quad (3.30)$$

using that  $g_{L'L}^{n'n}(E) = g_{LL'}^{nn'}(E)$ . Hence we obtain for the scattered waves of all angular momenta  $L'$  from all sites  $n'$  ( $\neq n$ ) in an expansion in the cell  $n'$

$$\sum_L j_L(\vec{r}; E) \sum_{L', n' \neq n} g_{LL'}^{nn'}(E) t_{L'}^{n'}(E) \Phi_{L'}^{n'}. \quad (3.31)$$

The total effective incident wave on the cell  $n$  is then given by the sum of (3.31) and (3.26)

$$\sum_L \Phi_L^n j_L(r; E) Y_L(\hat{r}) = \sum_L \left[ C_L^n + \sum_{L', n' \neq n} g_{LL'}^{nn'}(E) t_{L'}^{n'}(E) \Phi_{L'}^{n'} \right] j_L(r; E) Y_L(\hat{r}) \quad (3.32)$$

Therefore the fields  $\Phi_L^n$  have to satisfy the multiple scattering equation

$$\Phi_L^n = C_L^n + \sum_{L', n' \neq n} g_{LL'}^{nn'}(E) t_{L'}^{n'}(E) \Phi_{L'}^{n'} \quad (3.33)$$

The full solution of our multiple scattering problem can then be written in the cell  $n$  as

$$\psi(\vec{r}) = \sum_L \Phi_L^n R_L^n(r; E) Y_L(\hat{r}) \quad (3.34)$$

with the coefficients  $\Phi_L^n$  from eq. (3.33).

If there is no external incident wave, the coefficients  $C_L^n$  are null. If moreover we are interested in an infinite ideal crystal with equal potentials ( $t_{L'}^n(E) = t_{L'}(E)$ ) then the eigensolutions can be chosen as Bloch waves ( $\Phi_L^n = e^{i\vec{k}\vec{R}^n} \Phi_L^0$ ).

Thus, one obtains from eq. (3.33)

$$\Phi_L^0 = \sum_{L'} g_{LL'}(\vec{k}, E) t_{L'} \Phi_{L'}^0, \quad (3.35)$$

with

$$g_{LL'}(\vec{k}, E) = \sum_{n' \neq n} g_{LL'}^{nn'}(E) e^{i\vec{k}\vec{R}^n - \vec{R}^{n'}} \quad (3.36)$$

are the free space structure constants.

One can rewrite eq. (3.35) as

$$\sum_{L'} \left( \delta_{LL'} - g_{LL'}(\vec{k}, E) t_{L'} \right) \Phi_{L'}^0 = 0 \quad (3.37)$$

In the perfect crystal, the electronic eigenvalues are given by the solutions of (3.37), *i.e.*, in the absence of an external wave. In order to have non-trivial solutions of the system (3.37), the necessary and sufficient condition is that the determinant vanishes:

$$\text{Det} \left[ \left( \delta_{LL'} - g_{LL'}(\vec{k}, E) t_{L'} \right) \right] = 0 \quad (3.38)$$

### 3.5 Multiple-Scattering: The Green Function Approach

As mentioned earlier, in the method of Korringa, Kohn and Rostoker (KKR) [21] the Schrödinger equation is solved by multiple scattering theory, describing the propagation of a wave in the solid as a repetition of single scattering events at the different atoms. Thus first the single scattering event of the wave at the potential of the different single atoms  $n$  is calculated, described by the single site "t-matrix"  $t_n$ , and then the multiple scattering at the given arrangement of the atoms in the crystal. The resulting equations show a beautiful separation between potential and structural properties, which are typical for the KKR method. In the following we summarize the most important results.

In the KKR-Green function method one divides the whole space into non-overlapping and space-filling cells centered at positions  $\vec{R}^n$ . In each cell the electrons are scattered by potentials  $v^n$ , which in this section are assumed to be spherically symmetric and centered at  $\vec{R}^n$ . By introducing cell-centered coordinates the Green function  $G(\vec{r} + \vec{R}^n, \vec{r}' + \vec{R}^{n'}; E)$  can then be expanded in each cell as a function of  $\vec{r}$  and  $\vec{r}'$  into spherical harmonics:

$$G(\vec{R}_n + \vec{r}, \vec{R}_{n'} + \vec{r}'; E) = -i\sqrt{E} \sum_L R_L^n(\vec{r}_<; E) H_L^n(\vec{r}_>; E) \delta_{nn'} \quad (3.39)$$

$$+ \sum_{LL'} R_L^n(\vec{r}; E) G_{LL'}^{nn'}(E) R_{L'}^{n'}(\vec{r}'; E)$$

Here  $\vec{r}$  and  $\vec{r}'$  are restricted to the cells  $n$  and  $n'$  and  $\vec{r}_<$  and  $\vec{r}_>$  denote the one of the two vectors  $\vec{r}$  and  $\vec{r}'$  which has the smaller or larger absolute value. The  $R_L^n(\vec{r}; E)$  and  $H_L^n(\vec{r}; E)$  are the product of spherical harmonics and radial eigenfunctions to the central potential  $v^n(r)$ :

$$R_L^n(\vec{r}; E) = R_L^n(r; E) Y_L(\hat{r}), \quad (3.40)$$

$$H_L^n(\vec{r}; E) = H_L^n(r; E) Y_L(\hat{r}). \quad (3.41)$$

$R_L^n(\vec{r}, E)$  is the regular solution which varies at the origin as  $r^l$  and which represents the solution for an incoming spherical Bessel function  $j_l(\sqrt{E}r)Y_L(\hat{r})$ , while  $H_L^n$  is the corresponding irregular solution varying as  $1/r^{l+1}$  at the origin and being identical with the spherical Hankel function  $h_l(\sqrt{E}r)$  outside the range of the potential. Both radial functions are connected by the Wronskian relation, which guarantees that the first term in eq. (3.40) represents the exact Green function for the single potential  $v^n(r)$  in free space. Since this term satisfies already the source condition  $-\delta(\vec{r} - \vec{r}')$  for the Green function, the second term is source free and contains in the double angular momentum expansion only the regular solutions  $R_L^n$  and  $R_{L'}^{n'}$ .

By construction, the expression (3.40) for the Green function satisfies in each cell  $n$  the general solution of the Schrödinger equation for the Green function,

while the matrix  $G_{LL'}^{nn'}(E)$ , the so-called *structural Green function*, describes the connection of the solutions in the different cells and thus contains all the information about the multiple scattering problem, which is in this way reduced to the solution of an algebraic problem. The clear separation between the single-site properties, described by the radial solutions  $R_L^n(\vec{r})$  and  $H_L^n(\vec{r})$  and the multiple scattering properties as described by the matrix  $G_{LL'}^{nn'}$ , is the main advantage of the KKR method.

In principle, the structural Green function matrix  $G_{LL'}^{nn'}(E)$  can be determined by matching the solutions of the neighboring cells at the cell boundaries. However at the cell boundaries the angular momentum expansion converges rather slowly, so that presumably a large  $l_{\max}$  cut-off would be needed. The more elegant and at the same time more efficient way consists in using the power of multiple scattering theory, where the Green function is basically only needed in the inner region of the cell, where the potential is strong, so that the  $l$ -convergence represents no problem. As shown by Beeby and others [21], the structural Green function matrix can be determined from the corresponding matrix  $g$  in free space by the Dyson equation

$$G_{LL'}^{nn'}(E) = g_{LL'}^{nn'}(E) + \sum_{n''L''} g_{LL''}^{nn''}(E) t_{L''}^{n''}(E) G_{L''L'}^{n''n'}(E) \quad (3.42)$$

where the  $t$ -matrix  $t_l^n$  for the potential  $v^n(r)$  is given by eq. (3.21)

$$t_l^n(E) = \int_0^R r^2 dr j_l(\sqrt{E}r) v^n(r) R_l^n(r; E) \quad (3.43)$$

The derivation of this equation is lengthy and straightforward, so that we refer for this to the literature cited above. An elementary derivation, valid also for the full-potential case, has been given by Zeller [51].

Once the structural Green function  $\overset{\circ}{G}_{LL'}^{nn'}(E)$  of the ideal crystal is known, the Green function  $G_{LL'}^{nn'}(E)$  for the crystal with impurity can be evaluated by a modified Dyson equation

$$G_{LL'}^{nn'} = \overset{\circ}{G}_{LL'}^{nn'} + \sum_{n''L''} \overset{\circ}{G}_{LL''}^{nn''} \Delta t_{L''}^{n''} G_{L''L'}^{n''n'} \quad , \quad \Delta t_l^n = t_l^n - \overset{\circ}{t}_l^n \quad (3.44)$$

where  $\Delta t_l^n$  is the difference  $t_l^n - \overset{\circ}{t}_l^n$  between the  $t$ -matrices in the perturbed and in the ideal lattice. Since this difference, determined by the perturbation of the potential, is restricted to the vicinity of the impurity, the Green function in this subspace can be easily determined in real space by matrix inversion. The rank of the matrices to be inverted is given by  $(l_{\max} + 1)^2 \cdot n_d$ , i.e. the number  $n_d$  of perturbed potentials times the number  $(l_{\max} + 1)^2$  of angular momenta used. Here  $l_{\max}$  is the maximum angular momentum used in the calculations, e.g.  $l_{\max} = 3$ .

For a single impurity it is often sufficient to neglect the perturbation of the neighboring host atoms and to take into account in eq. (3.42) only the perturbation due to the impurity potential into account. This so-called single site

approximation gives a quite reasonable description of the electronic structure of the impurity and is the essential ingredient of the coherent potential approximation for random alloys. For a more accurate description the perturbations of the neighbors have to be included. The size of the perturbation naturally increases, if impurity pairs, trimers or larger clusters of impurities are included. As a rule one should not only take the strong scattering centers into account, but also the perturbations of all first neighbor atoms.

If we consider an impurity or an adatom on a surface, the structure of the Dyson equation 3.42 is the same. One has only to replace the host Green function  $\overset{\circ}{G}_{LL'}^{nn'}$  by the Green function of the ideal (unperturbed) surface and has to identify  $\Delta t_i^n$  by the change of the  $t$ -matrix on site  $n$  with respect to the value of the unperturbed surface. Thus it is the structural Green function  $\overset{\circ}{G}_{LL'}^{nn'}$ , which describes the correct embedding in the local environment. Therefore the calculation of  $\overset{\circ}{G}_{LL'}^{nn'}$  represents the high entrance fee one has to pay in Green function calculations.

### 3.6 Description of the Full Potential

All-electron methods based on a spherical potential of muffin-tin type or on the atomic sphere approximation (ASA) have in general proven to be very successful and efficient for the description of the electronic structure of solids. However systems with lower symmetry and/or open structures require a more accurate treatment going beyond the spherical approximation. In particular this is necessary, if forces and lattice relaxations are calculated, since for these problems the spherical approximation fails completely.

The multiple scattering expansion (3.40) of KKR-Green function (seen earlier) is still valid in the full potential case, so that the important separation between the single-potential problem and the multiple-scattering problem fully survives. However the single-site eigenfunctions  $R_L^n(\vec{r}; E)$  and  $H_L^n(\vec{r}; E)$  are now the solutions for the general potential  $v^n(\vec{r})$  being no longer spherical [51]. For instance,  $R_{L'}(\vec{r}; E)$  is the solution of the Schrödinger equation for a spherical wave  $j_\nu(\sqrt{E}r)Y_{L'}(\hat{r})$  incident on the potential  $v(\vec{r})$

$$R_{L'}(\vec{r}; E) = j_\nu(\sqrt{E}r)Y_{L'}(\hat{r}) + \int d\vec{r}' g(\vec{r}, \vec{r}'; E) v(\vec{r}') R_{L'}(\vec{r}'; E) \quad (3.45)$$

where  $g(\vec{r}, \vec{r}'; E)$  is the Green function for free space. Clearly the index  $L'$  refers to the angular momentum of the incoming partial wave. Solving the previous equation in this form would require a three dimensional integration. By expanding both the potential as well as the wave function  $R_{L'}(\vec{r}; E)$  into spherical harmonics:

$$v(\vec{r}) = \sum_L v_L(r) Y_L(\hat{r}) \quad (3.46)$$

$$R_{L'}(\vec{r}; E) = \sum_L R_{LL'}(r) Y_L(\hat{r}) \quad (3.47)$$

We obtain coupled radial equations for the double indexed radial functions  $R_{LL'}$

$$R_{LL'}(r, E) = \delta_{LL'} j_{l'}(\sqrt{E}r) + \int_0^S dr' r'^2 g(r, r'; E) \sum_{L''} v_{LL''}(r) R_{L''L'}(r'; E) \quad (3.48)$$

Here the first index  $L$  refers to the  $\vec{r}$ -coordinate of the outgoing partial wave and the second one  $L'$  to the angular momentum of the incoming wave. The radial integral extends up to the range  $S$  of the potential. Moreover

$$v_{LL'}(r) = \sum_{L''} C_{LL'L''} v_{L''}(r) \quad (3.49)$$

where  $C_{LL'L''} = \int d\Omega Y_L Y_{L'} Y_{L''}$  are the Gaunt coefficients.

The solution of the integral equation (3.48) or of the equivalent differential equation is rather complicated. In order to avoid numerical problems one transforms eq. (3.48) into a modified integral equation [52], where the effect of the spherical part where the effect of the spherical part of the potential is already included in the incident radial wave function  $\mathring{R}_l(r; E)$  [52] (an analog expression is obtained for the irregular function  $H_{LL'}$ )

$$R_{LL'}(r, E) = \delta_{LL'} \mathring{R}_l(r, E) + \int_0^S dr' r'^2 G_l(r, r'; E) \sum_{L''} \Delta v_{LL''}(r) R_{L''L'}(r'; E) \quad (3.50)$$

and where  $G_l(r, r'; E)$  is the  $l$ -dependent radial Green function for the spherical component of the potential

$$G_l(r, r'; E) = \sqrt{E} \mathring{H}_l(r_>; E) \mathring{R}_l(r_<; E) \quad (3.51)$$

and  $\Delta v_{LL'}$  the non-spherical component of the potential

$$\Delta v_{LL'}(r) = \sum_{L'' \neq 0} C_{LL'L''} v_{L''}(r) \quad (3.52)$$

which provides the coupling between the different angular momenta. Since the non-spherical potential  $\Delta v$  is always rather small, we rewrite eq. (3.50) in order to solve it by iteration:

$$R_{LL'}(r; E) = A_{LL'}(r; E) \mathring{R}_l(r; E) + B_{LL'}(r; E) \mathring{H}_l(r; E), \quad (3.53)$$

$$H_{LL'}(r; E) = C_{LL'}(r; E) \mathring{R}_l(r; E) + D_{LL'}(r; E) \mathring{H}_l(r; E), \quad (3.54)$$

where the coefficients  $A$ ,  $B$ ,  $C$  and  $D$  are defined as following

$$A_{LL'}(r; E) = \delta_{LL'} + \sqrt{E} \int_r^s dr' r'^2 \overset{\circ}{H}_l(r'; E) \sum_{L''} \Delta V_{LL''}(r') R_{L''L'}(r'; E) \quad (3.55)$$

$$B_{LL'}(r; E) = \sqrt{E} \int_0^r dr' r'^2 \overset{\circ}{R}_l(r'; E) \sum_{L''} \Delta V_{LL''}(r') R_{L''L'}(r'; E), \quad (3.56)$$

$$C_{LL'}(r; E) = \sqrt{E} \int_r^s dr' r'^2 \overset{\circ}{H}_l(r'; E) \sum_{L''} \Delta V_{LL''}(r') H_{L''L'}(r'; E), \quad (3.57)$$

$$D_{LL'}(r; E) = \delta_{LL'} - \sqrt{E} \int_r^s dr' r'^2 \overset{\circ}{R}_l(r'; E) \sum_{L''} \Delta V_{LL''}(r') H_{L''L'}(r'; E) \quad (3.58)$$

The solution of eq. (3.53) and eq. (3.54) by iteration is equivalent to a Born series expansion in powers of  $\Delta v$ . Usually 2-4 iterations are sufficient for convergence.

For a small distance  $r < r_{cut}$  in the core region the potential is in a very good approximation spherical, so that  $\Delta V_{LL''}(r)$  can be neglected. Thus the functions  $A$ ,  $B$ ,  $C$  and  $D$  are constants for  $r < r_{cut}$ :

$$R_{LL'}(r; E) = A_{LL'}(r_{cut}; E) \overset{\circ}{R}_l(r; E), \quad (3.59)$$

$$H_{LL'}(r; E) = C_{LL'}(r_{cut}; E) \overset{\circ}{R}_l(r; E) + D_{LL'}(r_{cut}; E) \overset{\circ}{H}_l(r; E). \quad (3.60)$$

While for non-spherical potentials the general eq. (3.40) for the Green function remains valid and only  $R_L \vec{r}$  and  $H_L \vec{r}$  have to be replaced by the single-site solutions for the anisotropic potential, the same is also true for the Dyson equations (3.42) and (3.44) describing the multiple scattering. Only the spherical t-matrix  $t_l^n(E)$  has to be replaced by the t-matrix  $t_{LL'}^n(E)$  for a general potential  $v^n(\vec{r})$  being given by

$$\Delta t_{LL'}^n(E) = \int_0^S dr' r'^2 j_l(\sqrt{E}r') \sum_{L''} v_{LL''}^n(r') R_{L''L'}^n(r'; E). \quad (3.61)$$

The difference  $\Delta t_{LL'}^n(E) = t_{LL'}^n(E) - \delta_{LL'} t_l^n(E)$  is then simply

$$\Delta t_{LL'}^n(E) = \int_0^S dr' r'^2 R_l(\sqrt{E}r') \sum_{L''} \Delta v_{LL''}^n(r') R_{L''L'}^n(r'; E) \quad (3.62)$$

more details on lattice relaxation and forces calculations are given in Appendix.11.

### 3.7 Self-Consistency Algorithm

We proceed with a short description of the self-consistency algorithm (see Fig. 3.1) for the calculation of the electronic structure by the KKR method. As

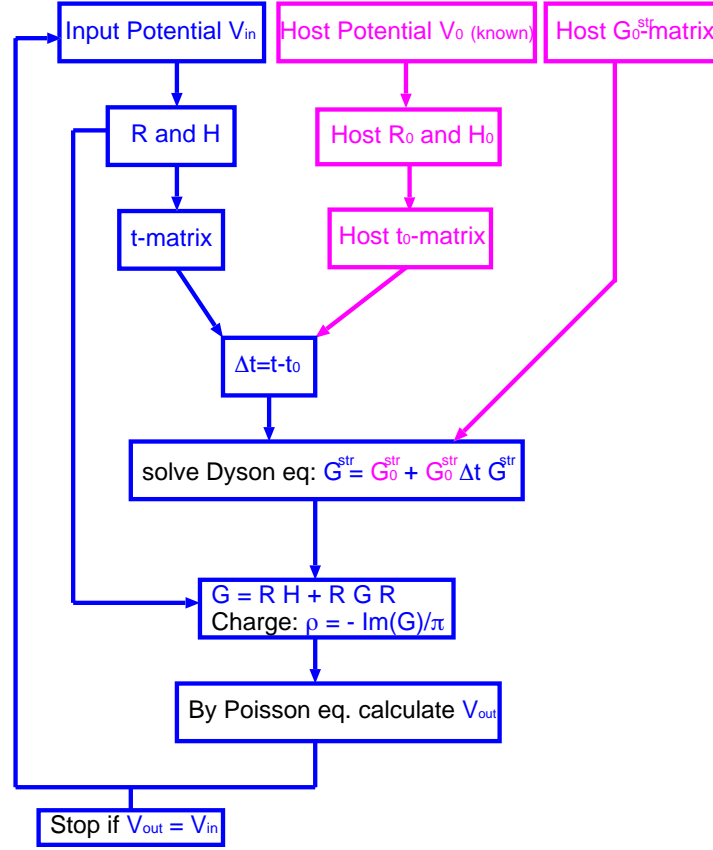


FIG. 3.1 – Diagram showing the self-consistent scheme used to in the KKR method in order to calculate the electronic structures of impurity and impurity clusters.

in all first-principles schemes, the central quantity is the charge density which is found by solving the Kohn-Sham equations. The steps followed are:

1. Start with an input potential  $V_s^{\text{in}}(\vec{r})$  ( $s$  is a spin index used in magnetic systems).
2. Calculate the wavefunctions  $R_L(\vec{r})$  and  $H_L(\vec{r})$  and, from these, the  $t$ -matrix  $t_{LL}$ .
3. Calculate the  $t$ -matrix of the reference system,  $t_{LL}^{\text{ref}}(E)$ , and the difference  $\Delta t_{LL}(E) = t_{LL}(E) - t_{LL}^{\text{ref}}(E)$ .
4. Calculate the structural Green function matrix of the reference system  $\overset{\circ}{G}_{LL}^{\text{str } nm'}(E)$ .

5. Solve the algebraic Dyson equation by matrix inversion for the structural Green function  $G_{LL'}^{mn'}(E)$  of the real system.
6. Calculate the Green function using the structural Green function and  $R_L$  and  $H_L$ . Integrate the Green function over complex energies  $Z$  from the bottom of the valence band  $E_b$  up to  $E_F$  by using a complex-energy contour (see below) and take the imaginary part to find the valence electron spin density:  $\rho_s^v(\vec{r}) = -\frac{1}{\pi} \text{Im} \int_{E_b}^{E_F} G_s(\vec{r}, \vec{r}; Z) dZ$ .
7. Calculate the core-electron wave functions and core-electron spin density  $\rho_s^c(\vec{r})$ ; here the multiple-scattering formalism is not needed, because the core wavefunctions are assumed to be highly localized at the atomic sites. Obtain the total spin density  $\rho_s = \rho_s^c + \rho_s^v$ .
8. Find the output potential  $V_s^{\text{out}}(\vec{r})$  by solving the Poisson equation and adding the exchange-correlation potential  $V_{xc}(\vec{r})$ . If  $V_s^{\text{out}} = V_s^{\text{in}}$  to a reasonable accuracy, exit the cycle, otherwise:
9. Properly mix  $V_s^{\text{out}}$  with  $V_s^{\text{in}}$  to obtain a new input potential, and return to step 1.

In Fig. 3.1 we present a diagram showing the self consistent scheme used for impurity calculations which is basically similar to the case of bulk calculations. The essential quantity to know is the Host green functions.



## Chapter 4

# KKR for Non-collinear Magnetism

### 4.1 Introduction

Theoretically, extensive work is carried out in the area of complex non-collinear magnetism, particularly for surface and bulk systems. A lot of interesting physics would be missed if only collinear magnetic structures were considered. In fact, magnetic nanostructures on magnetic or non-magnetic substrates are attractive to the scientific community due to their novel and unusual properties [4, 53, 54, 55] being of relevance both for theory as well as for the applications in the magneto-electronics devices.

One of these properties is the non-collinear magnetic order occurring for geometrically frustrated antiferromagnets, *e.g.* on a triangular lattice, in disordered systems, exchange bias systems, and molecular magnets, or for systems which exhibit either competing exchange interactions, or competition between exchange and spin-orbit interactions. A simple model for frustration is the following (see Fig. 4.1): Starting with an antiferromagnetic (AF) Cr dimer, the addition of a third Cr atom to form an equilateral triangle leads to a frustrated geometry. Each atom would like to couple AF to both other atoms. Since this is impossible, the moments of the three atoms rotate until a compromise is found. The ground state is then non-collinear, characterized by an angle of  $120^\circ$  between each two atoms. The number of non-collinear solutions in such a free Cr-trimer is infinite. Indeed, each magnetic moment can be in a plane which is rotated by an angle of  $120^\circ$  from the plane containing the neighboring magnetic moment. Thus for each set of three planes there is an infinite number of moments which satisfy the rotation angle criterion. The same situation will also occur for an AF Cr dimer on a ferromagnetic substrate, since the interaction of both Cr atoms with the ferromagnetic substrate atoms is either ferromagnetic or antiferromagnetic. As we will show in the next chapters, also in this case a non-collinear structure can result.

The majority of the *ab-initio* methods available for the treatment of non-

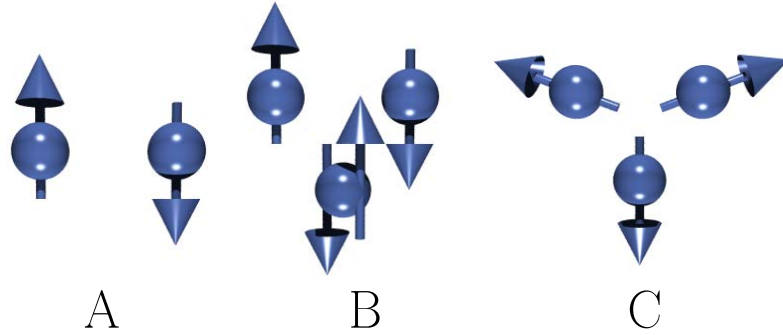


FIG. 4.1 – Example of frustration seen with an antiferromagnetic Cr dimer (A) for which we add a third equidistant atom. A magnetic frustration is obtained because all three atoms want to couple antiferromagnetically (B) leading then to a non-collinear magnetic coupling (C) as a ground state.

collinear magnetism make explicit use of Bloch's theorem and are thus restricted to periodic systems (bulk or films). Then, even for collinear magnetism, one needs large supercells to simulate impurities in a given host (bulk or film) in order to avoid spurious interactions of the impurities from adjacent supercells. In contrast, as described in the previous chapter, KKR does not require a supercell. Motivated by this, we developed a KKR code for non-collinear magnetic clusters on surfaces and in the bulk.

First non-collinear calculations by the KKR Green function method, though not self-consistent, were already performed in 1985. Oswald *et al.* [56] could show by using the method of constraints that the exchange interaction between the moments of Mn and Fe impurity pairs in Cu is in good approximation described by the  $\cos\theta$ -dependence of the Heisenberg model.

Sandratskii *et al.* [57] and Kübler *et al.* [58, 59] pioneered the investigation of non-collinear magnetic structures using self-consistent density functional theory. One of the first systems studied by Sandratskii *et al.* [57] was the spin spiral of bcc Fe with the KKR method. Later on,  $\Delta$ -Fe was a hot topic, and the appearance of the experimental work of Tsunoda *et al.* [60, 61] led to the development of other first-principles methods able to deal with non-collinear magnetism such as LMTO [62], ASW [63] and FLAPW. [64, 65, 66]

Several papers [67, 68] describe how symmetry simplifies the calculational effort for the spiral magnetic structures in the case of perfect periodic systems—this involves the generalized Bloch theorem. In *ab-initio* methods, this principle is used together with the constrained density functional theory [69, 70] giving the opportunity of studying arbitrary magnetic configurations where the orientations of the local moments are constrained to nonequilibrium directions.

Concerning free clusters, few methods are developed. For example, Oda *et al.* [71] developed a plane-wave pseudopotential scheme for non-collinear magnetic structures. They applied it to small Fe clusters for which they found non-collinear magnetic structures for Fe<sub>5</sub> and linear-shape Fe<sub>3</sub>. This last result was in contradiction with the work of Hobbs *et al.* [72] who found only a collinear ferromagnetic configuration using a projector augmented-wave method. Small Cr clusters were found magnetically non-collinear, [71] as shown also by Kohl and Bertsch [73] using a relativistic nonlocal pseudopotential method after optimization of the ionic structure by a Monte Carlo technique. However, within the generalized gradient approximation (GGA) of density-functional theory, Hobbs *et al.* [72] find that in many cases the non-collinear states can be metastable, while the ground-state solutions are collinear and arise after geometrical optimization of the free-standing clusters.

One main result of Oda *et al.* [71] and Hobbs *et al.* [72] concerns the variation of the magnetization density with the position. The spin direction changes in the interstitial region between the atoms where the charge and magnetization densities are small, while the magnetization is practically collinear within the atomic spheres. This supports the use of a single spin direction for each atomic sphere as an approximation in order to accelerate the computation; this approximation is followed also here.

The aim of this chapter is to present a method based on the full-potential KKR scheme [37] which can deal with non-collinear magnetism in systems of reduced symmetry. This method is ideal for treating impurities or small clusters on surfaces or in bulk.

## 4.2 Non-collinear KKR Formalism

We have seen in the previous chapter that the KKR method uses multiple-scattering theory in order to determine the one-electron Green function in a mixed site and angular-momentum representation. For convenience we rewrite the expansion of the retarded Green function:

$$G(\vec{R}_n + \vec{r}, \vec{R}_{n'} + \vec{r}'; E) = -i\sqrt{E} \sum_L R_L^n(\vec{r}_<; E) H_L^n(\vec{r}_>; E) \delta_{nn'} \quad (4.1) \\ + \sum_{LL'} R_L^n(\vec{r}; E) G_{LL'}^{nn'}(E) R_{L'}^{n'}(\vec{r}'; E)$$

Details about this equation are described in eq. (3.40). The structural Green functions  $G_{LL'}^{nn'}(E)$  which are obtained by solving the algebraic Dyson equation:

$$G_{LL'}^{nn'}(E) = \overset{\circ}{G}_{LL'}^{nn'}(E) + \sum_{n'', L'' L'''} \overset{\circ}{G}_{LL''}^{nn''}(E) \Delta t_{L'' L'''}^{n''}(E) G_{L'' L'''}^{n'' n'}(E) \quad (4.2)$$

In case of spin-dependent electronic structure, spin indexes enter in the  $t$ -matrix, the Green functions and in eq. (4.2). Especially in the case of non-collinear magnetism, these quantities become  $2 \times 2$  matrices in spin space, denoted by  $\mathbf{t}$  and  $\mathbf{G}$ .

Once the spin-dependent Green function is known, all physical properties can be derived from it. In particular, the charge density  $n(\vec{r})$  and spin density  $\vec{m}(\vec{r})$  are given by an integration of the imaginary part of  $\mathbf{G}$  up to the Fermi level  $E_F$  and a trace over spin indexes  $s$  (putting the Green function in a matrix form in spin space):

$$n(\vec{r}) = -\frac{1}{\pi} \text{ImTr}_s \int^{E_F} \mathbf{G}(\vec{r}, \vec{r}; E) dE \quad (4.3)$$

$$\vec{m}(\vec{r}) = -\frac{1}{\pi} \text{ImTr}_s \int^{E_F} \vec{\sigma} \mathbf{G}(\vec{r}, \vec{r}; E) dE. \quad (4.4)$$

Here,  $\text{Tr}_s$  means the trace operation in spin space and  $\vec{\sigma} = (\sigma_x, \sigma_y, \sigma_z)$  are the Pauli matrices given explicitly by

$$\sigma_x = \begin{bmatrix} 0 & 1 \\ 1 & 0 \end{bmatrix}, \quad \sigma_y = \begin{bmatrix} 0 & -i \\ i & 0 \end{bmatrix}, \quad \sigma_z = \begin{bmatrix} 1 & 0 \\ 0 & -1 \end{bmatrix}. \quad (4.5)$$

The basic difference between non-collinear and collinear magnetism is the absence of a natural spin quantization axis common to the whole crystal. The density matrix is not anymore diagonal in spin space as in the case of collinear magnetism. Instead, in any fixed frame of reference it has the form

$$\rho(\vec{r}) = \begin{bmatrix} \rho_{\uparrow\uparrow}(\vec{r}) & \rho_{\uparrow\downarrow}(\vec{r}) \\ \rho_{\downarrow\uparrow}(\vec{r}) & \rho_{\downarrow\downarrow}(\vec{r}) \end{bmatrix} = \frac{1}{2} [n(\vec{r}) + \vec{\sigma} \cdot \vec{m}(\vec{r})] \quad (4.6)$$

At any *particular point* in space, of course, a *local* frame of reference can be found in which  $\rho$  is diagonal using rotation matrices defined in section 4.3, but this local frame can change from point to point.

### 4.3 Rotation Matrices

Working with non-collinear magnetism leads inevitably to work with different spin coordinate frames and consequently with rotation matrices. A common way to specify a general three-dimensional rotation is the use of the Euler angles. Here the rotation is separated into three rotations about the axes of a coordinate frame. These rotations in 3-dimensional space are represented by  $3 \times 3$  matrices, e.g. a rotation around the  $x$ -axis by an angle  $\phi$  is performed by applying the matrix

$$\mathbf{R}_x(\phi) = \begin{bmatrix} 1 & 0 & 0 \\ 0 & \cos(\phi) & -\sin(\phi) \\ 0 & \sin(\phi) & \cos(\phi) \end{bmatrix}. \quad (4.7)$$

There are different ways to choose the axes of the three rotations. We use the convention of rotations around the  $z$ - and  $y$ - axis, where the axes of the coordinate system we rotate around are kept fixed during the whole rotation. The three rotations are as follows. First, we rotate around the  $z$ -axis by an angle  $\gamma$ . Second we rotate around the  $y$ -axis by an angle  $\beta$  and the last rotation is again around the  $z$ -axis by an angle  $\alpha$ . Thus a general rotation matrix takes the form

$$\mathbf{R}(\alpha, \beta, \gamma) = \mathbf{R}_z(\alpha) \cdot \mathbf{R}_y(\beta) \cdot \mathbf{R}_z(\gamma) = \quad (4.8)$$

$$\begin{bmatrix} \cos(\alpha) \cos(\beta) \cos(\gamma) - \sin(\alpha) \sin(\gamma) & -\cos(\alpha) \cos(\beta) \sin(\gamma) - \sin(\alpha) \cos(\gamma) & \cos(\alpha) \sin(\beta) \\ \sin(\alpha) \cos(\beta) \cos(\gamma) + \cos(\alpha) \sin(\gamma) & -\sin(\alpha) \cos(\beta) \sin(\gamma) + \cos(\alpha) \cos(\gamma) & \sin(\alpha) \sin(\beta) \\ -\sin(\beta) \cos(\gamma) & \sin(\beta) \sin(\gamma) & \cos(\beta) \end{bmatrix}$$

As we mentioned earlier, the usage of different spin coordinate frames leads to a necessary transformation of quantities like the local magnetic moment of a given atom  $n$ ,  $\vec{M}_n$ , from one spin axis frame 1 to another 2. If the first frame 1 is the local frame where the density matrix is diagonal, *e.g.*, where the  $z$ -direction is along the local magnetic moment, then we have the freedom of rotating the local frame around its  $z$ -axis. We make a choice for the Euler angle  $\gamma = 0$  for the rotation that rotates the global frame 2 to the local frame 1. The corresponding rotation matrix is

$$\mathbf{R}_n^{21} = \mathbf{R}_n(\alpha, \beta, 0) = \begin{bmatrix} \cos(\alpha) \cos(\beta) & -\sin(\alpha) & \cos(\alpha) \sin(\beta) \\ \sin(\alpha) \cos(\beta) & \cos(\alpha) & \sin(\alpha) \sin(\beta) \\ -\sin(\beta) & 0 & \cos(\beta) \end{bmatrix}. \quad (4.9)$$

With this choice, the Euler angles  $\alpha$  and  $\beta$  are equal to the standard polar angles of the local  $z$ -axis in the global frame,  $\alpha = \phi$  and  $\beta = \theta$  (Fig. 4.2). The relation between the representations of a vector quantity like the magnetic moment is given by:

$$\vec{M}^{(1)} = \mathbf{R}^{12} \cdot \vec{M}^{(2)} \quad (4.10)$$

Let us now write the fundamental relation between the angular momentum of a system  $\vec{J}$  and its rotation operator  $\mathbf{R}_{\vec{u}}$  about an arbitrary axis  $\vec{u}$  [74]:

$$\mathbf{R}_{\vec{u}}(\phi + \delta\phi) = \mathbf{R}_{\vec{u}}(\delta\phi) \mathbf{R}_{\vec{u}}(\phi). \quad (4.11)$$

For an infinitesimal rotations it is known that

$$\mathbf{R}_{\vec{u}}(\delta\phi) = 1 - i\vec{J} \cdot \vec{u} \delta\phi, \quad (4.12)$$

which means that

$$\mathbf{R}_{\vec{u}}(\phi + \delta\phi) = (1 - i\vec{J} \cdot \vec{u} \delta\phi) \mathbf{R}_{\vec{u}}(\phi), \quad (4.13)$$

or

$$\frac{\delta \mathbf{R}_{\vec{u}}(\phi)}{\delta\phi} = \frac{\delta \mathbf{R}_{\vec{u}}(\phi + \delta\phi)}{\delta\phi} = -i\vec{J} \cdot \vec{u} \delta\phi \mathbf{R}_{\vec{u}}(\phi) \quad (4.14)$$

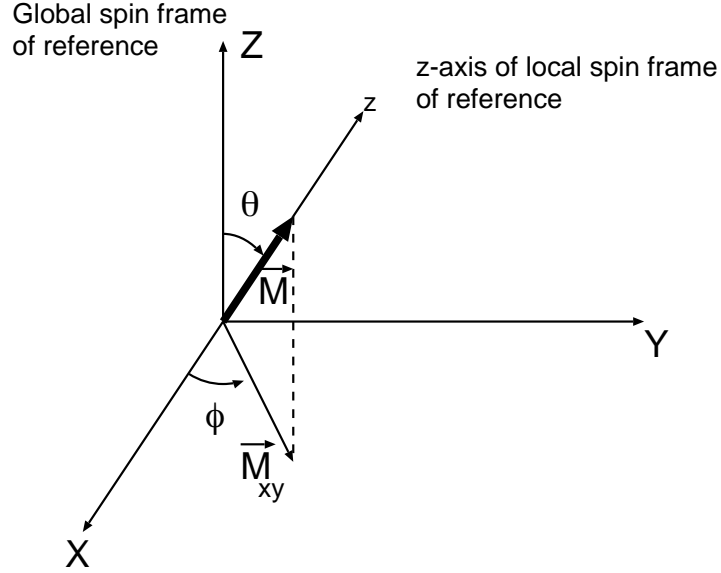


FIG. 4.2 – Rotation of a magnetic moment  $\vec{M}$  from the local spin frame of reference defined by the  $z$ -direction parallel to  $\vec{M}$  into the global spin frame of reference ( $OXYZ$ ) using the polar angles  $(\theta, \phi)$ .  $\vec{M}_{xy}$  is the projection of  $\vec{M}$  into the plane ( $OXY$ ).

This differential equation is easily integrated to give

$$\mathbf{R}_{\vec{a}}(\phi) = e^{-i\phi\vec{J}\cdot\vec{a}}. \quad (4.15)$$

Thus equation (4.8) becomes

$$\mathbf{R}(\alpha, \beta, \gamma) = e^{-i\alpha J_x} \cdot e^{-i\beta J_y} \cdot e^{-i\gamma J_z} \quad (4.16)$$

The particles we are interested to study are electrons and characterized by a total angular momentum  $\vec{J} = \vec{L} + \vec{S}$ . Since  $\vec{L}$  and  $\vec{S}$  commute (in the absence of spin-orbit coupling), the rotation operator  $\mathbf{R}(\alpha, \beta, \gamma)$  takes the form of a product of two commuting operators:

$$\mathbf{R}(\alpha, \beta, \gamma) = \mathbf{R}^S(\alpha, \beta, \gamma) \cdot \mathbf{R}^L(\alpha, \beta, \gamma) \quad (4.17)$$

$\mathbf{R}^S$  rotates the spin whereas  $\mathbf{R}^L$  rotates the orbital variables. The first operator is defined as:

$$\mathbf{R}^S(\alpha, \beta, \gamma) = e^{-i\alpha\sigma_x/2} \cdot e^{-i\beta\sigma_y/2} \cdot e^{-i\gamma\sigma_z/2}, \quad (4.18)$$

$\vec{\sigma} = (\sigma_x, \sigma_y, \sigma_z)$  being the Pauli operator. Finally in the two-dimensional space of Pauli spinors the rotation matrices that we note  $\mathbf{U}$  are given by (see [74]).

$$\mathbf{R}^S(\alpha, \beta, \gamma) = \mathbf{U}(\alpha, \beta, \gamma) = \begin{bmatrix} \cos(\frac{\beta}{2})e^{-\frac{i(\alpha+\gamma)}{2}} & -\sin(\frac{\beta}{2})e^{-\frac{i(\alpha-\gamma)}{2}} \\ \sin(\frac{\beta}{2})e^{\frac{i(\alpha-\gamma)}{2}} & \cos(\frac{\beta}{2})e^{\frac{i(\alpha+\gamma)}{2}} \end{bmatrix} \quad (4.19)$$

which in the case of  $\gamma = 0$  and standard polar angles notation  $(\theta, \phi)$  simplifies to

$$\mathbf{U} = \begin{bmatrix} \cos(\frac{\theta}{2})e^{-\frac{i}{2}\phi} & -\sin(\frac{\theta}{2})e^{-\frac{i}{2}\phi} \\ \sin(\frac{\theta}{2})e^{\frac{i}{2}\phi} & \cos(\frac{\theta}{2})e^{\frac{i}{2}\phi} \end{bmatrix}. \quad (4.20)$$

In the the local spin frame of reference 1 the spinor eigenstates are uniquely defined as

$$\chi_{\uparrow}^1 = \begin{bmatrix} 1 \\ 0 \end{bmatrix}, \quad \chi_{\downarrow}^1 = \begin{bmatrix} 0 \\ 1 \end{bmatrix}. \quad (4.21)$$

In the non-collinear case (global spin frame of reference 2), the spin-up and spin-down means up and down in terms of the local quantization axis. The spinors in spin frame of reference 2 are defined by

$$|\chi^2 \rangle = \mathbf{U}|\chi^1 \rangle, \quad (4.22)$$

which leads to

$$\chi_{\uparrow}^2 = \begin{bmatrix} \cos(\frac{\theta}{2})e^{-\frac{i}{2}\phi} \\ \sin(\frac{\theta}{2})e^{\frac{i}{2}\phi} \end{bmatrix}, \quad \chi_{\downarrow}^2 = \begin{bmatrix} -\sin(\frac{\theta}{2})e^{-\frac{i}{2}\phi} \\ \cos(\frac{\theta}{2})e^{\frac{i}{2}\phi} \end{bmatrix}. \quad (4.23)$$

In order to rotate the expectation value of the operator  $\mathbf{A}^1$  from reference system 1 to reference system 2 we proceed as following

$$\langle \chi^2 | \mathbf{A}^2 | \chi^2 \rangle = \langle \chi^1 | \mathbf{A}^1 | \chi^1 \rangle \quad \text{with} \quad \mathbf{A}^1 = \mathbf{U}^\dagger \mathbf{A}^2 \mathbf{U}, \quad (4.24)$$

## 4.4 Host Green Functions and $t$ -matrices

In order to deal with non-collinear magnetism, we have to solve the appropriate Dyson equation. First we define the reference system which is a bulk system or a perfect surface characterized by collinear magnetism for which a schematic view is shown in Fig. 4.3. Although the collinearity of the reference system is not a necessary requirement, it serves our purpose of calculating the electronic structure of the ferromagnetic or non-magnetic surfaces which are used as reference systems. Thus the host Green functions  $\overset{\circ}{\mathbf{G}}$  and  $t$ -matrices  $\overset{\circ}{\mathbf{t}}$  are assumed diagonal in spin space. In this way, in the case of a magnetic host, a global spin frame of reference is defined. The host  $\overset{\circ}{\mathbf{G}}$  and  $\overset{\circ}{\mathbf{t}}$  are thus of the form:

$$\overset{\circ}{\mathbf{G}}(E) = \begin{bmatrix} \overset{\circ}{G}_{\uparrow\uparrow}(E) & 0 \\ 0 & \overset{\circ}{G}_{\downarrow\downarrow}(E) \end{bmatrix}; \quad \overset{\circ}{\mathbf{t}}(E) = \begin{bmatrix} \overset{\circ}{t}_{\uparrow\uparrow}(E) & 0 \\ 0 & \overset{\circ}{t}_{\downarrow\downarrow}(E) \end{bmatrix} \quad (4.25)$$

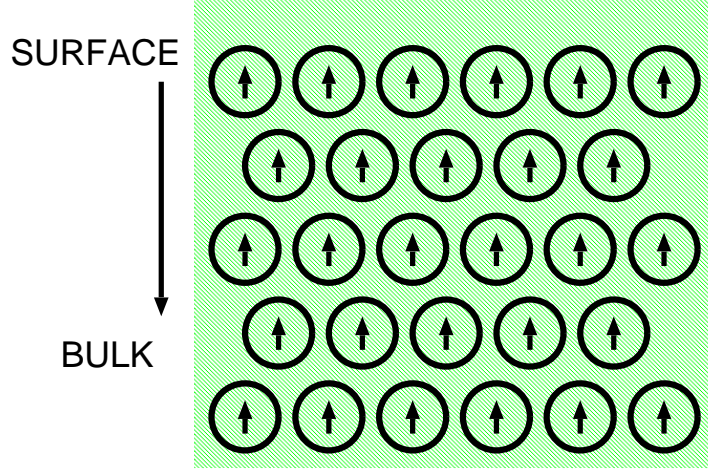


FIG. 4.3 – A schematic view of a host system prototype. The figure shows a perfect surface characterized by collinear magnetism.

In practice, the host structural Green functions are first calculated in  $\vec{k}$ -space using matrix inversion; a subsequent Fourier transform gives us the real-space quantities. We write, then,

$$\overset{\circ}{G}_{LL'}(\vec{k}; E) = \sum_{n'} \overset{\circ}{G}_{LL'}^{nn'}(E) e^{-i\vec{k} \cdot (\vec{R}^n - \vec{R}^{n'})} \quad (4.26)$$

(which, due to translational symmetry, is independent of  $n$ ). The algebraic Dyson equation (3.42) becomes

$$\overset{\circ}{G}_{LL'}(\vec{k}; E) = g_{LL'}(\vec{k}; E) + \sum_{L''} g_{LL''}(\vec{k}; E) t_{L''}(E) \overset{\circ}{G}_{L''L'}(\vec{k}; E) \quad (4.27)$$

(the  $t$ -matrix is independent of  $n$ , again due to translational symmetry). Here  $g_{LL'}$  are the reference structural green function of the original system before perturbing it by the surface. This original system can be for example free space. The structural Green functions  $G_{LL'}$  and  $g_{LL'}$ , and the  $t$ -matrix  $t_l$ , are considered as matrices in  $L$  and  $L'$ , and (4.27) is solved by matrix inversion after a cutoff at some  $l = l_{\max}$  for which the  $t$ -matrix becomes negligible (usually  $l_{\max} = 3$  or 4 suffices). The result is

$$\overset{\circ}{G}_{LL'}^{nn'}(E) = \frac{1}{V_{\text{BZ}}} \int_{\text{BZ}} d^3k e^{i\vec{k} \cdot (\vec{R}^n - \vec{R}^{n'})} \left[ \left( 1 - \mathbf{g}(\vec{k}; E) \mathbf{t}(E) \right)^{-1} \mathbf{g}(\vec{k}; E) \right]_{LL'} \quad (4.28)$$

where the integral is over the Brillouin zone volume  $V_{\text{BZ}}$ . For the calculation of the charge density or of the density of states, only the on-site term  $n = n'$ ,  $G_{LL'}^{nn}(E)$ , is needed.

Here, for non-primitive lattices the  $t$ -matrix  $\mathbf{t}(E)$  depends on the atom-type  $\mu$  and on angular-momentum indexes (it is site-diagonal,  $(\mathbf{t})_l^{\mu\mu'} = t_l^n \delta_{\mu\mu'}$ ). The structure constants  $\mathbf{g}(\vec{k}; E)$  are considered as matrices in both  $(L, L')$  and  $(\mu, \mu')$ , and thus the computational effort for the matrix inversion increases as  $O(N_{\text{at}}^3)$ . A considerable speed-up can be achieved for large systems by using the concept of the screening transformation (see section 4.4.1).

#### 4.4.1 Screened (tight-binding) KKR Method

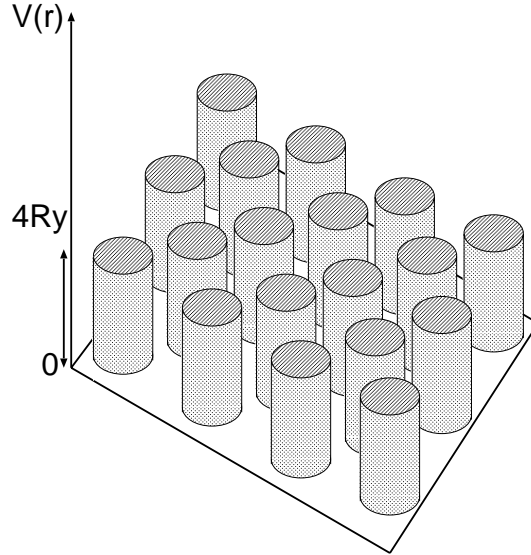


FIG. 4.4 – Schematic representation in two dimensions of repulsive  $4Ry$ -high muffin-tin potentials.

An improvement of the KKR method has been achieved by the so-called *screened* or *tight-binding* KKR formalism [38], which allows a considerable reduction of the calculation time for large systems. In particular, while the traditional KKR formalism requires a matrix inversion for the solution of the algebraic Dyson equation with computational effort of  $O(N^3)$  (for  $N$  different atoms in the unit cell), in the screened KKR method the same results can be obtained with an effort of, ideally,  $O(N)$ ; this is optimally achieved for layered systems. This

is made possible by choosing a new reference system of repulsive potentials (see Fig. 4.4) after which the reference Green function falls off exponentially with distance, thus allowing the inversion of sparse, or even tridiagonal, matrices, which is much faster than a full matrix inversion. Due to the decoupling between distant atomic sites which follows, the corresponding transformation is called *screening transformation* and the method *screened KKR*; due to its formal resemblance to tight-binding theory, the method is also called *tight-binding KKR* [38].

#### 4.4.2 Two-Dimensional Systems: Finite-Thickness Slabs and Half-Infinite Crystals

The extension of the KKR method to the treatment of layered systems, such as surfaces and interfaces, is straightforward, and most efficient within the screened KKR formalism, where  $O(N)$  scaling can be achieved (where  $N$  is the number of layers) as discussed in section 4.4.1.

When treating a layered system, a surface-adapted geometry is used, in the sense that the two-dimensional periodicity of the atomic layers parallel to the surface (or interface) is exploited while the direction perpendicular to these layers is treated as if these were different atoms in a unit cell. The Fourier transforms are done now within the two-dimensional surface Brillouin zone (SBZ), and the corresponding integration is over all  $\vec{k}_{\parallel}$  in the SBZ. Thus, we have

$$\begin{aligned} \mathring{G}_{LL'}^{n\mu,n'\mu'}(E) &= \frac{1}{A_{\text{SBZ}}} \int_{\text{SBZ}} d^2k_{\parallel} e^{i\vec{k}_{\parallel} \cdot (\vec{R}^n - \vec{R}^{n'})} e^{i\vec{k}_{\parallel} \cdot (\vec{\chi}^{\mu} - \vec{\chi}^{\mu'})} \\ &\times \left[ \left( 1 - \mathbf{G}^r(\vec{k}_{\parallel}; E) \Delta \mathbf{t}(E) \right)^{-1} \mathbf{G}^r(\vec{k}_{\parallel}; E) \right]_{LL'}^{\mu\mu'}. \end{aligned} \quad (4.29)$$

where now  $\vec{R}^n$  are in-plane position vectors of the two-dimensional Bravais lattice, while  $\vec{\chi}^{\mu}$  are vectors connecting atomic positions in different layers;  $A_{\text{SBZ}}$  is the area of the SBZ.

In the case of surfaces, the vacuum is described by empty sites, meaning that the lattice structure is continued into the vacuum but no nuclei are positioned there. In this way, the vacuum potential and charge density are calculated within the multiple-scattering formalism on the same footing as the bulk. In practice, three or four monolayers of vacuum sites are enough for the calculation of the electronic structure; equation (4.29) can be cut-off after that.

Depending on the problem, one can choose to use a slab of finite thickness in order to represent a surface or interface, or one can choose to take half-infinite boundary conditions. In the latter case, and starting from a “boundary” layer, the crystal is continued by periodically repeating the potential of this boundary layer to all subsequent layers up to infinity. One is then faced with a problem of inverting an infinite matrix, which due to the screening transformation has a

tridiagonal form, in order to find the Green function in the region of interest. This is done efficiently by the decimation technique [75], which is based on a iterative inversion of matrices of doubled size at each step. In this way the number of layers which are included in the Green function grows exponentially with the number of steps, and the limit of the half-infinite crystal is rapidly achieved.

## 4.5 t-matrix for Perturbed Atoms

The next step is the construction of the perturbed system. The impurity atoms which might couple magnetically in a non-collinear way reside at the surface (see Fig. 4.5), perturbing the potential at a few neighboring sites (atoms or empty cells representing the potential in the vacuum). Within this finite cluster of perturbed sites the magnetization can be non-collinear leading to the appearance of non-diagonal elements of the *t*-matrix:

$$\mathbf{t}(E) = \begin{bmatrix} t_{\uparrow\uparrow}(E) & t_{\uparrow\downarrow}(E) \\ t_{\downarrow\uparrow}(E) & t_{\downarrow\downarrow}(E) \end{bmatrix} \quad (4.30)$$

The non-diagonal *t*-matrix contains the information on spin-flip scattering by the atomic potential.

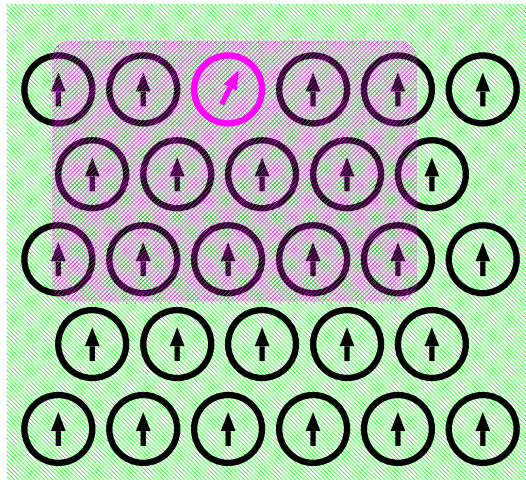


FIG. 4.5 – A schematic view of a system characterized by two perturbations: first by the presence of an impurity sitting in the surface layer and second by taking into account non-collinear magnetism. The extension of the perturbations is delimited by a pink color.

At this stage an approximation enters our method. It is assumed that, separately for each atom, there exists an intra-atomic spin quantization axis common to the whole atomic cell. This axis is identified with the spatial average of the magnetization density  $\vec{m}_n(\vec{r})$  in each cell  $n$ . This defines the local spin frame of reference. In this way we neglect the variation of the spin quantization axis within the cell, avoiding the time-consuming numerical solution of the potential of coupled Schrödinger equations of the two spin channels. Within the local density approximation of density-functional theory, the exchange correlation potential has the same reference frame as the local magnetization  $\vec{m}_n(\vec{r})$ . Then for each atom we have a potential which is collinear in the local frame, and we obtain the solutions of the Schrödinger equation,  $R_{nLs}^{\text{loc}}(\vec{r}; E)$  and  $H_{nLs}^{\text{loc}}(\vec{r}; E)$ , depending on the spin index  $s$  of the local frame.

The solution of the Schrödinger equation separately for each spin channel provides also the diagonal  $t$ -matrix of each atomic cell  $n$  in the local frame of reference:

$$\mathbf{t}_n^{\text{loc}}(E) = \begin{bmatrix} t_{\uparrow\uparrow}^{\text{loc}}(E) & 0 \\ 0 & t_{\downarrow\downarrow}^{\text{loc}}(E) \end{bmatrix} \quad (4.31)$$

Then the  $t$ -matrix is rotated from the local to the global spin frame of reference using the spin rotation matrix  $\mathbf{U}_n$  defined in the section 4.3:

$$\mathbf{t}_n^{\text{glob}}(E) = \mathbf{U}_n \mathbf{t}_n^{\text{loc}}(E) \mathbf{U}_n^\dagger, \quad (4.32)$$

The polar angles  $\theta_n$  and  $\phi_n$  entering in the expression of  $\mathbf{U}_n$  define the direction of the local magnetic moment  $\vec{M}_n$  with respect to the global spin frame of reference. Normally,  $\theta_n$  and  $\phi_n$  vary within the atomic cell, but in the approximation used here, average angles are defined for each cell via an averaging of the magnetization density within the cell. Of course, when self-consistency is achieved, both the averaged and the point-by-point varying magnetization direction can be extracted from the output density matrix. Thus the assumption of a unique spin direction in each cell is only made for the spin-dependent potential.

The  $t$ -matrix in the global spin frame of reference can be rewritten in the following way:

$$\mathbf{t}_n^{\text{glob}}(E) = \mathbf{U}_n \begin{bmatrix} t_{\uparrow\uparrow}^{\text{loc}}(E) & 0 \\ 0 & t_{\downarrow\downarrow}^{\text{loc}}(E) \end{bmatrix} \mathbf{U}_n^\dagger. \quad (4.33)$$

To continue let us define new useful quantities  $t_{sum}^{\text{loc}}$  and  $t_{diff}^{\text{loc}}$  as following:

$$t_{sum}^{\text{loc}}(E) = t_{\uparrow\uparrow}^{\text{loc}}(E) + t_{\downarrow\downarrow}^{\text{loc}}(E) \quad \text{and} \quad t_{diff}^{\text{loc}}(E) = t_{\uparrow\uparrow}^{\text{loc}}(E) - t_{\downarrow\downarrow}^{\text{loc}}(E) \quad (4.34)$$

Equation 4.33 is equivalent to

$$\mathbf{t}_n^{\text{glob}}(E) = \frac{1}{2} \mathbf{U}_n \begin{bmatrix} t_{\text{sum}}^{\text{loc}}(E) + t_{\text{diff}}^{\text{loc}}(E) & 0 \\ 0 & t_{\text{sum}}^{\text{loc}}(E) - t_{\text{diff}}^{\text{loc}}(E) \end{bmatrix} \mathbf{U}_n^\dagger \quad (4.35)$$

$$= \frac{1}{2} \mathbf{U}_n \left\{ t_{\text{sum}}^{\text{loc}}(E) \begin{bmatrix} 1 & 0 \\ 0 & 1 \end{bmatrix} + t_{\text{diff}}^{\text{loc}}(E) \begin{bmatrix} 1 & 0 \\ 0 & -1 \end{bmatrix} \right\} \mathbf{U}_n^\dagger \quad (4.36)$$

$$= \frac{1}{2} \mathbf{U}_n [t_{\text{sum}}^{\text{loc}}(E) \mathbf{1} + t_{\text{diff}}^{\text{loc}}(E) \boldsymbol{\sigma}_z] \mathbf{U}_n^\dagger, \quad (4.37)$$

or

$$\mathbf{t}_n^{\text{glob}}(E) = \frac{1}{2} [t_{\text{sum}}^{\text{loc}}(E) \mathbf{1} + t_{\text{diff}}^{\text{loc}}(E) \mathbf{U}_n \boldsymbol{\sigma}_z \mathbf{U}_n^\dagger], \quad (4.38)$$

In order to write eq. (4.38) in a more elegant way it is convenient to define the projection matrices  $\boldsymbol{\sigma}_{ns}$  for the local spin-up ( $\uparrow$ ) and spin-down ( $\downarrow$ ) directions as:

$$\boldsymbol{\sigma}_{ns} = \frac{1}{2} \mathbf{U}_n (\mathbf{1} \pm \boldsymbol{\sigma}_z) \mathbf{U}_n^\dagger = (\boldsymbol{\sigma}_{ns})^2 \quad (+ \text{ for } s = \uparrow, - \text{ for } s = \downarrow) \quad (4.39)$$

Then  $\mathbf{t}_n^{\text{glob}}(E)$  is written as:

$$\mathbf{t}_n^{\text{glob}}(E) = t_{n\uparrow}^{\text{loc}}(E) \boldsymbol{\sigma}_{n\uparrow} + t_{n\downarrow}^{\text{loc}}(E) \boldsymbol{\sigma}_{n\downarrow}. \quad (4.40)$$

The projection matrices  $\boldsymbol{\sigma}_{ns}$  are more explicitly given by

$$\boldsymbol{\sigma}_{ns} = \frac{1}{2} \begin{bmatrix} 1 \pm \cos(\theta_n) & \pm \sin(\theta_n) e^{-i\phi_n} \\ \pm \sin(\theta_n) e^{i\phi_n} & 1 \mp \cos(\theta_n) \end{bmatrix} \quad (+ \text{ for } s = \uparrow, - \text{ for } s = \downarrow). \quad (4.41)$$

In the collinear case the local and global frames are identical and the projection operators reduce to:

$$\boldsymbol{\sigma}_\uparrow = \begin{bmatrix} 1 & 0 \\ 0 & 0 \end{bmatrix}, \quad \boldsymbol{\sigma}_\downarrow = \begin{bmatrix} 0 & 0 \\ 0 & 1 \end{bmatrix} \quad (\text{collinear case}). \quad (4.42)$$

## 4.6 Structural Green Function

At this stage, the difference between the  $t$ -matrices  $\Delta \mathbf{t}_n^{\text{glob}} = \mathbf{t}_n^{\text{glob}} - \overset{\circ}{\mathbf{t}}_n$  is calculated in order to get all the ingredients to solve the Dyson equation for the structural Green function ( $\overset{\circ}{\mathbf{t}}_n$  has been defined in the global frame in eq. (4.25)). This is the analogue of eq. (4.2) in matrix form in spin space:

$$\mathbf{G}_{\text{str}}(E) = \overset{\circ}{\mathbf{G}}_{\text{str}}(E) + \overset{\circ}{\mathbf{G}}_{\text{str}}(E) \Delta \mathbf{t}_n^{\text{glob}}(E) \mathbf{G}_{\text{str}}(E). \quad (4.43)$$

Here, in analogy to eq. (4.2) and eq. (4.2),  $\mathbf{G}_{\text{str}}(E)$  are matrices of size  $2 \times 2$  in spin space, size  $(l_{\text{max}} + 1)^2 \times (l_{\text{max}} + 1)^2$  in angular momentum space, and size

$N \times N$  (with  $N$  the number of sites) in real space; all these indices are combined to form  $2 \times (l_{\max} + 1)^2 \times N$ -dimensional matrices. The  $t$ -matrix itself is diagonal in real space site indexes. The solution of eq. (4.43) for the structural Green function requires matrix inversion, yielding  $\mathbf{G}_{\text{str}}(E)$  in the global frame:

$$\mathbf{G}_{\text{str}}(E) = \mathring{\mathbf{G}}_{\text{str}}(E)(1 - \Delta t^{\text{glob}}(E) \mathring{\mathbf{G}}_{\text{str}}(E))^{-1}. \quad (4.44)$$

## 4.7 Green Function for Perturbed Atoms

Equation (4.2) can be now rewritten in the non-collinear case in order to obtain the Green function in the local frame. Using the matrices  $\sigma_{ns}^{\text{loc}}$  (eq. (4.42)) to project the wavefunctions to the local frame, the Green function is written as:

$$\begin{aligned} \mathbf{G}^{\text{loc}}(\vec{R}_n + \vec{r}, \vec{R}_{n'} + \vec{r}'; E) &= -i\sqrt{E} \sum_{Ls} R_{nLs}^{\text{loc}}(\vec{r}_{<}; E) \sigma_{ns}^{\text{loc}} H_{nLs}^{\text{loc}}(\vec{r}_{>}; E) \sigma_{ns}^{\text{loc}} \\ &+ \sum_{LL'ss'} R_{nLs}^{\text{loc}}(\vec{r}; E) \sigma_{ns}^{\text{loc}} \mathbf{G}_{LL'nn'}^{\text{loc}}(E) \sigma_{n's'}^{\text{loc}} R_{n'L's'}^{\text{loc}}(\vec{r}'; E). \end{aligned} \quad (4.45)$$

As  $R^{\text{loc}}$  and  $H^{\text{loc}}$  are scalar quantities, the product operators within the single particle term  $\sigma_{ns}^{\text{loc}} \sigma_{ns}^{\text{loc}}$  reduces to  $\sigma_{ns}^{\text{loc}}$ . This simplification cannot occur in the second term because of the structural Green function. In order to derive the Green function in the global frame we rotate both sides of eq. (4.45) by using rotation matrices  $\mathbf{U}$ :

$$\begin{aligned} \mathbf{U} \mathbf{G}^{\text{loc}}(\vec{R}_n + \vec{r}, \vec{R}_{n'} + \vec{r}'; E) \mathbf{U}^\dagger &= -i\sqrt{E} \sum_{Ls} R_{nLs}^{\text{loc}}(\vec{r}_{<}; E) H_{nLs}^{\text{loc}}(\vec{r}_{>}; E) \mathbf{U} \sigma_{ns}^{\text{loc}} \mathbf{U}^\dagger \\ &+ \sum_{LL'ss'} R_{nLs}^{\text{loc}}(\vec{r}; E) \mathbf{U} \sigma_{ns}^{\text{loc}} \mathbf{G}_{LL'nn'}^{\text{loc}}(E) \sigma_{n's'}^{\text{loc}} \mathbf{U}^\dagger R_{n'L's'}^{\text{loc}}(\vec{r}'; E). \end{aligned} \quad (4.46)$$

Introducing the terms  $\mathbf{U} \mathbf{U}^\dagger = \mathbf{1}$  at the right and left of the structural Green function  $\mathbf{G}_{LL'nn'}^{\text{loc}}(E)$  in (4.46) gives

$$\begin{aligned} \mathbf{U} \mathbf{G}^{\text{loc}}(\vec{R}_n + \vec{r}, \vec{R}_{n'} + \vec{r}'; E) \mathbf{U}^\dagger &= -i\sqrt{E} \sum_{Ls} R_{nLs}^{\text{loc}}(\vec{r}_{<}; E) H_{nLs}^{\text{loc}}(\vec{r}_{>}; E) \mathbf{U} \sigma_{ns}^{\text{loc}} \mathbf{U}^\dagger \\ &+ \sum_{LL'ss'} R_{nLs}^{\text{loc}}(\vec{r}; E) \mathbf{U} \sigma_{ns}^{\text{loc}} \mathbf{U}^\dagger \mathbf{U} \mathbf{G}_{LL'nn'}^{\text{loc}}(E) \mathbf{U}^\dagger \mathbf{U} \sigma_{n's'}^{\text{loc}} \mathbf{U}^\dagger R_{n'L's'}^{\text{loc}}(\vec{r}'; E). \end{aligned} \quad (4.47)$$

The term  $\mathbf{U} \sigma_{ns}^{\text{loc}} \mathbf{U}^\dagger$  is nothing else than the projector operator to the global spin frame of reference  $\sigma_{ns}^{\text{glob}}$  that we note for simplification as just  $\sigma_{ns}$ . We arrive finally at an expression giving the Green function in the global frame of reference depending explicitly on the structural Green function in the global frame ( $\mathbf{G}_{LL'nn'}^{\text{glob}}(E) = \mathbf{U} \mathbf{G}_{LL'nn'}^{\text{loc}}(E) \mathbf{U}^\dagger$ ) and on the solutions of the Schrödinger

equation in the local frame:

$$\begin{aligned} \mathbf{G}^{\text{glob}}(\vec{R}_n + \vec{r}, \vec{R}_{n'} + \vec{r}'; E) &= -i\sqrt{E} \sum_{Ls} R_{nLs}^{\text{loc}}(\vec{r}_{<}; E) H_{nLs}^{\text{loc}}(\vec{r}_{>}; E) \boldsymbol{\sigma}_{ns} \\ &+ \sum_{LL'ss'} R_{nLs}^{\text{loc}}(\vec{r}; E) \boldsymbol{\sigma}_{ns} \mathbf{G}_{LL'nn'}^{\text{glob}}(E) \boldsymbol{\sigma}_{n's'} R_{n'L's'}^{\text{loc}}(\vec{r}'; E). \end{aligned} \quad (4.48)$$

If needed, the Green function can be rotated to the local frame of any atom by the use of the transformation matrices  $\mathbf{U}_n$  (eq. (4.20)). We point out that, even in the local frame of reference, the Green function is not in general diagonal in spin space. Finally we calculate the charge density and spin density from Equations (4.3, 4.4). The spin dependent local density of states within the Wigner-Seitz cell WS of each site  $n$  is:

$$n_{ns}(E) = -\frac{1}{\pi} \int_{\text{WS}} \text{Im} G_{ss}(\vec{R}_n + \vec{r}, \vec{R}_n + \vec{r}; E) d^3r \quad (4.49)$$

The spin density  $\vec{m} = (m^x, m^y, m^z)$  (eq. (4.4)) is non-collinear with the following expressions for its components

$$m^x(\vec{r}) = -\frac{1}{\pi} \int^{E_F} \text{Im} \left[ G_{\uparrow\downarrow}(\vec{r}, \vec{r}; E) + G_{\downarrow\uparrow}(\vec{r}, \vec{r}; E) \right], \quad (4.50)$$

$$m^y(\vec{r}) = -\frac{1}{\pi} \int^{E_F} \text{Im} \left[ i G_{\uparrow\downarrow}(\vec{r}, \vec{r}; E) - i G_{\downarrow\uparrow}(\vec{r}, \vec{r}; E) \right], \quad (4.51)$$

$$m^z(\vec{r}) = -\frac{1}{\pi} \int^{E_F} \text{Im} \left[ G_{\uparrow\uparrow}(\vec{r}, \vec{r}; E) - G_{\downarrow\downarrow}(\vec{r}, \vec{r}; E) \right]. \quad (4.52)$$

Thus, knowing the components of the spin-density vector we are able to calculate the new polar angles at each site  $n$  for each point by

$$\tan\theta_n(\vec{r}) = \frac{m_n^z(\vec{r})}{m_n^x(\vec{r})}, \quad \tan\phi_n(\vec{r}) = \frac{m_n^y(\vec{r})}{m_n^x(\vec{r})} \quad (4.53)$$

or as an average over the local Wigner-Seitz cell

$$\tan\theta_n = \frac{\int_{\text{WS}} m_n^z(\vec{r}) d\vec{r}}{\int_{\text{WS}} m_n^x(\vec{r}) d\vec{r}}, \quad \tan\phi_n = \frac{\int_{\text{WS}} m_n^y(\vec{r}) d\vec{r}}{\int_{\text{WS}} m_n^x(\vec{r}) d\vec{r}} \quad (4.54)$$

At this step, we know the average angle of each Wigner-Seitz cell which we use to rotate back the charge densities to the local spin frame of references using the rotation matrices. These charge densities are later on used to calculate the exchange correlation potential and the Hartree potential.

## 4.8 Total Energy

Within density-functional theory, the total energy of a many-electron system is written as a sum of three terms: the single-particle kinetic energy  $T_0[\rho]$ , the Hartree energy  $E_H[\rho]$  (including the interaction with the nuclear charge), and the exchange and correlation energy  $E_{xc}[\rho_s]$  ( $s = (+, -)$  is the spin index defined in the local spin frame of reference related to each Wigner-Seitz cell). The kinetic and the exchange-correlation energy, as well as the total energy, are functionals of the spin density  $\rho_s(\vec{r}) := (\rho_+(\vec{r}), \rho_-(\vec{r}))$ , while the Hartree energy is a functional of the charge density  $\rho = \rho_+ + \rho_-$ . We have:

$$E_{\text{tot}}[\rho_+, \rho_-] = T[\rho_+, \rho_-] + E_H[\rho] + E_{xc}[\rho_+, \rho_-] \quad (4.55)$$

Given the single-particle energies  $\epsilon_{is}$  (eigenenergies of the Kohn-Sham equations), the kinetic energy can be written in terms of these and of the effective Kohn-Sham potential  $V_s^{\text{eff}}(\vec{r})$  as:

$$T[\rho_+, \rho_-] = \sum_s \left( \sum_i \epsilon_{is} - \int \rho_s(\vec{r}) V_s^{\text{eff}}(\vec{r}) d^3r \right) \quad (4.56)$$

In this way, the sum of the single-particle energies

$$E_{\text{sp}} = \sum_{is} \epsilon_{is} \quad (4.57)$$

is singled out and can be thought of a “band energy”, which would be relevant if we had non-interacting electrons in an external potential, while the remaining terms are packed up together in what is called the “double-counting energy terms”, as corrections to the single-particle picture:

$$E_{\text{dc}}[\rho_+, \rho_-] = - \sum_s \int \rho_s(\vec{r}) V_s^{\text{eff}}(\vec{r}) d^3r + E_H[\rho] + E_{xc}[\rho_+, \rho_-]. \quad (4.58)$$

The total energy is the sum of the two:

$$E_{\text{tot}}[\rho_+, \rho_-] = E_{\text{sp}}[\rho_+, \rho_-] + E_{\text{dc}}[\rho_+, \rho_-]. \quad (4.59)$$

We proceed to analyze each term separately. The sum of single-particle energies can be written in terms of the spin-dependent density of states  $n_s(E)$  as

$$\begin{aligned} E_{\text{sp}} &= \sum_{is} \epsilon_{is} \\ &= \sum_s \int^{E_F} E n_s(E) dE \end{aligned} \quad (4.60)$$

$$= E_F N - \sum_s \int^{E_F} N_s(E) dE. \quad (4.61)$$

In the last step we introduced  $N_s(E)$  as the integrated density of states up to energy  $E$  and used the fact that the total number of electrons per spin is just  $N_s = \int_{E_F} n(E) dE$ , and  $N = N_+ + N_-$ . In practice, expression (4.60) can be used for periodic systems. Expression (4.61) is useful for systems with broken periodicity, such as impurities in crystals, where the perturbed charge density converges very slowly with distance from the impurity due to Friedel oscillations. Then,  $N_s(E)$  is calculated not by integration of  $n_s(E)$ , but by using the Friedel sum rule (or its multiple-scattering analogue, Lloyd's formula), which takes into account the Friedel oscillations up to infinity.

The double-counting term includes the electrostatic energy and the exchange-correlation energy. The electrostatic (Hartree) energy depends on the charge densities at each cell  $n$ ,  $\rho_n(\vec{r}) := \rho(\vec{r} + \vec{R}^n)$ , and on the nuclear charges  $Z^n$ . We have:

$$E_H[\rho] = \sum_{nn'} \int_{\Omega^n} d^3r \int_{\Omega^{n'}} d^3r' \frac{\rho^n(\vec{r}) \rho^{n'}(\vec{r}')}{|\vec{r} + \vec{R}^n - \vec{r}' - \vec{R}^{n'}|} - 2 \sum_{nn'} Z^{n'} \int_{\Omega^n} d^3r \frac{\rho^n(\vec{r})}{|\vec{r} + \vec{R}^n - \vec{R}^{n'}|} + \sum_n \sum_{n' \neq n} \frac{Z^n Z^{n'}}{|\vec{R}^n - \vec{R}^{n'}|} \quad (4.62)$$

where  $\Omega^n$  is the volume of the atomic cell  $n$ . It proves convenient to define the Coulomb potential

$$V_C^n(\vec{r}) = 2 \sum_{n'} \int_{\Omega^{n'}} d^3r' \frac{\rho^{n'}(\vec{r}')}{|\vec{r} + \vec{R}^n - \vec{r}' - \vec{R}^{n'}|} - 2 \sum_{n'} \frac{Z^{n'}}{|\vec{R}^n - \vec{R}^{n'}|} \quad (4.63)$$

The Madelung potential  $V_M(\vec{R}^n)$  is the Coulomb potential at position  $R^n$  if we exclude the term  $n' = n$  from the second sum of (4.63):

$$V_M(\vec{R}^n) = 2 \sum_{n'} \int_{\Omega^{n'}} d^3r' \frac{\rho^{n'}(\vec{r}')}{|\vec{R}^n - \vec{r}' - \vec{R}^{n'}|} - 2 \sum_{n'(\neq n)} \frac{Z^{n'}}{|\vec{R}^n - \vec{R}^{n'}|} \quad (4.64)$$

Using the above definitions we re-write the electrostatic energy as

$$E_H[\rho] = \frac{1}{2} \left[ \sum_n \int_{\Omega^n} d^3r \rho^n(\vec{r}) V_C^n(\vec{r}) - \sum_n Z^n V_M(\vec{R}^n) \right] \quad (4.65)$$

The Coulomb potential and the charge density at site  $n$  are expanded in spherical harmonics around  $\vec{R}^n$ :

$$V_C^n(\vec{r}) = \sum_L V_{C,L}^n(r) Y_L(\vec{r}); \quad (4.66)$$

$$\rho^n(\vec{r}) = \sum_L \rho_L^n(r) Y_L(\vec{r}). \quad (4.67)$$

In this way the calculation of the Coulomb potential is reduced to summing up terms containing the moments  $\rho_L^n(r)$  of the charge density over all lattice sites. For the higher  $l$  terms the corresponding summations converge rapidly, but for low  $l$  an Ewald summation is required. The details of this procedure are omitted here. Once the expansion (4.66) of the Coulomb potential is known, the Madelung potential can be calculated using the value of  $V_C^n$  at a sphere of radius  $R$  around  $\vec{R}^n$  and by knowledge of the charge distribution within this sphere. The result can be obtained by solving the corresponding boundary-value problem in electrostatics (the proof is omitted here):

$$V_M(\vec{R}^n) = 2\sqrt{4\pi} \int_0^R \rho_{l=0}^n(r) dr + \frac{2}{R}(Z^n - N^n(R)) + \frac{1}{\sqrt{4\pi}} V_{C,l=0}^n(R), \quad (4.68)$$

where  $N^n(r)$  is the number of electrons within the sphere of radius  $R$ .

After self-consistency the effective Kohn-Sham potential at cell  $n$  can be written in terms of the Coulomb potential and the exchange-correlation energy:

$$V_{\text{eff},s}^n(\vec{r}) = V_C^n(\vec{r}) + \frac{\delta E_{xc}[\rho_+, \rho_-]}{\delta \rho_s(\vec{r})}. \quad (4.69)$$

Otherwise  $V_{\text{eff},s}^n$  has to be considered as a trial potential. For instance during iterations  $V_{\text{eff},s}^n(\vec{r})$  is determined by the input densities, but  $E_H[\rho]$  and  $E_{xc}[\rho]$  are determined by the output densities. Finally, the exchange-correlation energy within the local density approximation is given by

$$E_{xc}^{\text{LDA}}[\rho] = \int \rho(\vec{r}) \epsilon_{xc}(\rho_+(\vec{r}), \rho_-(\vec{r})) d^3r \quad (4.70)$$

where  $\epsilon_{xc}(\rho_+, \rho_-)$  is the exchange-correlation energy density for a homogeneous electron gas of spin density  $\rho_s$ . This is again expanded in spherical harmonics as

$$\epsilon_{xc}(\rho_+^n(\vec{r}), \rho_-^n(\vec{r})) = \sum_L \epsilon_{xc,L}^n(r) Y_L(\vec{r}), \quad (4.71)$$

and the exchange-correlation energy is given by

$$E_{xc}^{\text{LDA}}[\rho] = \sum_n \sum_{LL'L''} C_{LL'L''} \int_0^{R_c^n} \Theta_L^n(r) \rho_{L'}^n(r) \epsilon_{xc,L''}^n(r) r^2 dr. \quad (4.72)$$

## 4.9 Lloyd's Formula

Contrary to the usual band-structure methods where  $E_F$  is adjusted to yield charge neutrality, this cannot be achieved in point-defect calculations since the Fermi energy is fixed by the host. In metals perfect screening can only occur if an infinitely long-ranged perturbation potential is allowed meaning that the Friedel

sum rule cannot be satisfied exactly in the calculations. In addition, however, perfect screening also requires the inclusion of infinitely many angular momenta, *i.e.*  $l_{max} = \infty$ . In the special case of a point defect in an otherwise ideal crystal one needs for an accurate total energy calculation, *i.e.* the calculation of the single particle energy term, the exact change  $\Delta n(E)$  of the density of states due to the defect or the change  $\Delta N(E)$  of the integrated density of states. This change is calculated elegantly by the Lloyd's formula [76, 77] which was adapted later into the case of the KKR method by Drittler *et al.* [78] in the following form<sup>1</sup>:

$$\Delta N(E) = \frac{1}{\pi} \sum_n \ln \det |\Delta \alpha_{LL'}^n(E)| - \frac{1}{\pi} \ln \det |\delta_{LL'}^{nn'} - \overset{\circ}{G}_{LL'}^{nn'}(E) \Delta t_{LL'}^{n'}(E)|, \quad (4.73)$$

The sum is over the cells and the  $\Delta t$  and  $\Delta \alpha$  matrices are changes with respect to the reference system. Note that in this expression all angular momenta in the expansion of the wave function as well as the infinite extension of the scattered waves in real space are implicitly summed up and included. For real calculations we proceed to a cut-off in angular momenta as well as in real space is only made for the potentials and not for the host Green function. The KKR determinant  $\det |1 - \overset{\circ}{G} \Delta t|$  is over combined angular-momentum and cell indices, whereas the determinant  $\det |\Delta \alpha|$  is over angular-momentum indices alone. The size of the KKR-matrix is determined by the matrix  $\Delta \alpha$  which describes the different behavior of the single-scattering solutions of the perturbed system ( $R_{L'}^n$ ) and host system ( $\overset{\circ}{R}_{L'}^n$ ) at the origin

$$R_{L'}^n(\vec{r}, E) = \sum_{L'} \overset{\circ}{R}_{L'}^n(\vec{r}, E) \Delta \alpha_{L'L}^n(E) \quad \text{for } r \rightarrow 0 \quad (4.74)$$

and can be calculated by

$$\Delta \alpha_{L'L}^n(E) = \delta_{L'L} + \int_n d\vec{r} \overset{\circ}{H}_{L'}^n(\vec{r}, E) \Delta V^n(\vec{r}) R_{L'}^n(\vec{r}, E). \quad (4.75)$$

The extension of the Lloyd's formula into the non-collinear case is simple. Since one works in the global spin-frame of reference it is only needed to take all the quantities of eq. (4.73) in the global spin frame of reference. However, we would like to show here that as far as we are concerned with the change of the integrated density of states, we may do the calculation either in the global spin frame of reference or in the local spin frame of reference. We will prove this statement for the first part of eq. (4.73) *i.e.* the  $\Delta \alpha$ -matrix while the same can be used for the KKR determinant  $\det |1 - \overset{\circ}{G} \Delta t|$  for which we use instead the result obtained immediately when solving the Dyson equation (eq. (3.42)) in the global spin frame of reference by inverting the denominator.

1. see also the generalization to finite electronic temperatures done by Zeller [79]

The determinant of the matrix  $\Delta\alpha$  in eq. (4.73) is already obtained in the local spin frame of reference and can be rotated to the global spin frame of reference using rotation matrices

$$\ln \det |\Delta\alpha^{\text{glob}}| = \ln \det |\mathbf{U}\Delta\alpha^{\text{loc}}\mathbf{U}^\dagger|. \quad (4.76)$$

Using the properties of matrix-algebra

$$\ln \det |\Delta\alpha^{\text{glob}}| = \ln \det |\Delta\alpha^{\text{loc}}\mathbf{U}^\dagger\mathbf{U}|, \quad (4.77)$$

and as  $\mathbf{U}^\dagger\mathbf{U}$  is the identity matrix one gets

$$\ln \det |\Delta\alpha^{\text{glob}}| = \ln \det |\Delta\alpha^{\text{loc}}|. \quad (4.78)$$

## 4.10 Frozen Potential Approximation for Magnetic Interactions

An important approximation used in electronic structure calculations was introduced twenty years ago by Oswald *et al.* [80] in Jülich concerning magnetic interactions. They have shown that the magnetic interaction energy, *i.e.* the total energy differences  $E_{FM} - E_{AF}$  between the ferromagnetic and antiferromagnetic configurations of two magnetic layers or impurities, can be calculated in first order from the single-particle energies alone.

Here we present briefly the validity of this approximation. We have seen earlier that in density functional theory, the total energy  $E\{n^+(\vec{r}), n^-(\vec{r})\}$  is a unique functional of the spin densities  $n^+(\vec{r})$  and  $n^-(\vec{r})$  and obeys a variational principle, such that  $E\{n^+(\vec{r}), n^-(\vec{r})\}$  is extremal against small variations  $\delta n^+(\vec{r})$ ,  $\delta n^-(\vec{r})$  around the exact solutions. Furthermore, we have also seen earlier that the total energy  $E = E_{sp} + E_{dc}$  can be split up into single particle contributions  $E_{sp}$  and double counting terms  $E_{dc}$ .

$$E_{sp} = \int^{E_F} dE (E - E_F) (n^+(E) + n^-(E)) \quad (4.79)$$

$$E_{dc} = - \int d\vec{r} (n^+(\vec{r}) v_{eff}^+(\vec{r}) + n^-(\vec{r}) v_{eff}^-(\vec{r})) + W\{n^+(\vec{r}), n^-(\vec{r})\} \quad (4.80)$$

$$W = \int d\vec{r} n(\vec{r}) V_{ext}(\vec{r}) + \int d\vec{r} d\vec{r}' \frac{n(\vec{r})n(\vec{r}')}{|\vec{r} - \vec{r}'|} + E_{xc}\{n^+(\vec{r}), n^-(\vec{r})\} \quad (4.81)$$

Here  $v_{eff}^\pm(\vec{r})$  are the spin dependent Kohn-Sham potentials, which in a variational sense can be replaced by trial potentials.  $W$  is the sum of the Coulomb energies and exchange correlation energies  $E_{xc}$ .  $V_{ext}(\vec{r})$  is the nuclear potential and  $n(\vec{r}) = n^+(\vec{r}) + n^-(\vec{r})$  the charge density.

In the following we use an additional extremal property of the double counting energy  $E_{dc}$ . For fixed trial potentials  $v_{eff}^\pm$  the double counting energy  $E_{dc}\{n^+(\vec{r}), n^-(\vec{r})\}$  is insensitive to variations in  $n^\pm(\vec{r})$ . In first order one obtains

$$\partial E_{dc}|_{v_{eff}^\pm} = \int d\vec{r} \left[ \left( \frac{\partial W}{\partial n^+(\vec{r})} - v_{eff}^+ \right) \partial n^+(\vec{r}) + \left( \frac{\partial W}{\partial n^-(\vec{r})} - v_{eff}^- \right) \partial n^-(\vec{r}) \right] \quad (4.82)$$

Since the exact solution requires  $v_{eff}^\pm = \partial W / \partial n^\pm(\vec{r})$ , the error in eq. (4.82) is in fact of second order. Therefore,  $E_{dc}\{n^+, n^-\}$  can be calculated with some approximate spin densities  $n^\pm(\vec{r})$  which do not need to be identical with those generated from the trial potentials  $v_{eff}^\pm(\vec{r})$ , which strongly enhances the variational freedom.

We picture a system of two magnetic impurities,  $i$  and  $j$ , in a host crystal. We want to calculate the energy difference between the FM and AF configurations. We take advantage of the extremal properties of both  $E$  and  $E_{dc}$ . First, we superimpose the changes  $\Delta v_{eff}^i$  and  $\Delta v_{eff}^j$  due to isolated defects to obtain the trial potential  $v_{eff} = v_{eff}^0 + \Delta v_{eff}^i + \Delta v_{eff}^j$  when  $v_{eff}^0$  refers to the potential of the host crystal. Since for larger distances the interaction is weak, the superposition is a very good first order approximation. Furthermore  $\Delta v_{eff}^{i,j}$  are assumed for simplicity of the discussion to be localized on the impurities although this is not a necessary assumption. Second for the spin densities  $n^\pm(\vec{r})$  in  $E_{dc}$  we assume that the charge density  $n(\vec{r}) = n^+(\vec{r}) + n^-(\vec{r})$  is the same for both configurations FM and AF. For instance, the average density of both configurations may be taken or we may use the superposition of the changes  $\Delta n_i(\vec{r})$  and  $\Delta n_j(\vec{r})$  of the individual impurities, which is identical for both configurations. For this reason, all troublesome Coulomb terms in the double counting energy  $E_{dc}$  are the same for both configurations and cancel each other for the magnetic interaction energy  $E_{FM} - E_{AF}$ . Finally, the genuine magnetic part  $E_{dc}^m$  of the double counting energy depends at least quadratically on the magnetization  $|m(\vec{r})|$ . Also here we assume that  $|m(\vec{r})|$  is the same for both configurations. This is *e.g.*, the case, if the moments are well localized on the impurity and if the interaction effects are small. Then also  $E_{dc}^m$  cancels in the total energy difference  $E_{FM} - E_{AF}$ . Note that small deviations from these approximations for  $n(\vec{r})$  and  $|m(\vec{r})|$  in  $E_{dc}$  affect due to eq. (4.82) the total energy only in second order.

Thus we have shown, that the magnetic interaction energy is in first order determined by the single particle energies only. Note that this proof applies only to the magnetic part of the interaction energies, but not to the “full” interaction, for which Coulomb terms are usually very important.

## 4.11 Formula for Exchange Interactions $\mathbf{J}_{ij}$

The Heisenberg model described by

$$\mathcal{H} = -\frac{1}{2} \sum_{i \neq j} J_{ij} \vec{e}_i \cdot \vec{e}_j \quad (4.83)$$

is very useful for a simple description of non-collinear magnetism. Here  $J_{ij}$  is the exchange integral between the atoms  $i$  and  $j$  and  $\vec{e}_i$  defines the direction of the local moment  $\vec{M}_i$ . The parameters  $J_{ij}$  can be found by fitting total energies obtained by ab-initio DFT calculations for different magnetic configurations (*e.g.* ferromagnetic and antiferromagnetic) to the model described above. However, we may face a problem of not being able to converge a given magnetic configuration creating then problems to determine  $J$  which we overcome by using a method introduced by Lichtenstein *et al.* [24]. This method rests on the force theorem described in the previous section and has the advantage of allowing the exchange integral calculations directly from one magnetic state. Here we give a slightly different proof of the method than the one published [24].

Let us determine the rotation energy of two spin moment at sites  $i$  and  $j$ , which are initially ferromagnetically aligned, by a rotation of both moments opposite to each other by angles of  $\pm\theta/2$ . It is also necessary to subtract interaction energies of the atoms  $i$  and  $j$  with the environment obtained when only one of the two atoms is rotated by  $+\theta/2$  or with  $-\theta/2$  with respect to all other atoms:

$$\Delta E_{ij} = E_{ij}(\theta) - E_i(\theta/2) - E_j(\theta/2) = J_{ij}(1 - \cos(\theta)), \quad (4.84)$$

which for small rotation angle  $\theta$  is equivalent to

$$\Delta E_{ij} = \frac{1}{2} J_{ij} \theta^2. \quad (4.85)$$

We know that the total energy  $E_{tot}$  is related to the density of states (DOS)  $n(E)$  by

$$E_{tot} = \int^{E_F} dE (E - E_F) n(E) = - \int^{E_F} dE N(E) \quad \text{with} \quad N(E) = \int^E dE' n(E'). \quad (4.86)$$

Here  $E_{tot}$  refers to the energy of the grand canonical system, for which the Fermi energy  $E_F$  as the chemical potential  $E_F$  is the basic variable. The second equality follows by partial integration.  $N(E)$  is the integrated density of states (IDOS), counting number of states with energy  $E'$  below  $E$ .

Therefore corresponding to eq. (4.84), the changes of IDOS are given by

$$\Delta N_{ij}(E) = \Delta N_{i+j}(E) - \Delta N_i(E) - \Delta N_j(E), \quad (4.87)$$

with  $\Delta N_{i+j}(E)$  is the change of the IDOS when both atoms  $i$  and  $j$  have their moments rotated by  $\pm\theta/2$ .  $\Delta N_i(E)$  and  $\Delta N_j(E)$  are changes of the IDOS when

only one moment is rotated *i.e.* either the moment of atom  $i$  with  $\theta/2$  or atom  $j$  with  $-\theta/2$ .  $\Delta N_{ij}(E)$  is the change of the IDOS corresponding to the interaction energy between the moments  $i$  and  $j$ .

The host Hamiltonian  $\mathcal{H}_0$  describing the ferromagnetic solution is perturbed by a potential difference  $\Delta V$  when one moment is rotated. The new Hamiltonian  $\mathcal{H}$  is then simply given by the sum  $\mathcal{H}_0 + \Delta V$ . In other words the green functions of the perturbed and of the host system, respectively  $\mathbf{G} = 1/(E - \mathcal{H})$  and  $\overset{\circ}{\mathbf{G}} = 1/(E - \mathcal{H}_0)$  are related by a Dyson equation:

$$\mathbf{G}(E) = \frac{1}{1 - \overset{\circ}{\mathbf{G}}\mathbf{V}}\overset{\circ}{\mathbf{G}} \quad \text{or} \quad \mathbf{G}(E) = \overset{\circ}{\mathbf{G}} + \overset{\circ}{\mathbf{G}}\mathbf{V}\frac{1}{1 - \overset{\circ}{\mathbf{G}}\mathbf{V}}\overset{\circ}{\mathbf{G}} \quad (4.88)$$

The change of the DOS  $\Delta n(E)$  due to the change of the potential  $\Delta V$  is related to the imaginary part of the Green function

$$\Delta n(E) = -\frac{1}{\pi} \text{Im} \text{Tr}_{\text{nLs}} \overset{\circ}{\mathbf{G}}\mathbf{V}\frac{1}{1 - \overset{\circ}{\mathbf{G}}\mathbf{V}}\overset{\circ}{\mathbf{G}} \quad (4.89)$$

$\text{Tr}_{\text{nLs}}$  means the trace operation in spin space, as well as with respect to angular momentum and cell indices. Since for the trace the identity  $\text{Tr}AB = \text{Tr}BA$  is valid, we can combine the right  $\overset{\circ}{\mathbf{G}}$  in the previous equation with the left one. Then by using the equation

$$\frac{d\overset{\circ}{\mathbf{G}}(E)}{dE} = \frac{d}{dE} \frac{1}{E - \mathcal{H}_0} = -\frac{1}{E - \mathcal{H}_0} \frac{1}{E - \mathcal{H}_0} = -\overset{\circ}{\mathbf{G}}(E)\overset{\circ}{\mathbf{G}}(E) \quad (4.90)$$

we obtain for  $\Delta n(E)$ :

$$\Delta n(E) = \frac{1}{\pi} \text{Im} \text{Tr}_{\text{nLs}} \frac{d\overset{\circ}{\mathbf{G}}(E)}{dE} \mathbf{V} \frac{1}{1 - \overset{\circ}{\mathbf{G}}\mathbf{V}} = \frac{1}{\pi} \frac{d}{dE} \text{Im} \text{Tr}_{\text{nLs}} \ln(\mathbf{1} - \overset{\circ}{\mathbf{G}}(E)\Delta\mathbf{V}), \quad (4.91)$$

from which we get the change of the IDOS after integrating over the energy

$$\Delta N(E) = -\frac{1}{\pi} \text{Im} \text{Tr}_{\text{nLs}} \ln(\mathbf{1} - \overset{\circ}{\mathbf{G}}(E)\Delta\mathbf{V}). \quad (4.92)$$

In the case of two potentials  $\mathbf{V} = \Delta\mathbf{V}_i + \Delta\mathbf{V}_j$  the interactive part of the integrated density of states according to eq. (4.87) is given by

$$\Delta N_{ij}(E) = -\frac{1}{\pi} \text{Im} \text{Tr}_{\text{nLs}} \ln\left(\frac{\mathbf{1} - \overset{\circ}{\mathbf{G}}(E)(\Delta\mathbf{V}_i + \Delta\mathbf{V}_j)}{(\mathbf{1} - \overset{\circ}{\mathbf{G}}(E)\Delta\mathbf{V}_i)(\mathbf{1} - \overset{\circ}{\mathbf{G}}(E)\Delta\mathbf{V}_j)}\right) \quad (4.93)$$

Here the arguments of the logarithm can be simplified by using the identity

$$\begin{aligned}
\mathbf{1} - \overset{\circ}{\mathbf{G}}(E)(\Delta\mathbf{V}_i + \Delta\mathbf{V}_j) &= (\mathbf{1} - \overset{\circ}{\mathbf{G}}(E)\Delta\mathbf{V}_i) \times \\
&\times \left[ \mathbf{1} - \frac{\mathbf{1}}{\mathbf{1} - \overset{\circ}{\mathbf{G}}(E)\Delta\mathbf{V}_i} \overset{\circ}{\mathbf{G}}(E)\Delta\mathbf{V}_i \overset{\circ}{\mathbf{G}}(E)\Delta\mathbf{V}_j \frac{\mathbf{1}}{\mathbf{1} - \overset{\circ}{\mathbf{G}}(E)\Delta\mathbf{V}_j} \right] \times \\
&\times (\mathbf{1} - \overset{\circ}{\mathbf{G}}(E)\Delta\mathbf{V}_j) \\
&= (\mathbf{1} - \overset{\circ}{\mathbf{G}}(E)\Delta\mathbf{V}_i) \times \\
&\times \left[ \mathbf{1} - \overset{\circ}{\mathbf{G}}(E)\Delta\mathbf{t}_i(E) \overset{\circ}{\mathbf{G}}(E)\Delta\mathbf{t}_j(E) \right] \times \\
&\times (\mathbf{1} - \overset{\circ}{\mathbf{G}}(E)\Delta\mathbf{V}_j)
\end{aligned} \tag{4.94}$$

where the t-matrices  $\Delta\mathbf{t}_i$  and  $\Delta\mathbf{t}_j$  describe all scattering processes at the isolated atoms  $i$  and  $j$ , *e.g.*

$$\Delta\mathbf{t}_i = \Delta\mathbf{V}_i \frac{\mathbf{1}}{\mathbf{1} - \overset{\circ}{\mathbf{G}}\Delta\mathbf{V}_i}. \tag{4.95}$$

The formulation giving the IDOS is now very much simplified:

$$\Delta N_{ij}(E) = -\frac{1}{\pi} \text{Im} \text{Tr}_{\text{nLs}} \ln \left( \mathbf{1} - \overset{\circ}{\mathbf{G}}(E)\Delta\mathbf{t}_i(E) \overset{\circ}{\mathbf{G}}(E)\Delta\mathbf{t}_j(E) \right), \tag{4.96}$$

For small rotation angles we can apply a first order perturbation theory on eq. (4.96)

$$\Delta N_{ij}(E) = \frac{1}{\pi} \text{Im} \text{Tr} \overset{\circ}{\mathbf{G}}(E)\Delta\mathbf{t}_i(E) \overset{\circ}{\mathbf{G}}(E)\Delta\mathbf{t}_j(E) \tag{4.97}$$

The previous equation is expressed in the global spin frame of reference meaning that the t-matrices have non-diagonal elements which is not the case of the magnetically collinear host Green function  $\overset{\circ}{\mathbf{G}}$ . It would be interesting to express eq. (4.97) in terms of t-matrices in local spin frame of reference related to each Wigner-Seitz cell. We have already seen previously (eq. (4.38)) that

$$\mathbf{t}_n^{\text{glob}}(E) = \frac{1}{2} [t_{\text{sum}}^{\text{loc}}(E)\mathbf{1} + t_{\text{diff}}^{\text{loc}}(E)\mathbf{U}_n\boldsymbol{\sigma}_z\mathbf{U}_n^\dagger], \tag{4.98}$$

with  $\mathbf{U}$  being a rotation matrix,  $t_{\text{sum}}^{\text{loc}}$  and  $t_{\text{diff}}^{\text{loc}}$  are equal to respectively  $t_{\uparrow\uparrow}^{\text{loc}} + t_{\downarrow\downarrow}^{\text{loc}}$  and  $t_{\uparrow\uparrow}^{\text{loc}} - t_{\downarrow\downarrow}^{\text{loc}}$ . Let us consider that the magnetic moment value does not change with the rotation<sup>2</sup> meaning that the values of the t-matrices are constant in

2. This is the case for a well localized magnetic moment in the Wigner-Seitz cell

the local spin frame of reference. We obtain then for the difference between the t-matrices of the perturbed and host system to linear terms in  $\theta$

$$\Delta \mathbf{t}_n^{\text{glob}}(E) = -\Delta t_{diff}(E) \begin{bmatrix} 0 & \frac{\theta}{2} e^{-i\frac{\phi}{2}} \\ \frac{\theta}{2} e^{i\frac{\phi}{2}} & 0 \end{bmatrix}, \quad (4.99)$$

which we insert in eq. (4.97) giving the following expression<sup>3</sup>

$$\Delta N_{ij} = -\frac{1}{16\pi} \text{Im Tr}_{\text{nLs}} \left[ \begin{array}{cc} \overset{\circ}{\mathbf{G}}_{\uparrow\uparrow} \Delta t_{diff}^i \overset{\circ}{\mathbf{G}}_{\downarrow\downarrow} \Delta t_{diff}^j \theta^2 & 0 \\ 0 & \overset{\circ}{\mathbf{G}}_{\downarrow\downarrow} \Delta t_{diff}^i \overset{\circ}{\mathbf{G}}_{\uparrow\uparrow} \Delta t_{diff}^j \theta^2 \end{array} \right] \quad (4.100)$$

The trace in spin space and site indices gives

$$\Delta N_{ij}(E) = -\frac{1}{8\pi} \text{Im Tr}_L \overset{\circ}{\mathbf{G}}_{\uparrow\uparrow}^{ij}(E) \Delta t_{diff}^j(E) \overset{\circ}{\mathbf{G}}_{\downarrow\downarrow}^{ji}(E) \Delta t_{diff}^i(E) \theta^2 \quad (4.101)$$

Finally the rotation energy (see eq. (4.84)) of two spin moments at sites  $i$  and  $j$  is given by

$$\Delta E_{ij} = -\int^{E_F} dE (E - E_F) n_{ij}(E) = -\int^{E_F} dE \Delta N_{ij}(E) \quad (4.102)$$

$$= \frac{1}{8\pi} \text{Im Tr}_L \int^{E_F} dE \overset{\circ}{\mathbf{G}}_{\uparrow\uparrow}^{ij}(E) \Delta t_{diff}^j(E) \overset{\circ}{\mathbf{G}}_{\downarrow\downarrow}^{ji}(E) \Delta t_{diff}^i(E) \theta^2 \quad (4.103)$$

$$\approx \frac{1}{2} J_{ij} \theta^2 \quad (4.104)$$

We conclude thus our proof by giving the expression we use and we implemented in our code in order to calculate the exchange interactions  $J_{ij}$  between two spin moments:

$$J_{ij} = \frac{1}{4\pi} \text{Im Tr}_L \int^{E_F} dE \overset{\circ}{\mathbf{G}}_{\uparrow\uparrow}^{ij}(E) \Delta t_{diff}^j(E) \overset{\circ}{\mathbf{G}}_{\downarrow\downarrow}^{ji}(E) \Delta t_{diff}^i(E) \quad (4.105)$$

## 4.12 Test of the Implementation

As no *ab-initio* calculations on complex magnetism of clusters on surfaces or in bulk are provided in the literature, we tried few simple tests, where the good sens leads to expected results. One simple case is to take for example two Cr atoms in Cu bulk and consider the two possible collinear magnetic configurations ferromagnetic ( $\theta = 0^\circ$ ) and antiferromagnetic ( $\theta = 180^\circ$ ). The latter one is in fact the ground state. What we did, for example, is to start a simulation from an intermediate non-collinear configuration *e.g.*  $\theta = 90^\circ$  and let the system relax. The

<sup>3</sup> We drop out the argument E for reason of clarity

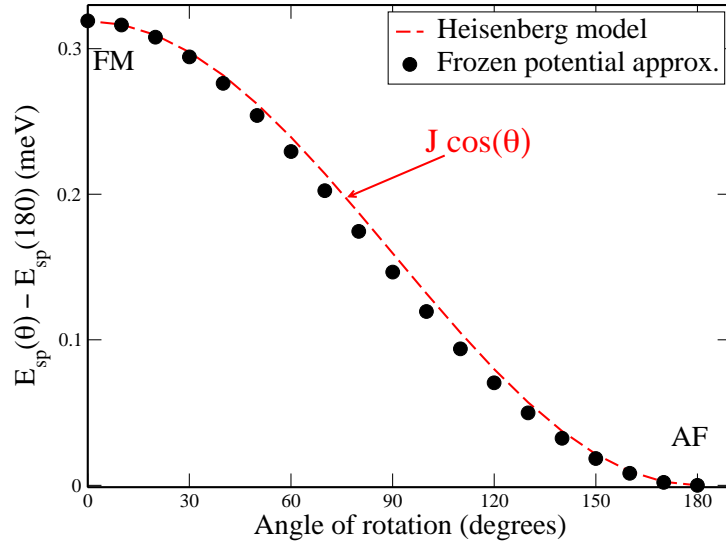


FIG. 4.6 – Variation of the single particle energies versus the rotation angle between the magnetic moments of a Cr-dimer in Cu-bulk. The energies are obtained with the frozen potential approximation and corrected with the Lloyd's Formula. The curve is a cosine-like function in accordance with the expected result from the Heisenberg model, with  $J$  fit to the F-AF total energy difference.

resulting final configuration is the expected one which is the antiferromagnetic ground state.

Another test possibility is to check the angle dependence of the energy which should be a cosine function following the Heisenberg model. To do so, we apply the frozen potential approximation described earlier: we do a one iteration calculation starting from a converged potential *e.g.* the antiferromagnetic one which we rotate by successive angles from  $0^\circ$  up to  $180^\circ$  with  $10^\circ$  steps. The resulting curve is drawn in Fig. 4.6 and has a cosine-like behavior.

Another test consisted on taking the simplest non-collinear example described by the Heisenberg model namely the case of a trimer of atoms characterized by equal antiferromagnetic exchange integrals between first neighboring atoms. The Heisenberg model predicts that for such case the magnetic ground state is a configuration with an angle of  $120^\circ$  between first neighboring atoms (see Fig. 4.1).

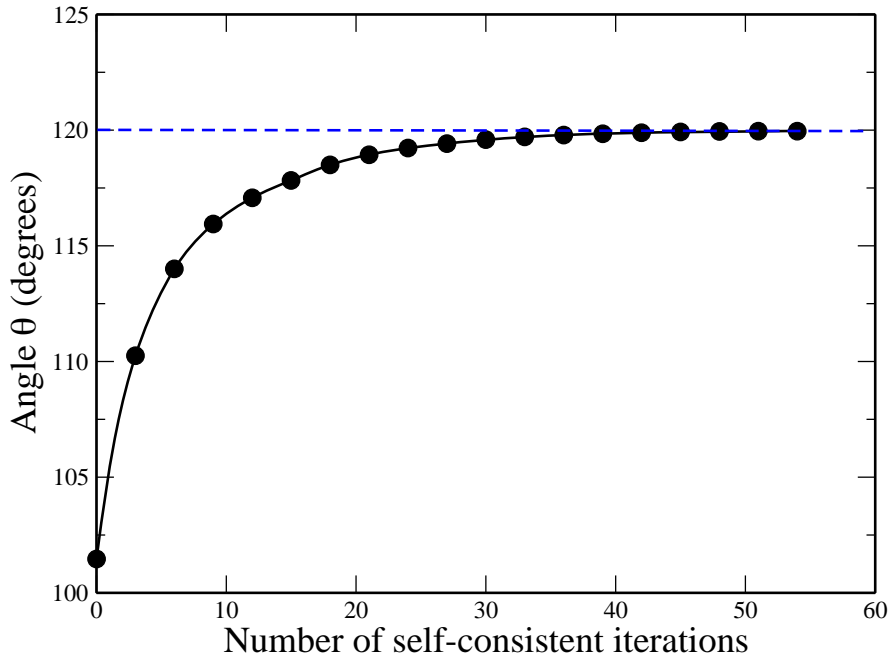


FIG. 4.7 – Variation of the moment magnetic angle of one Cr-atom versus the number of self-consistent iterations. We shifted the moment angle by angle of  $20^\circ$  from its initial ground state ( $120^\circ$ ) and let it rotate back.

We did this test for a Cr trimer in Cu-bulk. When constraining the magnetism to be collinear we found a solution with no magnetic moments. A striking effect appears when we allow the moments to rotate: a non-collinear magnetic configuration was obtained as expected from the Heisenberg model. This example shows how the magnetic frustration can kill magnetic moments when constraining the calculations within collinear magnetic configurations. Furthermore we rotated one magnetic moment from the ground state angle  $120^\circ$  to  $100^\circ$  and start a new self-consistent calculation. Fig. 4.7 shows the variation of the magnetic moment angle versus the self-consistent iteration. The converged solution is of-course the  $120^\circ$  configuration.



---

# Chapter 5

## Complex Magnetism of $3d$ Clusters on Ni(001)

### 5.1 Introduction

As a first application of our method, we study the magnetic state of  $3d$ -atom clusters in and on the Ni(001) surface. As a first step, we reexamine the adatom properties, which are already known from previous work. In the second step, we perform calculations for  $3d$  dimers and trimers and use the understanding gained from the single adatoms in order to explain the results.

### 5.2 Computational Details

Our calculations henceforth are based on the LSDA of density functional theory with the parametrization of Vosko *et al.* [35]. The full nonspherical potentials and charge densities are calculated, taking into account the correct description of the Wigner-Seitz atomic cells. [81] Angular momenta up to  $l_{\max} = 3$  were included in the expansion of the Green functions and up to  $2l_{\max} = 6$  in the charge density expansion. Relativistic effects were described in the scalar relativistic approximation.

First, the surface Green functions are determined by the screened KKR method for the (001) surface of Ni which serves as the reference system. The LSDA equilibrium lattice parameter of Ni was used (6.46 a.u.  $\approx 3.42 \text{ \AA}$ ). To describe the impurities on the surface (later we refer to these as *adatoms* and to the impurities sitting in the first surface layer as *inatoms*), we consider a cluster of perturbed potentials which includes the potentials of the impurities and the perturbed potentials of several neighboring shells, with typical size ranging from 19 perturbed sites for the single impurity to 32 for the dimers and trimers; in all cases, at least the first neighboring sites around the impurity atoms were taken into account in the calculation to ensure the correct screening of the impurity potentials. Test

calculations have shown that this is a very good approximation. We consider the adatoms at the unrelaxed hollow position in the first vacuum layer, and the inatoms at the unrelaxed position in the first surface layer.

The orientations assigned to the spin moments of the impurities are always relative to the orientation of the substrate moment, which we take as the global frame. This, in turn, depends on delicate physical quantities such as the magnetic anisotropy energy, which cannot be easily related to the local properties of the small clusters that we study. In the present approach such effects arising from spin-orbit interaction are not included. The direction of the host moments must therefore be considered as an input parameter from experiments or from independent *ab-initio* calculations.

### 5.3 Magnetic Properties of Ni(001) Surface

We simulate the Ni(001) surface using a slab of finite thickness, consisting of 10 layers of ferromagnetic Ni. We give in Tab. 5.3 a comparison with previously published *ab-initio* results on the same surface. Ernst *et al.* [82] have investigated the case of six Ni monolayers on Cu(001) using the KKR Green function method. Even though in those calculations the Cu lattice parameter was considered which is much larger than the Ni one, the surface layer (S) magnetic moments are identical to our results. This is explained by the high values of the Ni magnetic moment at the surface compared to the moment in bulk. Going in the slab, we notice a discrepancy of the magnetic moment value for the (S-1) layer which is due to the difference between lattice parameters considered in both calculations. The comparison with the results of Hjortstam *et al.* [83] is better as they considered a Ni(001) surface with Ni lattice parameter. Their calculated magnetic moments based on the full potential linear muffin tin orbital method are in agreement with our results.

Layer	Ernst <i>et al.</i> [82]	Hjortstam <i>et al.</i> [83]	Present work
S	0.71	0.73	0.70
S-1	0.67	0.61	0.61
S-2	0.67	0.61	0.60
S-3	0.66	/	0.58
C	/	0.58	0.59

**TAB. 5.1** —. Calculated spin moments (in  $\mu_B$ ) for the Ni(001) surface layers and comparison with theoretical results of Ernst *et al.* [82] and Hjortstam *et al.* [83].

## 5.4 3d Single Adatoms

3d adatoms on Fe(001) and on Ni(001) have been already studied previously, using the KKR method [84, 42, 85, 86] in the atomic sphere approximation. Here we repeat the calculations of 3d adatoms on Ni(001) using the full potential method (detailed results for Fe and Co on Ni(001) are presented in a recent article [87]). We give a brief analysis of the results, which are basically unchanged, in order to use them as the basis for understanding the behavior of dimers and trimers later on.

A collinear calculation of the magnetic state of a single adatom on a ferromagnetic substrate can give in some cases two solutions: one with ferromagnetic coupling (FM) to the substrate moments and one with antiferromagnetic coupling (AF). One of these states will correspond to the real ground state, and the other to a local minimum; this is actually a local minimum with respect to collinear variations of the magnetic moment, since the angle  $\theta$  between the local moment and the substrate moment cannot be varied in a collinear calculation. From total energy calculations of the two states, the ground state can be then determined. In some cases, when the intra-atomic exchange field is not strong (beginning or end of the 3d series), only one of the two minima exists. On the other hand, if non-collinear effects are included in the calculations, the higher one of the two minima usually becomes unstable against an angular rotation of the moment into the lower energy minimum, *i.e.*, it is then actually a saddle point.

The full diamonds in the Fig. 5.1(a) show the energy difference between the AF and the FM solution for 3d adatoms on Ni(001). The first elements of the 3d series (Sc, Ti, V, Cr) are AF coupled to the substrate whereas the coupling of Mn, Fe, Co and Ni is FM. Sc (AF), Ti (AF), and Ni (FM) are characterized by a single solution. Clearly, the AF-FM transition occurs when the adatom atomic number changes from Cr ( $Z = 24$ ) to Mn ( $Z = 25$ ). This transition can be interpreted as in the case of the interatomic interaction of magnetic dimers [88, 80], in terms of the energy gain due to the formation of hybrid states with the Ni substrate as the 3d virtual bound state comes lower in energy with increasing  $Z$ . An explanation (see Fig. 5.2) can be given in terms of the  $d$ - $d$  hybridization between the adatom 3d states and the Ni substrate 3d states. Energy is gained when a half-occupied  $d$  virtual bound state (VBS) at  $E_F$  is broadened by hybridization with the Ni minority 3d states, which lie at  $E_F$  (the Ni majority  $d$  states are fully occupied and positioned below  $E_F$ ). For the early 3d adatoms (Fig. 5.2a), it is the majority  $d$  VBS which is at  $E_F$ , thus the majority-spin direction of the adatom is favourably aligned with the minority-spin direction of Ni, and an AF coupling arises. For the late 3d adatoms (Fig. 5.2b), on the contrary, the minority  $d$  VBS is at  $E_F$ , and this aligns with the Ni minority  $d$  states; then a FM coupling arises. For our purposes we keep in mind that, since Cr and Mn are in the intermediate region, *i.e.*, near the AF-FM transition point, their magnetic coupling to the Ni substrate is weak; this has consequences to be seen in the behavior of dimers, trimers, etc.,

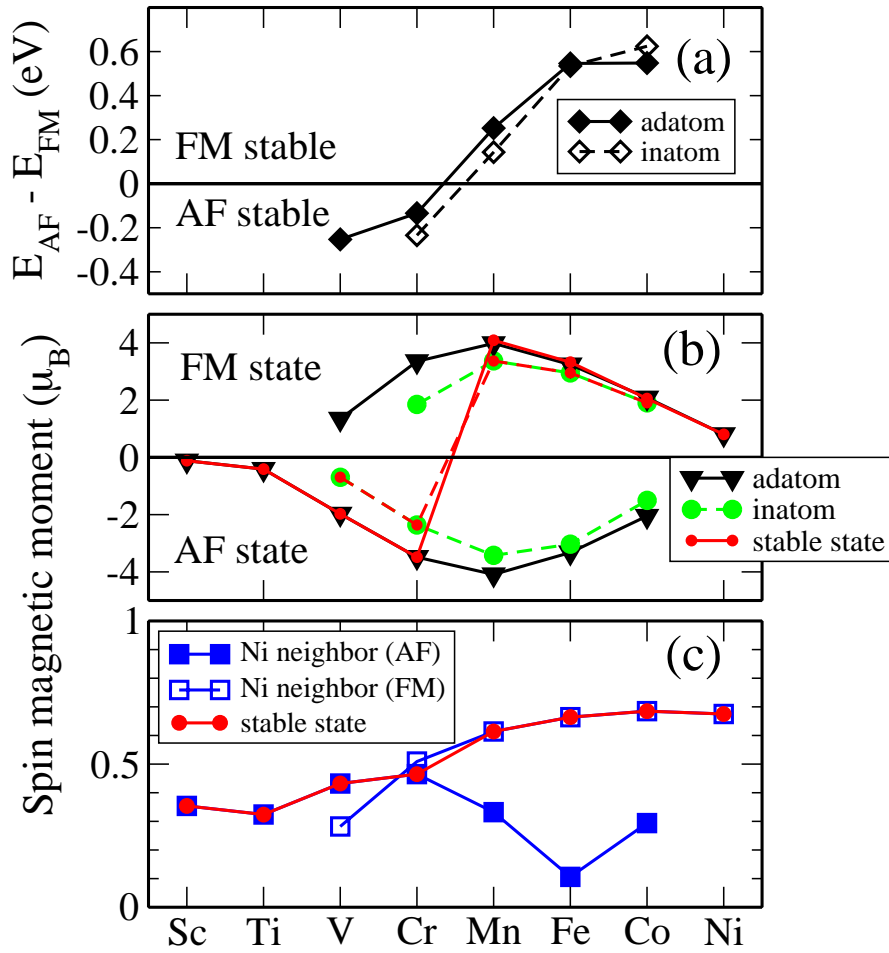


**FIG. 5.1** — 3d adatoms and inatoms on Ni(001): (a) Energy difference between the AF and FM coupling, the values related to adatom and inatom are described by respectively full and empty black diamonds; (b) magnetic moments of the adatoms (black triangles) and inatoms (green circles) within the 2 possible magnetic configurations FM and AF; (c) the variation of the magnetic moments of Ni first Nearest Neighbors of the adatoms.

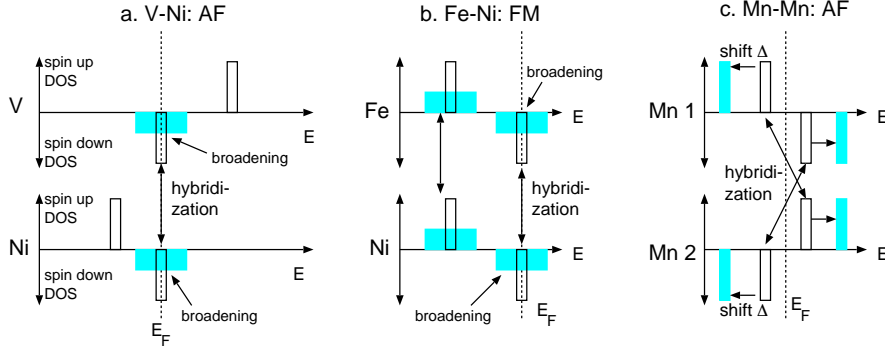


FIG. 5.2 – Alexander-Anderson model for neighboring magnetic atoms: (a) Early 3d transition elements in interaction with Ni surface atoms; (b) Late 3d transition elements in interaction with Ni surface atoms; (c) Cr or Mn dimer.

in the next subsections.

The magnetic moments of the adatoms and Ni first neighbors in the surface layer are shown in Fig. 5.1(b) and (c). Evidently the moment of the Ni first neighbors is strongly affected by the adatoms. Especially in the AF state for Mn, Fe, and Co adatoms, the Ni moment is strongly reduced and the FM configuration is stable. As regards the adatom moments, due to its half filled d band the Mn adatom carries the highest magnetic moment ( $4.09 \mu_B$ ) followed by Cr ( $3.48 \mu_B$ ) and Fe ( $3.24 \mu_B$ ).

## 5.5 3d Single Inatoms

To understand the effect of coordination and stronger hybridization on the magnetic behavior of the adatoms, we take the case of impurities sitting in the first surface layer (inatoms). We carried out the calculations for V, Cr, Mn, Fe and Co impurities. The corresponding spin moments are shown in Fig. 5.1b (green circles), and the FM-AF energy differences are shown in Fig. 5.1a (open diamonds and dashed line).

Compared to the adatom case, the spin moments are reduced, especially for V and Cr. This effect is expected due to the increase of the coordination number from 4 to 8 and the subsequent stronger hybridization of the 3d levels with the host wavefunctions. Moreover, the energy difference  $\Delta E$  between the AF and FM solutions is affected. The trend can be understood as follows. In the case of Cr, the reduction of the local magnetic moment  $M$  is accompanied by a reduction of the exchange splitting  $\Delta E_X$  as  $\Delta E_X \approx I \cdot M$ , where  $I \approx 1\text{eV}$  is the intra-atomic

exchange integral. This means for the inatom that the occupied 3d states are closer to  $E_F$  than for the adatom. In turn, this intensifies the hybridization of these states with the Ni 3d states (which are close to  $E_F$ ). At the same time, also the higher coordination number intensifies the  $d$ - $d$  hybridization. The hybridization-induced level shift in the AF configuration increases, and the energy of the AF state is thus lowered. The same mechanism is responsible for the weakening of the FM coupling of Mn inatom compared to the adatom. Similarly, the stronger hybridization of the Co-inatom  $d$ -states stabilizes even more its FM configuration due to the energy gain from the broadening of the  $d$  virtual bound state.

## 5.6 Adatom Dimers

Having established the single adatom behavior, we turn to adatom dimers. We considered three geometries of increasing distance: dimers as first, second, and fourth neighbors in the first vacuum layer. We will discuss the magnetic interaction between the dimer atoms and the resulting magnetic order, first looking only at collinear states and then allowing for non-collinear order. We will see how, in certain cases, the collinear state reduces the symmetry, while the non-collinear state restores the full symmetry of the system. Non-collinear order is finally established for certain first-neighbor dimers.

Fig. 5.3 represents schematically the different considered geometrical configurations of impurity dimers residing on the surface. We have investigated the dimer-1-type of geometry (the adatoms are first neighboring atoms), dimer-2-type (the adatoms are second neighbors) and dimer-3-type (the adatoms are fourth neighbors). This allows us to monitor the strength of the magnetic coupling as a function of the distance. Three collinear magnetic configurations were treated: (i) antiferromagnetic coupling within the dimer leading to a ferrimagnetic solution (Ferri), (ii) ferromagnetic coupling within the dimer with both atoms ferromagnetically coupled to the substrate (FM), or (iii) ferromagnetic coupling within the dimer with both atoms antiferromagnetically coupled to the substrate (AF).

Our calculations include V, Cr, Mn and Fe dimers. We found that all V and Fe dimer types behave like the adatoms: in all geometries, both V atoms are AF and both Fe atoms are FM to each other. On the other hand, Cr and Mn dimers show magnetic frustration. As shown in Fig. 5.3, both the Cr-dimer-1 and Mn-dimer-1 show (in a collinear calculation) a Ferri ground state (see Tab. 5.2). With increasing distance between the adatoms, a transition occurs to the single adatom magnetic behavior which is AF for Cr-dimers and FM for Mn-dimers. It is clear that, in the dimer-1 case, there is a competition of exchange interactions.

When we allow for a rotation of the magnetic moments, non-collinear solutions are obtained for the Cr- and Mn-dimer-1 systems. On the other hand the magnetic coupling of the V- and Fe-dimer-1 remains collinear. Let us start with

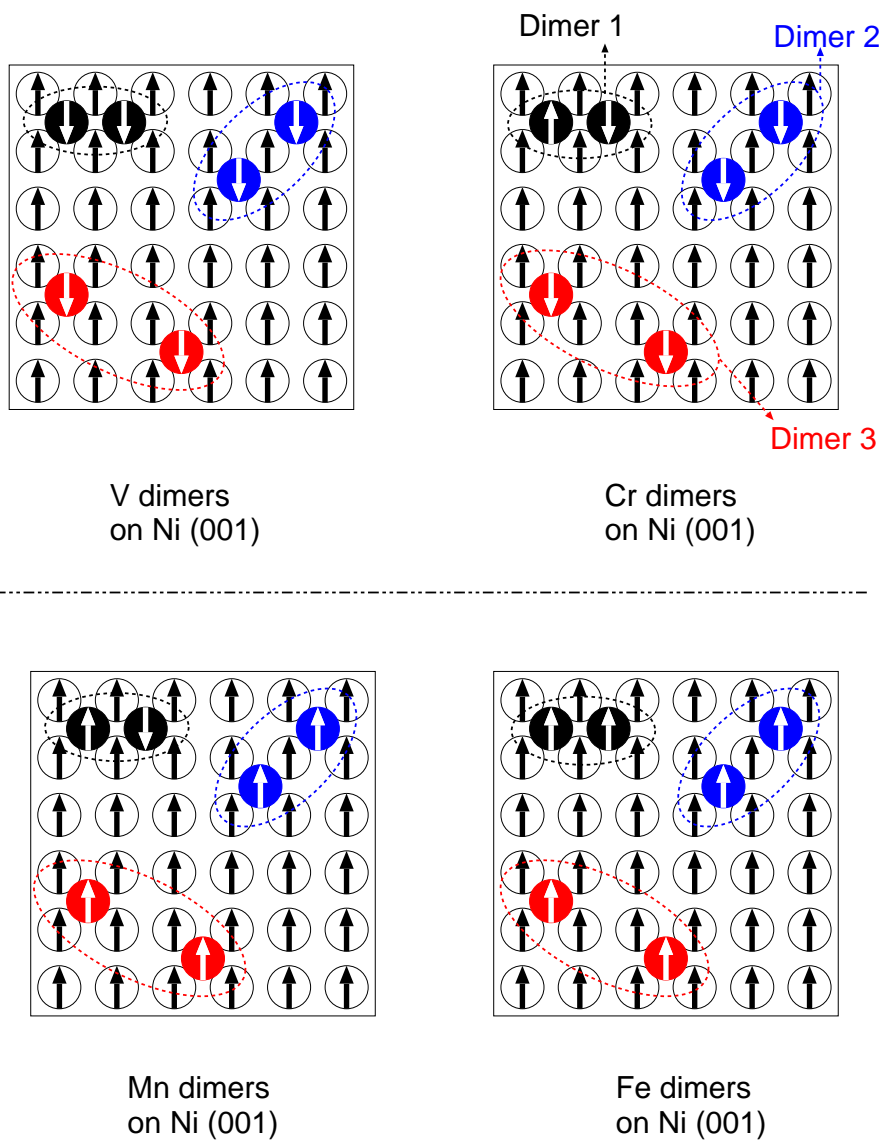


**FIG. 5.3** –. Different geometrical configurations considered for dimers at the surface of Ni(001). Dimer-1-type corresponds to the case where the atoms are first neighboring atoms, dimer-2-type where the atoms are 2'NN and finally dimer-3-type to 4'NN. The collinear magnetic ground state are also shown for V, Cr, Mn and Fe dimers.

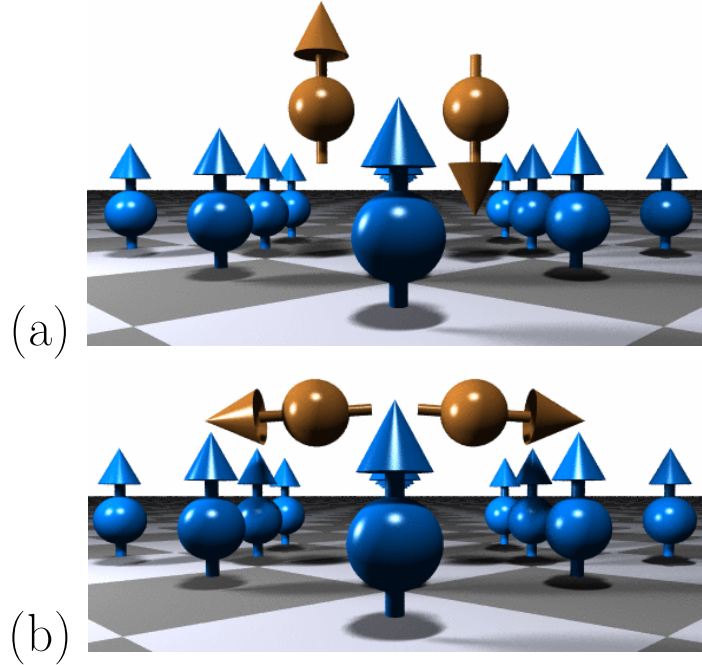


**FIG. 5.4** –. Most stable configurations of Cr dimer-1-type obtained with (a) the collinear KKR method and (b) the non-collinear KKR method. The rotation angle with respect to the  $z$  axis is equal to  $94.2^\circ$ . The collinear state is the ground state, with the non-collinear state being a local minimum (see text).

Cr-dimer-1: Fig. 5.4(a) represents the collinear magnetic ground state. As one expects from the adatom picture, both adatoms forming the dimer tend to couple AF to the substrate but due to their half filled  $d$  band they also tend to couple AF to each other. This can be understood in terms of the Alexander–Anderson model. [88, 80] To give a short explanation (see Fig. 5.2c), both Cr and Mn have their majority-spin VBS occupied, below  $E_F$ , and the minority-spin VBS unoccupied, above  $E_F$ . An antiparallel configuration between the moments in a Mn or Cr dimer lowers the energy, because the occupied  $d$  VBS of each atom hybridizes with the unoccupied  $d$  VBS of the other atom and is shifted to lower eigenvalues. Contrary to this, a parallel coupling does not lower the energy, since there is no level shifting, but only level broadening of the majority  $d$ -VBS. Since these are fully occupied, the broadening brings no energy gain.

Thus there is a competition between the interatomic coupling within the dimer, which drives it to a Ferri state, and the exchange interaction with the

	Cr			Mn		
	Dimer 1	Dimer 2	Dimer 3	Dimer 1	Dimer 2	Dimer 3
$E_{\text{FM}} - E_{\text{Ferri}}(\text{eV})$	0.451	0.130	0.120	0.065	-0.242	-0.239
$E_{\text{AF}} - E_{\text{Ferri}}(\text{eV})$	0.433	-0.093	-0.112	0.496	0.187	0.233

TAB. 5.2 – Energy differences between the Ferri solution and the FM (AF) configuration for the three types of dimers investigated.

substrate, which drives the moments of both atoms in the same direction: AF for Cr and FM for Mn. As discussed in the previous subsection, the magnetic exchange interaction (MEI) to the substrate is relatively weak for Cr and Mn. Thus, the *intra-dimer* MEI is stronger than the MEI with the substrate, and in the collinear approximation the ground state is found as ferrimagnetic (Ferri). Removing the collinear constraint, a compromise can be found such that both atoms are AF coupled to each other and at the same time (for Cr) slightly AF coupled to the substrate. This is shown in Fig. 5.4(b): the Cr adatom moments are aligned antiparallel to each other and basically perpendicular to the substrate moments. However, the weak AF interaction with the substrate causes a slight tilting towards the substrate, leading to an angle of  $94.2^\circ$  instead of  $90^\circ$ . We also observe a very small tilting ( $\approx 0.3^\circ$ ) of the magnetic moments of the four outer Ni atoms neighboring the Cr dimer (the two inner Ni atoms do not tilt for symmetry reasons).

Despite the above considerations, the collinear Ferri state (Fig. 5.4(a)) is also a self-consistent solution of the Kohn-Sham equations, even if the collinear constraint is removed. Total energy calculations are needed in order to determine if the non-collinear state is the true ground state, or if it represents a local minimum of energy with the collinear result representing the true ground state. After performing such calculations we find that the ground state is collinear with an energy difference of  $\Delta E_{\text{Ncol-Ferri}} = 19.9$  meV/adatom (increasing the angular-momentum cutoff to  $l_{\text{max}} = 4$  brought no significant change to this result).

The case is different for Mn dimers. Fig. 5.5 shows the collinear and the non-collinear solutions. The dimer atoms couple strongly antiferromagnetically to each other but the single Mn adatoms tend to couple (weakly) ferromagnetically to the substrate. Both adatom moments, while aligned AF with respect to each other, are tilted in the direction of the substrate magnetization, as opposed to the Cr-dimer. With a rotation angle of  $\approx 72.6^\circ$ , the tilting from the  $90^\circ$  configuration is rather large. Also the Ni moments are tilted by  $7.4^\circ$ . The main difference with the case of Cr-dimer-1 is that for Mn-dimer-1 the non-collinear solution is the ground state (total energy calculations yield  $\Delta E_{\text{Ncol-Ferri}} = -6.7$  meV/adatom). The spin moments of the V, Cr, Mn, and Fe dimers are given in Tab. 5.4.

In both cases (Cr and Mn dimers) the frustrated collinear solution is asymmetric, while the non-collinear ground state restores the twofold symmetry of the

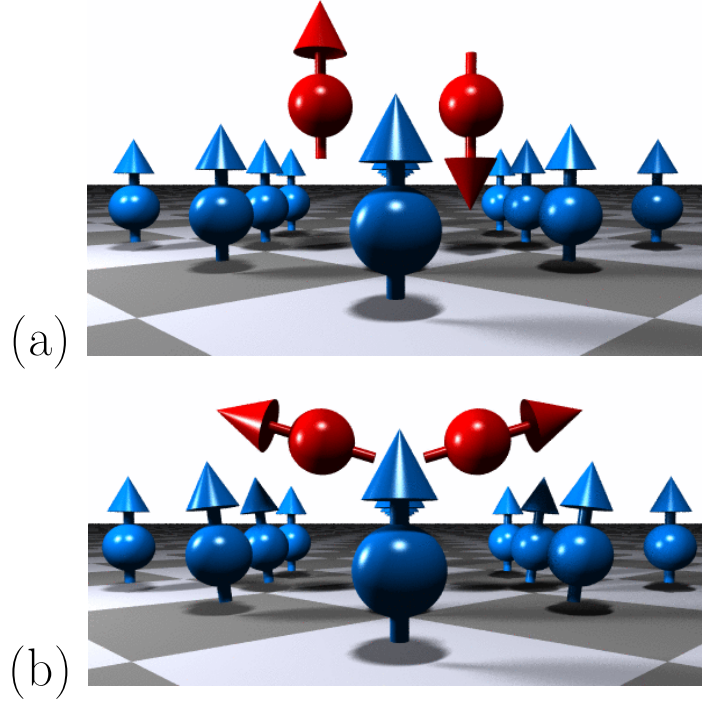


**FIG. 5.5** –. Most stable configurations of Mn dimer-1-type obtained with the collinear KKR method (a) and non-collinear KKR method (b). The rotation angle with respect to the  $z$ -axis is equal to  $72.6^\circ$ . The non-collinear state is the ground state.

system. The differences in energy between the Ferri and the non-collinear solutions are small and can be altered either by using a different type of exchange and correlation functional such as GGA or LSDA+ $U$ , or after relaxing the atoms. We note, however, that in a test calculation we found the Cr single-adatom relaxation to be small (3.23 % inward with respect to the interlayer distance), and thus we believe that the relaxation cannot affect the exchange interaction considerably.

As a cross-check, it is interesting to compare these non-collinear *ab-initio* results to model calculations based on the Heisenberg model with the exchange parameters fitted to the total energy results. We assume a classical spin Hamiltonian of the form

$$H = -\frac{1}{2} \sum_{i \neq j} J_{ij} \vec{e}_i \vec{e}_j. \quad (5.1)$$

Here,  $\vec{e}$  is a unit vector defining the direction of the magnetic moment and  $i$

$J_{ij}$ (meV)	(a)	(b)		
	Dimer 1	Dimer 1	Dimer 2	Dimer 3
$J_{\text{Cr-Ni}}$	-1.3	-11.6	-13.9	-14.5
$J_{\text{Cr-Cr}}$	-189.1	-221.3	-9.2	-2.0
$J_{\text{Mn-Ni}}$	13.0	27.0	26.8	29.5
$J_{\text{Mn-Mn}}$	-138.2	-140.2	13.7	1.5

**TAB. 5.3** –. Values of magnetic exchange parameters  $J_{ij}$  for Cr and Mn dimers on Ni(001), fitted from collinear first-principles total energy calculations (b) and obtained by the Lichtenstein formula [24] (a) ( $J_{\text{Cr-Ni}}$  and  $J_{\text{Mn-Ni}}$  are averaged over the different Ni first neighbours of the dimer atoms). Positive  $J_{ij}$  values correspond to ferromagnetic interactions, negative  $J_{ij}$  to antiferromagnetic ones.

and  $j$  indicate the dimer atoms and their first Ni neighbors. We can evaluate the interatomic exchange constants  $J_{\text{Cr-Ni}}$ ,  $J_{\text{Mn-Ni}}$ ,  $J_{\text{Mn-Mn}}$  and  $J_{\text{Cr-Cr}}$  via a fit to the total energy obtained from collinear LSDA calculations of the FM, AF, and Ferri configurations. Taking into account only first-neighbor interactions and neglecting the small rotation of Ni moments, we rewrite the Hamiltonian for the dimer in terms of the tilting angles  $\theta_1$  and  $\theta_2$  of the two Cr (or Mn) atoms (the azimuthal angles  $\phi$  do not enter the expression because of symmetry reasons):

$$H = -J_{\text{Cr-Cr}} \cos(\theta_1 - \theta_2) - 4J_{\text{Cr-Ni}}(\cos \theta_1 + \cos \theta_2) + \text{const.} \quad (5.2)$$

We note the two extreme cases arising from this Heisenberg Hamiltonian: (i)  $|J_{\text{Cr-Ni}}| \gg |J_{\text{Cr-Cr}}|$  leads to the stabilization of the collinear FM or AF configuration (adatom-like behavior) and (ii)  $|J_{\text{Cr-Ni}}| \ll |J_{\text{Cr-Cr}}|$  leads to antiferromagnetic coupling within the dimer if  $J_{\text{Cr-Cr}} < 0$ . Within the Heisenberg model the Ferri solution and the non-collinear solution with  $\theta = 90^\circ$  have the same energy. However there is an important difference between both configurations. In the Ferri configurations the angles  $\theta_1$ ,  $\theta_2$ , and  $\theta_1 - \theta_2$  are either  $0^\circ$  or  $180^\circ$ , and for small deviations  $\Delta\theta$  around these values the cos-functions in eq. (5.2) vary quadratically in  $\Delta\theta$ , showing that this configuration is always an extremum. However, for small deviations of  $\theta_1$  and  $\theta_2$  from the  $90^\circ$  values both  $\cos(\theta_1)$  and  $\cos(\theta_2)$  vary linear in  $\Delta\theta$ , showing that this configuration is not stable. In fact, any small value of  $J_{\text{Cr-Ni}}$  leads to a small tilting of the adatom moments either towards the substrate (as for Cr in fig. 5.4) or away from the substrate (as for Mn in fig. 5.5).

Table 5.3 summarizes the estimated exchange parameters. Two effects are striking: (i) The strong antiferromagnetic Cr-Cr and Mn-Mn interaction for the dimer-1 (nearest neighbors), being an order of magnitude larger than the exchange interactions with the substrate and being responsible for the stabilization of the non-collinear state structures shown in Fig. 5.4 and Fig. 5.5. (ii) The very weak Cr-Cr and Mn-Mn interactions in the dimer-2 and -3 configurations. Whereas

for the nearest-neighbors configuration (dimer-1) the direct overlap of the  $d$ -wavefunctions of the Cr and Mn atoms leads to the strong coupling, this overlap is missing for larger distances and the interaction can only proceed through the substrate. However, this interaction is weak, in fact considerably smaller than the interaction of both adatoms with the four neighboring Ni atoms of the substrate. Therefore these dimers are effectively decoupled, and behave like the isolated adatoms, being antiferromagnetically coupled to the substrate in the case of Cr and ferromagnetically for Mn. The exchange constants  $J_{ij}$  fitted to total energy results can be compared to the ones obtained by using the Lichtenstein formula [24] (starting from the Ferri ground state). This rests on the force theorem, and yields the exchange constants relevant to an infinitesimal rotation of the moments. The results of the two methods agree best for the Mn-Mn interaction, and reasonably well for the Cr-Cr interaction, but not for Mn-Ni and Cr-Ni.

With the parameters from Tab. 5.3 one can also recalculate the non-collinear structure of the ground state. The agreement with the *ab-initio* results is quite reasonable. For the Cr dimer, one finds a slightly smaller tilting, i.e.  $96^\circ$  instead of  $94.2^\circ$ , while for the Mn dimer the angle is  $67.3^\circ$  instead of  $70.6^\circ$ .

The differences in energy calculated within this simple model, show that in this model the Cr-dimer-1 has a non-collinear ground state ( $\Delta E_{\text{Ncol-Ferri}} = -4.8$  meV/adatom) as well as the Mn-dimer-1 ( $\Delta E_{\text{Ncol-Ferri}} = -20.8$  meV/adatom). The discrepancy obtained for the case of Cr-dimer-1 (the LSDA calculation gives the collinear Ferri ground state) can be attributed to the restrictions of the Heisenberg model. For instance, for the Ferri and non-collinear configurations, the Cr moments are slightly different, and also the reduction of the Ni moments as a function of the rotation angle (*e.g.* for the single adatom) cannot be described by the Heisenberg model, where the absolute values of the moments are assumed to be constant.

In order to illuminate the magnetic stability found in our calculations we did a one-iteration calculations starting from Ferri Cr-potentials and applying the frozen potential approximation. We did two kind of calculations: first, we froze one magnetic moment in the parallel direction ( $\theta=0^\circ$ ) and rotated the other moment by an angle-sequence of  $15^\circ$  up to an antiparallel coupling ( $\theta=180^\circ$ ); second, we froze one magnetic moment at  $94^\circ$  angle and rotate the other moment by again an angle-sequence of  $15^\circ$  into the opposite direction from a parallel up to an antiparallel coupling with respect to the host. The single particle energies calculated using the Lloyd's formula are plotted in Fig. 5.6: we notice that in the first case the Ferri solution is the ground state (black circles) while a local minimum appears in the second case (red circles). However, the energy difference between the  $94^\circ$  state and the ground state is unrealistically large, since the relaxation of the moments are not correctly described.

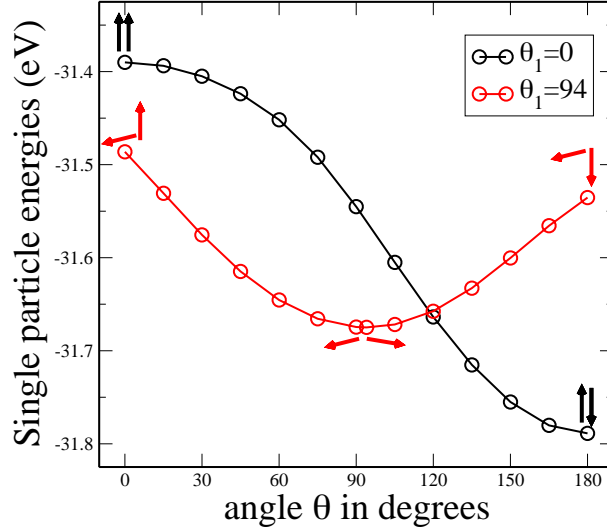


**FIG. 5.6** –. Variations of single particle energies, obtained by the frozen potential approximation using the Lloyd’s formula, versus the rotation angle of the second magnetic moment of a Cr-dimer/Ni(001). The black circles show the energy variation when the first magnetic moment is frozen at zero angle (parallel), while the red circles describe the energy variation for the first magnetic moment frozen at  $\approx 94^\circ$ .

## 5.7 Inatom Dimers

To evaluate the effect of change in coordination and hybridization, we have undertaken a study of inatom first-neighbor dimers for V, Cr, Mn and Fe. The V and Fe inatom-dimers were found to behave like the adatom dimers. The V dimer prefers an AF state, the Fe dimer the FM state, while the Cr and Mn dimers are in a Ferri state (in case of collinear constraint). The spin moments in the collinear and non-collinear states are given in Tab. 5.4. Within the Ferri-dimers, the difference between the moments of the two atoms arises from the different coupling of each inatom with the the substrate (AF or FM). One notices also that the magnetic moments in the ground state decrease compared to the values obtained for the single inatoms and single adatoms. When the rotation of the moments is allowed, Cr-dimer can be stabilized at an angle of  $107^\circ$  (instead of  $94.2^\circ$  found for the adatom-dimer case), and Mn-dimer at an angle of  $80.9^\circ$  (instead of  $72.6^\circ$ ). Thus the non-collinear solutions obtained for inatom-dimers are rather similar to what was obtained for adatom-dimers. Energetically, however, both the Cr and the Mn inatom dimers show a lower total energy in the collinear Ferri state (for

Dimer	On	In
V(AF)	(-1.28, -1.28)	(-0.32, -0.32)
Cr(Ferri)	(-3.04, 3.05)	(-2.00, 1.96)
Cr(Ncol)	(3.03, 3.03)	(1.97, 1.97)
Mn(Ferri)	(-3.84, 3.69)	(-3.32, 3.20)
Mn(Ncol)	(3.75, 3.75)	(3.26, 3.26)
Fe(FM)	(3.10, 3.10)	(2.88, 2.88)

TAB. 5.4 – Atomic spin moments (in  $\mu_B$ ) of the adatom and inatom dimers (of type 1, i.e., nearest-neighbors) in the collinear and non-collinear configurations. A minus sign of the collinear moments indicates an antiparallel orientation with respect to the substrate magnetization. Embedding the dimer into the surface causes, as expected, a decrease of the spin moments due to stronger hybridization of the  $d$  wavefunctions.

Cr,  $\Delta E_{\text{Ncol-Ferri}} = 12.1$  meV/adatom; for Mn,  $\Delta E_{\text{Ncol-Ferri}} = 11.2$  meV/adatom).

## 5.8 Trimers

Following the same procedure as for dimers we first investigated several collinear magnetic configurations for the most compact trimer on the Ni(001) surface, which has the shape of an isosceles rectangular triangle (see Fig. 5.7) of side  $\sqrt{2}a/2$  and hypotenuse  $a$  ( $a$  is the Ni fcc lattice constant). It is expected, and verified by total-energy calculations, to find the  $\downarrow\uparrow\downarrow$  configuration as the collinear magnetic ground state for Cr and the  $\uparrow\uparrow\uparrow$  for the Mn trimer ( $\uparrow$  means an atomic moment parallel to the substrate,  $\downarrow$  an antiparallel one; the middle arrow represents the direction of the atomic moment at the right-angle corner of the triangle). In Tab. 5.5, the energy differences among the possible collinear configurations are given; for the  $\uparrow\uparrow\uparrow$  and  $\downarrow\downarrow\downarrow$  Cr trimers, no self-consistent solution could be found.

Magn. Config.	$\uparrow\uparrow\downarrow$	$\downarrow\uparrow\downarrow$	$\downarrow\downarrow\uparrow$	$\uparrow\downarrow\uparrow$	$\uparrow\uparrow\uparrow$	$\downarrow\downarrow\downarrow$
Cr: $E - E_{\downarrow\uparrow\downarrow}$ (eV)	0.420	0	0.390	0.193	—	—
Mn: $E - E_{\downarrow\uparrow\downarrow}$ (eV)	0.116	0	0.318	-0.184	0.239	0.817

TAB. 5.5 – Energy differences between the different calculated collinear magnetic configurations with the  $\downarrow\uparrow\downarrow$  configuration. The direction of the arrows represents the direction of the atomic moments relative to the substrate magnetization ( $\uparrow$  parallel,  $\downarrow$  antiparallel). The middle arrow represents the atom at the right-angle corner of the trimer.

Allowing free rotation of the magnetic moments leads to no change for the

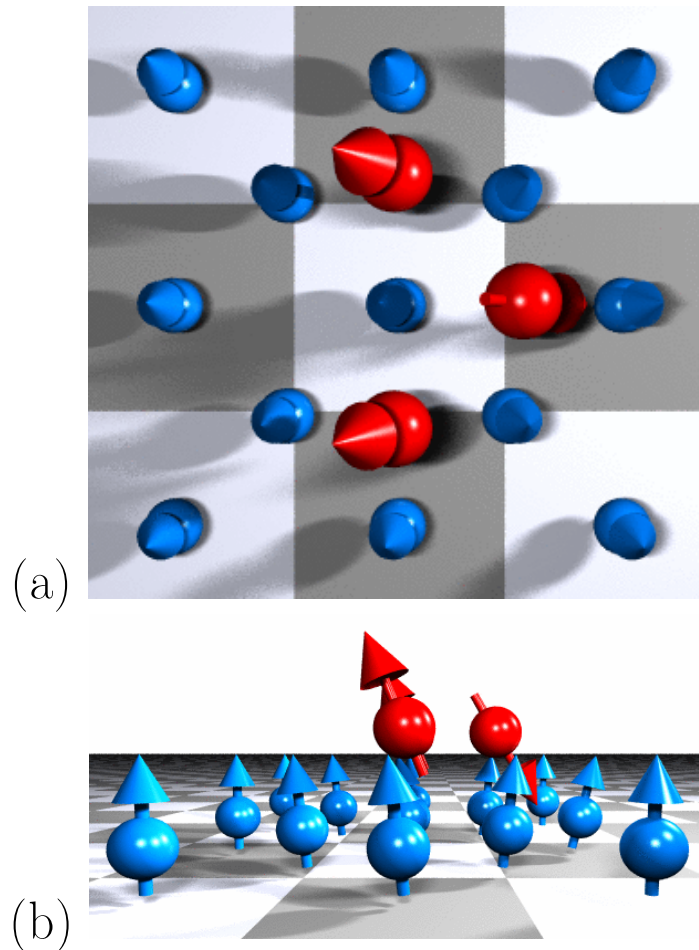


**FIG. 5.7** –. *Non-collinear state of the Mn trimer on Ni(001) surface. Side view (a) and top view (b) are shown. This represents a local minimum in energy, with the collinear state being the ground state (see text).*

Cr trimer  $\downarrow\uparrow\downarrow$ —the state remains collinear (within numerical accuracy). On the other hand, for the Mn trimer a non-collinear solution is found (Fig. 5.7) with the nearest neighbours almost antiferromagnetic to each other, but with a collective tilting angle with respect to the substrate. This tilting angle is induced by the ferromagnetic MEI between the central Mn atom with the substrate, competing with the antiferromagnetic MEI with its two companions. The top view

of the surface shows that the in-plane components of the magnetic moments are collinear.

The tilting is somewhat smaller ( $21.7^\circ$ ) for the two Mn atoms with moments up than for the Mn atom with moment down ( $28.5^\circ$ ). Also the neighboring Ni-surface atoms experience small tilting, with varying angles around  $4^\circ - 10^\circ$ . From the energy point of view, the ground state is the collinear one,  $\uparrow\downarrow\uparrow$ , with an energy difference of  $\Delta E_{\text{Ncol-}\uparrow\downarrow\uparrow} = 7.6$  meV/adatom with respect to the non-collinear solution.

As done for the dimers, we proceed here also to frozen potential approximation to show that the non-collinear solution is a local minimum. In the present case: first, we froze the two *outer* magnetic moments in the parallel direction ( $\theta=0^\circ$ ) and rotated the *central* moment by an angle-sequence of  $15^\circ$  up to an antiparallel coupling ( $\theta=180^\circ$ ); second, we froze the two *outer* magnetic moments at  $22^\circ$  angle and rotate the other moment by again an angle-sequence of  $15^\circ$  into the opposite direction up to an antiparallel coupling. The single particle energies are shown in Fig. 5.8. It is clear that a local minimum appears in the second case at an angle of  $\approx 150^\circ$  which has a very small energy difference compared to the  $\uparrow\downarrow\uparrow$  case.

We have also investigated the cases where the trimers are sitting in the surface layer. No non-collinear solution was found, while there is no change in the collinear ground state which is  $\downarrow\uparrow\downarrow$  for the Cr trimer and  $\uparrow\downarrow\uparrow$  for the Mn trimer.

One should note that the moments of the two first neighboring impurities are almost compensated in the Ferri solution. Therefore the third moment determines the total interaction between the substrate and the trimer which has then a net moment arising mainly from the uncompensated moment of the third impurity.

## 5.9 Tetramers and Pentamers

Finally we present results for compact, symmetric tetramers and pentamers of Cr and Mn adatoms. In these cases, the collinear solutions are stabilized for Cr as well as Mn clusters (shown in Fig. 5.9(a) and Fig. 5.9(b)). The inter-atomic MEI leads to a  $C(2 \times 2)$  collinear antiferromagnetic order, which is the expected result in the case of full coverage. In Tab. 5.3 we saw that the intra-dimer antiferromagnetic interaction between first neighbors is much stronger than the adatom-substrate interaction; however, in that case, the greater number of Ni neighbors had a significant influence in creating a non-collinear state. For tetramers and pentamers, on the other hand, each adatom has two or more companion adatoms as first neighbors, so that this interaction dominates.

Concerning tetramers, three magnetic configurations were converged: the AF where all adatoms are AF coupled to the substrate Ni atoms, the FM where all adatoms are FM coupled to the surface and finally the magnetic ground state *i.e.* Ferri or  $C(2 \times 2)$  in which the first neighboring adatoms are AF coupled to each other (see Tab. 5.6). We point out that this configuration is double de-

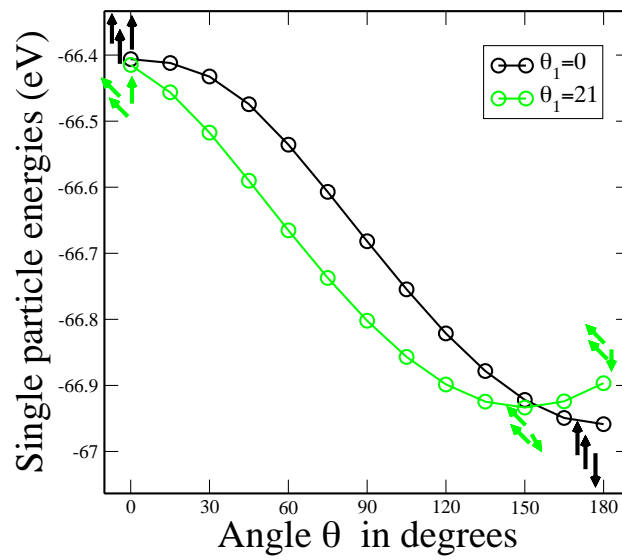


**FIG. 5.8** –. Variations of single particle energies, obtained by the frozen potential approximation using the Lloyd's formula, versus the rotation angle of the second magnetic moment of a Mn-trimer/Ni(001). The black circles show the energy variation when the two outer magnetic moments are frozen at zero angle (parallel), while the green circles describe the energy variation for the third central magnetic moment frozen at  $\approx 22^\circ$ .

generate because all the moments can be rotated by an angle of  $180^\circ$  (total flipping) without changing the magnetic coupling picture. For the Cr-tetramer the Ferri configuration is characterized by considerably higher magnetic moments ( $2.62\mu_B, -2.56\mu_B$ ) compared to the AF ( $1.01\mu_B, 1.01\mu_B$ ) and FM ( $0.70\mu_B, 0.70\mu_B$ ) ones. The moments values are almost doubled in the Ferri solution leading to a doubling of the exchange splitting  $\Delta E_X$  which depends on the magnetic moment as  $\Delta E_X \approx I \cdot M$ . This explains the stability of the Ferri solution compared to the other collinear solutions.

The degeneracy mentioned earlier for the tetramer is removed by adding a fifth adatom in order to form a compact pentamer (see Fig. 5.9b). The adatoms sitting at the square corners have all their moments coupled to the substrate as the single adatoms do *i.e.* AF for the case of Cr and FM for Mn while the central adatom is forced to couple antiparallel to the surrounding adatoms.

In order to check the proximity of the two magnetic configurations: collinear and non-collinear, calculations using the Full potential Linear Augmented Plane Waves (FLAPW) were carried out by Paolo Ferriani [89] for one monolayer of Mn and Cr on Ni(001). If we consider the monolayer as the upper limit size of a two dimensional adcluster, the comparison is then propitious. Ferriani found that the two magnetic configurations: perpendicular and parallel to the surface magnetization are almost degenerate for both transition elements (Cr and Mn). This is explained by the simple Heisenberg model discussed previously for the dimer case. Within this model, the magnetic behavior is determined by the cosine-like coupling: For an even number of adatoms the two magnetic configurations are degenerate, because the terms  $\cos(0)$  and  $\cos(180)$  cancel each other in the Ferri solution while they are zero for  $\cos(90)$  ( $\approx$  non-collinear solution). For an odd number of adatoms the magnetic behavior is mainly driven by the additional adatom. This explains why, for example, we get for the Mn-trimer a non-collinear solution tilted a bit from the the collinear one. When we increase the number of adatoms, the oddness effects disappear and the adcluster behave like an even adcluster. At the monolayer limit, as verified by Ferriani, the magnetic behavior should be similar to adclusters with even number of adatoms, and no real difference was found between the magnetic configurations.

## 5.10 Summary

We have investigated the magnetism of 3d adclusters on the Ni(001) surface emphasizing on Cr and Mn clusters, for which we found that magnetic frustration can lead to non-collinear magnetic order. The origin of the frustration is the competition of the antiferromagnetic exchange coupling among the Cr or Mn adatoms with the antiferromagnetic (for Cr) or ferromagnetic (for Mn) exchange coupling between the adatoms and the substrate. In this respect, the result is different than the prototype non-collinear configurations arising from antiferromagnetic

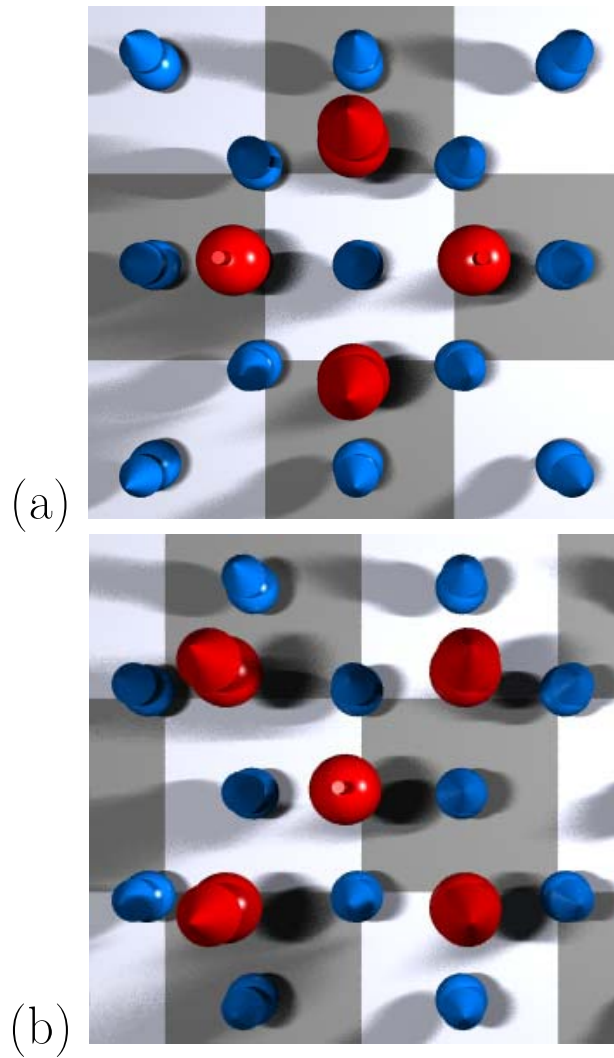


**FIG. 5.9** –. Top views of (a) Mn-, Cr-tetramer and (b) Mn-pentamer on Ni(001) (the magnetic moments are rotated to the opposite direction in the case of Cr-pentamer). Both clusters are found to be magnetically collinear. The magnetic coupling is AF between first neighboring atoms within the cluster.

interactions among atoms in triangular geometry.

We found that Cr and Mn first-neighbouring adatom dimers can show a non-

Adcluster	Magn. Config.	Magn. Mom.	$E_{\text{Conf}} - E_{\text{Ferri}}$
Cr-tetramer	Ferri	$(2.62\mu_B, -2.56\mu_B)$	0
	AF	$(-1.01\mu_B, -1.01\mu_B)$	303.7 meV/adatom
	FM	$(0.70\mu_B, 0.70\mu_B)$	280.9 meV/adatom
Mn-tetramer	Ferri	$(3.38\mu_B, 3.50\mu_B)$	0
	AF	$(-3.49\mu_B, -3.49\mu_B)$	390.4 meV/adatom
	FM	$(3.66\mu_B, 3.66\mu_B)$	232.6 meV/adatom
Cr-pentamer	Ferri	$(2.08\mu_B, -3.22\mu_B)$	/
Mn-pentamer	Ferri	$(-3.22\mu_B, 3.34\mu_B)$	/

**TABLE 5.6** –. *Magnetic moments and energy differences per adatom of the collinear magnetic configurations obtained for Cr-, Mn-tetramer and pentamers. The first moment given for the pentamers is related to the central adatom while the second moment is carried by the four square corner adatoms. The minus sign means an AF coupling between the adatom and the surface atoms.*

collinear behavior, while increasing the distance between the adatoms of the dimer leads to the same state as for single adatoms. The energy differences between the collinear ferrimagnetic state and the non-collinear one are  $\Delta E_{\text{Ncol-Ferri}}^{\text{Cr}} = 39.84$  meV (the ground state is collinear),  $\Delta E_{\text{Ncol-Ferri}}^{\text{Mn}} = -13.45$  meV (the ground state is non-collinear). Embedding the dimers in the first surface layer restores the Ferri collinear solution as the ground state also for Mn adatom dimers ( $\Delta E_{\text{Ncol-Ferri}}^{\text{Cr}} = 24.11$  meV,  $\Delta E_{\text{Ncol-Ferri}}^{\text{Mn}} = 22.5$  meV).

Our *ab-initio* results for dimers are compared to the solution of a classical Heisenberg model with exchange parameters fitted to total energy results. The agreement for the tilting angles in the non-collinear state is good, but the Heisenberg model does not capture the collinear ground state for the Cr dimer. This discrepancy occurs because the Heisenberg model cannot describe the changes of the absolute values of localized moments.

The trimers studied so far are characterized by a collinear ground state:  $\downarrow\uparrow\downarrow$  for the Cr trimer and  $\uparrow\downarrow\uparrow$  for the Mn trimer. The Mn trimer has also a non-collinear metastable solution with an energy difference  $\Delta E_{\text{Ncol-}\uparrow\downarrow\uparrow} = 7.6$  meV/adatom.

Compact tetramers and pentamers are Ferri for Cr and Mn adatoms meaning that the first neighboring atoms are AF coupled to each other, in particular, the central adatom of the pentamer is forced to couple antiparallel to its neighboring adatoms. This additional adatom in the pentamer removes the magnetic degeneracy observed for the Ferri solution of the pentamer.

We predicted that the upper-size limit of a two dimensional adcluster, *i.e.* a monolayer of Cr and Mn on Ni(001) should behave like the adclusters with an even number of adatoms. This prediction was verified, at least, theoretically by Paolo Ferriani [89] who shows by using the FLAPW method that the two configurations Ferri or C(2×2) perpendicular (non-collinear:  $\approx 90^\circ$ ) and parallel

---

(collinear) are almost degenerate. This can be understood by the simple Heisenberg model used in this chapter which through the cosine coupling gives the same energy for the two configurations when the number of adatoms is even. The close magnetic proximity of both configurations suggests, that during island growth both magnetic configurations might occur on the same surface.

We believe that the energetic proximity of the collinear to the non-collinear states is directly related to the weakness of the exchange interaction with the Ni substrate. Replacing it by an fcc Fe substrate will possibly change the ground state drastically, as we see in the next chapter (see chapter 6).



# Chapter 6

## Complex Magnetism of Small Clusters on $\text{Fe}_{3\text{ML}}/\text{Cu}(001)$

### 6.1 Introduction

In the previous chapter, we have already shown the possibility of non-collinear magnetic coupling for Cr and Mn impurities on Ni(001) and discussed the energetic proximity of the collinear and non-collinear states. We believe that this is directly related to the weakness of the exchange interaction with the Ni substrate. Replacing it by a stronger ferromagnetic (FM) substrate will possibly change the ground state drastically. The choice of this new substrate was mainly motivated by an experiment carried by the group of W. Wurth [5]. They deposited Cr clusters by a soft-landing technique, the principle of which we will explain briefly later, on three monolayers (ML) of Fe deposited on Cu(001) and measured the magnetic moments by x-ray Magnetic Circular Dichroism (XMCD). Indeed this substrate is ideal for our purpose, considering that the Fe layers for such a low thickness are ferromagnetic and stabilized in an *fcc* structure due to the deposition on *fcc* Cu. This gives a perfect opportunity for a comparison with the ferromagnetic Ni substrate we already investigated. The aim of this work is thus to present the complex magnetic behavior of *3d* impurities on *fcc* Fe.

### 6.2 Magnetic Properties of Fe/Cu(001) Surface

The Fe/Cu(001) surface has challenged experimentalists and theoreticians for several years through its complex magnetic behavior. In such a system, the atomic structure, the growth mode, the film morphology, and the magnetic properties are intimately interwoven. The experimental work on the structure, magnetism, electronic structure, growth and morphology has led to the following picture: for experimental deposition at room temperature three different regimes are distinguished as a function of the Fe coverage  $C$ . In the first regime *i.e.*  $C < 4 \sim 5$  ML

the spin configurations are FM [90, 91] throughout the tetragonal distorted film. In the second regime *i.e.*  $5 < C < \sim 11$  ML, the film is antiferromagnetic (AF) *fcc* [92]. The third regime is obtained for thicker Fe films ( $C > \sim 11$  ML) where *fcc* Fe becomes unstable and transforms into FM *bcc* [90, 93].

Theoretically, a detailed study was done by Asada and Blügel [94] on this system using the full-potential linearized augmented plane-wave method. They found ferromagnetism for 1 up to 3 ML *fcc* Fe, bilayer antiferromagnetism for even numbers of layers (4 and 6 ML), and the coexistence of several spin states for an odd number of layers (5 ML) which is consistent with the experimental picture. Stepanyuk *et al.* [95] considered also the surface of one FM Fe ML on Cu(001) in order to investigate magnetism of *3d* and *4d* adatoms. We note, however, that only collinear magnetism was considered.

As we are interested in the FM regime, we considered in the present work 3 ML of Fe on Cu(001) which corresponds to the approximate number of layers analyzed experimentally by the group of Wirth. We calculated the electronic and magnetic properties of this system considering the theoretical lattice parameter of Cu (6.64 a.u.  $\approx 3.51 \text{ \AA}$ ) obtained by LSDA [35]. The full nonspherical potential was used, taking into account the correct description of the Wigner-Seitz atomic cells [81]. Angular momenta up to  $l_{\text{max}} = 3$  were included in the expansion of the Green functions and up to  $2l_{\text{max}} = 6$  in the charge density expansion. Relativistic effects were described in the scalar relativistic approximation.

Three magnetic configurations were obtained: (i) The FM configuration with all Fe layers FM coupled to each other ( $(S) \uparrow, (S-1) \uparrow, (S-2) \uparrow$ , where S labels the surface layer), (ii) the antiferromagnetic AF-type 1 ( $(S) \uparrow, (S-1) \downarrow, (S-2) \uparrow$ ) and (iii) the AF-type 2 ( $(S) \downarrow, (S-1) \downarrow, (S-2) \uparrow$ ). After comparing the total energies of the different magnetic solutions, we found the FM solution as the most stable state with the following magnetic moments:  $m_S^{Fe} = 2.66\mu_B$ ,  $m_{S-1}^{Fe} = 2.09\mu_B$  and  $m_{S-2}^{Fe} = 2.18\mu_B$  which are in good agreement with the previous theoretical results obtained by Stepanyuk *et al.* [95] ( $2.76 \mu_B$ ) for one monolayer Fe/Cu(001).

### 6.3 Calculations Setup for Clusters

First, the surface Green functions are determined by the screened KKR-method [38] for  $\text{Fe}_{3\text{ML}}/\text{Cu}(001)$  which serves as the reference system. To describe the adatoms on the surface, we consider a cluster of perturbed potentials which includes the potentials of the impurities and the perturbed potentials of several neighboring shells, with typical size ranging from 19 perturbed sites for the single impurity to 32 for the dimers and trimers, and to 36 atoms for tetramers and pentamers; in all cases, at least the first neighboring sites of the impurity atoms were included in the calculation to ensure the correct screening of the impurity charge. Tests have shown that this is adequate for our calculations. We consider

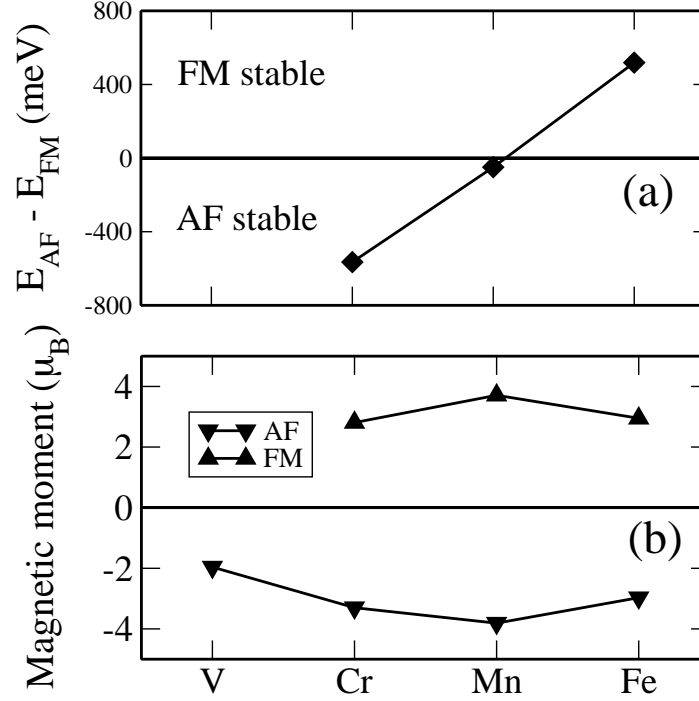


**FIG. 6.1** – *3d adatoms on  $Fe_{3ML}/Cu(001)$ : (a) energy difference between the AF and FM coupling; (b) magnetic moments of the adatoms within the 2 possible magnetic configurations FM and AF.*

all our impurities at the unrelaxed hollow position in the first vacuum layer. We allow for the relaxation of the magnetic moment directions using our full potential KKR Green function method for non-collinear magnetism.

## 6.4 Single Adatoms

Let us start with the adatoms: the full diamonds in Fig. 6.1.(a) show the energy difference between the AF and the FM configuration for the four transition adatoms investigated on  $Fe_{3ML}/Cu(001)$ . The basic difference with Ni(001) surface lies on the stronger magnetic coupling of the adatoms with respect to the surface. An additional difference is the (weak) AF coupling of Mn adatom with the substrate contrary to the FM coupling on Ni surface. For Mn, the difference in energy ( $\Delta E_{AF} - E_{FM} = -49.25 meV$ ) is in the same order of magnitude with

previously published results [95] ( $\Delta E_{AF} - E_{FM} = -34\text{meV}$ ).

The magnetic moments of the adatoms are shown in Fig. 6.1.(b). As regards the adatom moments, due to its half filled  $d$  band the Mn adatom carries the highest magnetic moment ( $3.81 \mu_B$ ) followed by Cr ( $3.30 \mu_B$ ) and Fe ( $2.95\mu_B$ ).

Cr adatoms are antiferromagnetically (AF) coupled to the substrate as for the case of Cr adatoms on the Ni(001) surface. The energy difference  $\Delta E_{FM-AF} = 564.9 \text{ meV}$  is four times stronger than the energy difference obtained on Ni(001) surface. As was expected, this shows the strength of the interaction on Fe and yields an exchange coupling constant  $J_{Cr-Fe} = 141\text{meV}$  (see eq. (5.1)). The preference of the antiferromagnetic configuration shows up also in a considerably larger AF Cr-moment of  $3.30\mu_B$  compared to the metastable ferromagnetic configuration ( $2.80\mu_B$ ).

## 6.5 Adatom Dimers

Having established the single adatom behavior, we turn now to the adatom dimers. We considered the two atoms sitting on first neighbor sites. The results are summarized in the Tab. 6.5. Three collinear magnetic configurations were treated: (i) Antiferromagnetic coupling within the dimer leading to a ferrimagnetic solution (Ferri), (ii) ferromagnetic coupling within the dimer with both atoms ferromagnetically coupled to the substrate (FM), or (iii) ferromagnetic coupling within the dimer with both atoms antiferromagnetically coupled to the substrate (AF). Concerning the geometrical configurations, we have considered only the adatoms as first neighbors since we have shown previously (Sec. 5.6) that the exchange interaction between the adatoms decreases drastically when increasing the distance between the impurities. This means that the magnetic dimer behavior for a bigger distance is expected to be identical to the one of the adatom.

We notice that the only dimer which is characterized by a non-collinear magnetic solution is the Mn-dimer. In the collinear ground state, the two atoms are antiferromagnetically coupled to each other. One Mn atom is thus forced to couple ferromagnetically to the substrate despite the fact that the Mn-adatom prefers an AF coupling to the surface atoms. The two moments are highly saturated which explains their near equality ( $3.55\mu_B, -3.58\mu_B$ ). Once the collinear constraint is released a non-collinear magnetic solution is obtained. The two atoms are still AF coupled to each other, however, they couple slightly AF to the substrate ( $\theta = 115^\circ$ ) contrary to the non-collinear solution obtained on Ni(001) ( $\theta = 76^\circ$ ). The inward moment direction found in the present case is due to the AF coupling preference of the single Mn adatom to the substrate.

The other kinds of dimers studied are all magnetically collinear: For the V-dimer only the AF solution was obtained with a magnetic moment of  $1.80\mu_B$ ; the Fe-dimer is characterized by a FM solution ( $M_{Fe} = 3.01\mu_B$ ). For Cr the FM

	FM	AF	Ferri	Non-collinear
$(m_V, m_V)(\mu_B)$ $\Delta E_{\text{Conf}}^V - E_{\text{Ferri}}^V$	/	(-1.80,-1.80)	/	/
$(m_{\text{Cr}}, m_{\text{Cr}})(\mu_B)$ $\Delta E_{\text{Conf}}^{\text{Cr}} - E_{\text{Ferri}}^{\text{Cr}}$	/	(-3.20,-3.20)	(2.64,-2.93)	/
$(m_{\text{Mn}}, m_{\text{Mn}})(\mu_B)$ $\Delta E_{\text{Conf}}^{\text{Mn}} - E_{\text{Ferri}}^{\text{Mn}}$	(3.59,3.59)	(-3.53,-3.53)	(3.55,-3.58)	(3.55,3.55)
$(m_{\text{Fe}}, m_{\text{Fe}})(\mu_B)$ $\Delta E_{\text{Conf}}^{\text{Fe}} - E_{\text{Ferri}}^{\text{Fe}}$	(3.01,3.01)	/	(2.79,-2.92)	/
	583.34	-236.20	0	-458.17
	-430.90	/	0	/

**TAB. 6.1** – Differences between energies of the studied magnetic configurations (in meV) and magnetic moments for each adatom  $\mu_B$ . the negative sign of the magnetic moments means an AF coupling to the substrate.

configuration is not stable and could not be found within the self-consistency. Among the two remaining collinear configurations, the AF one is the most stable state with an energy difference  $\Delta E_{\text{Ferri-AF}} = 344.2$  meV/adatom which is again much higher than the value obtained on Ni(001) surface ( $\Delta E_{\text{Ferri-AF}} = 216.5$  meV/adatom). The moments obtained in the Ferri solution ( $2.64\mu_B$ ,  $-2.93\mu_B$ ) are lower than the value obtained in the AF ground state ( $3.20\mu_B$ ,  $3.20\mu_B$ ). Surprisingly, we did not find a non-collinear solution which would be expected by the following argument: Both Cr atoms tend to couple AF to the substrate as we have seen for single adatoms, but they also tend to couple AF to each other as expected for elements having a half filled  $d$ -band and as explained by the Alexander–Anderson model[88, 80] (see section 5.4). These competing interactions should lead to magnetic frustration and to a non-collinear solution. However, when we introduce rotated moments as starting point in our *ab-initio* calculations, both impurity moments relax back to the AF coupling to the substrate even though there is an AF interaction between the adatoms. In order to explain this we introduce a Heisenberg model with the exchange parameters calculated from eq. (5.1).

The angle defining the non-collinear solution is obtained after a minimization

of the Heisenberg Hamiltonian as:

$$\cos(\theta) = -2 \frac{J_{\text{Cr-Fe}}}{J_{\text{Cr-Cr}}} \text{ for } 2J_{\text{Cr-Fe}} < J_{\text{Cr-Cr}} \quad (6.1)$$

If  $2|J_{\text{Cr-Fe}}| > |J_{\text{Cr-Cr}}|$ , the angle is not defined and the non-collinear solution does not exist. This is clearly realized in the present case:  $2|J_{\text{Cr-Fe}}| = 2 \times 80.8 > |J_{\text{Cr-Cr}}| = 77.6$  meV. Note that the Cr-Fe coupling constants are considerably smaller than for the single adatom.

## 6.6 Trimers

Following the same procedure as for the dimer we first investigated several collinear magnetic configurations for the most compact trimer on the surface, which has the shape of an isosceles rectangular triangle (see Fig. 6.2(a)) of side  $\sqrt{2}a/2$  and hypotenuse  $a$  ( $a$  is the Cu *fcc* lattice constant).

For V-trimer only the  $\uparrow\downarrow\uparrow$  configuration  $\uparrow\downarrow\uparrow^1$  was obtained after self-consistency. The three atoms are FM coupled to each other and AF coupled to the substrate. This was expected from the single adatom behavior. We notice also a strong decrease of the magnetic moments carried by each adatom: the adatom sitting at the right-angle corner of the trimer has a very low moment of  $0.66 \mu_B$  which is 66% smaller than the single adatom moment ( $1.96 \mu_B$ ). This decrease is principally due to a hybridization with the two first neighboring V adatoms which experience a smaller reduction of the magnetic moments ( $1.31 \mu_B$ ). This reduction is not as strong as for the *central* adatom because contrary to the latter one these two adatoms have only one first neighboring adatom. On the other hand, the Fe-trimer prefers the FM configuration with high magnetic moments as obtained for the single adatom, *i.e.* the *central* magnetic moment is equal to  $2.82 \mu_B$  while the other magnetic moments are equal to  $2.93 \mu_B$ .

For the Cr-trimer, after self-consistency all different collinear configurations converged to the FM solution with drastically reduced moments, *i.e.*  $0.19 \mu_B$  for the atom sitting at the right-angle corner of the triangle and  $0.42 \mu_B$  for both remaining impurities. If we allow the directions of the moments to rotate, the moments strongly increase to “normal” values ( $2.57 \mu_B$  for the right-angle atom and  $2.92 \mu_B$  for the two remaining atoms). As seen earlier, the AF interaction within the dimer was not high enough to compete with the adatom-substrate interaction. The third adatom of the system induces a rotation of the moments. The two second neighboring impurities have a moment tilted down by an angle of  $156^\circ$  and the central adatom moment is tilted up with an angle of  $77^\circ$ . The total energy difference between the non-collinear and collinear solution is  $\Delta E_{\text{Ncol-FM}} = -360$  meV/adatom, *i.e.* the non-collinear state is the ground state.

---

1. For the nomenclature see section 5.8

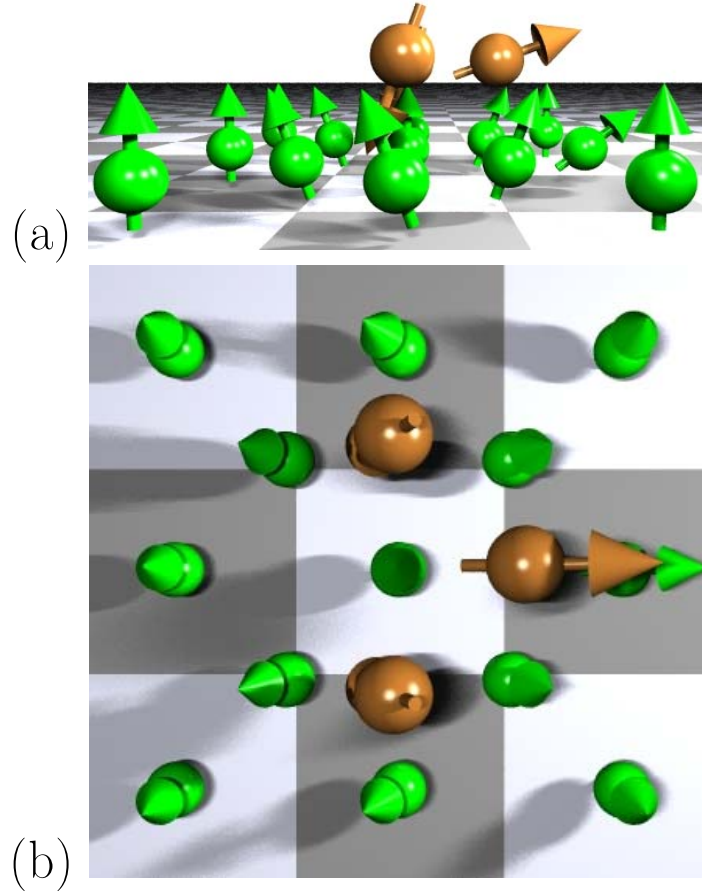


**FIG. 6.2** –. *Non-collinear ground state of the Cr trimer on  $Fe_3ML/Cu(001)$  surface. Side view (a) and top view (b) are shown.*

The Mn-trimer is also interesting considering the magnetic behavior found for the dimer. Contrary to the Cr-trimer, here we found an antiferromagnetic configuration where the *central* Mn-atom couples FM to the substrate whereas the two remaining *outer* atoms are AF coupled to the substrate (we call this configuration Ferri). In this configuration, however, the magnetic moments of these *outer* atoms are rather small ( $0.12 \mu_B$ ) and much smaller than the moment of the *central* atom ( $-3.10 \mu_B$ ). Furthermore we found another collinear magnetic configuration which is the collinear magnetic ground state such that the three atoms are AF coupled to the substrate ( $E_{Ferri} - E_{AF} = 40.28 \text{meV/atom}$ ).

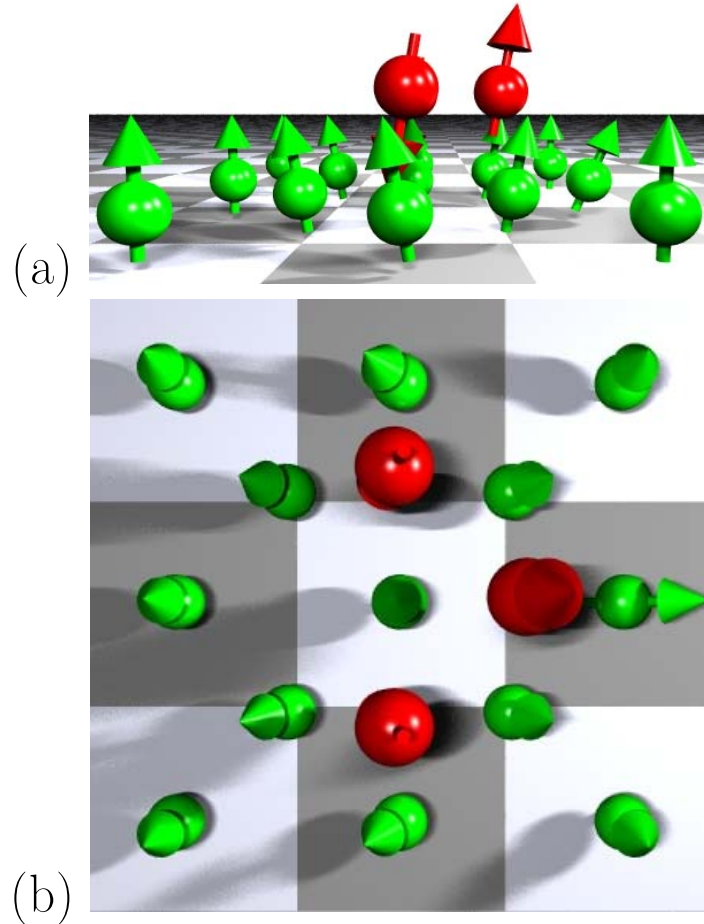


**FIG. 6.3** –. Non-collinear ground state of the Mn trimer on  $Fe_{3ML}/Cu(001)$  surface. Side view (a) and top view (b) are shown.

The *outer* adatoms still have low magnetic moments ( $-0.30 \mu_B$ ) while the *central* adatom has a saturated moment of  $-3.08 \mu_B$ . It seems that we have here a competition between the AF coupling of the first neighboring adatoms and the FM coupling with the substrate. Indeed in a constrained collinear magnetic calculations, the moments can not rotate in order to release the magnetic frustration; instead, their value can only decrease or increase to reduce the magnetic frustration. In the present case, the moments are trapped in some local minimum with low magnetic moments. Therefore, it is tempting to predict that unconstrain-

ing the magnetic coupling leads to a non-collinear solution with higher magnetic moments. In fact, after self-consistent calculations, the converged non-collinear solution is characterized by a restored high value of the outer magnetic moments ( $3.62 \mu_B$ ). The orientation of the magnetic moments is similar to the Ferri one (see Fig. 6.3): the *central* magnetic moment rotates by an angle of  $20^\circ$  and the *outer* magnetic moments rotate by half the value of the previous angle ( $10^\circ$ ) from the AF coupling ( $170^\circ$ ). This is explained by the fact that the central magnetic moment experiences twice the AF exchange coupling from its two first neighboring atoms ( $2 \times 10^\circ$ ). Contrary to the Ni(001) surface on which we found that the non-collinear solution of Mn-trimer is just a local minimum, here, the total energy calculations show that the ground state is non-collinear with an energy difference  $E_{AF} - E_{Ncol} = 544.93 \text{meV/adatom}$  compared to the AF solution.

## 6.7 Tetramers

As experimental data on Cr clusters deposited on *fcc* Fe are available, we considered in our investigation two different tetramer structures for Cr. The two tetramers are: tetramer 1 is the most compact and forms a square (Fig. 6.4), while tetramer 2 has a T-like shape (Fig. 6.6). For Mn we considered only the tetramer 1 which is very probable the most stable tetramer as indicated by the Cr results.

Two collinear configurations were obtained for Cr-tetramer 1: the AF solution were all impurities are coupled antiferromagnetically to the substrate and a Ferri solution were in each dimer of the tetramer the first neighboring impurities are coupled AF to each other. The Ferri state is less stable than the AF as can be seen from the energy difference  $\Delta E_{\text{Ferri-AF}} = 543.8 \text{ meV/adatom}$ . The Ferri configuration is characterized by magnetic moments of  $-2.45 \mu_B$  and  $2.29 \mu_B$  whereas in the AF configuration the atoms carry lower moments ( $1.94 \mu_B$ ). However, the ground state configuration is non-collinear (Fig. 6.4) with an energy difference  $\Delta E_{\text{AF-Ncol}} = 80 \text{ meV/adatom}$ . This solution is characterized by a large magnetic moment of  $2.5 \mu_B$  carried by each impurity. One notices that the first neighboring adatoms are almost AF coupled to each other (the azimuthal angle  $\phi$  is either equal to  $0^\circ$  or to  $180^\circ$ ) with all moments rotated by the angle  $\theta = 111^\circ$ .

Contrary to Cr, Mn-tetramer 1 has a collinear Ferri magnetic ground state. In fact the total energy of the converged non-collinear magnetic solution is  $2.3 \text{ meV/adatom}$  higher than the Ferri configuration. This value is, as we notice, very small and can be altered by temperature or relaxation. However the proximity of these two solutions show that in reality one can find coexistence of both non-collinear and Ferri solutions for bigger cluster. The Ferri solution is characterized by magnetic moments of  $3.51 \mu_B$  and  $3.39 \mu_B$  while in the non-collinear configuration the atoms carry equal moments ( $3.44 \mu_B$ ). As for Cr-tetramer 1, the first neighboring adatoms are almost AF coupled to each other with moments rotated

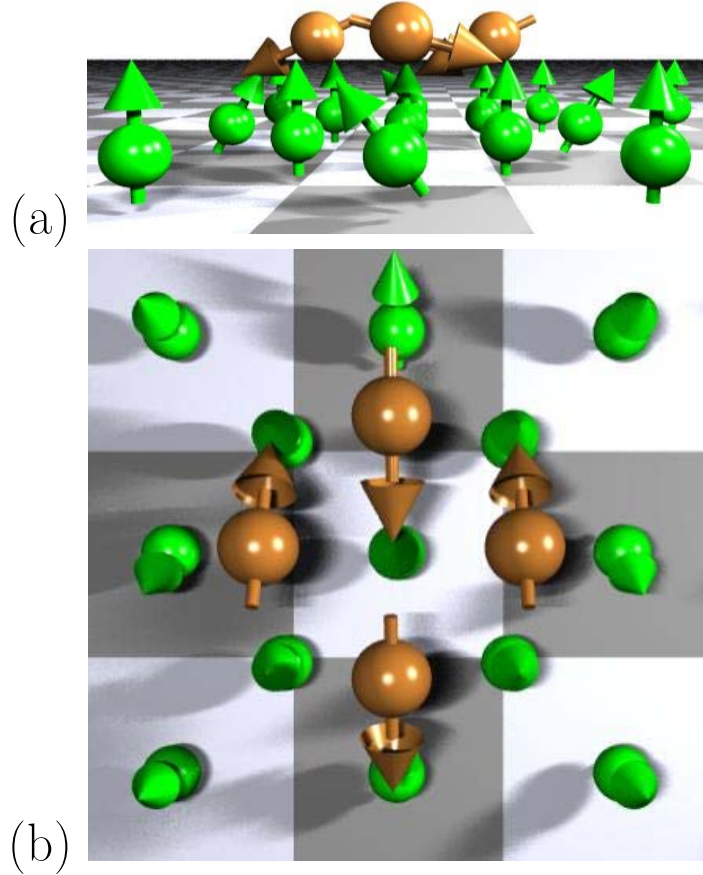


**FIG. 6.4** –. *Non-collinear state of the Cr tetramer on  $\text{Fe}_{3\text{ML}}/\text{Cu}(001)$  surface. Side view (a) and top view (b) are shown.*

by an angle  $\theta = 84^\circ$  (Fig. 6.5).

For Cr-tetramer 2 (see Fig. 6.6) we obtained several collinear magnetic configurations. The most favorable is characterized by an AF coupling of the three corner atoms to the substrate. The fourth Cr adatom surrounded by the remaining Cr impurities is then forced to couple FM to the substrate. When we allow for the direction of the magnetic moment to relax, we get a non-collinear solution having a similar picture, energetically close to the collinear one ( $\Delta E_{\text{Ncol-col}} = 2.3 \text{ meV/adatom}$ ). The Cr adatom which was previously coupled FM to the substrate has now a moment a bit tilted by  $13^\circ$  ( $\mu = 2.31 \mu_B$ ) whereas

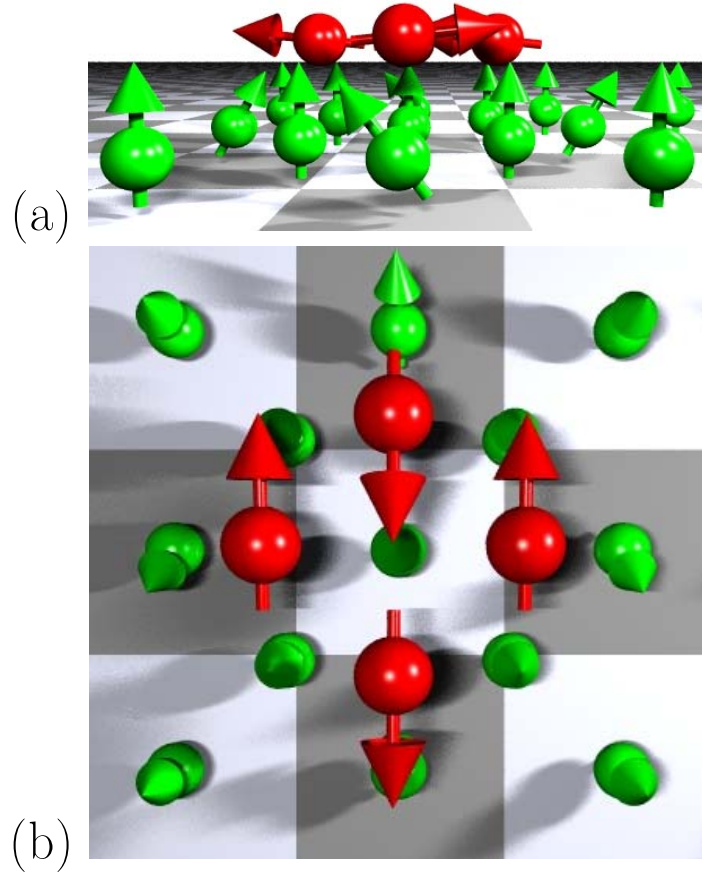


**FIG. 6.5** —. *Non-collinear ground state of the Mn tetramer on  $Fe_{3ML}/Cu(001)$  surface. Side view (a) and top view (b) are shown.*

the adatom sitting at the right angle corner of the tetramer has a moment tilted in the opposite direction by  $172^\circ$  ( $\mu = 2.85 \mu_B$ ). The remaining adatoms have a moment with an angle of  $176^\circ$  ( $\mu = 2.87 \mu_B$ ).

We note that tetramer 1 having the highest number of first neighboring adatom bonds (four instead of three for tetramer 2) is the most stable one ( $\Delta E_{tet2-tet1} = 14.5 \text{ meV/adatom}$ ) with the non-collinear solution shown in fig. 6.4.

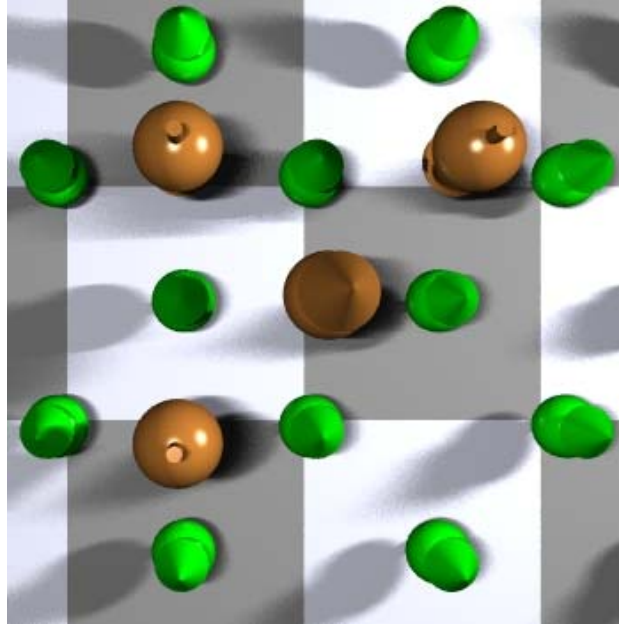


**FIG. 6.6** —. Top view of non-collinear state of the T-shape Cr tetramer (tetramer 2) on  $Fe_{3ML}/Cu(001)$  surface.

## 6.8 Cr-pentamer

To study Cr-pentamer, we have chosen a structural configuration (Fig. 6.7) with the highest number of first neighboring adatom bonds (five). This pentamer consists on a tetramer of type 1 plus an adatom and is characterized by a non-collinear solution. We could not find any collinear magnetic solution within self-consistency due to the high degree of frustration in this system. Let us understand the solution obtained in this case: The tetramer 1 is characterized by a non-collinear almost in-plane magnetic configuration (see Fig. 6.4). As we have seen previously a single adatom is strongly AF coupled to the substrate. However when one moves it closer to the tetramer it affects in first order the first neighboring impurity by tilting the magnetic moment from  $111^\circ$  to  $46^\circ$  (with a moment of  $2.17 \mu_B$ ). The additional adatom is also affected by this perturbation and experiences a tilting of its moment from  $180^\circ$  to  $164^\circ$  ( $\mu = 2.89 \mu_B$ ). As a second order effect, the second neighboring Cr impurity is also affected and has a moment which rotates from  $111^\circ$  to  $138^\circ$  ( $\mu = 2.44 \mu_B$ ). As we have noticed the AF coupling between first neighboring adatoms is always stable, thus the

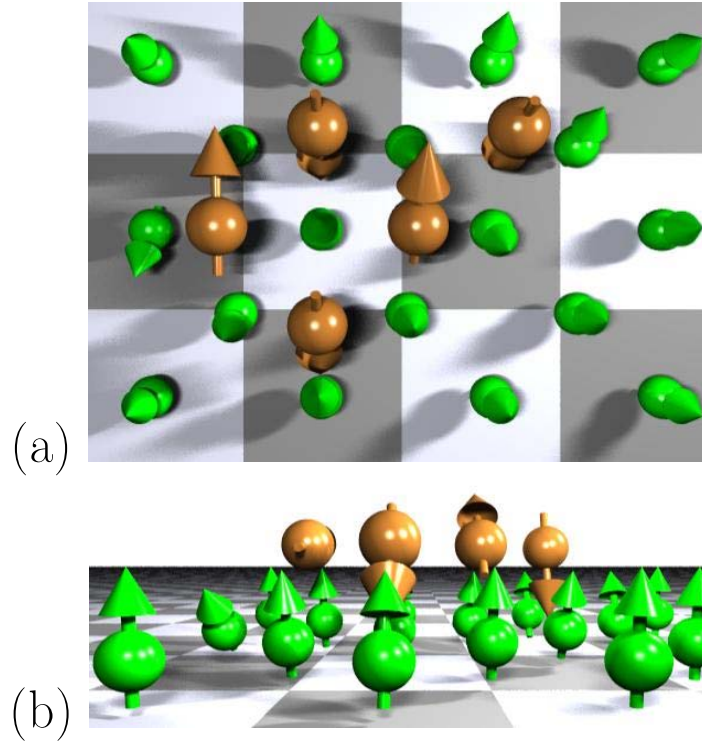


**FIG. 6.7** –. *Non-collinear state of the Cr pentamer on  $Fe_{3ML}/Cu(001)$  surface. Side view (a) and top view (b) are shown.*

third neighboring adatom also has a moment rotated in direction opposite to the magnetization direction of the substrate with an angle of  $155^\circ$  ( $\mu = 2.48 \mu_B$ ). As the last adatom of the pentamer wants to couple AF to its neighboring Cr adatoms, its magnetic moment tilts into the positive direction with an angle of  $85^\circ$  ( $\mu = 2.47 \mu_B$ ).

## 6.9 Comparison with Experiment: Case of Cr

### 6.9.1 Experimental Setup

The magnetic properties of the deposited clusters have been determined experimentally by Reif *et al.*[5] using XMCD. The experiments were performed at the beamline UE56/1- PGM at the BESSY II storage ring in Berlin. The mass selected chromium clusters were generated using a UHV-cluster source [96] and

deposited in-situ onto ultrathin Fe layers epitaxially grown on a Cu(100) surface. Sample preparation included the following steps. The iron multilayers were prepared by evaporating iron from a high purity iron sheet onto the clean copper crystal. Subsequently the iron films were magnetized perpendicular to the surface plane using a small coil. To achieve an easy magnetization axis normal to the surface plane, the iron layer thickness was chosen to be in the range of  $\sim 3$ -5 monolayers (ML). The magnetization of the iron films was monitored by recording Fe 2p XMCD spectra. Before cluster deposition Argon multilayers were frozen onto the iron surface at temperatures below 30K. A layer thickness of 10ML of argon was used to ensure soft landing conditions [97]. After depositing the mass-selected clusters into the argon buffer layers, the remaining argon was desorbed by flash heating the crystal to  $\sim 80$ K. Low temperatures in the range of 30K and low Cr coverages of 3% of a monolayer (ML) were used to prevent cluster-cluster interaction. The measurements have been carried out at a base pressure  $p < 3 \cdot 10^{-10}$  mbar. Spectra have been measured from the cluster samples prepared as described above, in a size range of 1 to 13 atoms per cluster. Every step of the preparation has been checked using x-ray Photoelectron Spectroscopy (XPS) and/or x-ray Absorption Spectroscopy (XAS). The absorption signal has been measured using the Total Electron Yield TEY, i.e. the sample current.

The experimental results for the magnetic moments per d-hole shown in Fig. 6.8 have been determined applying XMCD sum rules [6]. After a standard background treatment, difference and sum spectra are generated by subtraction and addition of the x-ray absorption spectra measured with different photon helicity. For the application of the sum rules, the areas of the  $2p_{3/2}$  and  $2p_{1/2}$  peaks of the difference spectra have been determined. The  $2p_{3/2}$  peak shows positive and negative contributions in the difference spectra. For determining the values of the areas of the  $2p_{3/2}$  absorption in the difference spectra, the integration has been performed over both contributions. Spin (and orbital magnetic moments (not shown)) per d-hole have been calculated for all cluster samples from the areas determined from the spectra. The values for the spin and orbital magnetic moments have been corrected for a degree of circular polarization of 90%. The contribution of the spin magnetic dipole operator  $\langle T_z \rangle^2$  in the values of the spin moments is presently ignored. In other words, the spin values calculated from the values of the spectra are  $\langle S_{eff} \rangle = \langle S_z \rangle + 7/2 \langle T_z \rangle$ , containing the contribution of the spin dipole operator.

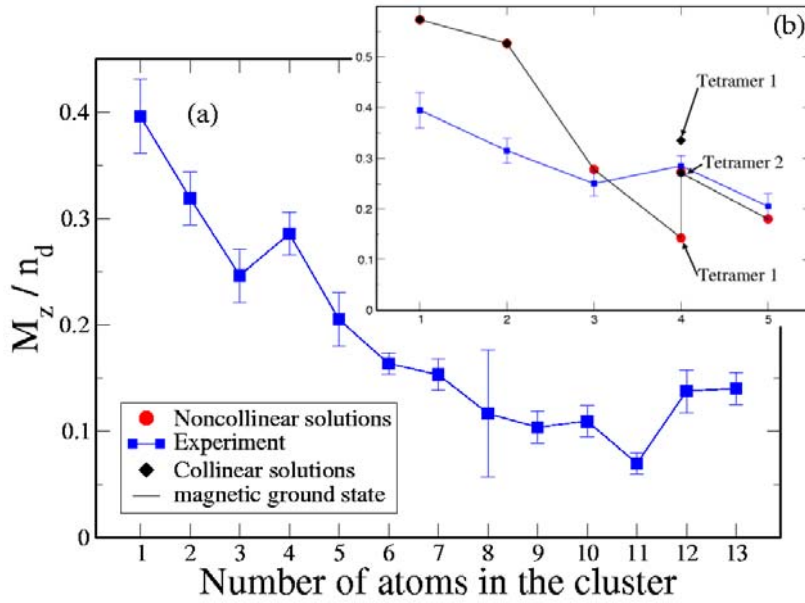
### 6.9.2 Comparison

We note that the XMCD sum rules was applied by the experimentalists without empirical corrections which have been proposed for chromium. This may lead to absolute values for the spin magnetic moments too small by a factor of two

---

2. which can be seen as a measure of the asphericity of the spin magnetization.

**FIG. 6.8** –. Ratio between the moment and number of holes per atom versus cluster size. Fig. (a) shows the experimental results for cluster-sizes up to 13 adatoms while Fig.b gives the comparison with *ab initio* results for cluster-sizes up to 5 adatoms. In Fig. (b) blue squares describe the experimental values, black diamonds show results obtained with collinear configurations, red circles correspond to results obtained with non-collinear configurations and finally a black line connect the ratios obtained in the magnetic ground states.



due to the problems in the application of the simple XMCD sum rules for the early transition metals with smaller spin-orbit splitting. However, this should not affect the relative trends seen in the experimental data (Fig. 6.8.(a)). One notices the strong decrease of  $S_{eff}$  with increasing the cluster size which is probably due to the appearance of antiferromagnetic or non-collinear structures as mentioned earlier in the theory part. In order to understand the peak formed for the tetramer we plot in Fig. 6.8.(b) the ratio between the moment along the  $z$ -direction (defined by the magnetization of the substrate) and number of  $d$  holes per atom (which is shown in Fig. 6.9) obtained by theory. Black circles show the ratio calculated by taking into account the collinear solutions and the red

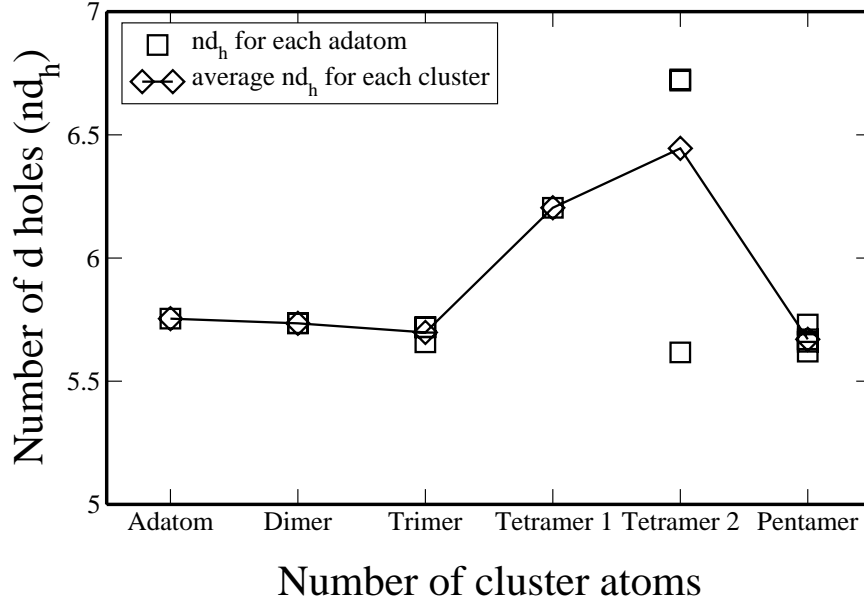


**FIG. 6.9** –. The calculated number of unoccupied  $d$  states ( $nd_h$ ) of Cr in Cr-adclusters on  $Fe_{3ML}/Cu(001)$  surface. the squares represent the bunch of values obtained for each atom of the adcluster while the diamonds connected by a line are the average of number of  $d$  holes per adcluster. One notices that the values of  $nd_h$  are almost constant for the adatom, dimer and trimer while it experiences a jump for the tetramer 1 and tetramer 2 before going back to the adatom value in the case of the pentamer. We add also that these values are really different for the inequivalent atoms of tetramer 2.

ones show the ratio calculated from the non-collinear solutions. The black line connects the ratio obtained in the magnetic ground states. The general trend is in good agreement to the experimental one that there is a decrease of the ratio with increasing the number of Cr atoms in the cluster. The theoretical value clearly lies outside the experimental error but the agreement can still be judged to be fair in view of the remaining uncertainties which can be in our case related to the  $T_z$  moment which was neglected experimentally. Indeed it was already shown by ab-initio DFT calculations for Co-adcluster/Pt(111) that taking into account the spin dipole moment  $T_z$  reduces the effective spin moment measured by XMCD by a factor of 62% [98]. Moreover it was noticed that this contribution almost vanishes for bigger clusters. The non-collinear tetramer 1 has a much lower value than what was seen experimentally whereas the collinear tetramer 1 and

tetramer 2 give a better description of the kink seen experimentally. As regards to the small energy difference ( $\Delta E = 14.5V$  meV) between the two tetramers we considered, we believe that in reality one can easily find an average of solutions with non-collinear tetramers 1, collinear and non-collinear tetramer 2. We believe that this mechanism contributes highly in increasing the tetramer's ratio value higher than the one obtained for a trimer. The pentamer is clearly well described by the theory and fits to the experimental measurements.

## 6.10 Comparison with Experiment: Case of Mn

Unfortunately, in our knowledge, there were no experiments on non-collinear magnetism of Mn-cluster deposited on magnetic or non-magnetic surfaces. Considering, however, that the monolayer of Mn is the upper size limit of a two-dimensional cluster, we can thus compare our results to the experiments done by the group of Carbone using XMCD on one monolayer of Mn deposited on *bcc* Fe surface. Nevertheless, we point out that in *bcc* (001) surface the first neighboring distance in the surface layer is larger than the second neighboring distance for an *fcc* (001) surface layer. Their results which are compared to DFT calculations using a Pseudo-potential method were published [99]. Theoretically it was found that the magnetic ground state is non-collinear consisting in a chessboard arrangement where these moments form angles of  $\approx 80^\circ$  with respect to those of the underlying Fe atoms. It is surprising to find these results coinciding with our results for non-collinear Mn-adcluster with an even number of adatoms *e.g.* non-collinear Mn-dimer and non-collinear Mn-tetramer. We remind the reader that odd number of adatoms (1:adatom, 3:trimer, 5:pentamer) tend to have magnetic moments parallel to the surface magnetization whereas for even number of adatoms (2:dimer, 4:tetramer) the moments are almost perpendicular to the surface magnetization. It seems that when going to bigger two-dimensional Mn-adclusters up to monolayer limit, the effects which are driven by the parity of number of adatoms (even or odd) is averaged out and lead to a perpendicular magnetization. Experimentally the moments were evaluated to be larger than  $3.5 \mu_B$ , and the orientation is suggested to be perpendicular to the magnetization of Fe. This behavior is attested by recent *ab-initio* results of Hafner and Spisak [100] using the projected augmented-wave method. For one monolayer of *bcc* Mn/Fe(001), the non-collinear solution energy is found to be lower by 75 meV/Mn atom compared to the most stable collinear in-plane AF. The calculated angles  $82^\circ$  are similar to our results.

## 6.11 Summary

As for Ni(001) surface, we carried out an investigation on complex magnetism of  $3d$ -adclusters deposited on a ferromagnetic  $\text{Fe}_{3\text{ML}}/\text{Cu}(001)$ . The latter substrate was chosen since its structure (*fcc*) is similar to Ni(001) with, however, stronger surface magnetic moments and since this substrate was chosen by the experimental group of Wurth for the deposition of Cr-adclusters.

The single adatoms are behaving similar as on Ni(001) surface, *i.e.* V is AF, Cr is also AF and Fe is FM while Mn is AF with a magnetic coupling strength much higher than on Ni(001). The dimers are behaving like the single adatoms when constraining the magnetic coupling to be collinear. Releasing this constraint leads to non-collinear magnetism occurs only for the Mn-dimer for which the two moments are AF coupled to each other and are almost in-plane (perpendicular to the surface magnetization) ( $\theta=115^\circ$ ). While collinear magnetism was expected for V and Fe, it was, however, surprising to find a collinear magnetic configuration as a ground state for Cr. We explain this last result by a Heisenberg model in which the strong Fe-Cr coupling constant does not allow a non-collinear solution.

V-trimer is characterized by the  $\uparrow\downarrow\uparrow$  configuration and Fe-trimer prefers to be FM. Cr- and Mn-trimer have a non-collinear ground state in which the magnetic moments reach “normal” values in contrast to the strongly reduced values obtained in constrained collinear magnetic calculations.

Two kind of Cr-tetramers were considered in our work, a square (tetramer 1) and a T-shape tetramer (tetramer2). The first one is the most stable one with a rather small energy difference (14.5 meV/adatom) and is characterized by a non-collinear (almost in-plane) magnetic ground state. On the other hand the Mn-tetramer 1 shows a Ferri collinear magnetic ground state with a tiny energy difference with the non-collinear solution (2.3 meV/adatom) while the non-collinear solution is defined by a rotation angle of  $84^\circ$  *i.e.* in the opposite direction to what we found for the dimer. This means that by increasing the number of Mn-adatoms FM coupling with the substrate is preferred.

As explained in the text, the availability of experimental data from the group of Wurth for comparison motivated us to increase the size of Cr-adclusters. Thus Cr-pentamer has been found highly frustrated. Considering possible problems in the experimental analysis, the complexity of the different clusters and their non-collinear spin structures the agreement between theory and experiment is gratifying. For an improved comparison, detailed STM observations with spin-polarization analysis would be highly desirable. We can, however, add that in the light of our findings, the kink observed in the experimental curve concerning the tetramer is due to the presence of different structural and magnetic configurations. The average of the magnetic moments is then higher compared to the non-collinear magnetic ground state we found for Cr-tetramer 1. Concerning Mn, we could show that our results for even number of adatoms in the cluster are in total agreement with the results published by Grazioli *et al.* [99] *i.e.* the mag-

---

netic moments are AF to each other and are almost perpendicular to the surface magnetization ( $\theta = 80^\circ$ ). It seems that for bigger even number of adatoms in the clusters, Mn tend to couple FM to the substrate as found for Ni(001) surface.



# Chapter 7

## Cr and Mn Clusters on Ni(111)

### 7.1 Introduction

As a continuation of the work presented in the previous chapters, we concentrate here on another orientation of the *fcc* surface. Namely the (111) direction in which the surface geometry is triangular which means in terms of magnetic coupling, that having a compact trimer with antiferromagnetic interactions sitting on the surface leads necessarily to magnetic frustration. In fact, similar investigations have been carried out for a full monolayer of Cr and Mn on Cu(111) [101, 102]. Kurz *et al.* [101] applied the full-potential augmented plane waves method (FLAPW) to determine the ground state for Mn and Cr on Cu(111). It was found by the same authors that, in the case of Mn, the magnetic ground state consists of a multiple spin-density wave of three row-wise antiferromagnetic spin-states which leads to a three-dimensional non-collinear spin structure on a two dimensional triangular lattice. This structure comes about due to higher order spin-interactions *i.e.* to magnetic interactions beyond the nearest neighbors. On the other hand Cr is found to be stabilized in a coplanar non-collinear periodic  $120^\circ$  Neel structure. Using the tight-binding linear muffin tin method (TB-LMTO), Spisak and Hafner [102] found a different result concerning Mn/Cu(111) which prefers than a similar magnetic structure than Cr/Cu(111).

Experimentally, Cr-trimers have been deposited on Au(111) [10]. It was stated that changing the shape of the trimer from equilateral to isosceles by moving two adatoms leads to a loss of the  $120^\circ$  noncollinearity. This has been confirmed using the Anderson model [103]. In other words, the group of Crommie [10] showed that moving a Cr adatom of a compact trimer leads to a switching from the Kondo state to a magnetic one. This may lead to reach an important goal for a magnet's storage capability: the bit 0 can be considered when no (or very small) magnetic moment is measured while a high magnetic moment of the cluster can be considered as 1. Very recently, calculations [104] on compact (equilateral) Cr-trimer were carried out using a pseudo-potential method and confirmed the

non-collinear solution with an angle of  $120^\circ$ .

Magnetic excitations may degrade the performance of high-density memories. Indeed, using scanning tunneling microscopy (STM) Heinrich *et al.* [17] could elucidate the spin-flip of individual magnetic atoms that are dispersed on a non-magnetic matrix. Therefore, we will also discuss the energetic stability of the high-moment collinear and low-moment, non-collinear states.

Larger clusters on Cu(111) were considered by Bergman *et al.* [105] using a real-space TB-LMTO recently developed to treat non-collinear magnetism. They also found, the same expected result for the compact trimers.

In summary, for such noble metal (111) substrates, the frustration is present in the plane containing the Cr (or Mn) contrary to what is observed on Ni(001). The already studied Cu(111)-substrate is of-course non-magnetic, but replacing it by a magnetic surface like Ni would provide an additional magnetic coupling which affects the magnetic state of the adclusters. Hence, in such a system we face an interplay between a non-collinear coupling tendencies arising from the interaction among the adatoms in the cluster and the substrate atoms. This is very different to the Ni(001) surface where the frustration and non-collinear state arises from the competition between the coupling in the cluster and with the substrate. In the following, we present calculations on Cr and Mn small clusters (up to tetramers) with different shapes (see Fig. 7.1) deposited on Ni(111) surface.

## 7.2 Computational Details

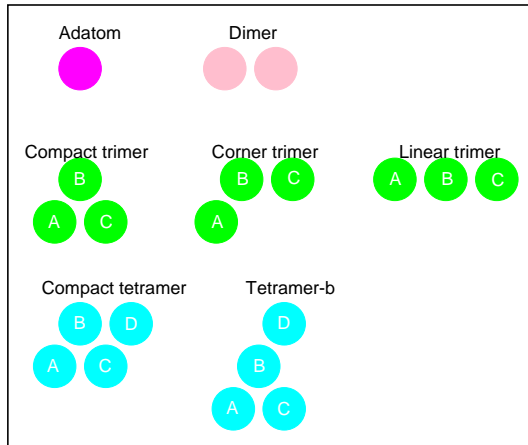


**FIG. 7.1** – *Different geometrical configurations considered for adclusters at the surface of Ni(111). For the dimer we considered the first neighboring adatoms while for the trimer we considered three geometrical configurations: compact, corner, and linear. Two tetramers were considered: the compact and the one we name tetramer-b.*

Our calculations are based as usually on the Local Spin Density Approximation (LSDA) of density functional theory with the parametrization of Vosko *et al.* [35]. The full nonspherical potential was used, taking into account the correct

description of the Wigner–Seitz atomic cells. [81] Angular momenta up to  $l_{\max} = 3$  were included in the expansion of the Green functions and up to  $2l_{\max} = 6$  in the charge density expansion. Relativistic effects were described in the scalar relativistic approximation.

First, the surface Green functions are determined by the screened KKR method for the (111) surface of Ni which serves as the reference system. The LSDA equilibrium lattice parameter of Ni was used (6.46 a.u.  $\approx 3.42 \text{ \AA}$ ). To describe the adatoms on the surface we consider a cluster of perturbed potentials which includes the potentials of the impurities and the perturbed potentials of several neighboring shells, with a size of 48 perturbed sites for all kind of adclusters considered (see Fig. 7.1). We consider the adatoms at the unrelaxed hollow position in the first vacuum layer.

### 7.3 Surface of Ni(111)

Layer of the slab	Magnetic moments (in $\mu_B$ )
(S) Surface layer	0.64
(S-1)	0.64
(S-2)	0.61
(S-3)	0.60
(S-4)	0.59
C	0.60

**TAB. 7.1** –. *Magnetic moments in  $\mu_B$  for a slab of 12 Ni layers in the (111) direction. (S-*i*) labels the position of the layer with respect to the top-layer of the slab (S) while with C we note the center of the slab.*

The moments ( $0.63 \mu_B$ ) at the surface of Ni(111) are lower than on the surface of Ni(001) because the atoms of the (111) surface have more neighbors than the atoms of the (001) surface. This means more hybridization of the  $d$  wavefunctions and thus a decrease of the magnetic moments. The magnetic moments are shown in Tab. 7.1.

### 7.4 Single Adatoms

Our calculations show that the single Cr adatom is AF coupled to the surface with an increase of the magnetic moments ( $M_{\text{AF}} = 3.77 \mu_B$  and  $M_{\text{FM}} = 3.70 \mu_B$ ) compared to the results obtained for Ni(001) ( $M_{\text{AF}} = 3.48 \mu_B$  and  $M_{\text{FM}} = 3.35 \mu_B$ ). This increase arises from the weaker hybridization of the  $3d$  wavefunctions with the substrate—the adatom has three neighbours on the (111) surface and

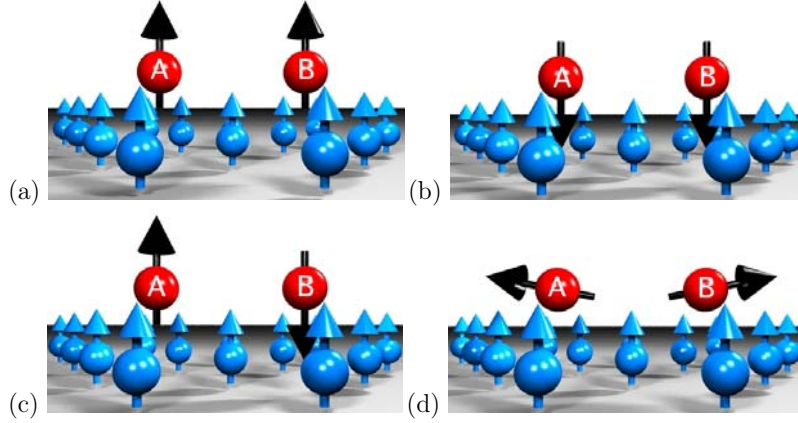


**FIG. 7.2** –. *Different magnetic configurations of Mn Dimer on Ni(111). The Mn atoms are labeled by A and B; unlabeled atoms correspond to the Ni substrate. The configurations correspond to FM in (a), AF in (b), Ferrimagnetic in (c) which is the ground state, and the non-collinear additional local minimum in (d). See text for the discussion.*

four on the (001). The calculated energy difference between the FM and AF configurations is high so that the AF configuration is stable at room temperature ( $\Delta E_{\text{AF-FM}} = -93.54$  meV, corresponding to 1085 K). Also our results for the Mn adatom on Ni(111) are similar to what we found on Ni(001). The single Mn adatom prefers to couple ferromagnetically to the substrate. The energy difference between the two possible magnetic configurations is  $\Delta E_{\text{AF-FM}} = 208$  meV. For the (001) surfaces the energy differences are both for Cr and Mn larger, since they roughly scale with the coordination number ( $\Delta E_{\text{AF-FM}}^{\text{Cr}} = -134$  meV,  $\Delta E_{\text{AF-FM}}^{\text{Mn}} = 252$  meV). The magnetic moments of Mn are high and reach a value of  $4.17 \mu_B$  for the FM configuration and  $4.25 \mu_B$  for the AF configuration. The moments are higher than for the Mn adatoms on Ni(001) ( $M_{\text{AF}} = 4.09 \mu_B$  and  $M_{\text{FM}} = 3.92 \mu_B$ ), again due to the lower coordination and hybridization of the  $3d$  levels. This type of coupling to the substrate (AF for Cr and FM for Mn) can be understood in terms of the  $d$ - $d$  hybridization of the adatom wavefunctions with the ones of the substrate.

## 7.5 Adatom dimers

For the compact dimers, three collinear configurations are possible: ferromagnetic (FM) (see Fig. 7.2(a)), with the moments of both atoms parallel to the substrate moments, antiferromagnetic (AF) (Fig. 7.2(b)), with the moments of

both atoms antiparallel to the substrate moments, and ferrimagnetic (Ferri) (see Fig. 7.2(c)), where the magnetic moment of one of the dimer atoms is parallel to the moments of the substrate, while the other one is antiparallel. Since the direct exchange in a Cr pair (or a Mn pair) is antiferromagnetic (for an explanation in terms of the Alexander-Anderson model [88] see Chapter 5), and stronger than the adatom-substrate interaction, the Ferri solution is expected to prevail. Indeed, Cr dimers on Ni(111) as on Ni(001) are characterized by a collinear Ferri coupling as a ground state. The difference is, however, that no non-collinear solution was found on Ni(111), as opposed to Ni(001) (Chapter 5). This is understandable, because the non-collinear state in the dimer on Ni(001) arises from the competition between the intra-dimer Cr-Cr antiferromagnetic interaction and the Cr-Ni antiferromagnetic interaction. On the Ni(111) surface, the coordination to the Ni substrate is lower, therefore the interaction with the substrate is insufficient to overcome the Cr-Cr interaction. In fact the Ferri total energy is 317.32 meV/adatom lower than the AF one and 352.54 meV/adatom lower than the FM one.

Similar trends are found for the Mn dimers on Ni(111): The Ferri solution is the most stable collinear solution. However, in addition a non-collinear solution is found, which is only slightly higher, *i.e.* by 4.44 meV/adatom than the Ferri solution. Note that on the Ni(001) surface, this type of dimer state, shown in Fig. 7.2(d), represents the ground state, which is, however, not the case for the dimer on (111) preferring the Ferri configuration. In the non-collinear configu-

		Cr <sub>2</sub>	Mn <sub>2</sub>
AF	moments	(-3.47, -3.47)	(-4.02, -4.02)
Ferri	moments	(-3.30, 3.31)	(-3.97, 3.85)
FM	moments	(3.38, 3.38)	(3.98, 3.98)

**TAB. 7.2** –. Atomic spin moments (in  $\mu_B$ ) of the adatom dimers on Ni(111) in the collinear configurations. A minus sign of the collinear moments indicates an antiparallel orientation with respect to the substrate magnetization.

ration (Fig. 7.2(d)), both adatom moments ( $3.90 \mu_B$ ), while aligned antiferromagnetically with respect to each other, are slightly tilted in the direction of the substrate magnetization with a rotation angle of  $\theta = 79^\circ$  (instead of  $90^\circ$ ). The energy differences between the Ferri and the other local minima AF and FM are respectively 243.2 meV/adatom and 76.31 meV/adatom. The magnetic moments and energy differences are given in Tables 7.2 and 7.3. Note that the local Cr and Mn moments are considerably higher than the corresponding local moments in dimers on Ni(001)5, again a result of the reduced coordination number.

As we have discussed in the previous chapter, the different magnetic configurations of the Ni substrate atoms cannot be described well by the Heisenberg model, since the moments of the atoms adjacent to the adatoms are strongly re-

Dimer type:	Cr <sub>2</sub>	Cr <sub>2</sub>	Mn <sub>2</sub>	Mn <sub>2</sub>
Substrate:	Ni(111)	Ni(001)	Ni(111)	Ni(001)
$E_{\text{FM-Ferri}}$	353	451	76	65
$E_{\text{AF-Ferri}}$	317	433	243	496

**TAB. 7.3** –. *Dimer energies (in meV/adatom) in the FM, AF, and Ferri configurations of Cr and Mn dimers on Ni(111). Results of the same dimers on Ni(001) are also shown for comparison.*

duced. Such longitudinal moment relaxations cannot be described by this model.

## 7.6 Trimers

Trimers in equilateral triangle geometry are, in the presence of antiferromagnetic interactions, prototypes for non-collinear magnetism, with the magnetic moments of the three atoms having an angle of  $120^\circ$  to each other [106, 105]. This  $120^\circ$ -configuration is a well-known consequence of the magnetic frustration in such triangular systems. In our case, the  $120^\circ$  state is perturbed by the exchange interaction with the substrate, and therefore the magnetic configuration is expected to be more complicated.

Let us start with a Cr dimer (Mn dimer) that we approach by a single Cr adatom (Mn adatom). As shown in Fig. 7.1, three different types of trimers can be formed: i) the compact trimer with an equilateral shape, ii) the corner trimer with an isosceles shape and iii) the linear trimer. The adatoms are named A, B and C.

When the distance between the ad-dimer and the single adatom is large enough that their magnetic interaction is weak (second-neighboring positions), the total moment is  $-3.78 \mu_B$  for the Cr case and  $4.05 \mu_B$  for the Mn one.

Let us move the single adatom close to the dimer and form a compact trimer. The distance between the three adatoms is the same, meaning that this is a prototype geometry which leads for a trimer in free space to a  $120^\circ$  rotation angle between the magnetic moments. This is attested for the Cr case for which we had difficulties finding a collinear solution. Our striking result, as depicted in Fig. 7.3a-b, is that the non-collinear  $120^\circ$  configuration is conserved with a slight modification. Indeed, our self-consistent  $(\theta, \phi)$ -angles are  $(2^\circ, 0^\circ)$  for adatom B and  $(126^\circ, 0^\circ)$  for adatom A and  $(122^\circ, 180^\circ)$  for adatom C. The angle between B and A is equal to the angle between B and C ( $124^\circ$ ) while the angle between A and C is  $112^\circ$ . The small variation from the prototypical  $120^\circ$  configuration is due to the additional exchange interaction with Ni atoms of the surface. Let us suppose that we start with a  $120^\circ$  configuration of a compact Cr trimer, neglecting at first the exchange interaction with the substrate. This gives an infinite number

of degenerate configurations being distinguished by an arbitrary rotation of all moments in spin space. This degeneracy is (partly) removed by coupling to the substrate atoms, the moments of which are fixed by anisotropy, *e.g.* in [111] direction. Since the adatom-substrate interaction is AF, the moments of two adatoms rotate so that they are partly oriented opposite to the substrate magnetization, while the moment of the third adatom rotates to the opposite direction, driven by the AF interaction to its Cr neighbors. The coupling with the substrate leads thus to a deviation from the prototype  $120^\circ$  state, with an additional rotation of  $2^\circ$  for the FM adatom and of  $4^\circ$  for the two other adatoms. The Cr B-atom carries a moment of  $2.94 \mu_B$ , smaller than the neighboring moments ( $3.31 \mu_B$ ). Hence, the total magnetic moment of all the adatoms is  $-0.76 \mu_B$ . Note the huge jump of the total magnetic moment (80%) from  $-3.78 \mu_B$ , which is the initial non-interacting dimer-adatom total moment.

For the compact Mn trimer, three non-collinear configurations were obtained: As in the case of the compact Cr trimer, the free Mn trimer must be in a  $120^\circ$  configuration. Nevertheless, the magnetism of the substrate changes this coupling taking into account the single adatom behavior: Mn adatoms prefer a FM coupling to the substrate and an AF coupling with their neighboring Mn adatom.

The first non-collinear magnetic configuration (NCOL1) is similar to the Cr one (Fig. 7.3a-b), *i.e.* adatom B couples FM ( $3.61 \mu_B$ ) with the substrate moments while adatom A ( $3.67 \mu_B$ ) and C ( $3.67 \mu_B$ ) are rotated into the opposite direction with an angle of  $114^\circ$  between B and A and between B and C (see Table 7.4).

The second non-collinear configuration (NCOL2) has the opposite magnetic picture (Fig. 7.3c-d) as compared to compact Cr trimer. Atoms A and C tend to couple FM to the substrate, with a tilting of  $\theta = 49^\circ$ ,  $\phi = 0^\circ$  for atom A and  $\theta = 51^\circ$ ,  $\phi = 180^\circ$  for atom C; each of them carries a moment of  $3.62 \mu_B$ . The AF interaction of atom B with A and C forces it to an AF orientation with respect to the substrate, characterized by  $\theta = 179^\circ$ ,  $\phi = 0^\circ$ , and a moment of  $3.70 \mu_B$ . Thus the trimer deviates from the  $120^\circ$ -configuration: the angles between A and B moments and B and C moments are about  $130^\circ$ , and the angle between A and C is about  $100^\circ$ .

In the third magnetic configuration (NCOL3) the three moments ( $3.65 \mu_B$ ) are almost in-plane and perpendicular to the substrate magnetization (see Fig. 7.3e-f). They are also slightly tilted in the direction of the substrate magnetization ( $\theta = 86^\circ$ ) due to the weak FM interaction with the Ni surface atoms. Within this configuration, the  $120^\circ$  angle between the adatoms is kept. Total energy calculations show that the NCOL2 configuration is the ground state which is almost degenerate with NCOL1 and NCOL3 ( $\Delta E_{\text{NCOL1-NCOL2}} = 1.27 \text{ meV/adatom}$  and  $\Delta E_{\text{NCOL3-NCOL2}} = 5.61 \text{ meV/adatom}$ ). Thus already at low temperatures trimers might be found in all three configurations; in fact the spin arrangement might fluctuate between these three  $120^\circ$  configurations or at even lower temperatures between the three degenerate configurations of the NCOL1 or the NCOL2 state. Compared to the collinear state energy of the compact trimer, the NCOL2 en-

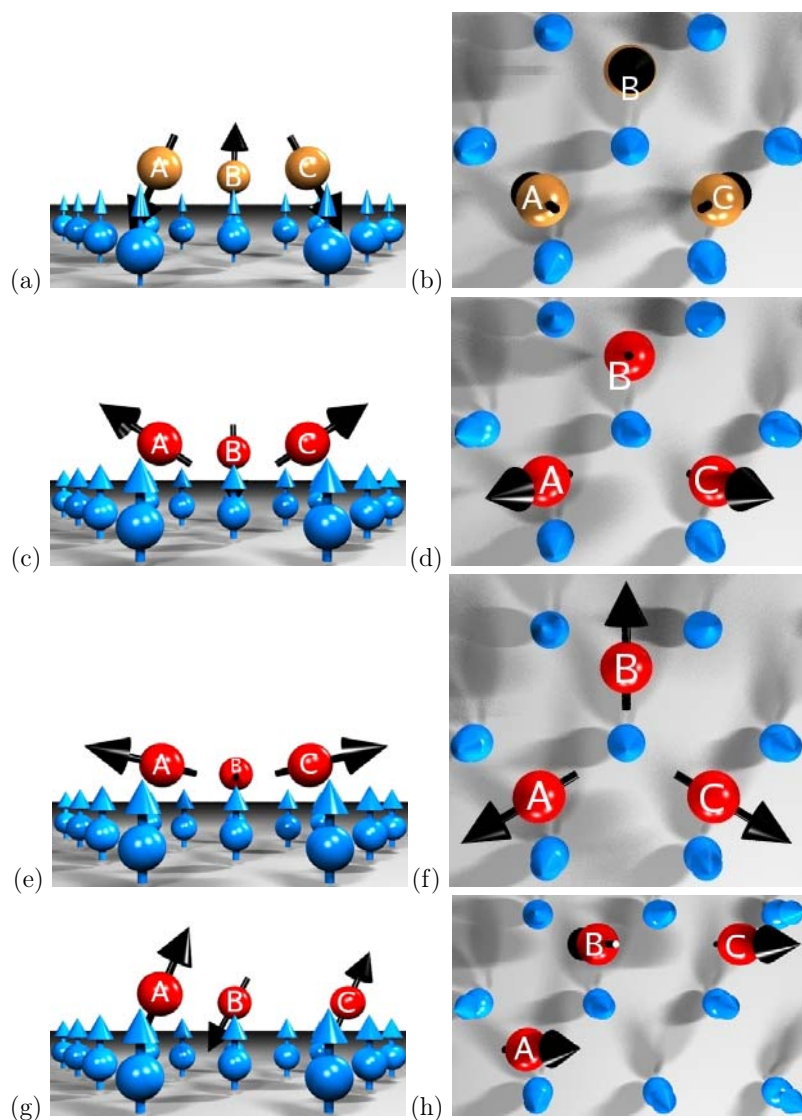


**FIG. 7.3** —. Side view (a) and top view (b) are shown for the most stable configuration of Cr compact trimer on Ni(111) (in blue). (c) and (d) represent the side view and top view of the ground state (NCOL2) of Mn compact trimer on Ni(111) while (e) and (f) depict an almost degenerate state (NCOL3) of the same Mn trimer. Finally, the side view (g) and top view (h) are shown for the most stable configuration of Mn (in red) corner trimer on Ni(111). See text for more details.

**TAB. 7.4** –. *Size and rotation angles of the magnetic moments of Mn adatoms forming a compact trimer on Ni(111) surface. For the adatom notation see Fig. 7.1. All three states are calculated to be local energy minima. The energy difference per adatom with respect to NCOL2 is also shown. The collinear state is energetically 138.23 meV/adatom higher than NCOL2.*

Noncol. config.	Adatom	Moment ( $\mu_B$ )	$\theta$	$\phi$	Energy/adatom (meV)
NCOL1	A	3.67	115°	0	1.27
	B	3.61	1°	0	
	C	3.67	113°	180°	
NCOL2	A	3.62	49°	0	0
	B	3.70	179°	0	
	C	3.62	51°	180°	
NCOL3	A	3.65	86°	240°	5.61
	B	3.65	86°	0	
	C	3.65	86°	120°	

ergy is lower by 138.23 meV/adatom. This very high energy difference is due to frustration, even higher than breaking a bond as shown in the next paragraphs. Contrary to this, the corner trimer shows a collinear ground state because it is not frustrated. For instance, the total moment of the non-collinear compact trimer ( $0.95\mu_B$ ) experiences a decrease of 76% compared to the obtained value for the non-interacting dimer-adatom configuration.

The next step is to move the additional adatom C and increase its distance with respect to A in order to reshape the trimer into an isosceles triangle (what we call “corner trimer” in Fig. 7.1, with one angle of 120° and two of 30°). By doing this, the trimer loses the frustration and is characterized, thus, by a collinear ferrimagnetic ground state: the moments of adatoms A and C are AF oriented to the substrate (following the AF Ni-Cr exchange), while the moment of the central adatom B is FM oriented to the substrate, following the AF Cr-Cr coupling to its two neighbors. The magnetic moments do not change much compared to the compact trimer. The central adatom B carries a moment of  $2.94 \mu_B$  while the two others have a slightly more sizable moment of  $-3.32 \mu_B$ . Thus, the total magnetic moment ( $-3.70 \mu_B$ ) increases to a value close to the one obtained for non-interacting dimer-adatom system.

While the non-collinear state is lost for the corner Cr trimer, it is present for the corner Mn trimer as a local minimum with a tiny energy difference of 4.82 meV/adatom higher than the Ferri ground state. This value is equivalent to a temperature of  $\sim 56$  K, meaning that at room temperature both configurations co-exist. Here Ferri means that the central adatom B is AF oriented to the substrate with a magnetic moment of  $3.71 \mu_B$ , forced by its two FM companions A and C (moment of  $3.83 \mu_B$ ) which have only one first neighboring adatom and

are less constrained. The total moment of the adcluster is also high ( $3.95\mu_B$ ) compared to the compact trimer value, reaching the value of the non-interacting system (with the third atom of the trimer far away from the other two).

The Ferri solution is just an extrapolation of the non-collinear solution shown in Fig. 7.3g-h (with magnetic moments similar to the collinear ones) in which the central adatom B ( $3.70\mu_B$ ) tends to orient its moment also AF to the substrate ( $\theta = 152^\circ$ ,  $\phi = 0^\circ$ ) and the two other adatoms with moments of  $3.83\mu_B$  tend to couple FM to the surface magnetization with the same angles ( $\theta = 23^\circ$ ,  $\phi = 180^\circ$ ). It is important to point out that the AF coupling between these two latter adatoms is lost by increasing the distance between them. Indeed, one sees in Fig. 7.3g-h that the two moments are parallel. The total magnetic moment is also high and is equal to  $3.78\mu_B$ .

Let us move furthermore adatom C in order to form a linear trimer. For the Cr case, there is no non-collinear magnetism. The already stable Ferri solution for the corner trimer is comforted. The moments of the adatoms A and C are a bit higher than what obtained so far for the other structural configuration, *i.e.*, adatoms A and C have a moment of  $-3.40\mu_B$  while the central moment is equal to  $2.97\mu_B$ : the coupling between A and C is now indirect (through the central adatom). The total magnetic moment is also high ( $-3.83\mu_B$ ).

Concerning the Mn case for a linear trimer, a non-collinear configuration was obtained as a local minimum with a small energy difference compared to the ground state which is the collinear Ferri solution ( $8.50\text{ meV/adatom} \sim 99\text{ K}$ ). The magnetic moments do not change a lot compared to the values obtained for the corner trimer. The central adatom B carries a moment of  $-3.78\mu_B$  while the A and C have a higher moment of  $3.84\mu_B$ . In the non-collinear solution, the central Mn adatom with a moment of  $3.76\mu_B$ , as seen previously, tends to couple AF with ( $\theta = 142^\circ$ ,  $\phi = 0^\circ$ ) and the A and C with a similar moment of  $3.85\mu_B$  tend to couple FM to the substrate ( $\theta = 28^\circ$ ,  $\phi = 180^\circ$ ). The total moment is high for both magnetic configurations. For the Ferri solution, it reaches  $3.90\mu_B$ , while for the non-collinear solution the total moment value is smaller ( $3.84\mu_B$ ).

It is interesting to compare the total energies of the three trimers we investigated. The compact trimer has more first neighboring bonds and is expected to be the most stable trimer. The energy differences confirm this statement. Indeed the total energy of the Cr compact trimer is  $119\text{ meV/adatom}$  lower than the total energy of the corner trimer and  $198.16\text{ meV/adatom}$  lower than the total energy of the linear trimer. Similarly, the Mn compact trimer has a lower energy of  $53\text{ meV/adatom}$  compared to the corner trimer and a lower energy of  $100\text{ meV/adatom}$  than the linear trimer.

Summarizing the results for the total moments of the adatoms, we see that the non-interacting cluster consisting of a single adatom and an adatom dimer has a high moment. This large total moment also survives for linear and corner trimers. However the most stable compact trimer has a low moment,  $0.95\mu_B$  in the case of Mn and  $-0.76\mu_B$  for Cr.

## 7.7 Tetramers

We consider two types of tetramers, formed by adding a Cr or Mn adatom (atom D in Fig. 7.1) to the compact trimer. We begin with the compact tetramer (see Fig. 7.1 and Fig. 7.4a-b). For both elements Cr and Mn, the Ferri solution is the ground state (Fig. 7.4a). For Cr (Mn) compact tetramer, the A and D adatoms are FM oriented to the surface atoms with a moment of  $2.31 \mu_B$  ( $3.60 \mu_B$ ) while B and C are AF oriented to the substrate with a moment of  $2.87 \mu_B$  ( $3.43 \mu_B$ ). This gives a magnetic configuration with a low total magnetic moments of  $-1.12 \mu_B$  for the Cr tetramer and  $0.34 \mu_B$  for Mn tetramer. The Cr tetramer, in particular, shows also a non-collinear configuration (Fig. 7.4b) as a local minimum which has, however, a slightly higher energy of  $\Delta E_{\text{NCOL-Ferri}} = 1$  meV/adatom. Within this configuration the AF coupling between the adatoms is observed. However, the four moments are almost in-plane perpendicular to the substrate magnetization. The tilting is small ( $\theta = 93^\circ$ ) due to the weak AF coupling with the substrate.

An additional manipulation consists in moving the adatom D and forming a tetramer-b (Fig. 7.4c). For such a structure, the collinear solution for the Cr tetramer is only a local minimum. In this structure, atom D has less neighboring adatoms compared to A, B, and C. In the non-collinear solution which is the magnetic ground state, the moment of adatom D ( $3.34 \mu_B$ ) is almost AF oriented to the substrate ( $\theta = 178^\circ$ ,  $\phi = 0^\circ$ ). The remaining adatoms form a compact trimer in which the closest adatom to D, *i.e.* B, tends to orient its moment FM ( $2.45 \mu_B$ ) to the substrate ( $\theta = 19^\circ$ ,  $\phi = 0^\circ$ ) while the moments of A ( $2.90 \mu_B$ ) and C ( $2.80 \mu_B$ ) tend to be oriented AF ( $\theta_A = 124^\circ$ ,  $\phi_A = 0^\circ$ ) and ( $\theta_C = 107^\circ$ ,  $\phi_C = 180^\circ$ ). In the (metastable) collinear solution for this tetramer, the moment of adatom B is oriented FM to the substrate while the moments of all remaining adatoms are oriented AF to the surface atoms. Here, the total magnetic moment has a high value of  $-3.46 \mu_B$ . The total energy difference between the two configurations is equal to 49.32 meV/adatom. Compared to the total energy of the compact tetramer, our calculations indicate that the tetramer-b has a higher energy (108.72 meV/adatom).

Let us now turn to the case of the Mn tetramer-b. Also here, the non-collinear solution is the ground state while the collinear one is a local minimum. The energy difference between the two solutions is very small (2.82 meV/adatom). The moments are now rotated to the opposite direction compared to the Cr case, in order to fulfill the magnetic tendency of the single Mn adatom which is FM to the substrate. The Mn atom with less neighboring adatoms, *i.e.* D, has a moment of  $3.84 \mu_B$  rotated by ( $\theta = 27^\circ$ ,  $\phi = 0^\circ$ ), while its closest neighbor, the atom B with a moment of  $3.44 \mu_B$ , is forced by the neighboring companions to couple AF ( $\theta = 140^\circ$ ,  $\phi = 180^\circ$ ). The adatoms A and C with similar magnetic moments ( $3.63 \mu_B$ ) tend to couple FM with the following angles: ( $\theta = 81^\circ$ ,  $\phi = 0^\circ$ ) and ( $\theta = 34^\circ$ ,  $\phi = 0^\circ$ ). As in the case of Cr tetramer-b, the converged collinear solution

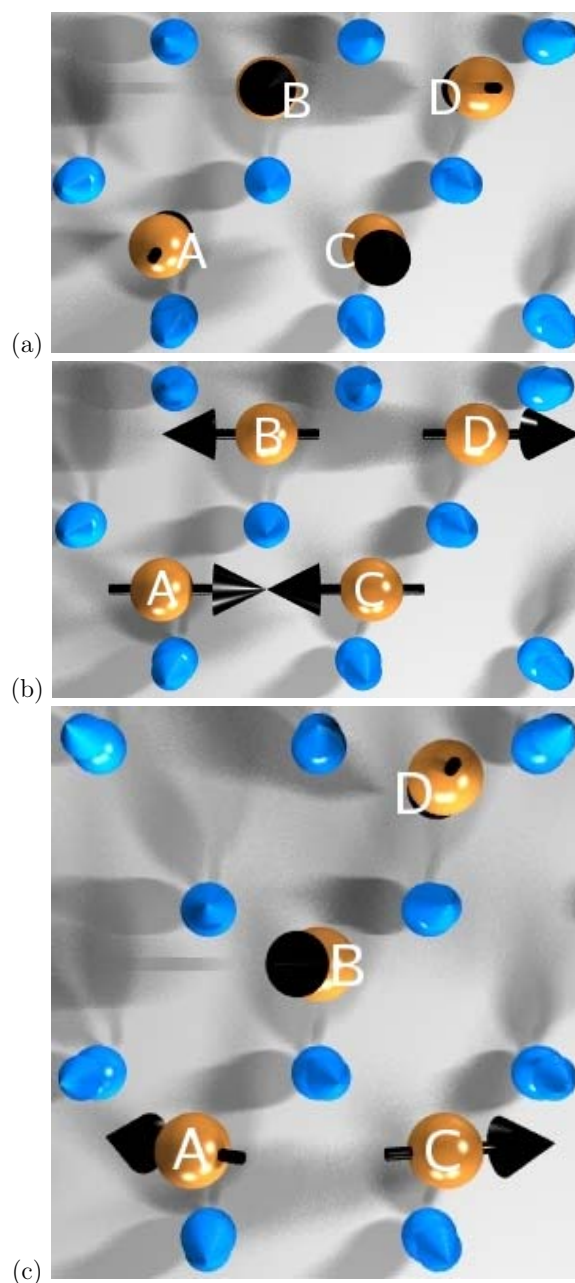


**FIG. 7.4** –. Top view of the collinear most stable solution (a) and the non-collinear metastable configuration (b) of compact Cr tetramer on Ni(111). In (c) is depicted the Cr tetramer-b magnetic ground state on Ni(111), which basically consists of the non-collinear trimer state of Fig. 7.3a coupled antiferromagnetically to the fourth adatom.

is just the extreme extension of the non-collinear one: The “central” adatom of the tetramer is forced by its FM Mn neighboring atoms to coupled AF to the substrate. The magnetic regime is similar to the one of Cr tetramer-b, *i.e.* high, with a total magnetic moment of  $4.37 \mu_B$ .

As expected, the most stable tetramer is the compact one, with an energy of 52.26 meV/adatom lower than tetramer b.

## 7.8 Discussion of Technical Assumptions within our Simulations

We now discuss the limitations of our calculations due to the following approximations: (i) neglect of structural optimization, (ii) neglect of spin-orbit coupling, and (iii) use of the local spin density approximation to density functional theory.

(i) Structural optimization can affect the results on the interatomic exchange interactions and magnetic ground state. In the case of Cr and Mn adatoms on Ni, the structural relaxations and the changes in the magnetic state are expected to be small. In order to test this, we compare the forces and exchange constants for two geometries of a magnetically collinear Mn dimer: the “unshifted”, ideal crystal geometry (with the dimer atoms at the lattice positions, as was done in the rest of this work) and a “shifted” geometry, with the dimer atoms appreciably shifted towards the surface by 10.4% of the Ni(111) interplanar distance (6% of the lattice constant). In both cases, the ferrimagnetic configuration corresponds to the collinear ground state. The forces are found to be different on the two magnetically inequivalent dimer atoms. In the unshifted geometry, the forces have a perpendicular component *toward* the surface,  $F_z = -16.5$  and  $-25$  mRyd/ $a_B$  ( $a_B$  is the Bohr radius), respectively corresponding to the adatom with moment parallel and antiparallel to the surface moment, and a lateral component pushing the dimer atoms apart,  $F_x = 24.4$  mRyd/ $a_B$ . In the shifted geometry, the perpendicular forces are about a factor four stronger,  $F_z = 84.9$  and  $82.4$  mRyd/ $a_B$ , pointing *away* from the surface, while the lateral forces are  $F_x = 30$  mRyd/ $a_B$ , again pushing the dimer atoms apart. We conclude that the dimer must relax toward the surface by about 2% of the interplanar distance, while the atoms will also move slightly away from each other. This is confirmed in calculations for a 2% perpendicular relaxation, giving rise to only very small perpendicular forces ( $F_z = 0.3$  and  $-4.5$  mRyd/ $a_B$  toward the surface). The energy difference,  $\Delta E = E_{\text{Ferri}} - E_{\text{Ferro}}$ , changes from  $\Delta E = -147$  meV in the unshifted geometry to  $\Delta E = -150$  meV in the 2%-shifted geometry and  $\Delta E = -182$  meV in the 10.4%-shifted geometry; *i.e.*, a 2% vertical shift induces only a 2% change in the interatomic exchange energies, while a 10% vertical shift induces a 25% change. The effect of the expected 2% relaxation (including the lateral relaxation) to the equilibrium position should therefore be small. Calculations on the Cr ferrimag-

netic dimer in the unshifted geometry show forces less than 5 mRyd/ $a_B$ , meaning that the structural relaxation of the dimer will be very small.

As a conclusion, our central result, namely that compact structures are in a noncollinear magnetic ground state, while open structures are in a collinear state, does not change by structural relaxations. What can change, however, are the exact angles of the moments in the noncollinear state, as well as the small energy differences between the various non-collinear energy minimum (which were of the order of a few meV).

(ii) Spin-orbit coupling is weak in these nanoclusters, because Cr and Mn atoms have a half-filled d-shell, *i.e.*, filled spin-up shell and unfilled spin-down shell. In the past, calculations [23, 107] on the magnetocrystalline anisotropy energy (MAE) of transition metal adatoms on Ag and Au surfaces (where the spin-orbit coupling is strong) have shown that Cr and Mn adatoms have a MAE of less than 5 meV. On Ni, the effect should be weaker, as on Cu, where the MAE of a single Co adatom was calculated [108] to be less than 1 meV. Much stronger MAE was found, [3] *e.g.*, for Co adatoms on Pt (MAE of the order of 10 meV) or for 5d adatoms on Ag and Au (MAE of the order of 30 meV), caused by the fact that the Fermi level is in the middle of the spin-down 3d shell of Co and by the strong spin-orbit coupling of the 5d adatoms and the Pt, Au, and Ag substrate. Moreover, as shown in Ref. [13], even the relatively strong MAE of 10 meV of the Co adatom on Pt drops rapidly with cluster size. Considering these effects, we believe that spin-orbit coupling cannot significantly affect the magnetic state of Cr and Mn ad-clusters on Ni.

(iii) Local approximations to density functional theory, *i.e.*, the LSDA (which was used here) and the generalized gradient approximation (GGA), are known to fail when electron correlations are strong. In the case of 3d adatoms and ad-clusters, however, hybridization with the substrate reduces the electron correlations so that local density functional theory becomes satisfactory (except in Kondo systems). Concerning the use of LSDA instead of GGA, in the case of the small deposited clusters considered here, the magnetic moments are pronounced and the exchange interactions clear: the interaction to the substrate is weakly ferromagnetic for Mn and antiferromagnetic for Cr, and the first-neighbor, intra-cluster interaction is strongly antiferromagnetic. Therefore, this is not a sensitive case, where the LSDA and GGA would give considerably different results. Small energy differences, of the order of 1 or 2 meV per atom (which are found comparing several non-collinear configurations) can depend on the type of functional used; however, such accuracy is beyond the predictive power of local density-functional theory (LSDA or GGA) for these systems.

## 7.9 Summary

We have investigated the complex magnetism of small Cr and Mn ad-clusters on Ni(111). This is a prototype system where two types of magnetic frustration occur: (i) frustration within the ad-cluster and (ii) frustration arising from antiferromagnetic coupling between the adatoms in the cluster and competing magnetic interaction between the adclusters and the surface atoms.

The triangular geometry of the Ni(111) substrate is a necessary condition for the first type of frustration. In this respect, the situation is fundamentally different from the one of Cr or Mn ad-clusters on Ni(001), where no compact trimers can be formed, and where thus only mechanism (ii) appears (see Chapter 5). The fundamental difference is also evident from the energy gain of the emerging non-collinear state (compared to the collinear state), which is much larger in the case of the Ni(111) substrate.

While the resulting collinear and non-collinear structures are very complex, a unifying feature is that all compact structures (dimers, trimers and tetramers) have very small total moments, as a result of the strong antiferromagnetic coupling between the cluster atoms leading to a non-collinear state with nearly complete compensation of the local moments. In most of these cases, the present local density functional calculations give more than one energy minima, corresponding to different non-collinear states, which are energetically very close (with differences of a few meV/atom). Thus the system can easily fluctuate between these states. However, all of them are characterized by a low total magnetic moment. On the other hand, the more open structures, like the corner and linear trimers and the tetramer b, have rather large total moments of about  $4 \mu_B$ . Since the transition between a compact and an open structure requires to move one adatom by just one atomic step, we might consider this motion as a magnetic switch, which via the local magnetic exchange field of the single adatom allows to switch the total moment on and off, and which therefore might be of interest for magnetic storage. Thus magnetic frustration might be useful for future nanosize information storage.



---

# Chapter 8

## Strong Even-Odd Effects in Magnetism of Nanochains

### 8.1 Introduction

Nanochains is a particular example of nanostructures which, excluding the ferromagnetic ones [110, 111, 112], were rarely studied. The aim of the present chapter is to investigate the ground state spin structure of nanowires with up to 10 adatoms using the screened KKR method based on density functional theory (DFT) and assess our findings with a Heisenberg model in order to show and predict the relation between parity and non-collinear ground states. We know from our previous work that the Mn-adclusters are well described by the Heisenberg model with first neighboring magnetic interactions. As previously we assume a classical spin Hamiltonian of the form

$$H = -\frac{1}{2} \sum_{i \neq j} J_{ij} \vec{e}_i \vec{e}_j. \quad (8.1)$$

We point out that the exchange interaction between the adatoms  $J_1$  is considered to be negative (antiferromagnetic nanochains) while the exchange interaction between the adatoms and the neighboring surface atoms  $J_2$  can be either positive or negative.

### 8.2 Ab-initio Results

We have already studied the simplest AF chain case consisting on a dimer (Cr or Mn) deposited for example on a ferromagnetic surface such as Ni(001). We recall here briefly the requisite results: Both the Cr- as well as the Mn-dimer adatoms couple strongly AF to each other, which is in competition with the interaction with the substrate atoms, favoring a parallel alignment of the dimer

moments and being, as we have mentioned, either of AF nature, for the Cr-dimer, or of FM one for the Mn-dimer. Thus frustration occurs and non-collinear structures can be expected. Total energy calculations showed that the collinear magnetic ground state which is ferrimagnetic (Ferri) is a local minimum. Within this solution the, no longer equivalent, dimer moments couple antiferromagnetically to each other and are collinear to the substrate moments. The non-collinear configuration which is the most stable state (see Fig. 8.1(a)) is characterized by the Mn adatom moments which are aligned antiparallel to each other and basically perpendicular to the substrate moments. However, the weak FM interaction with the substrate causes a slight tilting leading to an angle of  $73^\circ$  instead of  $90^\circ$ . An angle of  $94^\circ$  has been obtained for a Cr-dimer due to the preference of the Cr-adatom to couple AF with the substrate atoms. A small tilting of  $0.3^\circ$  up to  $7.4^\circ$  of the magnetic moments of the four outer Ni atoms neighboring the Cr-(Mn-) dimer is observed (the two inner Ni atoms do not tilt for symmetry reasons).

Let us consider a chain of three Mn adatoms (Fig. 8.1(b)). Here, we find the Ferri solution  $\uparrow\downarrow\uparrow$  being the ground state ( $\uparrow$  means an atomic moment parallel to the substrate magnetization direction,  $\downarrow$  an antiparallel atomic moment). The magnetic moments do not change a lot compared to what observed for the dimer. One sees already the beginning of an odd-even dependence of the magnetic ground state. Investigating the longer nanochains with an even number of adatoms shows that their ground state is always non-collinear. Examples are shown in Fig. 8.1(c)-(e)-(g)-(i). The magnetic moments are always in the plane perpendicular to the substrate magnetization keeping the magnetic picture seen for the dimer almost unchanged. In every first neighboring pair of adatoms, the magnetic moments are almost coupled AF to each other. The adatoms at both extremities of the chains have the most rotated moments towards a FM coupling with the substrate moments (see Table 8.1). The central adatoms A-B (see Fig. 8.1 for the notation) are the ones which keep their rotation angle obtained for the dimer almost unaltered. The angle  $\theta$  oscillates between  $70^\circ$  obtained for the chain with 6 adatoms up to  $87^\circ$  obtained for the chain with 4 adatoms. Note that the angle between two successive moments is around  $150^\circ$  similar to the dimer result. This explains the moments which rotate towards the substrate magnetization with an angle  $\sim 100^\circ$  (atoms C-D, E-F and G-H for the nanochains with 6, 8 and 10 adatoms respectively) since their first neighbors, which are at the extremities of the chains, have their moments rotated by an angle of  $\sim 50^\circ$  giving thus an angle difference of  $150^\circ$ . The energy differences between the non-collinear and the Ferri solutions are presented in Table 8.2.

The considered nanochains with an odd number of adatoms are characterized by a Ferrimagnetic ground state. In fact, here we have two possible Ferri configurations. In particular, when the number of adatoms is even, the two possible Ferri configurations are degenerate (*e.g.* for the dimer,  $\uparrow\downarrow$  and  $\downarrow\uparrow$  are equivalent). If the number of adatoms is odd, the two possible Ferri configurations are not anymore degenerate (*e.g.* for the trimer,  $\uparrow\downarrow\uparrow$  and  $\downarrow\uparrow\downarrow$ ). In that case, the most stable Ferri

**TAB. 8.1** –. *Size and angles of the magnetic moments in the calculated nanochains with an even number of adatoms. The adatoms connected by - sign have the same magnetic moment and rotation angle  $\theta$  but not necessary the same azimuthal angle  $\phi$ .*

Length	Adatom	$\theta(^{\circ})$	$\phi(^{\circ})$	M ( $\mu_B$ )
2 adatoms	A-B	73	0-180	3.71
4 adatoms	A-B,C-D	87, 54	0-180, 0-180	3.55, 3.72
6 adatoms	A-B, C-D,	70, 104,	0-180, 0-180,	3.46, 3.52,
	E-F	45	0-180	3.67
8 adatoms	A-B, C-D,	84, 65,	0-180, 0-180,	3.47, 3.46,
	E-F, G-H	106, 44,	0-180, 0-180,	3.52, 3.66
10 adatoms	A-B, C-D,	78, 85,	0-180, 0-180	3.47, 3.47
	E-F, G-H,	67, 102,	0-180, 0-180	3.46, 3.52
	I-J	48	0-180	3.67

configuration will be provided by the magnetic coupling preference of the single adatom. A Mn adatom prefers a FM coupling with Ni surface atoms leading to a configuration which maximizes the number of adatoms with a FM coupling with the substrate as a Ferri ground state (*e.g.*  $\uparrow\downarrow\uparrow$  for the Mn-trimer). For the sake of brevity, we do not present the converged NCOL local minimums solutions. We provide, however, the total energy differences in Table 8.2. Moreover, we note that the obtained NCOL configurations are similar to the calculated ones for the nanowires with an even number of adatoms in the sense that the adatom's moments are almost perpendicular to the surface magnetization.

### 8.3 Heisenberg Model Results

The Heisenberg model is valuable to determine the effects of parity of the number of adatoms on the nanowire's magnetic solutions. We rewrite the Hamiltonian of eq. 8.1 in terms of the tilting angles  $\theta$  of the adatoms neglecting the rotation angle of Ni moments and taking into account only first-neighbor interactions:

$$H = -J_1 \sum_{i=1}^{N-1} \cos(\theta_i - \theta_{i+1}) - J_2 \sum_{i=1}^N \cos(\theta_i) \quad (8.2)$$

We note that the azimuthal angles  $\Phi$  do not enter the previous expression of the Hamiltonian for symmetry reasons.  $J_1$  is the magnetic exchange interaction between two first neighboring adatoms *i.e.*  $J_1 = J_{\text{adatom-adatom}}$ , while  $J_2$  is the total magnetic exchange interaction between a given adatom and its first neighboring surface atoms *i.e.*  $J_2 = MJ_{\text{adatom-surface atom}}$  with  $M$  being the number of first neighboring surface atoms. In the case of a *fcc* (001) surface  $M = 4$ , while for

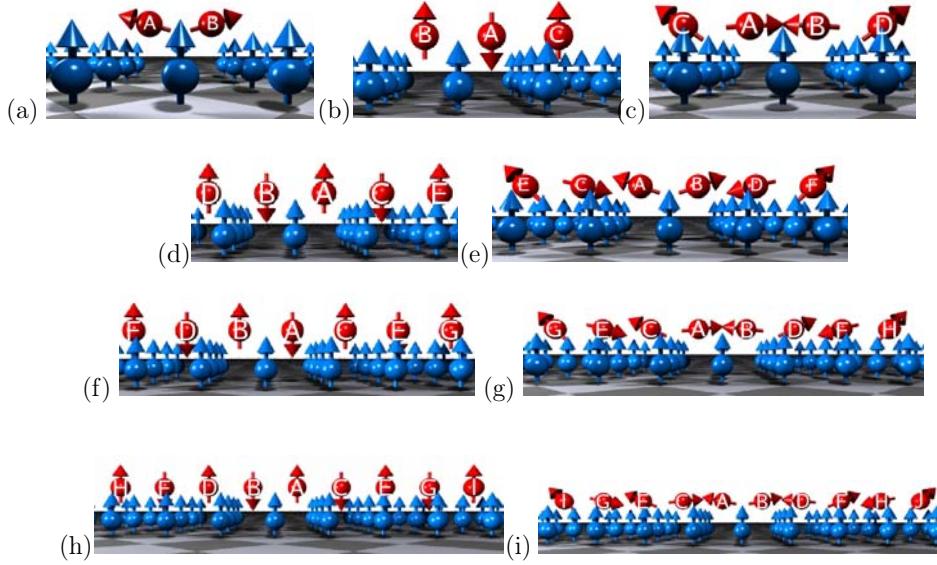


**FIG. 8.1** –. Different magnetic ground configurations of the Mn nanowires on Ni(001). The nanochains with an even number of Mn adatoms (2, 4, 6, 8, 10) prefer a non-collinear ground state, while for an odd number of adatoms a collinear Ferrimagnetic state is energetically more stable.

a *fcc* (111) surface  $M = 3$ .  $N$  is the number of adatoms in the chain ( $N > 1$ ). The magnetic exchange interactions can be extracted from our *ab-initio* DFT calculations and plugged in the present model.

As we have seen from the adatom and dimer magnetic picture, the two magnetic configurations which are relevant for our present investigations are the Ferri and the NCOL magnetic configurations which are solutions of the Heisenberg Hamiltonian.

We will try to solve the Heisenberg Hamiltonian by considering, at first stage, the rotation angle of the magnetic moments in the NCOL solution to have a constant value. In the second stage, we will consider the general case, *i.e.* the rotation angles can vary from adatom-site to adatom-site, by solving this Hamiltonian with an iterative scheme.

### 8.3.1 Case of Constant Rotation Angles

In this case, the NCOL configuration is described by the following Hamiltonian in which for simplicity we consider, as precised earlier, the rotation angle of the

**TAB. 8.2** –. *Size of the magnetic moments in the calculated Ferri nanochains with even and odd number of adatoms. The energy difference between the NCOL and Ferri are also shown. As described earlier the adatoms separated by - sign have the same magnetic moment.*

Length	Adatom	M ( $\mu_B$ ) for Ferri	$E_{\text{Ferri}} - E_{\text{NCOL}}$ (meV/adatom)
2 adatoms	A,B	-3.78, 3.65	11.16
3 adatoms	A, B-C	-3.78, 3.65	-8.85
4 adatoms	A, B, C, D,	3.48, -3.62 -3.82, 3.68	8.48
5 adatoms	A,B-C, D-E	3.43, -3.56 3.64	-9.52
6 adatoms	A, B, C, D, E, F	-3.54, 3.43, 3.45, -3.57, -3.77, 3.64	7.82
7 adatoms	A, B-C, D-E, F-G	-3.54, 3.43, -3.56, 3.64	-10.48
8 adatoms	A, B, C, D, E, F, G, H	3.43, -3.54, -3.54, 3.43 3.45, -3.56 -3.77, 3.64	5.46
9 adatoms	A, B-C, D-E, F-G, H-I	3.43, -3.54 3.43, -3.56 3.64	-9.29
10 adatoms	A, B, C, D, E, F, G, H, I, J	-3.54, 3.42 3.43, -3.54, -3.54, 3.43, 3.45, -3.57 -3.77, 3.64	3.53

adatoms to be the same:

$$H_{\text{NCOL}} = -(N-1)J_1 \cos(2\theta) - NJ_2 \cos(\theta), \quad (8.3)$$

This Hamiltonian is minimized by the angle  $\theta$  satisfying the following criteria:

$$\cos(\theta_{\min}) = -\frac{NJ_2}{4(N-1)J_1}. \quad (8.4)$$

The Hamiltonian of the most stable Ferri solution is given by

$$H_{\text{Ferri}} = (N-1)J_1 - P(N)|J_2|. \quad (8.5)$$

$P(N)$  is a parity function of the number  $N$  of adatoms which equals 0 when  $N$  is even or 1 if  $N$  is odd.

Let us calculate the difference  $\Delta H$  between the two Hamiltonians  $H_{\text{NCOL}}(\theta_{\min}) - H_{\text{Ferri}}$ :

$$\begin{aligned}\Delta H &= \frac{N^2 J_2^2}{8(N-1)J_1} + P(N)|J_2| \\ &= \frac{N^2 J_2^2}{8(N-1)J_1} \left[ 1 + \frac{8(N-1)J_1 P(N)}{N^2 |J_2|} \right]\end{aligned}\quad (8.6)$$

If the difference is negative, the NCOL configuration is the ground state while the opposite leads to the Ferri ground state.

The first term of the left side of eq. 8.6:  $N^2 J_2^2 / 8(N-1)J_1$  is negative because the adatoms couple AF between each other (*i.e.*  $J_1 < 0$ ). Two cases have to be considered for the second term. First, the number of adatoms  $N$  is even. This leads to  $P(N) = 0$  and gives a negative energy difference. In other words if  $N$  is even, the NCOL configuration is the ground state. Note that in the considered Heisenberg model, the two solutions Ferri and non-collinear with an angle  $\theta = 90^\circ$  are completely degenerate. For the latter configuration, a small variation of the angles  $\theta$  leads to a linear change of the energy  $\sim \Delta\theta$ , such that the exchange interaction energy with the substrate atoms can be gained by tilting either towards the substrate or away from the substrate depending on the sign of  $J_2$ . The energy gain by this tilting goes almost linearly with the number of adatoms (see eq. 8.6) meaning that the energy gain by the adatom is almost a constant.

Second, the number of adatoms is odd and  $P(N) = 1$ . The second term of eq. 8.6 is positive contrary to the first term and provides an energy counterbalance allowing the Ferri solution to be stable under some conditions. However, this additional term will vanish for a big number of adatoms as it decreases as  $1/N$ . Hence, we can already state that for a sufficiently high number of adatom the non-collinear solution will be the ground state. In general the NCOL ground state is provided for  $J_1 > -\frac{N^2}{8(N-1)}|J_2|$  or equivalently if  $|J_1| < \frac{N^2}{8(N-1)}|J_2|$ . Otherwise the Ferri solution is the ground state. One can express the last condition in terms of a second degree polynomial

$$N^2 |J_2| - 8(N-1)|J_1|, \quad (8.7)$$

with the unknown variable  $N$  and a discriminant  $\Delta = (8|J_1|)^2(1 - \frac{|J_2|}{2|J_1|})$ . The sign of this polynomial depends on the sign of the discriminant. If the total exchange interaction  $|J_2|$  is high enough compared to the exchange interaction between the adatoms or more precisely if  $|J_2| > 2|J_1|$  then  $\Delta < 0$ . In other words the polynomial would have the positive sign of  $N^2$  meaning that the nanochain would be non-collinear. If  $\Delta > 0$  ( $|J_2| < 2|J_1|$ ) then the two solutions can be found depending on the length of the nanochain. The transition from a magnetic state to another one is provided by the roots  $N_1$  and  $N_2$  of the previous polynomial. The nanowires are non-collinear unless their length is delimited between  $N_1$  and  $N_2$ .

**TAB. 8.3** –. Values of the magnetic exchange parameters  $J_{ij}$  using the Lichtenstein formula [24] for the Mn dimers on different surfaces: Ni(001), Ni(111) and Fe<sub>fcc</sub>(001). The calculated  $\theta$  angles from ab-initio and Heisenberg model are shown. The sign of the discriminant and roots of the polynomial, described in the text, are also given.

$J_{ij}$ (meV)	Mn <sub>2</sub> /Ni(001)	Mn <sub>2</sub> /Ni(111)	Mn <sub>2</sub> /Fe <sub>fcc</sub> (001)
$J_1$	-138.2	-145.0	-43.0
$J_2$	4×13.0	3×9.0	4×(-10.7)
$\theta_{\text{FP-KKR}}^{\text{dimer}}$	73°	79°	115°
$\theta_{\text{Heisenberg}}^{\text{dimer}}$	79°	85°	120°
Sign of $\Delta$	+	+	+
$N_1, N_2$	1.0, 20.2	1.0, 42.0	1.2, 6.9

In Table 8.3 are shown examples of the exchange interactions for Mn-dimers on different ferromagnetic substrates: on Ni(001), on Ni(111) and on *fcc* Fe(001). In case of an odd number of adatoms, the discriminant of the polynomial is positive meaning that the ground state is Ferri for a given range of number of adatoms. Following our model, we see that above 19 adatoms, the Mn nanochain on Ni(001) surface should experience a magnetic transition to a NCOL solution. Whereas this transition is expected to occur for a higher number, almost the double, of adatoms on Ni(111). The range of presence of the Ferri state as a ground state is much more limited (N=3, 5) on Fe<sub>fcc</sub>(001). In general, within the assumption of constant rotation angle of the adatoms magnetic moments, the Heisenberg model predicts a NCOL ground state for the infinite chains deposited on ferromagnetic surfaces.

### 8.3.2 General Case

Another possibility to investigate the problem of the nanochains within the Heisenberg model is to solve eq. 8.1 by allowing the rotations angles of the moments to be different within the chains.

Here, instead of using the angles  $\theta$  between the magnetization of the surface and the individual magnetic moment of the adatoms we prefer to use the angles  $\delta$  between the individual moment and the direction perpendicular to the surface magnetization ( $\delta_i = (-1)^{i+1}(\frac{\pi}{2} - \theta_i)$ ). Since our DFT results show that the angles  $\delta$  are expected to be small, the advantage of using Taylor's development will be easily taken and used when needed.

After the variable change, the Heisenberg Hamiltonian is:

$$H = -J_1 \sum_{i=1}^{N-1} \cos(\delta_i - \delta_{i+1}) - J_2 \sum_{i=1}^N \sin(\delta_i) \quad (8.8)$$

The minima of this Hamiltonian are determined by the three following equations:

$$\begin{aligned}
 i = 1 : \quad \frac{\partial H}{\partial \delta_1} &= -J_1 \sin(\delta_1 - \delta_2) - J_2 \cos(\delta_1) = 0 \\
 1 < i < N : \quad \frac{\partial H}{\partial \delta_i} &= -J_1 (\sin(\delta_i - \delta_{i-1}) - \sin(\delta_{i+1} - \delta_i)) - J_2 \cos(\delta_i) = 0 \\
 i = N : \quad \frac{\partial H}{\partial \delta_N} &= -J_1 \sin(\delta_N - \delta_{N-1}) - J_2 \cos(\delta_N) = 0
 \end{aligned} \tag{8.9}$$

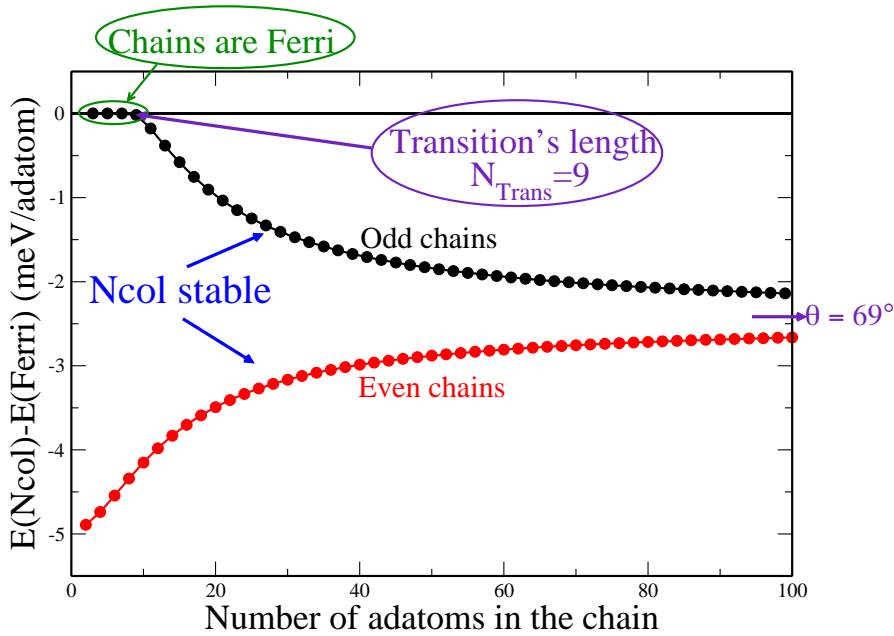


**FIG. 8.2** —. Energy differences obtained with the Heisenberg model between the NCOL configuration and the Ferri configuration for different lengths of the nanowires. Black circles represent the results obtained for chains with the odd parity while the red circles correspond to the chains with the even parity. The odd chains starts to prefer the non-collinear solution to be the ground state for lengths bigger than 9 adatoms, value which we call transition's length ( $N_{Trans}$ ).

One can solve these equations self-consistently and many physical quantities of our interest can be deduced. The energy differences between the NCOL and Ferri can be, for example, calculated. Fig. 8.2 shows the variation of the energy differences ( $E_{NCOL} - E_{Ferri}$ ) versus the length of the nanowires given by the number of adatoms. Negative values of the plotted energy differences mean that

the ground state is non-collinear. The red circles confirm our DFT results and show that the even chains have a non-collinear ground state. Within this model, the non-collinear solution is not even a metastable state for odd chains with a length smaller than 9 adatoms. This value corresponds to a quantity we name “transition’s length”. However, for a length bigger or equal 11 adatoms, the odd chains prefer the non-collinear solution to be the ground state. Another important remark is that when increasing the lengths of the nanowires both curves are converging to the same energy difference. This is expectable because if the chains are infinite then the concept of parity will vanish. In fact, the magnetic ground state in that case will be the one predicted when we assumed a constant rotation angle ( $\theta_{\text{NCOL}} = 69^\circ$ ).

The next point we are aiming to discuss is the transition’s length ( $N_{\text{Trans}}$ ) for the odd chains which has been found for the actual investigated case (Mn/Ni(001)) to be equal to 9 adatoms. We show in Fig. 8.3 the variation of  $N_{\text{Trans}}$  versus the ratios  $\frac{J_2}{J_1}$ . The obtained curve seems to have an exponentially decaying shape. On one hand, small exchange interactions ratios lead to very high transition lengths. This means that odd-even effects are expected to last for very high length values. On the other hand big values of  $J_2$  compared to  $J_1$  lead to very small transition lengths. One should mention that for even higher values of  $J_2$ , the ground state is ferromagnetic and not anymore non-collinear. The obtained curve is interesting and can be used to predict the behavior as well as the transition lengths for other kinds of antiferromagnetic chains deposited on ferromagnetic substrates. This model predicts for example a transition’s length of 5 adatoms for Mn/Fe(001) while Mn/Ni(111) is characterized by a value of 17 adatoms. Certainly, this transition’s length is subject to modifications depending on the accuracy of the exchange interactions, spin-orbit coupling and geometrical relaxations which depend on the investigated system.

It is interesting to look at the rotation angles obtained within this Heisenberg model and to compare them with the DFT values. Fig. 8.4 shows that the discrepancy between the two theories get smaller as soon as the length of the chains increases. The reason is indeed the assumption we included in our model concerning the equality of the exchange interactions ( $J_1$ ) between all the adatoms. The increase of the chain’s lengths smoothen in fact the discrepancies between the exchange interactions which improves the results obtained with the model. In other words, the angles obtained with the Heisenberg model can be trusted for very long chains which makes it very useful.

An additional interesting point is the linearity of the variation of the angles  $\delta$  for sites sharing the same index parity. This will be clearly explained in the following. Let us first assume that the angles  $\delta$  are very small which leads to a

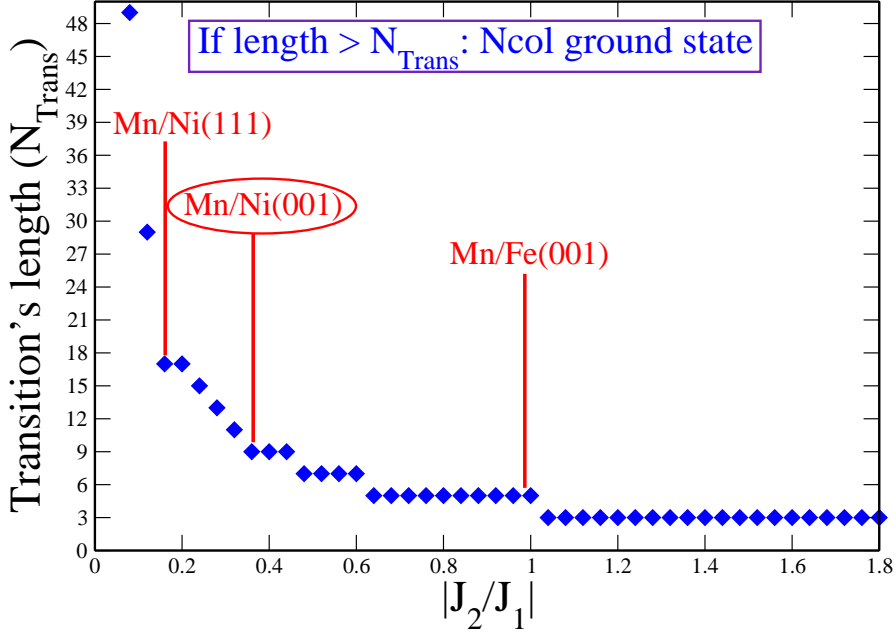


FIG. 8.3 –. Variation of the transition's lengths with respect to the ratio  $\frac{J_2}{J_1}$ . In addition to the particular case investigated in the actual chapter, results within the Heisenberg model for other systems such as Mn/Ni(111) and Mn/Fe(001) are shown.

first order Taylor expansion in equations 8.9:

$$\delta_1 + \delta_2 = -\frac{J_2}{J_1} \quad (8.10)$$

$$1 < i < N : 2\delta_i + \delta_{i+1} + \delta_{i-1} = -\frac{J_2}{J_1} \quad (8.11)$$

$$\delta_N + \delta_{N-1} = -\frac{J_2}{J_1} \quad (8.12)$$

A small manipulation of the above equations leads to

$$\text{If } i \text{ odd} : \delta_i - \delta_{i+2} = -\frac{J_2}{J_1} \quad (8.13)$$

$$\text{If } i \text{ even} : \delta_i - \delta_{i+2} = \frac{J_2}{J_1} \quad (8.14)$$

One sees clearly the linearity of the angle deviations for the atoms of the same index parity. In fact in order to solve these equations practically symmetry ar-

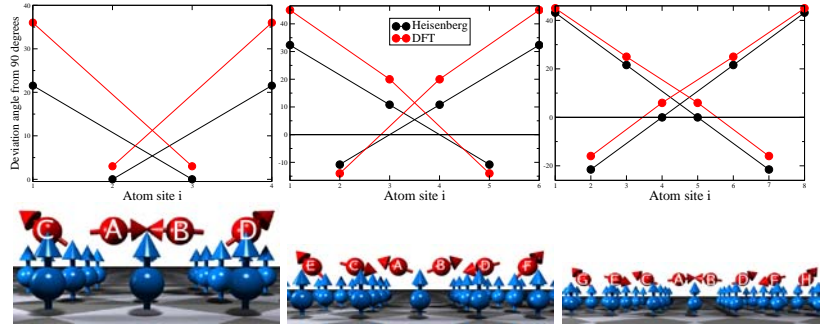


**FIG. 8.4** — Comparison of the deviation angles  $\delta$  obtained with the Heisenberg model and the DFT calculations. The results are shown for different lengths: 4, 6 and 8 adatoms.

guments have to be used. The linear variation of  $\delta$  explains the ability of the Heisenberg model to reproduce the magnetic behavior of the neighbor of the edge adatom. This adatoms as explained earlier couples slightly antiferromagnetically to the surface atoms moments. Moreover, the Heisenberg model predicts that for relatively long chains more adatoms close to the edge of the nanowires have tendencies for a slight antiferromagnetic coupling with the surface magnetization.

## 8.4 Summary

Parity of number of adatoms in finite antiferromagnetic nanowires is shown to be crucial in predicting whether the magnetic ground state is non-collinear or collinear. Our analysis shows that a non-collinear state is always the ground state for a nanochain with an even number of adatoms. The Ferri solution is the ground state for limited lengths of odd-chains. We predict the infinite chains to be of non-collinear magnetic nature. We believe that the magnetic state of these nanostructures can be measured by spin-polarized Scanning Tunneling Microscopy SP-STM and should show the parity dependence of the magnetic ground state predicted by our calculations.



---

# Chapter 9

## Surface State Scattering by Small Clusters

### 9.1 Introduction

At crystal surfaces the symmetry is lowered: The three dimensional periodicity in the bulk is lowered to the two dimensional periodicity at the surface. This leads to the occurrence of two-dimensional surface states [113, 114], which are spatially confined to the surface, since their wave functions decay rapidly into the crystal and are strongly damped in the vacuum. Surface states can exist only in regions of the two-dimensional Brillouin zone, where bulk Bloch states are not allowed. They are characterized by a two-dimensional Bloch vector  $\vec{k}_{\parallel}$  in this surface Brillouin zone, which describes the propagation in the surface plane. A projection of the bulk band structure to the surface plane can result in  $k_{\parallel}$ -regions, where bulk states are forbidden. In these gaps of the projected bulk band structure surface states can occur provided that their energy is lower than the work function. These two conditions guarantee that the wave functions of the surface states decay exponentially both into the crystal and into the vacuum region. An example of a Cu(111) band structure projected on the  $\bar{\Gamma} - \bar{M}$  line of the 2D-Brillouin zone is shown in Fig. 9.1. The shaded regions give the regions in  $E - k_{\parallel}$  space, for which bulk eigenstates (Blochwaves) exist. As mentioned earlier surface states can only exist in the white "gap"-regions. Two such states are indicated. Of special interest is the parabolic band with the minimum just below  $E_F$ , since this state is only partially occupied and gives rise to a two-dimensional metallic behaviour, which is of great interest for the following.

Recently a strong interest arose concerning an important physical effect associated with the interaction of a two dimensional surface state with the states of an adatom. It was shown that for Cu adatoms on Cu(111) a bound state splits off from the bottom of the Cu(111) surface state [26, 27]. This effect was basically predicted by Simon [28] who stated that in two-dimensional free space any

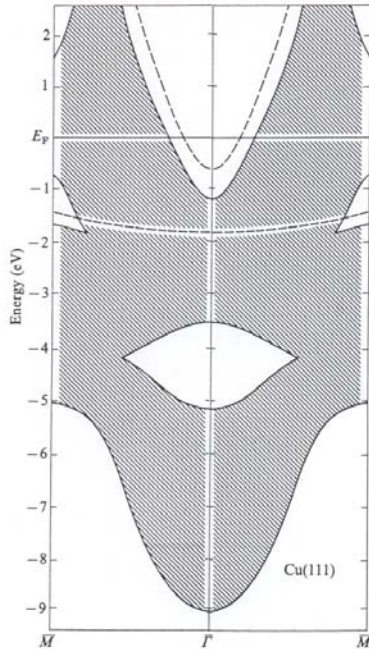


**FIG. 9.1** —. Surface states (dashed curves) and bulk projected bands at a Cu(111) surface according to a six-layer surface band structure calculation [115]. We note in addition to the usual  $\bar{\Gamma}$  surface state a second surface state positioned at  $\bar{M}$  (see section 9.6).

attractive potential has a bound state. Gauyacq *et al.* [116] suggested that an adatom-induced localization of the surface state may be observed in STS as a peak appearing just below the surface band edge when a Cs adatom is deposited on Cu(111).

Using low-temperature scanning tunneling spectroscopy (STS), Limot *et al.* [26] investigated silver and cobalt adatoms on Ag(111) as well as copper and cobalt adatoms on Cu(111). The bound state appears both for magnetic and non-magnetic adatoms as shown in Fig. 9.2. Moreover, using a Newns-Anderson model the authors explained the results as arising from the coupling of the adatom's orbital (which was supposed to be the  $s$ -orbital) with the surface-state electrons, and being broadened by the interaction with bulk electrons of the same energy. On the other hand, Olsson *et al.* [27] used the same type of experiment and performed pseudopotential calculations for single Cu adatoms on Cu(111). The calculated local density of states (LDOS) exhibits several adatom-induced peaks. Two of them are assigned to resonances deriving from the  $d_{z^2}$  atomic orbital and  $sp_z$  hybrid orbitals. The third one corresponds to a localization of the surface state at the adatom without a specified orbital origin. In fact, these adatom-induced peaks appearing at the bottom of the surface state were already observed by an other experiment [117], again without a clear assignment of their origin. Davis *et*

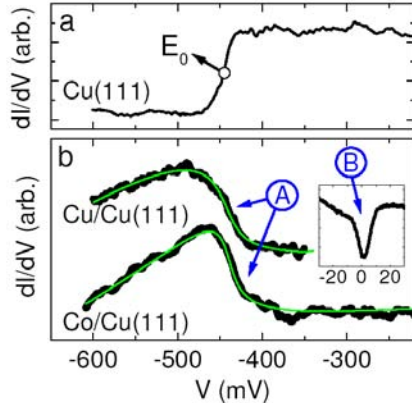


**FIG. 9.2** –. Data obtained experimentally by Limot *et al.* [26]:  $dI/dV$  spectrum over: (a) Center of a  $20 \times 20 \text{ nm}^2$  defect- and impurity-free area of Cu(111), (b) Center of a copper atom and of a cobalt atom on Cu(111). In the inset is shown a Kondo-Fano resonance of Co/Cu(111) near the Fermi level.

*al.* [118] have observed similar localized states in STS measurements for Cr atoms in the surface layer of Fe(001) surface. Ab-initio calculations of Papanikolaou *et al.* [119] confirmed this and showed that similar localized states occur for many other impurities in the Fe(001) surface.

In this work we study the origin and the condition of existence for such an impurity-induced split-off state on the Cu(111) surface. For this purpose we have performed ab-initio calculations using the Korringa-Kohn-Rostoker (KKR) Green function method for impurities on the Cu(111) surface. We consider single impurities of the  $3d$  and  $4sp$  elements as adatoms on the Cu(111) surface and as impurities in the first layer. We find that split-off states can appear both for adatoms on the surface as well as for substitutional impurities in the surface. In the case of magnetic impurities these states always appear in both spin channels and show a very small spin splitting.

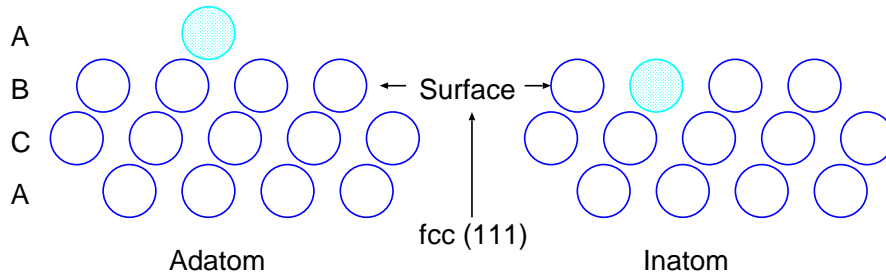
## 9.2 Computational Aspects

We considered a cluster of perturbed atomic potentials which includes the potentials of the impurities and the perturbed potentials of several neighbor shells. Also in the vacuum region the space is filled by cellular potentials, of which the ones close to the impurity are perturbed. The impurity potential and the perturbed potentials of the neighboring cells are embedded in an otherwise ideal unperturbed surface which is in the present case the ideal Cu(111) surface.

We have carried out our calculations in the local spin density approximation (LSDA) with the parameters of Vosko *et al.* [35]. Angular momenta up to  $l_{max} = 3$  are included in the expansion of the wave functions and up to  $2l_{max} = 6$  in the charge density expansion. We have checked these cut-offs to be adequate for our purpose.

First, the surface Green function was determined for the surface of Cu(111).

**FIG. 9.3** —. Schematic view of the two impurity configurations studied: the adatom is assumed to sit at the hollow position in the first vacuum layer, and the inatom is sitting in the first surface layer. Note that as the surface is a  $fcc(111)$  the layers stacking order is of ABCABC.. kind.



The LSDA equilibrium lattice parameter was used ( $6.63 \text{ a.u.} \approx 3.51 \text{ \AA}$ ). To describe the impurities on (adatom) or in (inatom) the surface (Fig. 9.3), we consider a cluster of perturbed potentials which includes the potentials of the impurities and the perturbed potentials of several neighbors shell, with typical size of 29 perturbed sites for the adatoms. All adatoms are assumed to sit at the hollow position in the first vacuum layer. In the following, we take as reference energy the Fermi level  $E_F$ .

From a practical point of view it is frequently desirable to gain an understanding of the STS without highly demanding and thus very time consuming model calculations. In principle, the Tersoff-Hamman model [120], which is based on the electronic structure of the analyzed surface, provides just such an easy method. According to this model [120] scanning tunneling spectra can be related to the  $s$ -DOS induced by the surface or by the adatom at the position of the STS tip. Adopting this model, we calculate the  $s$ -LDOS at a position  $z = 2.86 \text{ \AA}$  directly above the adatom. This corresponds to a regular lattice position in the third vacuum layer above the surface.

### 9.3 Tersoff-Hamann Model

The scanning tunneling microscopy and spectroscopy, introduced by Binnig and Rohrer in 1982 [2] (physics Nobel prize 1986), have opened the road to atomic resolution images of materials. The method is based on the tunnel effect, *i.e.* approaching the surface of a substrate material with a tip under voltage, tunneling current can flow between the surface and the material through the

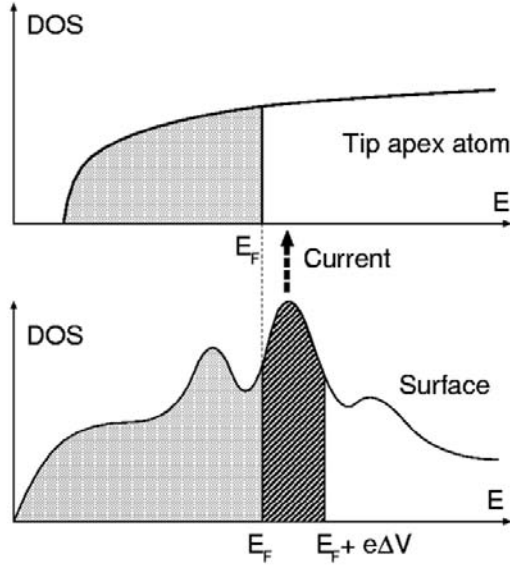


**FIG. 9.4** –. The underlying idea of STS. The dark shaded region in the surface density of states between  $E_F$  and  $E_F + e \cdot \Delta V$  corresponds to the states which contribute to the measured current  $I$  at voltage  $\Delta V$ . Thus the current is, in first approach, proportional to the number of states  $N$  in this interval, and the differential conductance  $\frac{dI}{dV}$  proportional to the density of states at  $E_F + \Delta V$ ,  $\frac{dN}{dV} = n(E_F + \Delta V)$ . Reverting the voltage, one has electron tunneling from the tip into the surface, thus probing the DOS below  $E_F$ .

vacuum without the tip actually touching the surface. The current measured gives the characteristic of the current voltage  $I(V)$  and the rather more used differential conductance  $\frac{dI}{dV}(V)$ . This gives the opportunity for STS and is useful because the signal shape contains more information than the current at a particular constant voltage. To understand this let us consider a prototype STS experiment: When applying a voltage  $\Delta V$  the surface states are raised by  $e \cdot \Delta V$  (see Fig. 9.4). Thus in the energy range between the tip Fermi level,  $E_F$  and the substrate Fermi level  $E_F + e \cdot \Delta V$ , the states of the tip are empty while those of the surface are filled. These states contribute to the electron current  $I$  from the substrate to the tip. If we assume that the density of states of the tip is approximately constant in this energy range, as in the example shown in Fig. 9.4, and that the tunneling amplitude  $M(E)$  between the surface and the tip does also not change much, then the current  $I$  should be proportional to the total number of states between  $E_F$  and  $E_F + e \cdot \Delta V$

$$I(V) \approx \int_{E_F}^{E_F + e \cdot \Delta V} n_{surf}(E) dE, \quad (9.1)$$

with  $n_{surf}(E)$  the surface density of states. This leads the differential conductance:

$$\frac{dI}{dV}(V) \approx n_{surf}(E_F + e \cdot \Delta V). \quad (9.2)$$

These equations can be derived from a more general theory of Bardeen [121] under the assumption of an energy-independent transmission probability and tip density of states. This is reasonable in some cases (*e.g.* for tips with *s*-like DOS around  $E_F$ ) and constitutes the Tersoff-Hamann model, giving quite acceptable results mainly when the following criteria are satisfied [122]: (i) No substantial chemical interactions exist between surface and tip, meaning that the distance has to be larger than for example 5-6  $\text{\AA}$  in the case of metal surfaces. (ii) The typical size of the surface structures to be studied is well above the typical length scale of the electronic states of the STM tip: Since the typical length scale of the tip is about  $1\text{\AA}$  to  $2\text{\AA}$ , for features of sizes well above this value the exact geometry of tip states will not enter the shape of the current contour in a decisive way.

## 9.4 Origin of the Localization

Let us go back to the effect we are interested in. It is very useful to give a simple explanation on how the localization appears contrary to the more involved Anderson-model used by Limot *et al.* [26]. This effect did not appear accidentally on the Cu(111) or Ag(111) surfaces. As shown in Fig. 9.1 these surfaces are characterized by surface states where the electrons behave like a two-dimensional gas. In such a two-dimensional model case the DOS  $\rho_0$  exhibits a van Hove singularity, resulting in a step-like jump of the DOS from zero to a constant value at the minimum of the surface state (Fig. 9.5).

Let us consider a simple 2D tight-binding model with *s*-orbitals  $|i\rangle$  and  $|j\rangle$  centered at the sites *i* and *j*. By denoting the atomic level by  $\epsilon_0$  and the hopping matrix elements between nearest neighbors (NN) *t*, the unperturbed hamiltonian is given by

$$\mathcal{H}_0 = \sum_i \epsilon_0 |i\rangle\langle i| + \sum_{i,j}^{NN} t |i\rangle\langle j|, \quad (9.3)$$

characterized by the Green function denoted by  $\overset{\circ}{G}$ . An introduction of a perturbed potential  $\Delta V$  on the ‘‘impurity’’ site 0 leads to a shift of the atomic level of the orbital  $|0\rangle$

$$\mathbf{V} = \Delta V |0\rangle\langle 0|. \quad (9.4)$$

The Dyson equation for the Green function, which is in operator form given by

$$\mathbf{G}(E) = \overset{\circ}{G} + \overset{\circ}{G}\mathbf{V}\mathbf{G} = \overset{\circ}{G} + \overset{\circ}{G}\mathbf{V} \frac{1}{1 - \overset{\circ}{G}\mathbf{V}} \overset{\circ}{G}, \quad (9.5)$$

can be solved exactly, leading to

$$G_{ij}(E) = \overset{\circ}{G}_{ij}(E) + \overset{\circ}{G}_{i0}(E)\Delta V \frac{1}{1 - \overset{\circ}{G}_{00}(E)\Delta V} \overset{\circ}{G}_{0j}(E) \quad (9.6)$$

A new bound state centered at the impurity site occurs, if the denominator has a pole at a certain energy  $E$ , meaning that

$$1 - \overset{\circ}{G}_{00}(E)\Delta V = 0 \quad (9.7)$$

which is equivalent to

$$1 - \text{Re}\overset{\circ}{G}_{00}(E)\Delta V = 0 \quad \text{and} \quad \text{Im}\overset{\circ}{G}_{00}(E) = 0 \quad (9.8)$$

If both can be satisfied for an energy  $E = E_0$ , a bound state with energy  $E_0$  exists at the impurity site. When  $\text{Im}\overset{\circ}{G}_{00}(E)$  is not zero, there is a broadening of the bound state. We see in Fig. 9.5 that this condition is obtained when the vertical line defining  $\frac{1}{\Delta V}$  crosses the real part of the Green function. The important point is the following: as the real part of the Green function experiences a logarithmic singularity because of the jump in the imaginary part of the Green function, the line  $\frac{1}{\Delta V}$  always crosses the real part of the Green function if the potential is negative, in other words when the potential is attractive.

Such an effect should be observed in all systems having a DOS characterized by a discontinuity which leads to a logarithmic singularity of the real part of the Green function. The impurity plays then the role of “bringing” or “connecting” this resonance to the imaginary part of the new Green function of perturbed system.

## 9.5 Surface State of Cu(111)

The first step of our work consists in calculating the energy of the bottom of the surface state. As depicted with the dashed line in Fig. 9.6, the s-LDOS is characterized by a surface state which appears at 0.68 eV below the Fermi energy. We note that experimentally, this threshold energy is higher and is situated at  $-0.45$  eV [123]. This inconsistency is mainly due to the LDA equilibrium lattice parameter ( $3.51 \text{ \AA}$ ) we used in our calculations since a test calculation with the experimental lattice parameter ( $3.62 \text{ \AA}$ ) gives a value of  $-0.49$  eV for the threshold energy (see the full line in Fig. 9.6) which is in much better agreement with the experiment. Note that for two dimensional bands the LDOS shows a jump at the energy of a band minimum or maximum, which is slightly broadened in Fig. 9.6 due to the use of a small imaginary part for the energies.

## 9.6 3d-impurities as Adatoms

The calculated LDOS for 3d adatoms presented in Fig. 9.7 exhibit several adatom-induced peaks. The LDOS refer to an unoccupied *lattice position* in the

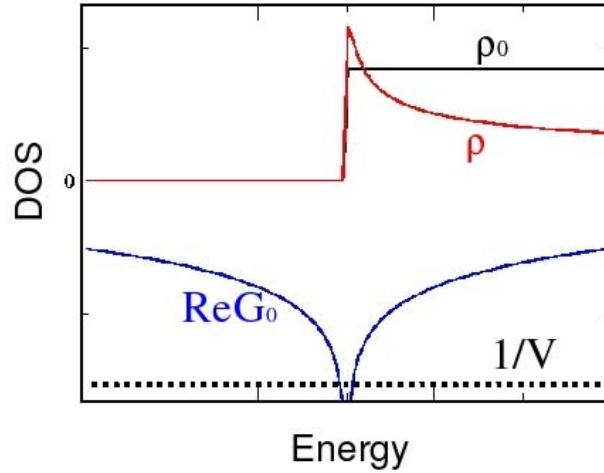


**FIG. 9.5** — In red is shown the density of states ( $\rho = -\frac{1}{\pi}\text{Im}\hat{G}$ ), or the imaginary part of the Green function if multiplied by  $-\frac{1}{\pi}$ , of a two-dimensional electron gas which experiences a jump to a constant value at an energy 0. The dashed line represents the inverse of the potential  $V$  which if negative crosses always the real part (in blue) of the Green function giving rise to a bound state shown in red (see text).

third vacuum layer above the surface, *i.e.*  $2.86 \text{ \AA}$  above the single adatoms in the first vacuum layer. We focused on the region where the split-off state appears experimentally, *i.e.*, around the bottom of the surface state, which, as stated above, is in our calculations located at  $-0.68 \text{ eV}$ .

Let us start with a Cu adatom. Below  $E_F$ , Fig. 9.7 shows that two states appear in the LDOS. The first one (see arrow (a) in Fig. 9.7) is a split-off state situated at the bottom of the surface state ( $\approx -0.68 \text{ eV}$ ) as was already found by Limot *et al.* [26] and by Olsson *et al.* [27]. To understand the origin of the second protrusion (see arrow (b)) we plot in Fig. 9.8 the  $d$ -partial LDOS of the adatoms which shows that it comes from a resonance of the  $d_{z^2}$  state at  $\approx -1.7 \text{ eV}$ .

For all the  $3d$ -adatoms examined, we find for both spin directions a peak in the LDOS in the region below the threshold value of the surface state. However, we also find peaks at other energies, *e.g.* for Cu at  $-1.7 \text{ eV}$  as mentioned earlier and for Co at  $-1.5 \text{ eV}$  for spin-up and at around  $0 \text{ eV}$  for spin-down states. In order to understand this behavior, we have in first place to understand the electronic and magnetic properties of the impurities and then which of the impurity states penetrate well into the vacuum, such that they show up in the LDOS of the second layer and can be detected by the STM.

Let us first address the second question. In the vacuum region, states with small in-plane  $\vec{k}$ -components  $\vec{k}_{\parallel}$  decay most slowly as a function of the perpendicular distance  $z$  from the surface. In fact, for a given energy  $E = -\chi^2$  be-

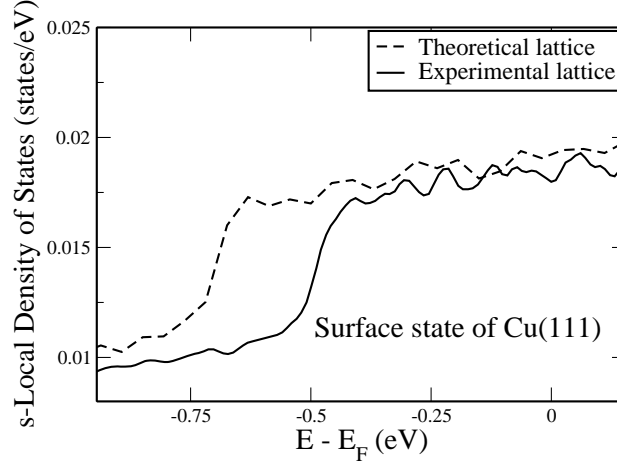


**FIG. 9.6** – *s*-Local density of states (LDOS) at the second vacuum layer above the Cu(111) surface. The full line represents the *s*-LDOS with the experimental lattice parameter and the dashed line refers to the *s*-LDOS with the LDA lattice constant.

low the vacuum barrier, a wave function with in-plane component  $k_{\parallel}$  decays as  $e^{-(\chi^2 + k_{\parallel}^2)^{\frac{1}{2}}z}$ . Therefore states with small  $k_{\parallel}$ -values decay slowest; for higher  $k_{\parallel}$  part of the kinetic energy is used for in-plane oscillations. Since the states with  $k_{\parallel} = 0$  show no in-plane oscillations and exhibit the full symmetry of the surface, we find that for the (111) surface states with  $s$ ,  $p_z$  and  $d_{z^2}$  show a slow decay in the vacuum region and can be well seen in STM, while other  $p$ - and  $d$ -states are strongly attenuated. An analogous argument holds for single adatoms on the (111) surface, since only these states exhibit the full point group symmetry of the adatom-on-surface configuration [119], and have thus no oscillations to use part of the kinetic energy.

To understand the magnetic properties of the adatoms, we have plotted in Fig. 9.8 the  $d$ -contribution to the local density of states (LDOS) at the adatom site. For the Cu-adatom, we find a sharp  $d$ -peak at  $-1.7$  eV, *i.e.* at the edge of the bulk  $d$ -band of Cu. This is a consequence of the repulsive potential, which the Cu adatom experiences in the first layer, shifting the  $d$  states to higher energies than in the bulk. All other impurities are magnetic and exhibit sizable moments, leading to a spin splitting of the so-called virtual bound states. For the different adatoms, the calculated local moments  $M_s$  are: Cr ( $4.06 \mu_B$ ), Mn ( $4.28 \mu_B$ ), Fe ( $3.21 \mu_B$ ), Co ( $1.96 \mu_B$ ) and Ni ( $0.34 \mu_B$ ). Note that the spin splitting is roughly given by  $I \cdot M_s$ , where  $I$  is the exchange integral of the order of 1 eV [124]. In

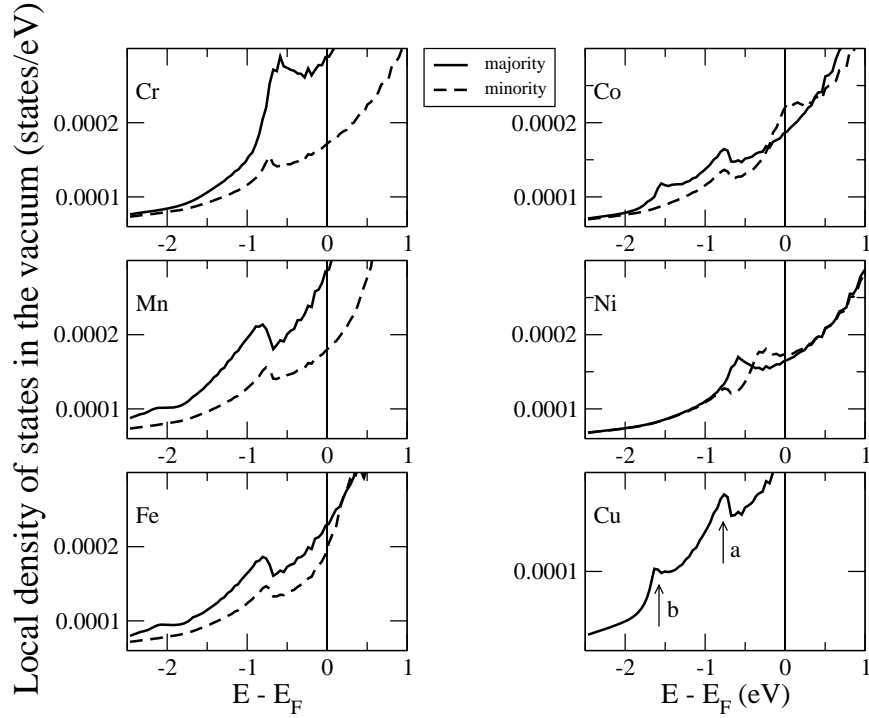


**FIG. 9.7** — Local density of states (LDOS) at the second vacuum layer above the 3d adatoms ( $2.86 \text{ \AA}$ ) on the Cu(111) surface. The full lines refer to majority-spin states, the dashed lines to minority-spin ones. The two arrows show the protrusions discussed in the text: (a) corresponds to a split-off state, (b) is a  $d_{z^2}$  resonance.

the case of the Cr adatom, the minority peak is at higher energies and cannot be seen in Fig. 9.8, while for Fe and Mn the majority peaks are at lower energies.

Let us now come back to the interpretation of Fig. 9.7, showing the LDOS in the second vacuum layer, at the position above the adatom, for majority and minority electrons. Independently of the peak structure, we observe a general increase of the DOS at higher energies, which arises from the increase of the spatial extent of the wave functions for larger energies. For Cu, the peak at  $-1.7 \text{ eV}$  coincides with the  $d_{z^2}$ -peak in the local DOS of the adatom, shown in Fig. 9.8. For clarification we show in Fig. 9.9 the local  $s$ -DOS and the  $d_{z^2}$ -DOS of the adatoms (the latter reduced by a factor of 10). For Cu, as well as for the

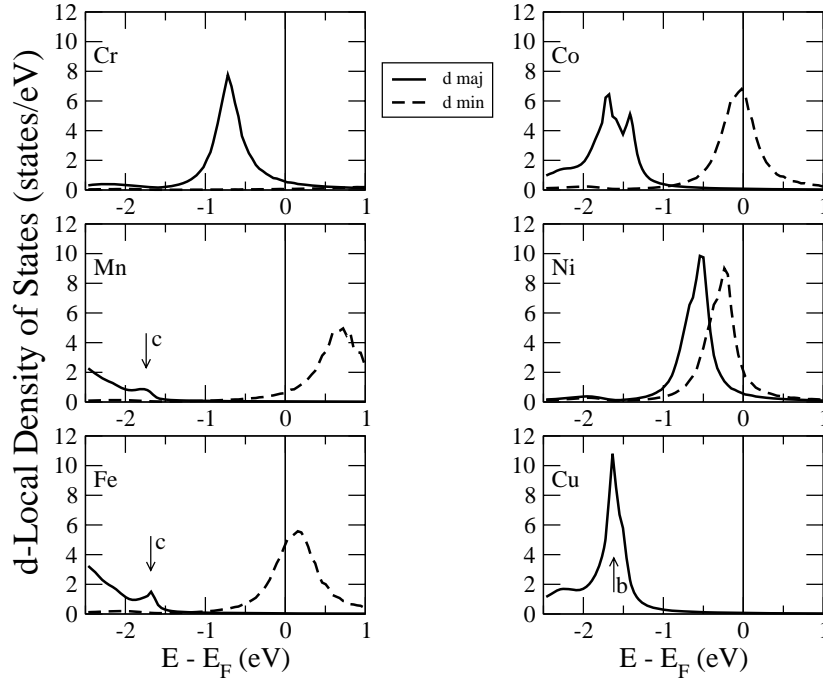


**FIG. 9.8** — *d*-contributions to the Local density of states (LDOS) of 3d adatoms on Cu(111) surface. The full lines describe the majority-spin states and the dashed lines describe the minority-spin states. Since the Cu adatom is non-magnetic, the majority and minority virtual bond states coincide.

majority states of Co, we see a maximum and minimum in the *s*-LDOS at the  $d_{z^2}$ -peak position, arising from the Fano-like resonant scattering of the *s*-states at the  $d_{z^2}$ -resonance. This effect cannot occur for a single adatom in free space or in jellium, since the *s*- and *d*-orbitals are orthogonal. Therefore it is brought about by the reduced symmetry, *i.e.* the scattering at the substrate atoms. The LDOS-peak below  $-0.68$  eV (arrow (a)) is the split-off state of the Cu adatom, induced by the attractive nature of the adatom potential in the first vacuum layer. The same states are also seen for the Co-adatom, more or less identical for both spin directions. In addition we see for the minority *s*-state of Co a Fano-like resonance behavior at the Fermi level, arising from the interaction with the minority  $d_{z^2}$ -virtual bound states.

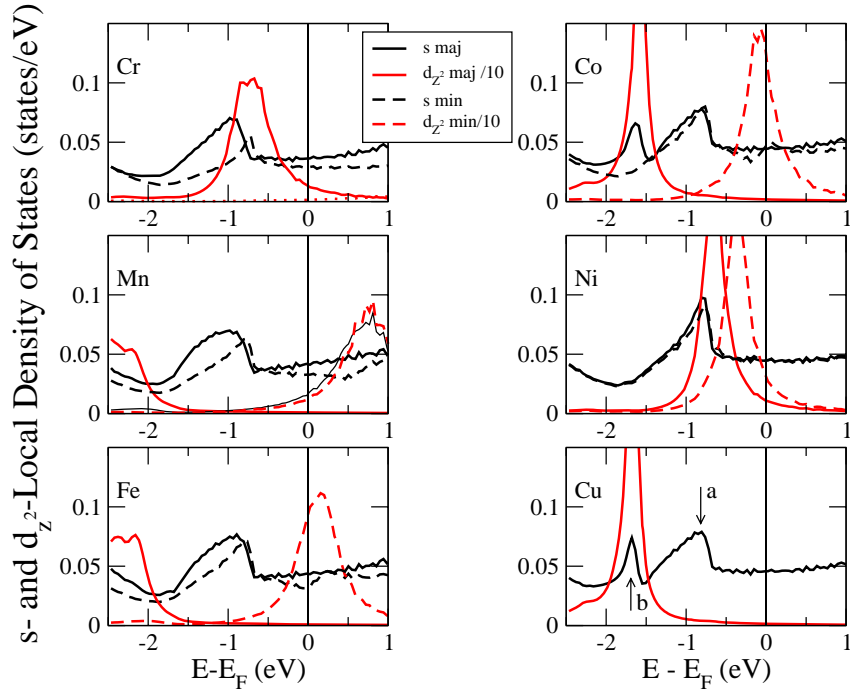


**FIG. 9.9** —. Focus on the  $s$ -partial LDOS (black curves) of the impurity atoms and  $d_{z^2}$ -partial LDOS (red curves) reduced by a factor 10. Full lines represent majority spin, dashed lines minority spin.

In the case of the Ni adatoms the virtual bound states for the two spin directions are only weakly split and more or less coincide with the energy level of the split-off surface state. Therefore in the local  $s$ -DOS the two effects, the formation of the split-off state and the resonant scattering at the  $d_{z^2}$  resonances, cannot be distinguished. However, in the vacuum region (Fig. 9.7) the spin splitting of the majority and minority  $d_{z^2}$ -states can be clearly seen.

For Fe-, Mn- and Cr-adatoms another effect can be seen in the vacuum LDOS (Fig. 9.7) and the local  $s$ -DOS in Fig. 9.9. The intensity in the majority split-off surface state is considerably higher than for the minority state. This can have several reasons. For instance, due to the exchange splitting the majority potential is somewhat stronger than the minority one, leading to a smaller lateral extension of the split-off states and to a larger intensity on the adatom site. In particular

in the case of Cr, also the resonant interaction with the impurity  $d_{z^2}$  virtual bound state becomes important, strongly increasing the majority intensity on the impurity site as well as in vacuum.

Moreover, we have noticed a small peak appearing in the Mn- and Fe-adatom majority  $d$ -LDOS (see arrow (c) in Fig. 9.8) at the same position where the virtual bound states of Cu-adatom is situated ( $\approx -1.7$  eV). However, these protrusions have a different origin since there is no peak at  $-1.7$  eV in the  $d_{z^2}$ -LDOS for Mn- and Fe-adatom contrary to Cu- or Co-adatoms (see Fig. 9.9). They appear at the remaining  $d$ -partial LDOS ( $d_{xy}$ ,  $d_{yz}$ ,  $d_{xz}$  and  $d_{x^2-y^2}$ ) which are strongly damped in the vacuum. For symmetry reasons they do not hybridize with the  $s$ -LDOS explaining thus why we do not see a peak at the  $s$ -LDOS of Mn and Fe-adatoms contrary to Cu and Co-adatoms. We believe, however, that these peaks can be interpreted as split-off states from a surface state at the  $\bar{M}$  point [115] shown in Fig. 9.1, which shows a negative dispersion, such that a repulsive impurity potential leads for these  $d$ -states to a split-off state at higher energies, *i.e.* above the corresponding surface band.

## 9.7 *sp*-impurities as Adatoms

We consider now some *sp*-impurities as adatoms, for which the behavior is not complicated by the spin polarized  $d$ -states. As a first candidate we consider Ca at the beginning of the  $3d$ -series. The calculations give a well defined split-off state at the same position as for Cu and the  $3d$  impurities, *i.e.* below the minimum of the surface band. In addition we performed calculations for Zn, Ga and Ge adatoms. The split-off state is still seen for Zn but not anymore for Ga and Ge atoms. The reason for this is that in the LDOS of Ga and Ge adatoms the  $s$ -states have moved to lower energies below the surface state minimum. In this case the  $s$ -scattering at the adatoms becomes effectively repulsive, so that no split-off state occurs. To explain this we note that the scattering behavior of a scattering center is directly related to the  $t$ -matrix, and only indirectly to the potential. Our results are in contradiction with the usual statement that any attractive potential leads to a split-off state of a two-dimensional surface state. This is not correct in our case, since the  $t$ -matrix of the adatom is basically a three-dimensional quantity. For  $s$ -scattering at low energies  $E \sim 0$ , the  $t$ -matrix is related to the so-called scattering length  $a$ , being discussed in many books on quantum mechanics. The quantity  $a$  is the length where the extrapolation of the asymptotic form of the wave function for  $E = 0$  vanishes. For the simple model of spherical potential well of depth  $V$  and radius  $r_0$  the scattering length  $a$  is plotted in Fig. 9.10. For a repulsive potential the scattering length is positive and approaches the well radius  $r_0$  for large  $V$ . For a weakly attractive potential  $a$  is negative. However, when the potential  $V$  becomes stronger attractive, the scattering length assumes even stronger negative values, until it jumps at a critical strength  $V = V_0$  from

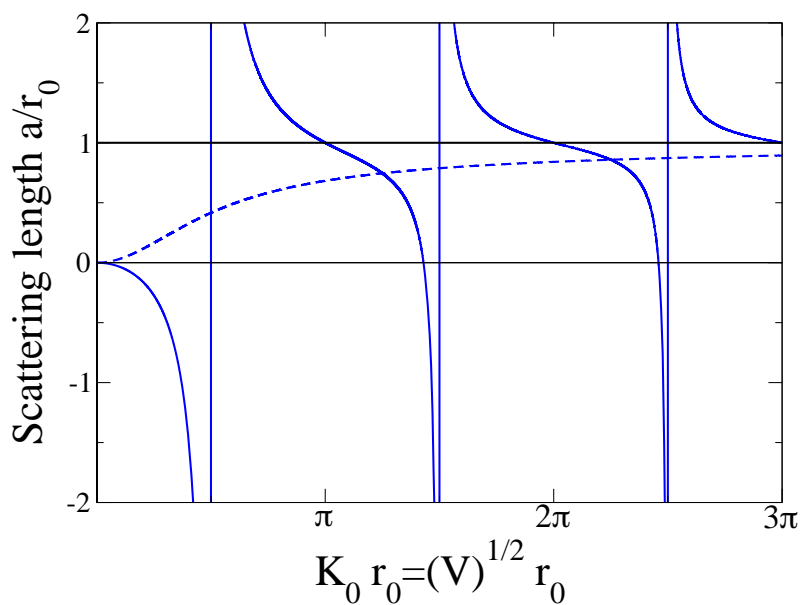


**FIG. 9.10** —. Variation of the scattering length  $a$  versus the potential. Full lines correspond to a negative potential while blue one describe the case of positive potential (always repulsive). The figure is obtained with a small positive energy value for an elastic  $s$ -scattering by a rectangular spherical potential depth.

$-\infty$  to  $+\infty$ , and is positive for further increased  $V$ -values. At the critical strength  $V_0$  a bound state appears at  $E = 0$ , moving to lower energies for further increased negative  $V$  values, and making the scattering length positive as for a repulsive potential. To compare with the real situation of the adatoms, the potential of the transition metal atoms is sufficiently weak so that a split-off state exists, since the atomic  $4s$ -level is far above the Fermi level and the scattering length is negative. However, for the Ge adatom the  $4s$ -level has moved below the minimum of the surface state, so that the scattering length is positive and no split-off state appears. When progressing further in the atomic table a split-off state can only appear again, when in the next series of the elements, say from Rb to Ag, the  $5s$ -level has moved down towards the Fermi level.

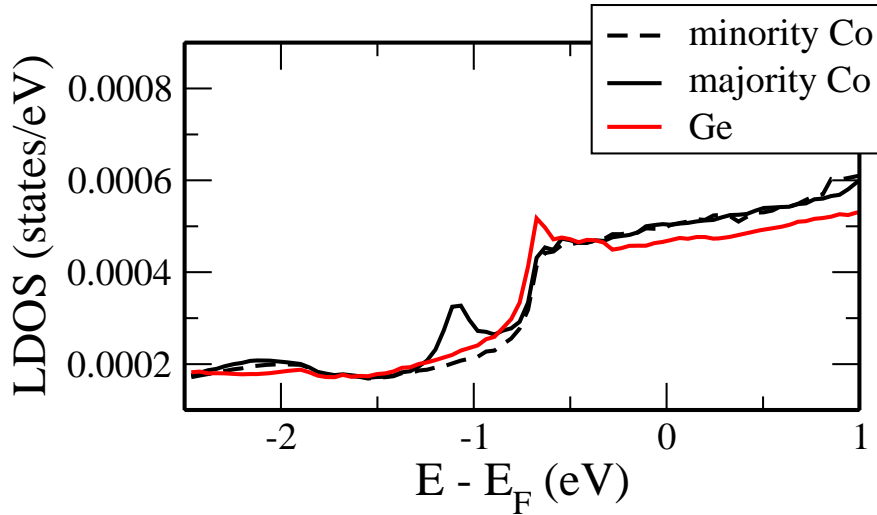


**FIG. 9.11** —. LDOS in vacuum at the second layer above the impurities which are sitting in the surface layer. One can see the appearance of the split-off state above Ge (red line) impurities but not above Co (black line). Above the last one, a protrusion appears at  $\approx -1.3$  eV on the majority spin channel which are due to the  $d$  state of the Co adatom.

## 9.8 Impurities in the Surface Layer

The scattering of the surface states at impurities in the first surface layer is basically different from the scattering at adatoms, since the effective potential for scattering is the difference between the potential of the impurity and the potential of the substituted Cu atom. Therefore all  $3d$ -impurities in the first layer do not show any split-off surface state, since the potential difference is very small (and moreover slightly repulsive). On the other hand for Ge impurities in the first layer, the calculations yield a split-off state, as is shown by the small peak in Fig. 9.11. Apparently the difference in potential is sufficiently attractive, such that a weakly localized state is formed. Therefore we obtain the opposite trend than for the adatoms. Transition metal impurities exhibit a split-off surface state as adatoms, but not as substitutional impurities in the first layer, whereas for Ga and Ge just the opposite is true.

## 9.9 Limitations of the LSDA

We now discuss the limitations of our calculations, in particular concerning the Kondo effect which cannot be captured by the LSDA. It is well-known that, at low temperatures, the spin moment of the magnetic impurities fluctuates, so that these appear non-magnetic. The temperatures at which the experiments are conducted are in many cases below the Kondo temperature; *e.g.*, a characteristic Kondo feature in the spectra was observed for Co on Cu [26].

The Kondo effect is characterized by a narrow Abrikosov-Suhl resonance of the DOS at  $E_F$  which is absent in our calculations. However, the split-off states are well below  $E_F$ . Furthermore, the split-off states appear by the interaction of impurity  $s$ -states with the surface band while the Abrikosov-Suhl resonance is due to the interaction of the localized impurity  $d$  states with the conduction electrons. Therefore our results on the split-off state are physically relevant.

On the other hand, the spin-dependent spectra of the magnetic impurities should be corrected towards an averaging of the two spin channels, if the temperature is below the Kondo temperature. Although the Kondo fluctuations kill the magnetic moment, the splitting of the  $d$  virtual bound states remains, corresponding to single- and double- occupancy of the impurity local state.

## 9.10 Summary

We have performed self-consistent calculations on single impurities deposited on Cu(111) surface in order to investigate the split-off state recently seen in experiment [26, 27]. We see two kinds of split-off states: One is due to an attractive potential below the  $\bar{\Gamma}$  surface state and the other one is due to a repulsive potential above the  $\bar{M}$  surface state. We found that Ca, all  $3d$  and Zn adatoms produce the first resonance which is not the case for the  $sp$  adatoms Ga and Ge. The presence of the split-off state for Ca means that  $s$  states have a stronger contribution to its realization than  $d$  states. The behavior is totally different if the impurities are embedded in the surface layer. In particular, Ga and Ge lead to a protrusion at the bottom of the surface band. One question addressed in this work is to explain the absence of a split-off state for  $sp$ -adatoms and  $3d$ -impurities embedded in the first surface layer. The former case is interpreted in terms of sign change of the scattering length for attractive potentials, which then may act effectively as repulsive potentials. In the latter case, the reference potential is the one of Cu surface, which is not too different from the potentials of all  $3d$  impurities. Therefore, in the latter case, we do not see any localization.

# Chapter 10

## Focusing Effect due to Subsurface Impurities

### 10.1 Introduction

Over the last decades a great deal of experimental and theoretical efforts has been devoted to study electrons in two-dimensional (2D) surface states. Here the (111) surface of the noble metals has served as a model system, exhibiting, as mentioned in the previous chapter, a surface state in the gap around the  $\Gamma$ -point of the bulk Brillouin zone. As is well known in metallic systems point defects cause long ranged oscillations of the charge density (Friedel oscillations), which are governed by the Fermi surface properties. For defects in the bulk, these Friedel oscillations of the charge perturbation vary for large distances  $r$  as  $1/r^3$  times an oscillatory function and are in the jellium model proportional to:

$$\delta n(r) \sim \frac{\cos(2k_F r + \delta)}{r^3} \quad (10.1)$$

with  $k_F$  being a Fermi wave number and  $\delta$  is a phase shift.

However in the case of adatoms on surfaces, the charge response decays for long in-plane distances  $r_{\parallel}$  slower than in the bulk and is determined by the surface states. In a free electron model, being well suited for the above surface state for Cu(111), the charge density is for large distances  $r_{\parallel}$  proportional to

$$\delta n(r_{\parallel}) \sim \frac{\sin(2k_F r_{\parallel} + \delta)}{r_{\parallel}^2} \quad (10.2)$$

However, since also bulk states exist, which span most of the phase space (see Fig. 9.1), the short range screening of the defect is dominated by these states, while only the long ranged behavior is determined by the surface state, which has a small wave vector  $k_F$  leading to long wave length oscillations.

Many authors have observed such long ranged oscillations around adatoms, small clusters and steps on the Cu(111) surface in STM experiments. One of

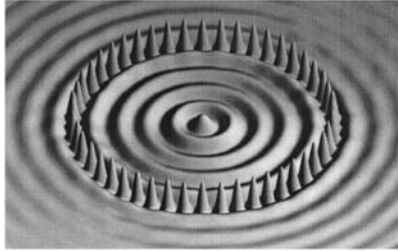


**FIG. 10.1** —. *LDOS at the Fermi energy in and around a 142.8 Angström diameter circular corral of 48 Fe atoms on Cu(111) [54].*

the most prominent among these is the work of Eigler *et al* [54]. By atomic manipulations they were able to construct a corral of Fe atoms on the (111) Cu surface, and have shown that the surface states in the corral are more or less localized and form a discrete spectrum of resonant states. As an illustration of these we show in Fig. 10.1 the result of KKR-calculations of Crampin *et al.* [125] for a circular corral of 48 Fe atoms on the Cu(111) surface. Shown are the local density of states at the Fermi energy and 5 Angström above the surface. Within the corral one sees a quantum well state with five maxima, corresponding to a localized state being more or less completely confined to the corral. Outside one sees oscillations arising from scattered surface state electrons at the corral, which decay with distance.

In contrast to the large amount of Scanning Tunneling Microscopy (STM) studies concerning electron scattering of the surface state electrons, only little experimental work has been reported on the scattering of bulk states. Concerning the scattering of bulk states, Schmid *et al.* [126] observed bulk state interference patterns of Argon bubbles in Al. Sprunger *et al.* [127] extracted short wavelength oscillations from constant current topographies and interpreted them as contributions of bulk states to the screening of surface defects. A fascinating result was obtained recently by Weismann *et al.* [32]. They investigated by STM at 8K Co atoms embedded in noble metals beneath the Cu(111) surface. The constant current topographies taken above the impurity atoms (Fig. 10.2) show two different charge density oscillations: (i) isotropic, long-wavelength standing wave of the surface state electrons and (ii) anisotropic short wavelength patterns with triangular shapes.

Basically the small rings are often observed in STM experiments but, to our knowledge, only Weismann and coworkers [32] proposed an explanation for the strange triangular shape of the charge oscillations (see also Fig. 10.3). They proceeded also to simulations of bulk electron scattering at a single point defect based on the bulk band structure of the host metal which are in good agreement with the observed STM topographies. The electron density at the surface is found to be shaped decisively by an electron focusing effect, which leads to anisotropic electron propagation due to the non-spherical geometry of the host metal's Fermi surface. As explained by these authors the scattering intensity is focused in spe-

cial directions being determined by regions of low curvature on the Fermi surface.

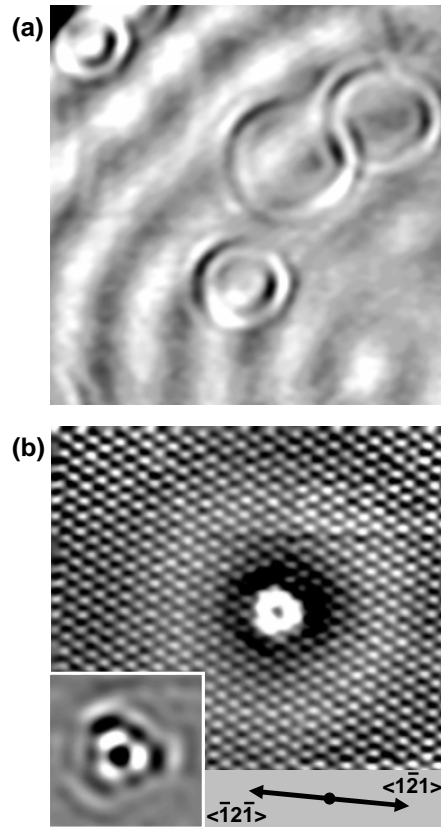


**FIG. 10.2** –. *STM-Topographies measured by Weismann et al. [32] of Co atoms buried below the (111) surface of a) Cu ( $9 \times 9$  nm;  $V_B = -80$  mV;  $I_T = 1$  nA) and b) Ag ( $8 \times 8$  nm;  $V_B = 100$  mV;  $I_T = 1$  nA). Inset: Fourier-filtered image (b) with the surface state and the atomic lattice removed (courtesy of Weismann et al. [32]).*

Motivated by this, we carried out a systematic theoretical investigation on the scattering effect of a Co impurity buried at different positions below the (001) and (111) surfaces of Cu. The wavelength patterns which are related to the curvature of the Fermi surface of the host have different shapes depending on the orientation of the surface. In addition we discuss typical anomalies arising from the reflection of the scattered waves at buried interfaces. We will show that

the rings observed by STM inform us about the position of the buried impurity, considered usually as dirt or imperfection of the surface sample, and can be used as a local probe atom in order to determine the position of buried imperfections such as interfaces and even to determine their magnetic properties.

The calculations were performed using the full-potential scalar-relativistic Korringa-Kohn-Rostoker Green-function method within Density Functional Theory.

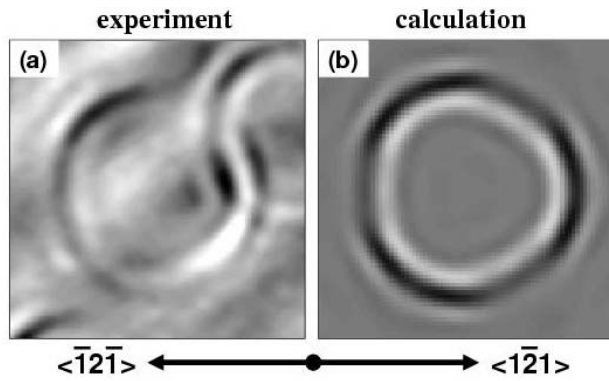


**FIG. 10.3** –. Comparison between experimental data and calculated LDOS-pattern [32]. Experimental data has been Fourier filtered to eliminate the surface state LDOS. a) and b):  $3 \times 3$  nm, with an impurity at the 7th layer below the surface (courtesy of Weismann et al. [32]).

## 10.2 Origin of the Effect

The shape of the “rings” observed by STM is related to the topological properties of the host Fermi surface as will be explained later. Furthermore, one has to say that this effect has the same origin as the Interlayer Exchange Coupling (IEC) [128, 129] which was one of the subjects of intense research in the last few years. The IEC consists on an oscillatory magnetic coupling between two magnetic interfaces (Fig. 10.4) separated by a non-magnetic spacer (usually a noble metal). The thickness of the latter affects strongly the magnetic coupling between the two magnetic interfaces and thus leads also to the Giant Magnetoresistance (GMR).

A great number of theoretical studies have been performed to investigate why the magnetic layers are coupled even with a large number of spacer ML in between. Firstly, in context of a Ruderman-Kittel-Kasuya-Yosida (RKKY) coupling mechanism, Bruno and Chappert [33] have given a general criterion how to obtain oscillation periods for the case of an arbitrary Fermi surface. But the existence of these oscillation periods does not rely on some of the strong restrictions entering the original RKKY model, like *e.g.* the point-like  $s-d$  exchange potential of the

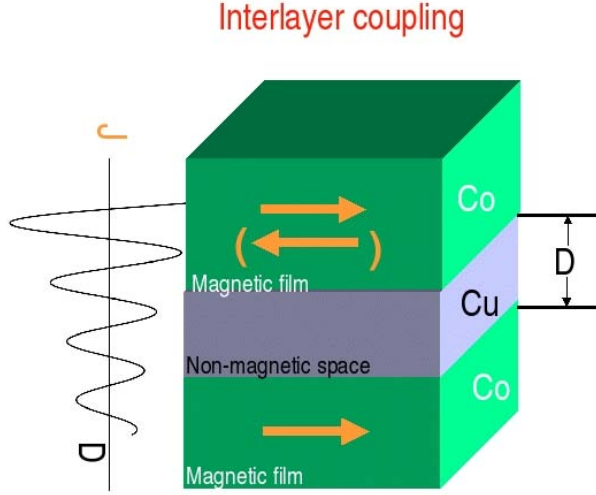


**FIG. 10.4** —. Schematic view of the Interlayer exchange coupling (IEC) with Co magnetic layers in green separated by a Cu-spacer. The left curve shows the oscillatory behavior of the magnetic coupling between the two magnetic interfaces versus the thickness  $D$  of the spacer.

magnetic layer. The essential approximation to obtain the oscillation periods is the so-called stationary phase approximation, being valid only for large spacer thickness.

We will derive in the following the asymptotic behavior of the Green function at a vacuum point  $\vec{r}$  located at a site  $\vec{R}_m$  with the presence of a buried impurity at a site  $imp$ .

We know that the Green functions of an ideal host perturbed by an impurity can be written as following

$$G^{mm}(\vec{r}, \vec{r}; E) = \overset{\circ}{G}^{mm}(\vec{r}, \vec{r}; E) + \int \int d\vec{r}_1 d\vec{r}_2 \overset{\circ}{G}^{m \text{ imp}}(\vec{r}, \vec{r}_1; E) t^{imp}(\vec{r}_1, \vec{r}_2; E) \overset{\circ}{G}^{imp m}(\vec{r}_2, \vec{r}; E), \quad (10.3)$$

$t$  being the t-matrix corresponding to the potential change  $\Delta V_{imp} = V_{imp} - V_{host}$  due to an impurity sitting at the site  $imp$

$$t^{imp}(\vec{r}_1, \vec{r}_2; E) = \Delta V^{imp}(r_1) (\delta(\vec{r}_1 - \vec{r}_2) + \int d\vec{r} \overset{\circ}{G}^{imp \text{ imp}}(\vec{r}_1, \vec{r}; E) t^{imp}(\vec{r}, \vec{r}_2; E)). \quad (10.4)$$

Thus, the space and energy resolved charge variation at site  $m$  between the unperturbed and host systems is given by

$$\Delta n^m(\vec{r}; E) = -\frac{1}{\pi} \text{Im} \Delta G^{mm}(\vec{r}, \vec{r}; E) \quad (10.5)$$

with

$$\Delta G^{mm}(\vec{r}, \vec{r}'; E) = \int \int d\vec{r}_1 d\vec{r}_2 \overset{\circ}{G}^{m \text{ imp}}(\vec{r}, \vec{r}_1; E) t^{imp}(\vec{r}_1, \vec{r}_2; E) \overset{\circ}{G}^{imp m}(\vec{r}_2, \vec{r}; E). \quad (10.6)$$

The spectral representation of the unperturbed Green functions of an ideal crystal

$$\overset{\circ}{G}^{mm'}(\vec{r}, \vec{r}'; E) = \sum_{\nu} \frac{1}{V_B} \int d\vec{k} \frac{\Psi_{\vec{k}\nu}(\vec{r} + \vec{R}_m) \Psi_{\vec{k}\nu}^*(\vec{r}' + \vec{R}_{m'})}{E + i\epsilon - E_{\vec{k}\nu}}, \quad (10.7)$$

with  $V_B$  being the volume of the Brillouin zone, allows us to rewrite eq. (10.6)

$$\begin{aligned} \Delta G^{mm}(\vec{r}, \vec{r}'; E) &= \sum_{\nu\nu'} \frac{1}{V_B} \int \int d\vec{k} d\vec{k}' \frac{\Psi_{\vec{k}\nu}(\vec{r} + \vec{R}_m)}{E + i\epsilon - E_{\vec{k}\nu}} \times \\ &\times \left[ \int \int d\vec{r}_1 d\vec{r}_2 \Psi_{\vec{k}\nu}^*(\vec{r}_1 + \vec{R}_{imp}) t^{imp}(\vec{r}_1, \vec{r}_2; E) \Psi_{\vec{k}'\nu'}(\vec{r}_2 + \vec{R}_{imp}) \right] \times \\ &\times \frac{\Psi_{\vec{k}'\nu'}^*(\vec{r} + \vec{R}_m)}{E + i\epsilon - E_{\vec{k}'\nu'}}. \end{aligned} \quad (10.8)$$

Using

$$\Psi_{\vec{k}\nu}(\vec{r}) = e^{i\vec{k}\vec{r}} U_{\vec{k}\nu}(\vec{r}) \quad \text{with} \quad U_{\vec{k}\nu}(\vec{r} + \vec{R}_m) = U_{\vec{k}\nu}(\vec{r}) \quad (10.9)$$

as a Bloch wavefunction in cell-centered coordinates around the lattice site  $\vec{R}_m$ , the term between square brackets can be simplified to

$$\int \int d\vec{r}_1 d\vec{r}_2 U_{\vec{k}\nu}^*(\vec{r}_1) e^{-i\vec{k}\vec{R}_{imp}} t^{imp}(\vec{r}_1, \vec{r}_2; E) U_{\vec{k}'\nu'}(\vec{r}_2) e^{i\vec{k}'\vec{R}_{imp}} \quad (10.10)$$

or simplified to a more compact form

$$e^{-i\vec{k}\vec{R}_{imp}} t_{\vec{k}\vec{k}'}^{\nu\nu'}(E) e^{i\vec{k}'\vec{R}_{imp}} \quad (10.11)$$

with

$$t_{\vec{k}\vec{k}'}^{\nu\nu'}(E) = \int \int d\vec{r}_1 d\vec{r}_2 U_{\vec{k}\nu}^*(\vec{r}_1) e^{-i\vec{k}\vec{r}_1} t^{imp}(\vec{r}_1, \vec{r}_2; E) e^{i\vec{k}'\vec{r}_2} U_{\vec{k}'\nu'}(\vec{r}_2) \quad (10.12)$$

$t_{\vec{k}\vec{k}'}^{\nu\nu'}$  is nothing else than the  $t$  matrix in a plane wave representation which is defined for any combination of  $k$  vectors of incoming and outgoing Bloch waves.

Let us go back again to eq. (10.8) in which the denominators can be rewritten in the following way

$$\frac{1}{E + i\epsilon - E_{\vec{k}\nu}} = \int_0^{\infty} \frac{dt}{i\hbar} e^{i(E+i\epsilon-E_{\vec{k}\nu})\frac{t}{\hbar}}, \quad (10.13)$$

and

$$\frac{1}{E + i\epsilon - E_{\vec{k}'\nu'}} = \int_0^\infty \frac{dt'}{i\hbar} e^{i(E+i\epsilon - E_{\vec{k}'\nu'})\frac{t'}{\hbar}}, \quad (10.14)$$

as Fourier integral over the time  $t$  and  $t'$ , so that

$$\Delta G^{mm}(\vec{r}, \vec{r}; E) = \sum_{\nu\nu'} \frac{-1}{\hbar^2 V_{BZ}^2} \int \int d\vec{k} d\vec{k}' \int_0^\infty \int_0^\infty dt dt' U_{\vec{k}\nu}(\vec{r}) t_{\vec{k}\vec{k}'}^{\nu\nu'}(E) U_{\vec{k}'\nu'}^*(\vec{r}) e^{i\Phi(\vec{k}, \vec{k}', t, t')}, \quad (10.15)$$

with the phase

$$\Phi(\vec{k}, \vec{k}', t, t') = (\vec{k} - \vec{k}')(\vec{R}_m - \vec{R}_{imp}) + (E + i\epsilon - E_{\vec{k}\nu})t/\hbar + (E + i\epsilon - E_{\vec{k}'\nu'})t'/\hbar. \quad (10.16)$$

In order to perform the integrals  $d\vec{k}$  and  $d\vec{k}'$  over the Brillouin zones, we divide the integrals in two-dimensional surface integrals over the constant energy surfaces  $E_{\vec{k}\nu} = \text{const.}$ ,  $E_{\vec{k}'\nu'} = \text{const.}$  and one-dimensional integrals  $dk_z$ ,  $dk'_z$ , perpendicular to these surfaces, the directions of which are given by the gradients  $\frac{\partial E_{\vec{k}\nu}}{\partial \vec{k}}$  and  $\frac{\partial E_{\vec{k}'\nu'}}{\partial \vec{k}'}$ . For a large difference  $\vec{R} = \vec{R}_m - \vec{R}_{imp}$ , the variation of  $\vec{k}_{||}$  over the constant energy surface leads to very rapid oscillations of  $e^{ik_z R}$  and also to cancellation of their contributions, so that only the neighborhood of the vectors  $\vec{k}_{||}$  for which  $k_z$  is “stable” or stationary contribute to the integral ( $k_z$  being normal to the surface). “Stable” means that the phase is stationary with respect to first order- $k_{||}$  variations on the constant energy surface around certain points. In the following, the index  $j$  specifies such a stationary point. The integral can, thus, be calculated by using the stationary phase approximation.

The stationary points are defined by

$$\partial_{\vec{k}} \Phi(\vec{k}, \vec{k}', t, t') = 0 \quad \text{which means} \quad \vec{R} - \frac{1}{\hbar} \frac{\partial E_{\vec{k}\nu}}{\partial \vec{k}} t = 0 \quad (10.17)$$

$$\partial_{\vec{k}'} \Phi(\vec{k}, \vec{k}', t, t') = 0 \quad \text{which means} \quad -\vec{R} - \frac{1}{\hbar} \frac{\partial E_{\vec{k}'\nu'}}{\partial \vec{k}'} t' = 0 \quad (10.18)$$

$$\partial_t \Phi(\vec{k}, \vec{k}', t, t') = 0 \quad \text{which means} \quad E - E_{\vec{k}\nu} = 0 \quad (10.19)$$

$$\partial_{t'} \Phi(\vec{k}, \vec{k}', t, t') = 0 \quad \text{which means} \quad E - E_{\vec{k}'\nu'} = 0 \quad (10.20)$$

The last two equalities describe the energy conservation from which we deduce that  $E_{\vec{k}\nu} = E_{\vec{k}'\nu'}$ . The first ones mean that: (i)  $\vec{k}$  and  $\vec{k}'$  are antiparallel and if they have the same length ( $\vec{k} = -\vec{k}'$ ), they describe then an elastic scattering situation; (ii) for a given direction of  $\vec{R}$  only contributions from identical  $\vec{k}$  values are obtained, in such a way that the group velocities are parallel or antiparallel to  $\vec{R}$ . The same is true for  $\vec{k}'$ . These equations determine, thus, the constant energy surface  $E = E_{\vec{k}\nu} = E_{\vec{k}'\nu'}$  as well as the points  $\vec{k}_j$ ,  $\vec{k}'_{j'}$  and the corresponding positive time-points  $t_j$ ,  $t'_{j'}$ .

Now we expand the phase  $\Phi(\vec{k}, \vec{k}', t, t') = \Phi_j(\vec{k}, t) + \Phi_{j'}(\vec{k}', t')$  around the stationary points up to second order and evaluate the integrals over the regions around the stationary points analytically for small variations  $\Delta\vec{k}_j$ ,  $\Delta\vec{k}'_{j'}$ ,  $\Delta t_j$  and  $\Delta t'_{j'}$ :

$$\Phi_j(\vec{k}, t) \approx \vec{k}_j \vec{R} - \frac{1}{2} \frac{t_j}{\hbar} \sum_{\alpha\beta} \frac{d^2 E}{dk_\alpha dk_\beta} \Big|_{\vec{k}_j} \Delta k_{\alpha j} \Delta k_{\beta j} - \frac{1}{\hbar} \frac{\partial E}{\partial \vec{k}} \Big|_{\vec{k}_j} \Delta \vec{k}_j \Delta t_j \quad (10.21)$$

$$\Phi_{j'}(\vec{k}', t') \approx -\vec{k}'_{j'} \vec{R} - \frac{1}{2} \frac{t'_{j'}}{\hbar} \sum_{\alpha\beta} \frac{d^2 E}{dk'_\alpha dk'_\beta} \Big|_{\vec{k}'_{j'}} \Delta k'_{\alpha j'} \Delta k'_{\beta j'} - \frac{1}{\hbar} \frac{\partial E}{\partial \vec{k}'} \Big|_{\vec{k}'_{j'}} \Delta \vec{k}'_{j'} \Delta t'_{j'} \quad (10.22)$$

Since for large  $R$  also  $t_j$  and  $t'_{j'}$  are large, the time integration can be extended from  $-\infty$  to  $\infty$  so that the integrals yield two  $\delta$ -functions. In particular, the integration over the time differences  $\Delta t_j$  gives

$$\int_{-\infty}^{+\infty} \frac{d\Delta t_j}{i\hbar} e^{-i\vec{v}_j \Delta \vec{k}_j \Delta t_j} = -\frac{2\pi i}{\hbar v_j} \delta(\Delta k_{zj}), \quad (10.23)$$

for the component  $\Delta k_{zj}$  of  $\Delta k_j$  in the direction of  $\vec{R}$  which coincides with the direction of the group velocity  $\vec{v}_j = \frac{dE}{\hbar dk_j}$ . The same can be done to  $\Phi_{j'}(\vec{k}', t')$ . Thus eq. (10.15) becomes

$$\begin{aligned} \Delta G^{mm}(\vec{r}, \vec{r}; E) &\approx \sum_{jj'} \frac{-4\pi^2}{\hbar^2 V_{BZ}^2 \hbar v_j v_{j'}} U_j(\vec{r}) t_{k_{zj} k'_{zj'}}(E) U_{j'}^*(\vec{r}) e^{i(k_{zj} - k'_{zj'})R} \times \\ &\times \int dS_j e^{-\frac{iR}{2\hbar v_j} \sum_{\alpha\beta} \frac{d^2 E}{dk_{\alpha j} dk_{\beta j}} \Delta k_{\alpha j} \Delta k_{\beta j}} \int dS_{j'} e^{\frac{-iR}{2\hbar |v_{j'}|} \sum_{\alpha\beta} \frac{d^2 E}{dk'_{\alpha j'} dk'_{\beta j'}} \Delta k'_{\alpha j'} \Delta k'_{\beta j'}}, \end{aligned} \quad (10.24)$$

with  $\alpha$  and  $\beta$  coordinates of the plane perpendicular to  $k_z$  which can be changed into new coordinates  $x$  and  $y$  such the mass tensor  $\frac{d^2 E}{dk_\alpha dk_\beta}$  is diagonal. Using the identity  $\int_{-\infty}^{+\infty} dx e^{-i\theta x^2} = \sqrt{\frac{\pi}{|\theta|}} e^{-i\frac{\pi}{4} \text{sign}(\theta)}$ , we arrive at the following form of the Green function:

$$\begin{aligned} \Delta G^{mm}(\vec{r}, \vec{r}; E) &\approx \sum_{jj'} \frac{16\pi^4}{V_{BZ}^2} U_j(\vec{r}) t_{k_{zj} k'_{zj'}}(E) U_{j'}^*(\vec{r}) \frac{e^{i[(k_{zj} - k'_{zj'})R + \phi_j + \phi_{j'}]}}{R^2} \times \\ &\times \frac{1}{\sqrt{\left| \frac{d^2 E}{dk_{zj}^2} \cdot \frac{d^2 E}{dk_{yj}^2} \right|} \sqrt{\left| \frac{d^2 E}{dk_{xj'}^2} \cdot \frac{d^2 E}{dk_{yj'}^2} \right|}}, \end{aligned} \quad (10.25)$$

with the phases  $\phi_j = -\frac{\pi}{4} \{ \text{sign}(\frac{d^2 E}{dk_{zj}^2}) + \text{sign}(\frac{d^2 E}{dk_{yj}^2}) \}$  and  $\phi_{j'} = -\frac{\pi}{4} \{ \text{sign}(\frac{d^2 E}{dk_{xj'}^2}) + \text{sign}(\frac{d^2 E}{dk_{yj'}^2}) \}$ .

$\phi_j$  is, respectively, equal to  $-\frac{\pi}{2}$ , 0 and  $\frac{\pi}{2}$  when  $k_{zj}$  is a maximum, a saddle point and a minimum of the surface of constant energy.

In the above derivation, we have implicitly assumed that the absolute contribution from the second derivatives  $\frac{\partial^2 E}{\partial k_x^2}$  and  $\frac{\partial^2 E}{\partial k_y^2}$  do not vanish at the critical point  $\vec{k}_j$  which in general is realized. However, if vanishing derivatives occur, we speak of a higher order critical point, for which the amplitude of the Green function decreases with an even smaller exponent than in  $\frac{1}{R^2}$ .

If we are interested in calculating the space resolved charge variation  $\Delta n(\vec{r})$  around *e.g.* the Fermi level we need to integrate  $\Delta n(\vec{r}; E)$  over the energies which corresponds to calculating the imaginary part of  $\Delta G^{mm}(\vec{r}, \vec{r}; E) = \int dE \Delta G^{mm}(\vec{r}, \vec{r}; E)$ . It is obvious from eq. (10.25) that the only terms depending on the energy are  $\frac{e^{i(k_{zj}-k'_{zj'})R}}{R^2}$  and  $t_{k_{zj}k'_{zj'}}(E)$  which can be considered as constant over a small region around the Fermi level. Using the fact that  $dE = \hbar v dk_z = \hbar v' dk'_{z'}$ , the former term after an energy integration is

$$\int dE \frac{e^{i(k_{zj}-k'_{zj'})R}}{R^2} = \hbar v_j \int dk_{jz} \frac{e^{i(1-\frac{v_j}{v_{j'}})k_{zj}R}}{R^2} \quad (10.26)$$

$$= \frac{\hbar v_j}{i(1-\frac{v_j}{v_{j'}})} \frac{e^{i(1-\frac{v_j}{v_{j'}})k_{zj}R}}{R^3} \quad (10.27)$$

We note that if  $j = j'$  and  $v_{j'} = -v_j$  then  $1 - \frac{v_j}{v_{j'}} = 2$ . This integration shows that the space resolved charge variation is proportional to  $1/R^3$  in agreement with the RKKY theory.

An important remark, is that the t-matrix  $t_{k_{zj}k'_{zj'}}$  also contributes a phase shift to the oscillations. Indeed

$$t_{k_{zj}k'_{zj'}}(E) = |t_{k_{zj}k'_{zj'}}| e^{i\delta_{k_{zj}k'_{zj'}}(E)}. \quad (10.28)$$

Thus eq. (10.25) becomes

$$\begin{aligned} \Delta G^{mm}(\vec{r}, \vec{r}; E) &\approx \sum_{jj'} \frac{16\pi^4}{V_{BZ}^2} U_j(\vec{r}) |t_{k_{zj}k'_{zj'}}(E)| U_{j'}^*(\vec{r}) \frac{e^{i[(k_{zj}-k'_{zj'})R + \phi_j + \phi_{j'} + \delta_{k_{zj}k'_{zj'}}(E)]}}{R^2} \times \\ &\times \frac{1}{\sqrt{\left| \frac{d^2 E}{dk_{xj}^2} \cdot \frac{d^2 E}{dk_{yj}^2} \right|} \sqrt{\left| \frac{d^2 E}{dk_{xj'}^2} \cdot \frac{d^2 E}{dk_{yj'}^2} \right|}}, \end{aligned} \quad (10.29)$$

Let us assume for simplification an elastic scattering process with one critical point meaning that  $j = j'$  and  $\vec{k}_j = -\vec{k}'_{j'}$  which leads then to

$$\Delta n^{mm}(\vec{r}; E) \approx \text{Im} \sum_j \frac{-16\pi^3}{V_{BZ}^2} U_j(\vec{r}) |t_{k_{zj}k_{zj}}(E)| U_j^*(\vec{r}) \frac{e^{i[2k_{zj}R + 2\phi_j + \delta_{k_{zj}k_{zj}}(E)]}}{R^2 \left| \frac{d^2 E}{dk_{xj}^2} \cdot \frac{d^2 E}{dk_{yj}^2} \right|} \quad (10.30)$$

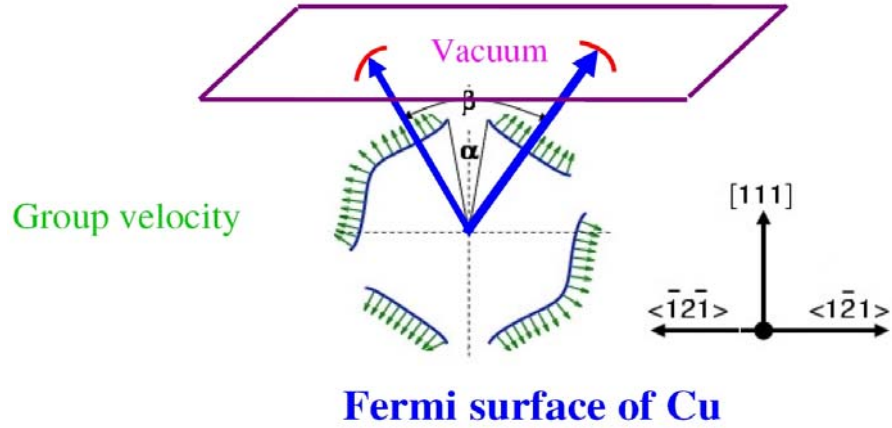


**FIG. 10.5** —. Appearance of high intensities (in red) in the vacuum charge due to the flatness of the Fermi surface of Cu in the directions of the blue vectors [32]. The small green arrows indicate directions of the electron's group velocity. We note the angle  $\beta$  between two flat areas is equal to about  $60^\circ$ .

Let us go back to our problem, namely a Co impurity sitting below the surface of Cu(111). Assume we have the two points  $r'$  and  $r$ : one is at the center of a Co impurity, the second is at the vacuum layer where the charge is calculated (see Fig. 10.5). These two points define  $\vec{R}$ . We see from the last equation eq. (10.30) that the most important factor is the denominator. If the denominator is very small meaning that the Fermi surface has a flat region, big values are obtained for the charge density from this  $\vec{k}$ -region, leading to a strong focusing of intensity in space region as determined by the group velocity  $v(\vec{k}_j) = \vec{v}_j$ .

The Fermi surface of bulk Cu which defines the behavior of the charge in the vacuum is rather simple compared to more complex Fermi surfaces of other materials. Indeed, the Cu Fermi surface is rather spherical apart from the eight band gaps in the  $L$ -directions; flat areas with strongly reduced curvature are present in the (110) directions enclosed by the two (111)-necks and two elevations in the (100) directions. The two blue vectors in Fig. 10.5 show an example of two directions which will produce high intensities (in red) in the vacuum. This is leading to the shape-anisotropy obtained experimentally. A totally spherical Fermi surface would lead to isotropic spherical oscillations of the vacuum charge. Thus in order to understand the anisotropic charge-shapes observed experimentally for the direction (111) or for the two other directions (001) and (110) we calculated also the denominator of eq. (10.30) or inverse mass tensor which is a measure of the flatness of the Fermi surfaces.

## 10.3 Computational details

First, we know that calculating the LDOS in a given vacuum layer above the surface, according to the model of Tersoff-Hamann [120], is proportional to the STS signal measured by the experimentalists. As shown with the experimental pictures (Fig. 10.2 and Fig. 10.3) we have to calculate a space-resolved density of state above a surface of a noble metal for a vacuum area of at least  $16 \text{ nm}^2$ . However we will calculate energy dependent charge density in the vacuum for larger areas, in some cases up to  $150 \times 150 \text{ nm}$ . To proceed to such calculations we need an approximation to overcome memory problems. We know already that the KKR method is ideal to treat perturbed systems. In fact, we proceeded to self-consistent calculations for an impurity sitting below the surface of Cu including the potential perturbations of first neighboring atoms. The converged potentials are then used to calculate the perturbed charge for a vacuum region above the surface of Cu(111). As in the experiment, the tunneling current at the Fermi level is measured, we average our space-dependent DOS over a small energy region around the Fermi energy  $E_F$ , *i.e.*  $E_F - 0.136 \text{ eV} < E < E_F$ . The number of K points in the irreducible two-dimensional Brillouin zone used in the calculations is sufficiently large to ensure correct charge calculations for such big systems (1250 K-points).

## 10.4 Co impurity below Cu(111)

We start by describing the results obtained for a Co impurity below the measured surface *i.e.* Cu(111). Figure 10.6 shows the impurity induced charge density at  $E_F$  in the vacuum region at  $6.1 \text{ \AA}$  above the surface after removing the surface state and the ideal surface background. In the present case the impurity is sitting at the  $6^{\text{th}}$  layer below the surface ( $12.15 \text{ \AA}$  below the surface). One notices the triangular shape of the charge difference with high values at the corners of the triangle. In addition, one notices a one and a half period oscillation from the red positive value to the blue negative values and finally to the almost null red values. The same period of oscillations was also noticed in the experiment. In front of the high intensities we get only small oscillations which can be understood from the figure 10.5 where the high flatness of the right side of the Fermi surface leads to higher intensities compared to the left side. This explains the triangle-shape with a three fold symmetry instead of the six fold symmetry of the *fcc*-(111) surface. On the right side of Fig. 10.6 is shown the Fermi surface of Cu in a (111)-direction on which we represented the inverse mass tensor or the denominator  $\sqrt{\left| \frac{d^2 E}{dk_x^2} \cdot \frac{d^2 E}{dk_y^2} \right|}$  from eq. (10.30) (we thank Peter Zahn from the University of Halle for providing us the results of this calculations). The low values are represented in red which correspond to the low curvature or to the high flat regions of the Fermi surface

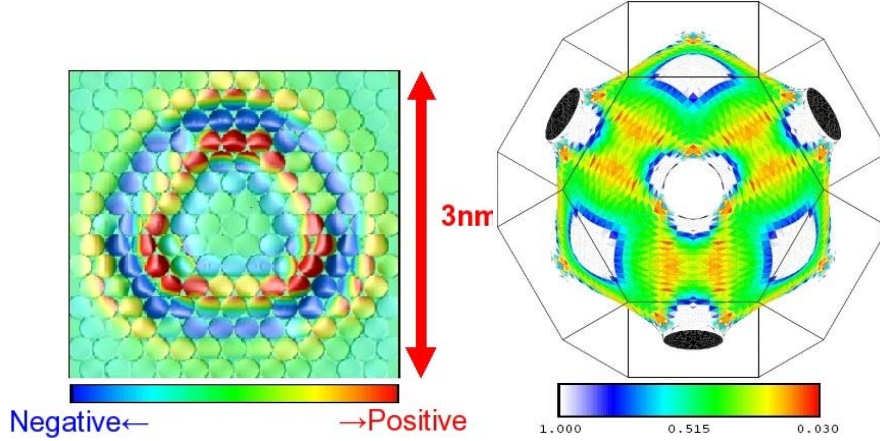


**FIG. 10.6** —. *Left: Impurity induced charge density at  $E_F$  after removing the ideal surface background charge (which includes the surface state) at a height of  $6.1 \text{ \AA}$  above the Cu(111) surface with an impurity sitting in the 6<sup>th</sup> layer below the surface. The triangular shape of the charge variation is in total accordance with the experiment of Weismann et al. [32] and is explained by the flat areas of the Fermi surface of bulk Cu represented in the right figure. The inverse mass tensor corresponding to the denominator of eq. (10.30) is represented on the Fermi surface in the (111) direction. Small values are represented in red lead to high intensities of the charge variation.*

which are in total accordance with the high intensity points calculated for the charge variation in the vacuum.

Let us go back another time to Fig. 10.5. Knowing the angle  $\beta = 60^\circ$  and the depth of the impurity  $Z_{imp}$  allows us, using trigonometric relations, to evaluate the diameter  $D$  of the “ring” or triangle we see at a given height above the surface and *vice-versa*: *i.e.* if we know the diameter of the ring we are able to determine the position of the impurity. This is a fascinating result which allows to determine experimentally the position of impurities below surfaces. The relation between the three mentioned quantities is simply given by  $D = 2Z \tan(\beta/2)$ . The circle having the theoretical diameter ( $21 \text{ \AA}$ ) obtained from the previous formula is shown in the left of Fig. 10.7. One can see that the result is very convincing.

The next step is to change the position of the impurity closer to the surface *e.g.* at third layer below the surface. This leads as depicted in the right picture of Fig. 10.7 to a smaller triangle with high intensities at the corners. The theoretical diameter ( $14 \text{ \AA}$ ) fits well with the charge-shape. This confirms again our finding

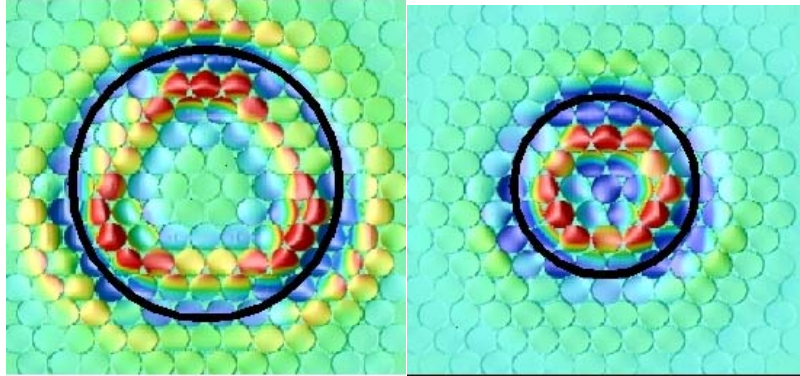


**FIG. 10.7** –. *Left: in black is the theoretical circle having a diameter calculated from the following trigonometrical relation  $D = 2Z \tan(\beta/2)$  using the exact position of the impurity. The results fit well with the charge variation in the vacuum above an impurity sitting at  $12.15 \text{ \AA}$  below the surface. Right: the impurity is moved closer to the surface and leads to a smaller triangle as well as smaller circle calculated trigonometrically.*

that the diameter of the ring leads to the position of any impurity below a noble metal surface.

We proceed by showing a broader picture (size  $100 \times 100 \text{ \AA}^2$ ) of the charge variation in the vacuum above an impurity which is sitting for example in the 6<sup>th</sup> layer below the surface (see Fig. 10.8). One is astonished by the presence of a second ring. The question is: where is it coming from? The answer is simply: from an artifact in our calculations arising from the slab geometry used to simulate the surface (see Fig. 10.9). Indeed, the waves leaving the impurity toward the upper surface hits the layer where the charge variation is calculated and leads to the first “ring” or triangle. The waves leaving the impurity from the opposite direction hits first the lower surface *i.e.* the vacuum layer from the lower side of the slab and are totally reflected there. Knowing the position of the other surface, we calculate easily the theoretical diameter of the second ring using again a simple trigonometric relation and obtain a value of  $77 \text{ \AA}$  which fits well with the oscillations obtained by DFT. This confirms the origin of the second ring. It is true that is only a simulation artifact but this opened us wide doors to unexpected applications of such results with an amazing property: The focused waves can travel through up to 23 monolayers. We will explain this in the next section.

Moreover, we point out that the second ring has high intensities rotated by an angle of  $\frac{\pi}{3}$  ( $60^\circ$ ) compared to the first ring. This is explained by the fact the necks

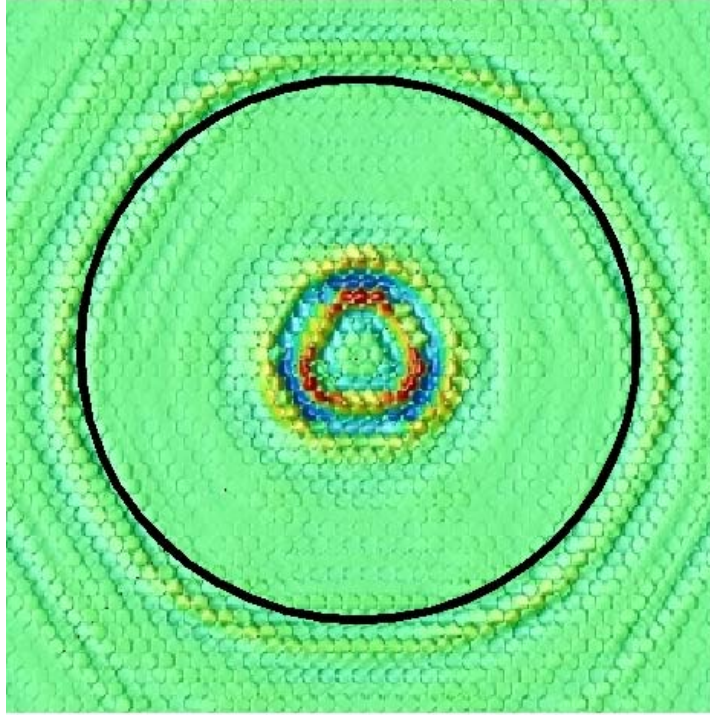


**FIG. 10.8** –. Charge variation due to the presence of a Co impurity at  $12.14 \text{ \AA}$  below a Cu(111) surface. Size of the vacuum charge shown is  $100 \times 100 \text{ \AA}^2$ . One notices a second ring appearing due to reflection of waves at the other side of the slab. Trigonometrical calculations leads to the black circle which has a diameter of  $77 \text{ \AA}$  and fits well with our DFT calculations.

from the down side of the Fermi surface are rotated by an angle of  $\frac{\pi}{3}$  compared to the upper side of the Fermi surface.

## 10.5 Magnetic effect: Interface Cu/Co(111)

The amazing idea we were talking about is to replace few monolayers of Cu from the other side of the slab by Co. We have chosen here six Co-monolayers. By doing this we calculate again the charge variation in the vacuum and we get the results in Fig. 10.10. The striking effect is the appearance of a third ring. This is interesting and as a first try, one explains it by the presence of the Co interface.

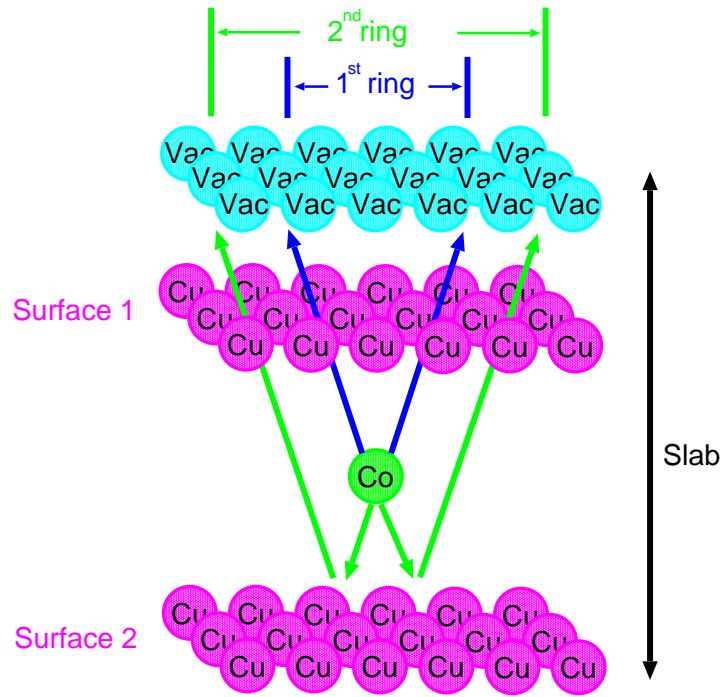


**FIG. 10.9** – Reflection of the waves from the other side of the slab leads to the second ring while the waves going directly to the vacuum-side where the charge is calculated gives rise to the first small ring.

Nice! but one needs to prove it. We do so by calculating as done classically throughout the present chapter using simple trigonometric relation relating the position of the impurity, the position of the interface and also the position of the second slab-surface. The latter one leads as noticed in the same figure to the second ring already observed previously without a Co interface in the precedent section plus a middle black ring with a diameter of  $49 \text{ \AA}$ . The waves leaving the impurity toward the second surface of the slab hit first the Co-interface and are reflected to form the third middle ring. For instance, there are also waves going through the Co layers and hit the second slab-surface, after which they are reflected to form the second outer ring.

This means that the Co impurity atom plays a role of a local probe which determines the exact position of the interface of Co. This is, in our mind, a very important result which may serve as a very convenient and simple tool for the experimentalists using simple trigonometric relations.

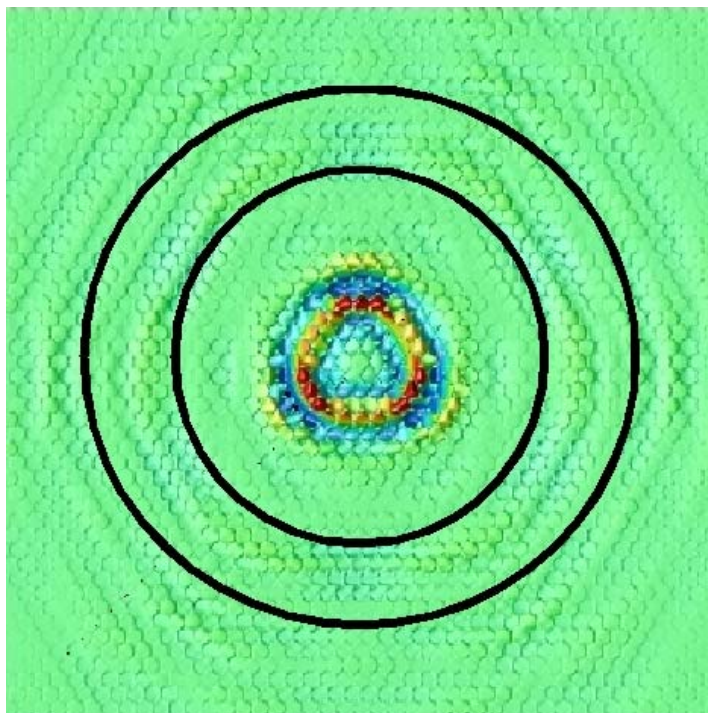


**FIG. 10.10** –. Charge variation in the vacuum above a  $\text{Cu}(111)$  surface below which is buried a Co impurity always at the same position ( $12.14 \text{ \AA}$ ). The difference from the previous pictures is the presence of a third middle ring due to the presence of a Co interface at which the waves are reflected. The diameter of the second ring is about  $49 \text{ \AA}$ .

By realizing that the Co film is ferromagnetic, we should also observe effect from the magnetism. Well, a good opportunity present in the actual case is the magnetic Co-interface. We assume that the local moment of the Co impurity is parallel to the moment of the Co film. The spin-resolved charge variation is shown in Fig. 10.11. In the left the majority-spin is depicted while in the right the minority-spin is shown. We have focused on the intensities of the outer region from the first triangle that we hid by an orange disk. The main result here is that the second ring of the majority-spin has lower intensities compared to the second ring of the minority-spin. With other words, the Co-interface acts like a spin-filter reflecting mainly the waves with a minority-spin character. This is explained by the fact that Co majority Fermi surface is very similar to the Fermi

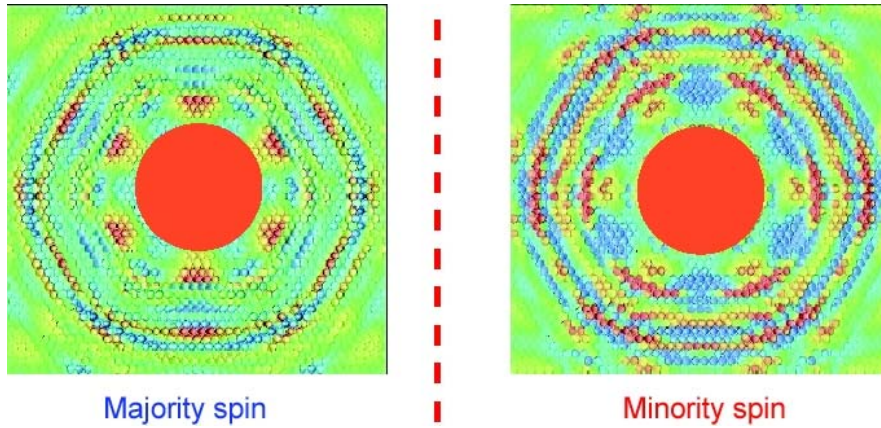


**FIG. 10.11** —. *Spin-resolved charge variation in the vacuum above a Cu(111) surface below which is buried a Co impurity plus a Co-interface. The first triangle is hidden by an orange disk in order to focus on the intensities of the second and third ring. The majority-spin charge is characterized by lower intensities for the middle ring compared to the minority-spin charge. The Co-interface plays here the role of spin-filter (see text for more details).*

surface of Cu (it has a filled majority band) whereas the minority-spin Fermi surface is different. In addition, one notices a phase shift between the minority and majority oscillations: when there is a positive intensity (in red) in the right picture of Fig. 10.11 we see a negative intensity (in blue or blue green) in the left picture.

This is also leading to an important result namely: we are able to determine the magnetic state of an interface buried at several monolayers below the surface by looking at the strength of charge-intensities of the third ring in the actual case. On the other hand, the first ring informs us about the magnetic state of the atom-probe.

## 10.6 Co impurity below Cu(001)

It is interesting to investigate the Co-impurity below Cu-surface oriented in other directions *e.g.* (001). Figure 10.12 shows the charge variation in the vacuum for a square of  $40\text{\AA} \times 40\text{\AA}$  at a height of  $3.5\text{\AA}$  above the surface. The impurity is sitting at the  $8^{\text{th}}$  layer below the surface (at  $14\text{\AA}$ ). The result is a square with high charge intensities at its corners. This fits well with the Fermi surface shown on Fig. 10.12 on which again the red values represent low values of the

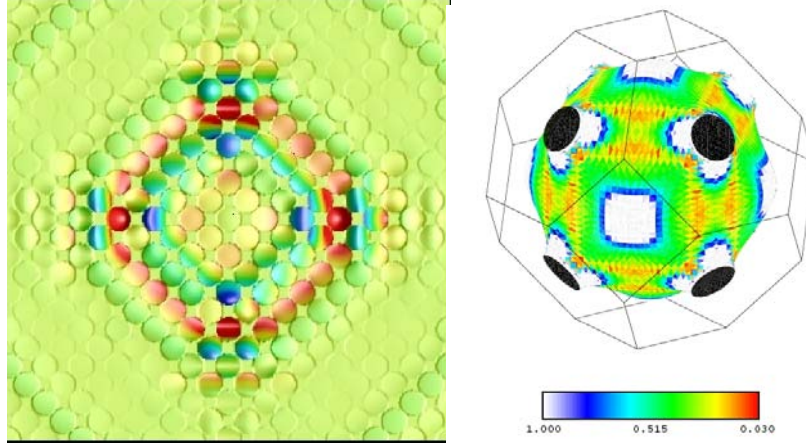


**FIG. 10.12** —. *Left: Charge after removing the surface state for an area of  $40\text{\AA} \times 40\text{\AA}$  at a height of  $3.5\text{\AA}$  above the  $\text{Cu}(001)$  surface with an impurity sitting in the  $8^{\text{th}}$  layer below the surface. The shape of the charge variation is a square and is explained by the flat areas of the Fermi surface of bulk Cu represented in the right figure. The inverse mass tensor corresponding to the denominator of eq. (10.30) is represented on the Fermi surface in the  $(001)$  direction. Small values are represented in red lead to high intensities of the charge variation.*

denominator of eq. (10.30). This means where the surface is flat.

Let us do an “experiment”: we can see from the Fermi surface in Fig. 10.12 that the angle  $\beta/2$  is now approximately equal to  $45^\circ$ . In fact, it has to be a bit smaller as the points with low curvature are not exactly situated between the  $(111)$  directions defining the necks of the Fermi surface. For an angle of  $45^\circ$ , we obtain, using the previous trigonometric relation, the dashed orange circle in Fig. 10.13. One sees that the diameter ( $35\text{\AA}$ ) is too big and has to be reduced. For a value of  $38^\circ$  we get the inner black circle (diameter of  $27\text{\AA}$ ) which fits well with the charge oscillations. In other words, knowing the shape of the oscillations observed by STS allows an information of the Fermi surface of the host, *i.e.* the direction of the group velocities at the critical points.

## 10.7 Summary

We investigated systems including up to 3000 vacuum Voronoi cells in order to verify experimental results concerning shapes of charge oscillations at  $E_F$  due to buried impurities. Usually these, even if always observed, are not explained. Here

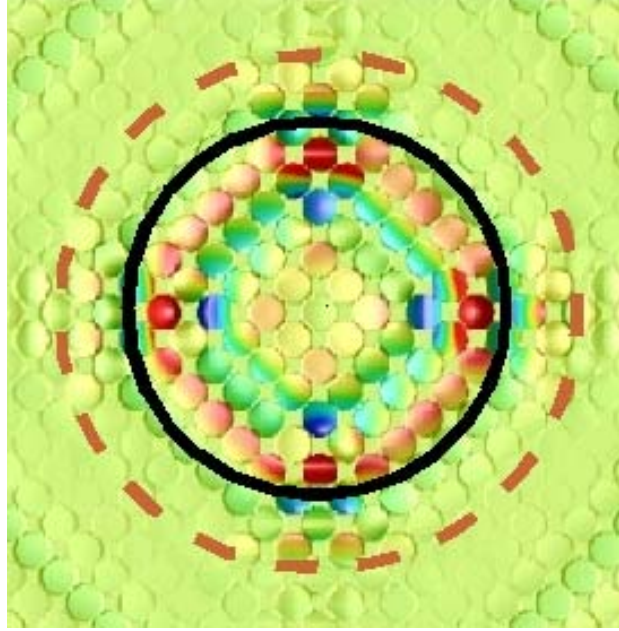


**FIG. 10.13** –. Representation of two rings calculated with different angles  $\beta/2$ : (i) dashed orange circle for an angle of  $45^\circ$  which would correspond to low curvature points sitting exactly between two neck of the Fermi surface, and (ii) a black circle for an angle of  $38^\circ$  being in good agreement with the charge oscillations.

we gave an explanation as also proposed by our collaborators [32] of the origin of these oscillations which fits very well with our DFT calculations and with the STS experiment. To understand this, we derived a formula describing the asymptotic behavior of the energy dependent charge density due to the presence of an impurity. The shape of the observed rings is determined by the flatness of the Fermi surface. This is basically the same effect which leads also to the IEC between magnetic layers separated by non-magnetic spacers. For the (001) surface, the anisotropy of the Cu Fermi surface leads to a square shape of the oscillations found in the vacuum. While for the (111) surface the oscillations have a triangular shape. The hexagonal symmetry of the Fermi surface close to the neck is still seen but a stronger flatness of the Fermi surface in three directions reduces the symmetry which leads to three high intensity directions dominating the oscillations.

Our results can lead to important experimental applications. First the diameter of the ring containing the triangle allows us to calculate the impurity-depth

using simple trigonometric relations. Second, the impurity is in fact a local probe atom which permits the determination of a hypothetical second imperfection such as an interface through back-scattering processes. We verified this for a Co-interface buried below the Cu-surface. Third, the local probe atom leads also to magnetic information concerning the buried imperfection. Indeed, we showed for the case of Co-interface that there are higher intensities of the minority-spin charge compared to the majority-spin charge due to a higher scattering of the electrons at the minority-spin charge of the Co-interface. We explain this by the fact that the majority-spin band of Co is filled leading to a majority Fermi surface being very similar to the one of Cu which is not the case for the minority-spin states.

# Chapter 11

## Conclusion

We aimed by the present thesis to reach three goals: first, to investigate the complex magnetism of ad-clusters deposited on surfaces; second, to determine eventual localizations of noble metal surface states caused by the presence of different kind of adatoms; third, to image Fermi surface in real space through STM or STS measurements using a local probe impurity buried below the surface. The latter one allows the determination of not only the position of buried interfaces but also of their magnetic state.

The most elegant ab-initio method for such a work is the KKR method which does not require periodic supercells.

**Complex Magnetism of Ad-Clusters:** To reach the first goal, we faced the problem of magnetic frustration between the ad-clusters and the substrate, plus the possible magnetic frustration within the clusters which lead to non-collinear magnetism. To solve the problem, we developed and implemented a new method based on the KKR formalism which allows the investigation of non-collinear magnetic configurations.

A prototype surface for studying the magnetic frustration between the ad-clusters and the substrate is the (001) *fcc* surface. We started with the Ni surface which has rather small surface magnetic moments and shows relatively weak hybridization with the adatoms. Then we continued with a surface characterized by larger magnetic moments ( $\text{Fe}_{3\text{ML}}/\text{Cu}(001)$ ) and a much stronger hybridization. The third step consisted on considering a substrate with a triangular geometry leading, thus, to an additional frustration within the ad-cluster. A common fact is that the origin of the frustration is the competition of the antiferromagnetic exchange coupling among the Cr or Mn atoms with the antiferromagnetic (for Cr) or ferromagnetic (for Mn) exchange coupling between the adatoms and the substrate.

On Ni(001), we found that Cr and Mn first-neighboring adatom dimers can show non-collinear behavior, while increasing the distance between the adatoms of the dimer leads to the same collinear state as for single adatoms. The com-

compact Cr and Mn dimers are characterized by a non-collinear solution where both magnetic moments are antiparallel and are almost perpendicular to the magnetization direction of the surface atoms. The energy differences between the collinear ground states and the non-collinear ones are very small. Concerning the trimers, only Mn has a metastable non-collinear solution while for bigger clusters we found only collinear configurations. A Heisenberg model indicates, however, that the two configurations non-collinear and collinear are almost degenerate for clusters with an even number of adatoms as well as for a full monolayer.

On  $\text{Fe}_{3\text{ML}}/\text{Cu}(001)$ , the magnetic interaction between the clusters and the surface atoms is stronger and destroys the non-collinear solution found for Cr-dimer, while it re-enforces the stability of the non-collinear ground state of Mn-dimer. Furthermore, Cr- and Mn-trimers are both characterized by a non-collinear ground state. We found that tetramers for different shapes have similar energies in their magnetic ground state. A Cr-pentamer which is non-collinear was also considered in order to compare our results with the XMCD measurements of the group of Wirth. We interpreted the presence of a kink seen in the experimental curve describing the effective magnetic moments versus the size of the clusters. This kink is due to the presence of different structural and magnetic configurations.

On the Ni-surface with a triangular geometry ( $fcc(111)$ ), we found interesting results, namely that the magnetic solutions for compact Cr or Mn ad-trimers are not so different from the expected non-collinear configuration of a free frustrated trimer (angle of  $120^\circ$  between neighboring adatoms). Indeed, the effect of the substrate leads to the stabilization of one adatom's moment as parallel (Cr) or antiparallel (Mn) to the substrate magnetization. On the other hand the two remaining adatoms tend to couple AF (Cr) or FM (Mn) to the substrate atoms with a small variation of the rotation angle compared to the expected  $120^\circ$ . The other shapes considered for the trimers lead to collinear solutions as ground states with very small energy differences with respect to the non-collinear local minimum for the case of Mn. Compact tetramers seem to be Ferri whereas tetramers-b are more subject to non-collinear magnetism.

We predicted the antiferromagnetic nanochains on ferromagnetic surfaces with an even number of adatoms to be non-collinear while an odd number of adatoms leads for restricted wire lengths to a ferrimagnetic state as a ground state. In the latter case, a transition from ferrimagnetic to non-collinear ground state is expected to occur at a length determined by a Heisenberg model depending on the strength of the magnetic interaction between the chains and the substrate compared to the intra-chains antiferromagnetic interaction.

**Surface State Scattering by Small Clusters:** The second goal of this thesis is to understand an interesting effect seen very recently with STS experiments [26, 27]. When surface state electrons scatter at perturbations, such as magnetic or non-magnetic adatoms or clusters on surfaces, an electronic reso-

nance, localized at the adatom site, can develop below the bottom of the surface state band for both spin channels. We carried out a systematic theoretical investigation of the electronic structure of these surface states in the presence of magnetic and non-magnetic atoms on Cu(111). We found that Ca and all  $3d$  adatoms lead to a split-off state at the bottom of the surface band which is, however, not seen for the  $sp$  elements Ga and Ge. The situation is completely reversed if the impurities are embedded in the surface: Ga and Ge are able to produce a split-off state whereas the  $3d$  impurities are not. The resonance arises from the  $s$ -state of the impurities and is explained in terms of sign change of the scattering length for attractive potentials, which then may act effectively as a repulsive potential.

**Focusing Effect due to Subsurface Impurities:** The third goal we wanted to achieve is the investigation of very anisotropic charge oscillations on noble metal surfaces arising from buried impurities. This effect was experimentally observed by our collaborators [32]. This was a challenging task for an ab-initio method as we had to calculate up to 3000 vacuum Voronoi cells in order to describe these oscillations which are shaped by the low curvature of the Fermi surface. The latter effect creates also the famous IEC between magnetic layers separated by non-magnetic spacers. Due to its anisotropy, the Cu Fermi surface leads for the (111) surface to respectively a triangular shape of the oscillations found in the vacuum while for the (001) surface the shape is square. To understand it, we derived a formula describing the asymptotic behavior of the charge due to the presence of an impurity.

Most important, however, is that we predicted and proposed a new method to determine the position as well as the magnetism of any other buried impurity or buried interface through the presence of a single local probe impurity. Indeed as we explained earlier, the scattering of Cu states by the impurity results in the appearance of rings in STS. The diameter of the first ring or triangle allowed us to calculate the impurity-depth using simple trigonometric relations. Additional observed rings are the result of the scattering of electron waves at an additional subsurface interface, and allowed to estimate their positions. Finally through the intensity of the spin-resolved charges, we get information about the magnetism of the impurity.



# Appendix A

## Force Calculations

An accurate treatment of the full potential is crucial for the calculation of forces, since in deriving an expression for the force, the extremal properties of the total energy are used, so that the force formula is no longer variationally invariant. By taking the derivative of the total energy with respect to the coordinate  $\vec{R}^m$  of atom  $m$ , the force is given by

$$\vec{F}^m = -\frac{\partial E}{\partial \vec{R}^m} \Big|_{n(\vec{r}; \vec{R}^m)} - \int d\vec{r} \frac{\delta E}{\delta n(\vec{r})} \frac{\partial n(\vec{r}; \vec{R}^m)}{\partial \vec{R}^m} = Z^m \frac{\partial V}{\partial \vec{r}} \Big|_{\vec{r}=\vec{R}^m} \quad (\text{A.1})$$

The first term, to be evaluated for density  $n(\vec{r}; \vec{R}^m)$  for the fixed position  $\vec{R}^m$  of the nucleus, is the Hellmann-Feynman (HF) force, being given by the electric field  $\frac{\partial V}{\partial \vec{r}}$  of the electrons on the nuclear charge  $Z^m$  of the nucleus. The second term gives corrections due to approximations made in the solution of the Kohn-Sham equations. It vanishes in an exact treatment, since then  $\frac{\delta E}{\delta n(\vec{r})} = E_F$  is a constant. Within the full potential KKR formalism, the Kohn-Sham equations for the valence electrons are solved practically exactly, with the only approximation being the  $l_{max}$  cut-off. However, the use of the HF-formula, i.e. the first term in (A.1), requires also a full potential treatment of the core electrons. If an atom is shifted, the charge density of the core electrons experiences in a solid a small anisotropic distortion induced by the crystal field, which leads to an important contribution to the force on the nucleus and which unfortunately cannot be described in a spherical-core treatment. This problem can be overcome by making a spherical ansatz for the core density entering in the total-energy expression. The force is then calculated as the derivative of the total energy with respect to the nuclear position assuming that the Kohn-Sham equations are solved exactly for the valence electrons only. The resulting expression for the force  $\vec{F}^m$  on the atom  $\vec{R}^m$  is given by[130]

$$\vec{F}^m = Z^m \frac{\partial V_M(\vec{r})}{\partial \vec{r}} \Big|_{\vec{r}=\vec{R}^m} - \int d\vec{r} n_c(\vec{r} - \vec{R}^m) \frac{\partial V(\vec{r})}{\partial \vec{r}} \quad (\text{A.2})$$

where  $Z^m$  is the nuclear charge and  $n_c(\vec{r} - \vec{R}^m)$  the core charge density of atom  $m$ . Furthermore  $V_M(\vec{r})$  is the Madelung potential and  $V(\vec{r})$  the Kohn-Sham potential. While the first term is the force on the nucleus as given by the Hellmann-Feynman theorem (but without the contribution from the core electrons at atom  $\vec{R}^m$ ), the second term represents the force on these core electrons and also includes an exchange-correlation contribution, arising from the exchange between valence and core electrons. Thus basically eq. (A.1) gives the force on the ion consisting of the nuclear charge and the core charge of atom  $m$ . Due to the vector character of the potential derivatives in eq. (A.1), only the  $l = 1$  components of the potentials  $V_M(\vec{r})$  and  $V(\vec{r})$  are needed for the force. Since in the present full-potential treatment the coefficients  $V_L(r)$  are anyhow calculated during the selfconsistency cycles, the calculation of the force does not require additional efforts. Moreover the  $l = 1$  components of the potentials are essentially determined by the  $l = 1$  components of the valence charge density  $n(\vec{r})$ . Therefore one obtains only contributions from the interference of wave functions differing by  $\Delta l = \pm 1$ , i.e. sp, pd, df, fg, ... interference terms.

## Appendix B

# Lattice Relaxations

All-electron methods based on a spherical potential of muffin-tin type or on the atomic sphere approximation (ASA) have in general proven to be very successful and efficient for the description of the electronic structure of solids. However systems with lower symmetry and/or open structures require a more accurate treatment going beyond the spherical approximation. In particular this is necessary, if forces and lattice relaxations are calculated, since for these problems the spherical approximation fails completely.

In contrast to the simplicity of the force calculation, the description of lattice relaxation effects is rather complicated within the KKR method. The main reason is the site-centered angular momentum expansions used in the Green function. In the case of lattice relaxations one needs an angular momentum expansion around the shifted position, i. e. around a non-lattice site. While in principle the host Green function can be calculated for any interstitial site by introducing a supercell with additional empty positions, this is a cumbersome procedure for the small lattice relaxations occurring for substitutional defects. In this case a transformation formalism, used e.g. in Ref. [130], is more convenient. The structural host Green function is transformed from the unshifted coordinates to the new ones being shifted by  $\vec{s}^n$

$$\tilde{G}_{LL'}^{nn'}(E) = \sum_{L''L'''} U_{LL''}(\vec{s}^n; E) G_{L''L'''}^{nn'}(E) U_{L'L'''}(\vec{s}^{n'}; E) \quad (\text{B.1})$$

where

$$U_{L'L}(\vec{s}; E) = 4\pi \sum_{L''} i^{l'+l''-l} C_{LL'L''} j_{l''}(\sqrt{E}s) Y_{l''}(\vec{s}) \quad (\text{B.2})$$

The  $\tilde{G}$  is the host Green function but expanded in the shifted coordinate system. An analogous U transformation has to be done for the t-matrix. Finally we must solve the following Dyson equation for the structural Green function to obtain the new Green function for potentials or t-matrices on the shifted sites.

$$\bar{G} = \tilde{G}^0 + \tilde{G}^0 [t - \tilde{t}^0] \bar{G} \quad (\text{B.3})$$

where  $\tilde{G}^0$  and  $\tilde{t}^0$  are the host Green function and host t-matrix in the angular momentum expansion around the shifted sites (B.1). Thus, apart from the  $U$ -transformation, the structure of the Dyson equation is unchanged. While the  $U$ -transformation eq. (B.1) is exact, if the sums over  $L''$  and  $L'''$  are extended over infinite angular momenta, in practical calculations an  $l_{max}$ -cut-off is used. As can be seen from eq. (B.2), for small  $s$  the  $U_{LL'}$ -matrix couples states with  $l-l' = \pm 1$ . Thus a relatively high  $l_{max}$  has to be chosen and the error increases with increasing displacements. Typically calculations with  $l_{max} = 4$  are for substitutional defects sufficiently accurate up to displacements of 10 % of the nearest neighbor distance. For larger displacements or interstitial defects the Green function  $\tilde{G}_{LL'}^{mn'}$  has to be determined by Brillouinzone integration.

## Bibliography

- 
- [1] Feynman, R. P. There's plenty of room at the bottom, *Eng. Sci.* **23**, 22-36 (1960).
  - [2] G. Binnig and H. Rohrer, *Helv. Phys. Acta* **55**, 726 (1982); G. Binnig, H. Rohrer, Ch. Gerber, and E. Weibel, *Phys. Rev. Lett.* **49**, 57 (1982).
  - [3] P. Gambardella, S. Rusponi, M. Veronese, S. S. Dhesi, C. Grazioli, A. Dallmeyer, I. Cabria, R. Zeller, P. H. Dederichs, K. Kern, C. Carbone, H. Brune, *Science* **300**, 1130 (2003).
  - [4] J. T. Lau, A. Fölsch, R. Nietubyc, M. Reif, and W. Wurth, *Phys. Rev. Lett.* **89**, 57201 (2002).
  - [5] M. Reif, Magnetic properties of small chromium and gadolinium clusters, deposited on magnetic substrates, PhD thesis, University of Hamburg (2005); M. Reif, L. Glaser, M. Martins, W. Wurth, private communication.
  - [6] G. van der Laan, *J. Synchrotron Rad.*, **6**, 694 (1999).
  - [7] P. Hohenberg and W. Kohn, *Phys. Rev.* **136**, B864-871, 1964.
  - [8] W. Kohn and L. J. Sham, *Phys. Rev.* **140**, A1133-1138, 1965.
  - [9] S. Rusponi, T. Cren, N. Weiss, M. Epple, P. Bulushek, L. Claude and H. Brune, *Nature Materials* **2**, 546 (2003); W. Kuch, *ibid.* **2**, 505 (2003).
  - [10] T. Jamneala, V. Madhavan, and M. F. Crommie, *Phys. Rev. Lett.* **87**, 256804 (2001).
  - [11] V. Madhavan, T. Jamneala, K. Nagaoka, W. Chen, Je-Luen Li, S. G. Louie, and M. F. Crommie, *Phys. Rev. B* **66**, 212411 (2003).
  - [12] F. Silly, M. Pivetta, M. Ternes, F. Patthey, J. P. Pelz, and W.-D. Schneider, *Phys. Rev. Lett.* **92**, 16101 (2004).
  - [13] P. Gambardella, A. Dellmeyer, K. Maiti, M. C. Malagoli, W. Eberhardt, K. Kern, and C. Carbone, *Nature (London)* **416**, 301 (2002).
  - [14] V. S. Stepanyuk, L. Niebergall, R. C. Longo, W. Herget and P. Bruno, *Phys. Rev. B* **70**, 75414 (2004).
  - [15] K. W. Edmonds, C. Binns, S. H. Baker, S. C. Thornton, C. Norris, J. B. Goedkoop, M. Finazzi, and N. B. Brookes, *Phys. Rev. B* **60**, 472 (1999).
  - [16] S. Heinze, M. Bode, A. Kubetzka, O. Pietzsch, X. Nie, S. Blügel, R. Wiesendanger, *Science* **288**, 1805 (2000).
  - [17] C. F. Hirjibehendin, C. P. Lutz, J. Heinrich, *Science* **312**, 1021 (2006).
  - [18] A. J. Heinrich, J. A. Gupta, P. Lutz, D. M. Eigler, *Science* **306**, 466 (2004); M. Bode, *ibid.* **306**, 423 (2004).
  - [19] J. Koringa, *Physica* **13**, 392 (1947).
  - [20] W. Kohn and N. Rostoker, *Phys. Rev.* **94**, 1111 (1954).
  - [21] T. H. Dupree, *Ann. Phys. (N. Y.)*, **15**, 63 (1961); J. L. Beeby, *Proc. Roy. Soc. London Ser. A* **302**, 113 (1967); G. J. Morgan, *Proc. Phys. Soc.* **89**, 365 (1966).
  - [22] R. Zeller and P. H. Dederichs, *Phys. Rev. Lett.* **42**, 1713 (1979).

- 
- [23] B. Nonas, I. Cabria, R. Zeller, P. H. Dederichs, T. Huhne and H. Ebert, *Phys. Rev. Lett.* **86**, 2146-2149 (2001).
- [24] A. I. Liechtenstein, M. I. Katsnelson, V. P. Antropov and V. A. Gubanov, *J. Magn. Magn. Mat* **67**, 65–74 (1987).
- [25] J. Lagoute, Xi Liu, and S. Fölsch. *Phys. Rev. Lett.* **95**, 136801 (2006).
- [26] L. Limot, E. Pehlke, J. Kröger, and R. Berndt, *Phys. Rev. Lett.* **94**, 036805 (2005); J. Kröger, L. Limot, H. Jensen, R. Berndt, S. Crampin and E. Pehlke, *Progress in Surface Science*, **80**,26 (2005).
- [27] F. E. Olsson, M. Persson, A. G. Borisov, J. –P. Gauyacq, J. Lagoute and S. Fölsch, *P. R. L.* **93**, 206803 (2004).
- [28] B. Simon, *Ann. Phys. (N.Y.)* **97**, 279 (1976).
- [29] S. Crampin, *J. Phys. J. Phys.: Condens. Matter*, **6** L613 (1994).
- [30] S. Heinze, R. Abt, S. Blügel, G. Gilarowski and H. Niehus, *Phys. Rev. B* **83**, 4808 (1999).
- [31] M. Schmid, W. Hebenstreit, P. Varga, and S. Crampin, *Phys. Rev. Lett.* **76**, 2298 (1996); M. Schmid, S. Crampin, P. Varga, *J. Elec. Spec. and Rel. Phen.* **109**, 71 (2000).
- [32] A. Weissmann, M. Wenderoth, N. Quaas, and R. G. Ulbrich, private communication (2005).
- [33] P. Bruno and C. Chappert, *Phys. Rev. Lett.* **67**, 1602 (1991); P. Bruno and C. Chappert, *Phys. Rev. Lett.* **67**, 2592 (1991).
- [34] N. David Mermin, *Phys. Rev.* **137**, A1441-1443, 1965.
- [35] S. H. Vosko, L. Wilk, and M. Nusair, *J. Chem. Phys.* **58**, 1200 (1980).
- [36] U. von Barth and L. Hedin, *J. Phys. C* **5**, 1629, 1972.
- [37] N. Papanikolaou, R. Zeller, and P. H. Dederichs, *J. Phys.: Condens. Matter* **14**, 2799 (2002).
- [38] R. Zeller, P. H. Dederichs, B. Újfalussy, L. Szunyogh, and P. Weinberger, *Phys. Rev. B* **52**, 8807 (1995); K. Wildberger, R. Zeller, and P. H. Dederichs *Phys. Rev. B* **55**, 10074 (1997).
- [39] M. Asato, A. Settels, T. Hoshino, T. Asada, S. Blügel, R. Zeller, and P. H. Dederichs *Phys. Rev. B* **60**, 5202 (1999).
- [40] I. Galanakis, G. Bihlmayer, V. Bellini, N. Papanikolaou, R. Zeller, S. Blügel, and P.H. Dederichs, *Europhys. Lett.* **58**, 751 (2002).
- [41] M. Freyss, N. Papanikolaou, V. Bellini, R. Zeller, and P. H. Dederichs *Phys. Rev. B* **66**, 014445 (2002).
- [42] B. Nonas, K. Wildberger, R. Zeller, P. H. Dederichs, and B. L. Gyorffy *Phys. Rev. B* **57**, 84 (1998) Magnetic properties of 4d impurities on the (001) surfaces of nickel and iron
- [43] H. Ebert and S. Mankovsky, *Phys. Rev. Lett.* **90**, 077404 (2003).
- [44] Ph. Mavropoulos, O. Wunnicke, and P. H. Dederichs *Phys. Rev. B* **66**, 024416 (2002).

- 
- [45] N. Papanikolaou, J. Opitz, P. Zahn, and I. Mertig Phys. Rev. B **66**, 165441 (2002).
- [46] A. Vernes, H. Ebert, and J. Banhart, Phys. Rev. B **68**, 134404 (2003).
- [47] V. Popescu, H. Ebert, B. Nonas, and P. H. Dederichs Phys. Rev. B **64**, 184407 (2001)
- [48] R. G. Newton, *Scattering Theory of Waves and Particles*, second edition, Springer (1982); reprint by Dover (2002).
- [49] E. N. Economou, *Green's functions in Quantum Physics*, Springer Series in Solid-State Sciences 7, Springer Verlag Berlin (1979).
- [50] G. Arfken, *Mathematical Methods for Physicists*, Academic Press International Edition (1970).
- [51] R. Zeller, J. Phys. C: Solid State Phys. **20** 2347 (1987).
- [52] B. Drittler, Dissertation, Rheinisch-Westfälische Technische Hochschule Aachen (1991).
- [53] D. M. Eigler and E. K. Schweizer, Nature **344**, 524 (1990).
- [54] M. F. Crommie, C. P. Lutz and D. M. Eigler, Science **262**, 218 (1993).
- [55] H. C. Monoharan, C. P. Lutz, and D. M. Eigler, Nature **403**, 512 (2000).
- [56] A. Oswald, R. Zeller and P. H. Dederichs, J. Magn. Magn. Mater. **54-57**, 1247 (1986).
- [57] L. M. Sandratskii and P. G. Gulsetskii, J. Phys. F: Met. Phys. **16**, L43 (1986).
- [58] J. Kübler, K. H. Höck, and J. Sticht, J. Appl. Phys. **63**, 3482 (1988).
- [59] J. Kübler, K. H. Höck, J. Sticht, and A. R. Williams, J. Phys. F: Met. Phys. **18**, 469 (1988).
- [60] Y. Tsunoda, J. Phys.: Condens. Matter **1**, 10427 (1989).
- [61] Y. Tsunoda, Y. Nishioka, and R. M. Nicklow, J. Magn. Magn. Mater. **128**, 133 (1993).
- [62] O. N. Mryasov, A. I. Liechtenstein, L. M. Sandratskii, and V. A. Gubanov, J. Phys.: Condens. Matter **3**, 7683 (1991).
- [63] K. Knöpfle, L. M. Sandratskii, and J. Kübler, Phys. Rev. B **62**, 5564 (2000).
- [64] Ph. Kurz, F. Förster, L. Nordström, G. Bihlmayer, and S. Blügel, Phys. Rev. B **69**, 24415 (2004).
- [65] L. Nordström and D. J. Singh, Phys. Rev. Lett. **76**, 4420 (1996)
- [66] E. Sjöstedt and Lars Nordström, Phys. Rev. B **66**, 14447 (2002).
- [67] L. M. Sandratskii, Solid State Communications, **75**, 527 (1990).
- [68] L. M. Sandratskii, Phys. Rev. B, **64**, 134402 (2001).
- [69] P. H. Dederichs, S. Blügel, R. Zeller, and H. Akai, Phys. Rev. Lett. **53**, 2512 (1984).
- [70] O. Grotheer, C. Ederer, and M. Fähnle, Phys. Rev. B **62**, 5601 (2000).
- [71] T. Oda, A. Pasquarello, and R. Car, Phys. Rev. Lett. **80**, 3622 (1998).

- 
- [72] D. Hobbs, G. Kresse, and J. Hafner, Phys. Rev. B. **62**, 11556 (2000).
- [73] C. Kohl and G. F. Bretsch, Phys. Rev. B. **60**, 4205 (1999).
- [74] C. Messiah, Vol. **2**, *Quantum mechanics*, John Wiley & Sons, New York (1978).
- [75] J. Kudrnovský, V. Drchal, I. Turek, and P. Weinberger, Phys. Rev. B **50**, 16105 (1994).
- [76] P. Lloyd, Proc. Phys. Soc. London **90**, 207 (1967); **90**, 217 (1967).
- [77] G. Lehmann, Phys. Status Solidi B **70**, 737 (1975).
- [78] B. Drittler, M. Weinert, R. Zeller, and P. H. Dederichs, Solid State Commun. **79**, 31 (1991).
- [79] R. Zeller, J. Phys.: Condens. Matter **17**, 5367 (2005).
- [80] A. Oswald, R. Zeller, P. J. Braspenning and P. H. Dederichs 1985 J. Phys. F: Met. Phys. **15**, 193 (1985).
- [81] N. Stefanou, H. Akai, and R. Zeller, Comp. Phys. Commun. **60**, 231 (1990); N. Stefanou and R. Zeller, J. Phys.: Condens. Matter **3**, 7599 (1991).
- [82] A. Ernst, G. van der Laan, W. M. Temmerman, S. S. Dhesi, and Z. Szotek, Phys. Rev. B **62**, 9543 (2000).
- [83] O. Hjortstam, J. Trygg, J. M. Wills, B. Johansson, and O. Eriksson, Phys. Rev. B **53**, 9204, (1996).
- [84] B. Nonas, K. Wildberger, R. Zeller, and P. H. Dederichs, J. Magn. Magn. mater. **165**, 137 (1997).
- [85] B. Nonas, K. Wildberger, R. Zeller, and P. H. Dederichs, Phys. Rev. Lett. **80**, 4574 (1998).
- [86] V. Popescu, H. Ebert, B. Nonas, and P. H. Dederichs, Phys. Rev. B **64**, 184407 (2001).
- [87] Ph. Mavropoulos, S. Lounis, R. Zeller, S. Blügel, Appl. Phys. **A** 82, 103 (2006).
- [88] S. Alexander and P. W. Anderson Phys. Rev. **133**, A1594 (1964).
- [89] Private communication (2005). The method used for these calculations is the Full potential Linear Augmented Plane Waves method (FLAPW).
- [90] J. Thomassen *et al.*, Phys. Rev. Lett. **69**, 3831 (1992).
- [91] Th. Detzel, M. Vonbank, M. Donath, and V. Dose, J. Magn. Magn. Mater. **147**, L1 (1995).
- [92] W. A. A. Macedo and W. Keune, Phys. Rev. Lett. **61**, 475 (1988).
- [93] N. Memmel and Th. Detzel, Surf. Sci. **307-309**, 490 (1994).
- [94] T. Asada, S. Bluügel, Phys. Rev. Lett. **79**, 507 (1997).
- [95] V. S. Stepanyuk, W. Hergert, P. Rennert, B. Nonas, R. Zeller, and P. H. Dederichs, Phys. Rev. B **61**, 2356 (2000).
- [96] J. T. Lau, U. Langenbuch, A. Achleitner, H.-U. Ehrke, M. Reif and W. Wurth, Rev. Sci. Instr. **76**, 063902 (2005).

- 
- [97] J. T. Lau, H.-U. Ehrke, A. Achleitner, and W. Wurth, *Low Temperature Physics*, **29**, 223 (2003).
- [98] J. Minár, S. Bornemann, O. Sipr, S. Polesya, and H. Ebert, *Appl. Phys. A* **82**, 139 (2006).
- [99] C. Grazioli, D. Alfè, S. R. Krishnakumar, S. S. Gupta, M. Veronese, S. Turchini, N. Bonini, A. D. Corso, D. D. Sarma, S. Baroni, and C. Carbone, *Phys. Rev. Lett* **95**, 117201 (2005).
- [100] J. Hafner, and D. Spisák, *Phys. Rev. B* **72**, 144420 (2005).
- [101] Ph. Kurz, G. Bihlmayer, K. Hirai, and S. Blügel, *Phys. Rev. Lett.* **86**, 1106 (2001).
- [102] D. Spisak and J. Hafner, *Phys. Rev. B*, **61**, 12728 (2000).
- [103] S. Uzdin, V. Uzdin, C. Demangeat, *Surf. Sci.* **482-485**, 965 (2001); S. Uzdin, V. Uzdin, C. Demangeat, *Comp. Mat. Sci.* **17**, 441 (2000); S. Uzdin, V. Uzdin, C. Demangeat, *Europhys. Lett.* **47**, 556 (1999).
- [104] H. J. Gotsis, N. Kioussis, and D. A. Papaconstantopoulos, *Phys. Rev. B* **73**, 14436 (2006).
- [105] A. Bergman, L. Nordtröm, A. B. Klautau, S. Frota-Pessôa, and O. Eriksson, *Cond-mat/0511542*, (2005).
- [106] G. M. Stocks, M. Eisenbach, B. Újfalussy, B. Lazarovits, L. Szunyogh, P. Weinberger, *Progress in Materials Science*, **25**, 371 (2006).
- [107] I. Cabria, B. Nonas, R. Zeller, and P. H. Dederichs, *Phys. Rev. B* **65**, 054414 (2002).
- [108] Š. Pick, V. S. Stepanyuk, A. N. Baranov, W. Hergert, and P. Bruno, *Phys. Rev. B* **68**, 104410 (2003).
- [109] J. A. Stroschio and R. J. Celotta, *Science* **306**, 242 (2004).
- [110] B. Lazarovits, L. Szunyogh, P. Weinberger, and B. Újfalussy *Phys. Rev. B* **68**, 024433 (2003); B. Újfalussy, B. Lazarovits, L. Szunyogh, G. M. Stocks, and P. Weinberger *Phys. Rev. B* **70**, 100404 (2004).
- [111] S. Baud, Ch. Ramseyer, G. Bihlmayer and S. Blügel, *Phys. Rev. B* **73**, 104427 (2006).
- [112] Y. Mokrousov, G. Bihlmayer, S. Heinze and S. Blügel, *Phys. Rev. Lett.* **96**, 147201 (2006).
- [113] I. E. Tamm, *Z. Phys.* **76**, 849, (1932).
- [114] W. Shockley, *Phys. Rev.* **56**, 317 (1939).
- [115] A. Euceda, D. M. Bylander and L. Kleinman, *PRB* **28**, 528 (1983).
- [116] J. P. Gauyacq, A. G. Borisov, and A. K. Kazansky, *Appl. Phys.* **78**, 141 (2004).
- [117] V. Madhavan, W. Chen, T. Jamneala, M. F. Crommie, and N. S. Wingreen, *Science* **280**, 567 (1998); V. Madhavan, W. Chen, T. Jamneala, M. F. Crommie, and Ned S. Wingreen, *Phys. Rev. B* **64**, 165412 (2001).

- 
- [118] A. Davies, J. A. Stroschio, D. T. Pierce, and R. J. Celotta, *Phys. Rev. Lett.* **76**, 4175 (1996).
- [119] N. Papanikolaou, B. Nonas, S. Heinze, R. Zeller, and P. H. Dederichs, *Phys. Rev. B* **62**, 11118 (2000).
- [120] J. Tersoff and D. R. Hamann, *Phys. Rev. Lett.* **50**, 1998 (1983); J. Tersoff and D. R. Hamann, *Phys. Rev. B* **31**, 805 (1985).
- [121] J. Bardeen, *Phys. Rev. Lett.* **6**, 57 (1961).
- [122] W. A. Hofer, A. S. Foster, A. L. Shluger, *Rev. Mod. Phys.* **75**, 1287 (2003).
- [123] F. Reinert, G. Nicolay, S. Schmidt, D. Ehm, and S. Hüfner, *Phys. Rev. B* **63**, 115415 (2001).
- [124] O. Gunnarsson, *J. Phys. F: Met. Phys.* **6**, 587 (1976); J. F. Janak, *PRB* **16**, 255 (1977).
- [125] S. Crampin and O. R. Bryant, *Phys. Rev. B* **54**, 17367 (1996).
- [126] M. Schmid, W. Hebenstreit, P. Varga, and S. Crampin, *Phys. Rev. Lett.* **76**, 13 (1996).
- [127] P. T. Sprunger, L. Petersen, E. W. Plummer, E. Laegsgaard, F. Besenbacher, *Science*, **275**, 1764 (1997).
- [128] P. Grünberg, R. Schreiber, Y. Pang, M. B. Brodsky, and H. Sower, *Phys. Rev. Lett.* **57**, 2442 (1986).
- [129] S. S. P. Parkin, N. More, and K. P. Roche, *Phys. Rev. Lett.* **64**, 2304 (1990).
- [130] N. Papanikolaou, R. Zeller, and P. H. Dederichs, and N. Stefanou, *Phys. Rev. B* **55**, 4157 (1997).



## Acknowledgments

This work has been done in the frame of a Ph.D thesis at the Forschungszentrum Jülich. It was accomplished during the period May 2003 to April 2006 under the warm and highly scientific atmosphere provided by the solid state physics department (IFF) and in particular by the institute of Quantum Theory of Materials. Many people have been visiting our group for short and long periods and certainly contributed directly or indirectly to the realization of the present thesis.

First and foremost, I sincerely like to thank Prof. Dr. Stefan Blügel, who gave me the opportunity to perform this thesis in his institute. I gratefully acknowledge his first trust in me when we met at the university of Osnabrück, his continuous support, energetic motivation and the inspiring and fruitful discussions concerning Physics and everything else. Stefan, thank you for putting few of your ideas in my brain.

I heartily thank Prof. Dr. Peter H. Dederichs for his patience and constant guidance along the past three years. He shared with me several of his ideas and never stopped his interest on my research works. I profited from his broad knowledge in physics and had the impression he did everything.

Warm thanks to Dr. Phivos Mavropoulos who introduced me to the KKR method and more important taught me many of the KKR-code tricks. He has always very nice ideas and I learnt from him a lot. Phivos you are a genius.

Special thanks to Dr. Rudolf Zeller for answering my questions about KKR. He has also parallelized my non-collinear KKR code. Rudi, without your help I would have treated only trimers!

I thank also Dr. Gustav Bihlmayer who was very helpful. In many occasions he explained me how non-collinear magnetism was implemented in the FLEUR code and many more things.

I warmly thank Prof. Dr. Mouloud Benakki from the University of Mouloud Mammeri of Tizi-Ouzou who put me on the rails of computational physics.

I am indebted to Mrs Ute Winkler for solving many of my administrative problems with her usual warm smile.

Fruitful collaborations and discussions with experimental colleagues were very helpful. Thus, I would like to thank: Dr. Matthias Reif, Dr Michael Martins and Prof. Dr. Wilfried Wurth from the university of Hamburg, Dr. Laurent Limot and Prof. Dr. Richard Berndt from the university of Kiel, and Dr. Alexander Weismann, Dr. Martin Wenderoth, and Prof. Dr. Rainer-G. Ulbrich from the university of Göttingen.

I would like to thank colleagues and friends with whom I shared enjoyable discussions, jokes, movies, beers and beers: Brahim Belhadji, Lars Bergqvist, Nicolae Atodiresei, Paolo Ferriani, Marcus Heide, Holger Höler, Masako Ogura, Yuriy Mokrousov, Manni Niesert, Diana Rata, Kasunori Sato.

Nothing would have been possible without the constant and lovely support of my family: To my wife Aziza, my parents Mustapha & Fazia, my brother Kosseila and my sister Ourdia, I dedicate with pleasure this thesis.

Samir Lounis

Jülich, April 2006.

## Curriculum Vitae

### Personal Details:

<b>Name:</b> Samir Lounis	<b>Date of birth:</b> 16/09/77
<b>Address:</b> Quantum Theory of Materials Institut für Festkörperforschung (IFF) Forschungszentrum Jülich, Germany	<b>Place of birth:</b> Larbâa Nath Irathen Tizi-Ouzou, Algeria
<b>Tel.:</b> [+49]-2461-61-6106	<b>E-mail:</b> s.lounis@fz-juelich.de
	<b>Fax.:</b> [+49]-2461-61-2850

### Education

**May 2003/April 2006** **PhD thesis:** *Theory of magnetic transition metal nanoclusters on surfaces*  
Oral exam on 17 April 2007  
Mit Auszeichnung, Summa cum laude  
Supervised by Prof. S. Blügel and Prof. P. H. Dederichs,  
Forschungszentrum Jülich, D-52425 Jülich, Germany.

**December 2002:** **Magister thesis** in Material Physics: *Study of the magnetic configurations of FeRh binary ordered alloy and Ni/Pt multi-layers by TB-LMTO method*,  
Very good with jury congratulations  
Supervised by Prof. M. Benakki and Dr. C. Demangeat,  
Mouloud Mammeri University, Tizi-Ouzou (Algeria) and  
IPCMS (CNRS), Strasbourg (France).

**December 2000:** **First year Post-Graduate studies** in Material Physics.  
Rank: first (valedictorian).  
Mouloud Mammeri University, Tizi Ouzou (Algeria).

**October 1999:** **DES** (second level degree) in Condensed Matter Physics.  
Rank: first (valedictorian).  
Mouloud Mammeri University, Tizi-Ouzou (Algeria).

**June 1994:** **Baccalauréat** (High School Diploma), Exact Sciences.  
El Illouli Secondary School, L. N. I.,  
Tizi-Ouzou (Algeria).

---

## National Exams and Awards

- July 2002:** **Scholarship** from the ORS Awards Committee in London (United Kingdom)
- December 2000:** **Valedictorian** of the post-graduate program at the Mouloud Mammeri University, Tizi-Ouzou (Algeria).
- November 1999:** **National Competitive Examination** for a position at the Theoretical Physics Post-graduate Program of the ENS (Superior National school) of Kouba, Algiers (Algeria)
- November 1999:** **National Competitive Examination** for a position at the Material Physics Post-graduate Program of the University of Bejaia, (Algeria).
- October 1999:** **Valedictorian** of the undergraduate physics department at the Mouloud Mammeri University, Tizi-Ouzou (Algeria).

## Experience

**Referee** for Physical Review

- Since May 2006** **Postdoc** at the Forschungszentrum Jülich, (Theory I) Germany.
- 2003/2006** **Research Assistant** at the Forschungszentrum Jülich, (Theory I) Germany.
- 2000/2003** **Research** (Magister) at the faculty of sciences of the Mouloud Mammeri University, Tizi-Ouzou (Algeria)
- Summer 2001** **Guest researcher** at the institute for Materials Physics and Chemistry of Strasbourg (IPCMS, France).
- 2000/2002** **Teaching** (4 semesters) at the Mouloud Mammeri University, Tizi-Ouzou (Algeria): Practical Works and Tutorials in Atomic Physics and Computational Sciences at different levels.

---

## Publications

- [14] Focusing effect on surfaces due to scattering of bulk electrons at impurities, **S. Lounis** *et al.* (to submit to PRL)
- [13] Electron Focusing: Mapping the single electron propagator in anisotropic media, A. Weismann, M. Wenderoth, **S. Lounis**, P. Zahn, R. G. Ulbrich, P. H. Dederichs, S. Blügel (submitted to Science)
- [12] Non-collinear Magnetism in Nanochains Driven by Adatoms Number's Parity, **S. Lounis**, P. H. Dederichs and S. Blügel (to submit to PRL)
- [11] Noncollinear magnetism of Cr nanostructures on  $\text{Fe}_{3ML}/\text{Cu}(001)$ : a first-principles and experimental investigation, **S. Lounis**, M. Reif, Ph. Mavropoulos, L. Glaser, P. H. Dederichs, M. Martins, S. Blügel and W. Wurth cond-mat/0608048 (submitted to PRL)
- [10] Noncollinear magnetism of Cr and Mn nanoclusters on Ni(111): Changing the magnetic configurations atom by atom, **S. Lounis**, Ph. Mavropoulos, R. Zeller, P. H. Dederichs and S. Blügel Accepted in Phys. Rev. B (2007), cond-mat/0608481
- [9] Surface state scattering by atomic-scale clusters on noble metals, **S. Lounis**, Ph. Mavropoulos, P. H. Dederichs and S. Blügel Phys. Rev. B **73**, 195421 (2006)
- [8] The Korringa-Kohn-Rostoker (KKR) Green Function Method: II. Impurities and Clusters in the Bulk and on Surfaces, P. H. Dederichs, **S. Lounis**, R. Zeller, Contribution to NIC-Winterschool in Forschungszentrum Jülich, 2006 Computational Nanoscience: Do It Yourself! J. Grotendorst, S. Blügel, D. Marx (editors) NIC Series Volume **31** ISBN 3-00-017350-17350-1
- [7] Fe clusters on Ni and Cu: size and shape dependence of the spin moment, Ph. Mavropoulos, **S. Lounis**, R. Zeller, and S. Blügel, Appl. Phys. **A**, **82**, 103 (2006)
- [6] Noncollinear magnetism in  $3d$  nanostructures on Ni(001) and on  $\text{Fe}_{3ML}/\text{Cu}(001)$ , **S. Lounis**, Ph. Mavropoulos, P. H. Dederichs, and S. Blügel,

Scientific report of the Jülich's Institute of Solid State Research, 42 (2004/2005)

[5] Noncollinear Korringa–Kohn–Rostoker Green function method:

Application to 3d nanostructures on Ni(001),

**S. Lounis**, Ph. Mavropoulos, P. H. Dederichs and S. Blügel,

Phys. Rev. B **72**, 224437 (2005)

[4] Antiferromagnetic polarization at Mn/V(001) interfaces,

B. Belhadji, **S. Lounis**, M. Benakki, and C. Demangeat,

Phys. Rev. B. **69**, 064431 (2004).

[3] Ferromagnetic stabilization of ordered B2 FeRh thin films,

**S. Lounis**, M. Benakki, and C. Demangeat,

Phys. Rev. B **67**, 094432 (2003).

[2] Ab initio study of the dead magnetic Ni layers at the Ni/Pt(111) interface,

**S. Lounis**, M. Benakki, S. Bouarab and C. Demangeat,

Surf. Sci. **518**, 57 (2002).

[1] Ab initio study of the magnetic configurations on the (001) surfaces of binary FePd and FeRh ordered alloys.

C. Dahmoune, **S. Lounis**, M. Talanana, M. Benakki, S. Bouarab and C. Demangeat, J. M. M. M. **240**, 368 (2002).

## Communications

[23] Strong Even-Odd Effects in Noncollinear Magnetism of Nanochains

**S. Lounis**, P. H. Dederichs, and S. Blügel,

DPG Meeting, Regensburg, March 25-30, 2007 (talk)

[22] First-principles Investigation of Complex Magnetism of Nanostructures on Surfaces

**S. Lounis**, Ph. Mavropoulos, R. Zeller, P. H. Dederichs and S. Blügel,

Quantum Simulation of Liquids and Solids: Tutorial, Lyon, France, 29.10.2006 - 10.11.2006 (talk)

[21] Non-collinear KKR Green function method: Application to 3d nanostructures on surfaces

**S. Lounis**, Ph. Mavropoulos, R. Zeller, P. H. Dederichs and S. Blügel,

KKR-Workshop 2006: University of Bristol, Bristol, United Kingdom, 20.10.2006 - 22.10.2006 (talk)

---

[20] Non-collinear magnetism of Cr and Mn nanoclusters on ferromagnetic surfaces

Ph. Mavropoulos, **S. Lounis**, P. H. Dederichs, S. Blügel,  
XXII Panhellenic Conference on Solid State Physics and Materials Science, Patra, Greece, 23.09.2006 - 01.10.2006 (talk)

[19] Real Space Imaging of Fermi Surface by STM,

**S. Lounis**, P. Zahn, P. H. Dederichs, S. Blügel,  
European Conference on Surface Science (ECOSS24), Paris, France, 03.09.2006 - 08.09.2006 (talk)

[18] Investigation of complex magnetic  $3d$  nanostructures on Ni(001), on Ni(111) and on *fcc* Fe(001) using the KKR-GF method,

**S. Lounis**, Ph. Mavropoulos, R. Zeller, P. H. Dederichs, S. Blügel,  
19<sup>th</sup> International Colloquium on Magnetic Films and Surfaces (ICMFS), Sendai, Japan, 20.08.2006 - 25.08.2006 (poster)

[17] Complex magnetism of nanoclusters on surfaces,

Ph. Mavropoulos, **S. Lounis**, P. H. Dederichs, S. Blügel,  
International Conference on Clusters on Surfaces (ICCS), Rostock, 29.05.2006 - 02.06.2006 (talk)

[16] Focusing effect on surfaces due to scattering of bulk electrons at subsurface impurities,

**S. Lounis**, P. Zahn, Ph. Mavropoulos, P. H. Dederichs and S. Blügel,  
DPG Meeting, Dresden, March 27th-31th, 2006 (talk)

[15] Investigation of complex magnetic  $3d$  nanostructures on Ni(001) and on *fcc* Fe/Cu(001) with the Korringa-Kohn-Rostoker method,

**S. Lounis**, Ph. Mavropoulos, R. Zeller, P. H. Dederichs and S. Blügel,  
Psi-k 2005 Conference, Schwäbig Gmünd, September 17th-21th, 2005 (poster)

[14] Magnetism of nanoclusters on surfaces,

Ph. Mavropoulos, **S. Lounis**, P. H. Dederichs and S. Blügel,  
Psi-k 2005 Conference, Schwäbig Gmünd, September 17th-21th, 2005 (talk)

[13] Magnetism of nanoscale clusters on surfaces,

Ph. Mavropoulos, **S. Lounis**, P. H. Dederichs and S. Blügel,  
Clustertreffen 2005, Karlsruhe Universität, September 11th-16th, 2005 (talk)

[12] Surface state scattering by atomic-scale clusters on noble metals,

**S. Lounis**, Ph. Mavropoulos, P. H. Dederichs and S. Blügel,  
DPG Meeting, Berlin, March 4th-9th, 2005 (talk)

- 
- [11] Complex magnetism of small  $3d$  transition metal clusters on Ni and Cu surfaces,  
Ph. Mavropoulos, **S. Lounis**, R. Zeller, P. H. Dederichs and S. Blügel,  
DPG Meeting, Berlin, March 4th-9th, 2005 (talk)
- [10] Magnetism of Transition–Metal Adatoms and Small Clusters on Surfaces  
Ph. Mavropoulos, **S. Lounis**, R. Zeller, S. Blügel, J. Kroha,  
Korrel05 meeting, Dresden, February 28th- March 4th 2005 (poster)
- [9] Magnetic Nanostructures on Surfaces  
**S. Lounis**, Ph. Mavropoulos, S. Blügel, J. Kroha,  
Nanoelectronic days, FZ-Jülich, Germany, February 9-11th 2005 (poster)
- [8] Understanding Nanomagnetism from First Principles,  
**S. Lounis**, Ph. Mavropoulos, R. Zeller, P. H. Dederichs, S. Baud, G. Bihlmayer,  
S. Blügel,  
3K2005 meeting, Badhonnef, Germany, January 5th-7th, 2005 (poster)
- [7] Noncollinear KKR method: Application to complex magnetic  $3d$  nanostructures on Ni(001),  
**S. Lounis**, Ph. Mavropoulos, S. Blügel and P. H. Dederichs,  
Theory I, IFF, FZ-Juelich, Germany, September 29th, 2004 (seminar)
- [6] Noncollinear magnetic nanostructures of  $3d$  clusters on Ni(001),  
**S. Lounis**, Ph. Mavropoulos, S. Blügel and P. H. Dederichs,  
Summer school on magnetism and transport in solids, Angstromlaboratoriet, Uppsala University, Sweden, June 14-18th, 2004 (poster)
- [5] Noncollinear magnetic  $3d$  nanostructures on Ni(001),  
**S. Lounis**, Ph. Mavropoulos, S. Blügel and P. H. Dederichs,  
Hamburg University, Germany, June 10th, 2004 (talk)
- [4] Collinear and noncollinear magnetic structures of  $3d$  clusters on Ni(001),  
**S. Lounis**, Ph. Mavropoulos, S. Blügel and P. H. Dederichs,  
DPG Meeting, Regensburg, Germany, March 08–12th, 2004 (poster).
- [3] Magnetic transition and reconstruction in (001) FeRh thin films,  
**S. Lounis**, M. Benakki and C. Demangeat,  
J'LPCQ, Tizi–Ouzou, Algeria, May 19th, 2002 (poster).
- [2] Magnetic properties of metallic low dimensional systems,  
**S. Lounis**, Seminar at the University of Osnabrück, Germany, April 15th, 2002

(talk).

[1] Ab initio study of the magnetic configurations on the (001) surfaces of binary FePd and FeRh ordered alloys,  
C. Dahmoune, **S. Lounis**, M. Talanana, M. Benakki, S. Bouarab, C. Demangeat,  
Symposium on Metallic Multilayers, Aachen, Germany, June 24 - 29, 2001 (poster).



1. **Physik der Nanostrukturen**  
Vorlesungsmanuskripte des 29. IFF-Ferienkurses vom 9. bis 20.3.1998 (1998), ca. 1000 Seiten  
ISBN: 978-3-89336-217-2
2. **Magnetische Schichtsysteme**  
Vorlesungsmanuskripte des 30. IFF-Ferienkurses vom 1. bis 12.3.1999 (1999), ca. 1300 Seiten, zahlreiche z.T. farb. Abb.  
ISBN: 978-3-89336-235-6
3. **Femtosekunden und Nano-eV: Dynamik in kondensierter Materie**  
Vorlesungsmanuskripte des 31. IFF-Ferienkurses vom 13. bis 24.3.2000 (2000), ca. 1000 Seiten, zahlreiche z. T. farb. Abb.  
ISBN: 978-3-89336-205-9 (Hardcover)
4. **Massenspektrometrische Verfahren der Elementspurenanalyse**  
Kurzfassungen der Vorträge und Poster des 5. Symposiums und des 12. ICP-MS-Anwendertreffens vom 18. bis 21. September 2000 in Jülich zusammengestellt von H.-J. Dietze, J. S. Becker (2000), XVI, 109 Seiten  
ISBN: 978-3-89336-267-7
5. **Neutron Scattering**  
Lectures of the Laboratory Course  
held at the Forschungszentrum Jülich from 26 September to 6 October 2000  
herausgegeben von Th. Brückel, G. Heger, D. Richter (2000), 382 Seiten  
ISBN: 978-3-89336-269-1
6. **Baryon Excitations**  
Lectures of the COSY Workshop  
held at the Forschungszentrum Jülich from 2 to 3 May 2000  
edited by T. Barnes and H.-P. Morsch (2000), 203 pages  
ISBN: 978-3-89336-273-8
7. **Neue Materialien für die Informationstechnik**  
Vorlesungsmanuskripte des 32. IFF-Ferienkurses vom 05. bis 16.03.2001  
herausgegeben von R. Waser (2001), ca. 1200 Seiten, zahlreiche z. T. farb. Abb.  
ISBN: 978-3-89336-279-0
8. **Deutsche Neutronenstreutagung 2001**  
Kurzfassungen der Vorträge und Poster der  
Deutschen Neutronenstreutagung 2001 vom 19. bis 21. Februar 2001 in Jülich  
zusammengestellt von Th. Brückel (2001), XVI, 186 Seiten  
ISBN: 978-3-89336-280-6

9. **Neutron Scattering**  
Lectures of the 5<sup>th</sup> Laboratory Course  
held at the Forschungszentrum Jülich from 18 September to 28 September 2001  
edited by Th. Brückel, G. Heger, D. Richter, R. Zorn (2001), 418 pages  
ISBN: 978-3-89336-288-2
10. **Soft Matter. Complex Materials on Mesoscopic Scales**  
Lecture manuscripts of the 33<sup>rd</sup> IFF winter school on March 04 - 14 2002  
edited by J. K. G. Dhont, G. Gompper, D. Richter (2002),  
c. 1000 pages, many partly coloured illustrations  
ISBN: 978-3-89336-297-4 (Hardcover)
11. **Proceedings of the symposium on threshold meson production in pp and pd interaction**  
Extended COSY-11 Collaboration Meeting Cracow, 20 - 24 June 2001  
edited by P. Moskal, M. Wolke (2002), 274 pages  
ISBN: 978-3-89336-307-0
12. **Polarized Neutron Scattering**  
Lectures of the 1<sup>st</sup> Summer School held at the Forschungszentrum Jülich  
from 10 to 14 September 2002  
edited by Th. Brückel, W. Schweika (2002), 360 pages  
ISBN: 978-3-89336-314-8
13. **Beam Cooling and Related Topics**  
255<sup>th</sup> International WE-Heraeus-Seminar, Bad Honnef, May 13 - 18, 2001  
Proceedings  
edited by D. Prasuhn (2002), PDF-Datei auf CD  
ISBN: 978-3-89336-316-2
14. **Fundamentals of Nanoelectronics**  
34<sup>th</sup> Spring School of the Department of Solid State Research,  
10 - 21 March 2003, Jülich, Germany  
edited by S. Bluegel, M. Luysberg, K. Urban, R. Waser (2003), c. 1000 pages  
ISBN: 978-3-89336-319-3 (Hardcover)
15. **Neutron Scattering**  
Lectures of the Laboratory course held at the Forschungszentrum Jülich  
edited by Th. Brückel, G. Heger, D. Richter, R. Zorn (2003), 375 pages  
New, revised edition of Materie und Material / Matter and Materials Volume 9  
ISBN: 978-3-89336-324-7
16. **Proceedings of the 1st Summer School 2002 and Workshop on COSY Physics**  
28. August - 4. September 2002  
Organizing Committee: K. Brinkmann, M. Büscher, et al. (2003), CD-ROM  
ISBN: 978-3-89336-331-5

17. **Resource-orientated Analysis of Metallic Raw Materials: Findings of CRC 525 for Aluminium**  
edited by W. Kuckshinrichs, P. N. Martens (2003), CD-ROM  
ISBN: 978-3-89336-342-1
18. **The Physics of Spallation Processes: Theory, Experiments and Applications**  
by F. Goldenbaum (2004), V, 174 pages  
ISBN: 978-3-89336-346-9
19. **Physics meets Biology: From Soft Matter to Cell Biology**  
Lecture manuscripts of the 35<sup>th</sup> IFF Spring School from March 22 – April 2, 2004, Jülich, Germany  
edited by G. Gompper, U. B. Kaupp, J. K. G. Dhont, D. Richter, R. G. Winkler (2004), c. 900 pages  
ISBN: 978-3-89336-348-3
20. **Advanced Cold Moderators ACoM-6**  
Proceedings of the 6<sup>th</sup> International Workshop on Advanced Cold Moderators held at Forschungszentrum Jülich from 11 to 13 September 2002  
edited by H. Conrad (2004), 223 pages  
ISBN: 978-3-89336-363-6
21. **Proceedings of the second symposium on threshold meson production in pp and pd interaction**  
Extended COSY-11 Collaboration Meeting, Cracow, 1-3 June 2004  
ed. by P. Moskal (2004), c. 300 pages  
ISBN: 978-3-89336-366-7
22. **Ferroelectric Tunnel Junctions**  
by J. Rodríguez Contreras (2004), VIII, 162 pages  
ISBN: 978-3-89336-368-1
23. **Development of Ellipsometric Microscopy as a Quantitative High-Resolution Technique for the Investigation of Thin Films at Glass-Water and Silicon-Air Interfaces**  
by F. Linke (2004), 135 pages  
ISBN: 978-3-89336-373-5
24. **Caucasian-German School and Workshop on Hadron Physics**  
Organizing Committee: M. Büscher, A. Kacharava, M. Nioradze, F. Rathmann, H. Ströher (2004), CD-ROM  
ISBN: 978-3-89336-375-9
25. **6<sup>th</sup> ANKE Workshop on Strangeness Production on Nucleons and Nuclei**  
Organizing Committee: M. Büscher, V. Kleber, Y. Valdau (2004), CD-ROM  
ISBN: 978-3-89336-376-6

26. **Magnetism goes Nano**  
Lecture manuscripts of the 36<sup>th</sup> IFF Spring School February 14 – 25, 2005, Jülich, Germany  
edited by S. Blügel, T. Brückel, C. M. Schneider (2005), c. 1000 pages  
ISBN: 978-3-89336-381-0
27. **Hochfrequenzeigenschaften gepulster, supraleitender Halbwellenresonatoren zur Beschleunigung leichter Ionen**  
von R. Stassen (2005), VI, 128 Seiten  
ISBN: 978-3-89336-394-0
28. **Neutron Scattering**  
Lectures of the Laboratory course held at the Forschungszentrum Jülich  
edited by Th. Brückel, G. Heger, D. Richter, R. Zorn (2005), c. 500 pages  
New, revised edition of Materie und Material / Matter and Materials Volume 15  
ISBN: 978-3-89336-395-7
29. **K<sup>+</sup>-Meson Production in Nuclei**  
by M. Büscher (2005), 1 CD-ROM  
ISBN: 978-3-89336-398-8
30. **STORI'05**  
6<sup>th</sup> International Conference on Nuclear Physics at Storage Rings  
23–26 May 2005, Jülich – Bonn  
edited by D. Chiladze, A. Kacharava, H. Ströher (2005), c. 400 pages  
ISBN: 978-3-89336-404-6
31. **Wetting and Interdiffusion:  
Establishment of a Bio-compatible System and Studies of its Dynamics**  
by A.-K. Prechtel (2005), 139 pages  
ISBN: 978-3-89336-421-3
32. **Computational Condensed Matter Physics**  
Lecture manuscripts of the 37<sup>th</sup> IFF Spring School March 06 – 17, 2006, Jülich, Germany  
edited by S. Blügel, G. Gompper, E. Koch, H. Müller-Krumbhaar, R. Spatschek, R. G. Winkler (2006), c. 1000 pages  
ISBN: 978-3-89336-430-5
33. **Spin in Hadron Physics**  
2<sup>nd</sup> Caucasian-German School and Workshop on Hadron Physics  
Organizing Committee: A. Kacharava ... (2006), CD-ROM  
ISBN: 978-3-89336-453-4

34. **Probing the Nanoworld**  
Microscopies, Scattering and Spectroscopies of the Solid State  
Lecture manuscripts of the 38th IFF Spring School March 12 – 23, 2007  
Jülich, Germany  
edited by K. Urban, C. M. Schneider, T. Brückel, S. Blügel, K. Tillmann, W. Schweika, M. Lentzen, L. Baumgarten (2007), c. 1000 pages  
ISBN: 978-3-89336-462-6
35. **Future Perspectives of European Materials Research**  
edited by G. Schumacher, St. Preston, A. Smith, St. Reschke (2007), c. 80 pages  
ISBN: 978-3-89336-477-0
36. **Physics of more than 11 years of COSY-11 – history, status, achievements, plans**  
edited by J. Przerwa, D. Grzonka, P. Klaja, P. Moskal, W. Oelert (2007), 127 pages  
ISBN: 978-3-89336-483-1
37. **ANKE/PAX Workshop on SPIN PHYSICS, Ferrara 2007**  
Organizing Committee: G. Ciullo, A. Kacharava, P. Lenisa, F. Rathmann, H. Ströher (2007), CD-ROM  
ISBN: 978-3-89336-487-9
38. **Neutron Scattering**  
Lectures of the JCMS Laboratory Course held at Forschungszentrum Jülich and the research reactor FRM II of TU Munich  
edited by Th. Brückel, G. Heger, D. Richter, R. Zorn (2007), c. 500 pages  
New, revised edition of Materie und Material / Matter and Materials Volume 28  
ISBN: 978-3-89336-489-3
39. **Magnetic and structural properties of thin films and nanoparticles studied by scattering methods**  
by M. Feygenson (2007), III, 121 pages  
ISBN: 978-3-89336-490-9
40. **Electronic Structure of Ferromagnet-Insulator-Interfaces: Fe/MgO and Co/MgO**  
by M. Müller (2007), 110 pages  
ISBN: 978-3-89336-493-6
41. **Theory of Magnetic Transition Metal Nanoclusters on Surfaces**  
by S. Lounis (2007), XII, 189 pages  
ISBN: 978-3-89336-501-2

Forschungszentrum Jülich  
*in der Helmholtz-Gemeinschaft*



**Band / Volume 41**  
**ISBN 978-3-89336-501-2**

**Materie und Material**  
**Matter and Materials**